Identifying time-varying multimodal manual control using recursive ARX model techniques

Final Thesis Report

M.J.J. Linssen

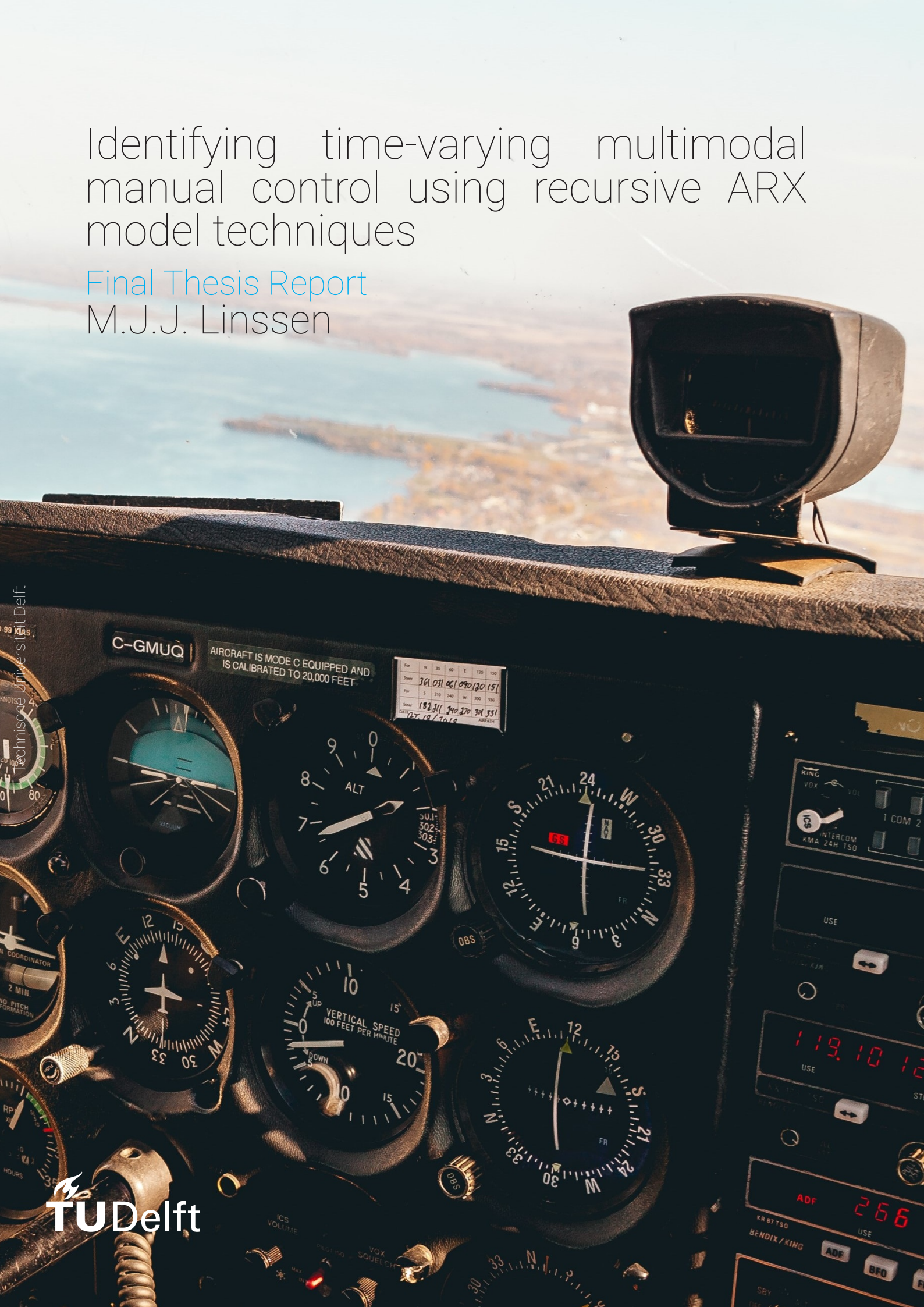

TU Delft

Identifying time-varying multimodal manual control using recursive ARX model techniques

Final Thesis Report

by

M.J.J. Linssen

to obtain the degree of Master of Science

Faculty of Aerospace Engineering · Delft University of Technology

Supervised by:

Dr. Ir. D.M. Pool
Prof. Dr. Ir. M. Mulder

January 14, 2020

TU Delft

Faculty of Aerospace Engineering
Department of Control & Operations, Section Control & Simulation

Delft, the Netherlands

The undersigned hereby certify that they have read, and recommend to the Faculty of Aerospace Engineering for acceptance, a thesis entitled: **"Identifying time-varying multimodal manual control using recursive ARX model techniques"**, by **M.J.J. Linssen**, in partial fulfillment of the requirements for the degree of **Master of Science**.

Dated: _____

Assessment Committee:

Professor: _____

Prof. dr. ir. M. Mulder

Daily Supervisor: _____

Dr. ir. D.M. Pool

External Examiner: _____

Dr. O.A. Sharpans'kykh

Preface

This final thesis report covers the complete thesis work that was done in order to obtain the degree of Master of Science in Aerospace Engineering at Delft University of Technology. In Part I a scientific paper is included covering the main results of this research. The paper focuses on the identification of multimodal time-varying manual control using recursive ARX identification. Part II contains the preliminary thesis report covering a literature study in multimodal time-varying manual control and recursive identification methods as well as results of a MATLAB simulation that was used for verification of the multimodal recursive ARX identification method. Part III contains appendices with additional results and supporting material. Both Part I and III are meant for the final thesis work AE5310, part II was already graded for the literature study AE4020.

I would like to thank Daan for providing me with exceptional supervision during all stages of this thesis. Not only did he engage me in interesting and profound discussions on the subject, but he also motivated me to deliver the best performance possible. His constructive feedback made it possible to lift this report to a higher level. Furthermore I want to thank Max for his enthusiasm and interest in my work and challenging me to understand this topic better and better. Lastly I want to thank family and friends, especially Marèse, for their continuous support during my thesis and the past years in Delft.

M.J.J. (Menno) Linssen
January 14, 2020

Cover image: William Topa

Contents

List of Figures

List of Tables

List of Symbols

Latin Symbols

a_{n_a}	ARX coefficient A polynomial	-
A_n	Forcing function amplitude	deg
$A(q)$	ARX model output polynomial	-
b_{n_b}	ARX coefficient B polynomial	-
$B(q)$	ARX model input polynomial	-
B_r	ARX model bias	-
e	Error signal	deg
f	Forcing function signal	deg
G	Sigmoid maximum rate of change	s^{-1}
$H_{CE}(j\omega)$	Continuous time controlled element transfer function	-
$H_{CE_{cl}}(j\omega)$	Continuous time closed-loop controlled element transfer function	-
$H_{HO}(j\omega)$	Continuous time human operator model transfer function	-
$H_n^m(j\omega)$	Continuous time remnant filter transfer function	-
$H_{ol}(j\omega)$	Continuous time open-loop transfer function	-
$H_{ves}(j\omega)$	Continuous time vestibular sensory dynamics transfer function	-
i	Sample number	-
j	Imaginary unit	-
I	Identity matrix	-
K_c	Controlled element gain	-
K_e	Visual proportional error gain	-
$K_{\dot{e}}$	Visual derivative error gain	-
$K[i]$	ARX RLS gain vector	-
K_n	Remnant filter gain	-
K_p	Visual error gain	-
K_x	Vestibular feedback gain	-
K_δ	SAS proportional gain	-
K_θ	SAS rate gain	-
n	Remnant signal	deg
N	Number of samples	-
n_a	Number of coefficients A polynomial	-
n_b	Number of coefficients B polynomial	-
n_k	Time delay coefficient	-
$P[i]$	ARX RLS Covariance matrix	-

p_f	Final parameter value	-
p_i	Initial parameter value	-
P_n	Remnant power	-
q	Discrete time shift operator	-
t	Simulation time	s
T_I	Visual lead time constant	s
T_L	Visual lag time constant	s
t_M	Sigmoid time of maximum rate of change	s
T_m	Measurement time	s
T_n	Remnant filter time constant	s
u	Control signal	deg
$\hat{u}$	Predicted control signal	deg
V	Fit criterion	-
w	Zero mean unit variance Gaussian white noise	deg
x	Output signal	deg
z	Discrete time Laplace variable	-

Greek Symbols

Δ	Difference	-
ϵ	ARX RLS model difference	deg
ζ_{nm}	Neuromuscular damping ratio	-
θ	ARX coefficient vector	-
$\hat{\theta}$	Predicted ARX coefficient vector	-
λ	ARX RLS forgetting factor	-
Λ	ARX RLS forgetting matrix	-
σ_n^2	Remnant signal variance	deg^2
σ_u^2	Control signal variance	deg^2
τ_e	Visual time delay	s
τ_{v1}	Vestibular sensory dynamics lead time constant	s
τ_{v2}	Vestibular sensory dynamics lag time constant	s
τ_x	Vestibular time delay	s
$\phi[i]$	Regression vector	-
$\Phi[i]$	Regression matrix	-
ϕ_n	Forcing function phase shift	rad
ω	Frequency	rad/s
ω_b	Controlled element break frequency	rad/s
ω_m	Forcing function base frequency	rad/s
ω_{nm}	Neuromuscular natural frequency	rad/s

Subscripts

d	Disturbance forcing function
del	Delayed signal
e	Visual feedback channel
t	Target forcing function
x	Vestibular feedback channel

Superscripts

c	Continuous time
d	Discrete time
m	Model order

List of Abbreviations

ARX	Autoregressive Exogenous
CE	Controlled Element
DI	Double Integrator Dynamics
FRF	Frequency Response Function
LPV	Linear Parameter Varying
LTI	Linear Time Invariant
MLE	Maximum Likelihood Estimate
OLS	Ordinary Least Squares
RLS	Recursive Least Squares
SAS	Stability Augmentation System
SI	Single Integrator Dynamics
SRS	SIMONA Research Simulator
TV	Time-Varying
VAF	Variance Accounted For

I

SCIENTIFIC ARTICLE

To be graded for AE5310 Final Thesis

Identifying time-varying multimodal manual control using recursive ARX model identification

M.J.J. Linssen *
Delft University of Technology, Faculty of Aerospace Engineering, the Netherlands

Supervised by: D.M. Pool † and M. Mulder ‡
Delft University of Technology, Faculty of Aerospace Engineering, the Netherlands

A better understanding of time-varying multimodal human operator control behaviour is required for the development of advanced adaptive control support systems for cases when vehicle dynamics suddenly change, e.g., a stability augmentation system failure. In this paper, an approach based on recursive autoregressive exogenous (ARX) models is verified and validated for the identification of time-varying multimodal manual control in compensatory tracking tasks. The multimodal recursive ARX method is an extension of the unimodal recursive ARX method developed in earlier work. The verification of the recursive multimodal ARX method was performed by means of Monte-Carlo simulations. The validation of this method is based on the identification results of a human-in-the-loop experiment. Both for the verification and validation it was investigated which forgetting method of the recursive least squares algorithm resulted in the estimates for the ARX coefficients and human operator model parameters with the best model fit. A forgetting matrix with an infinite memory horizon for the coefficients of the $A(q)$ polynomial and a memory horizon of 5 seconds for the coefficients of the $B(q)$ polynomials was found optimal for both tasks with time-varying as well as linear time-invariant controlled element dynamics. The estimation results for the human operator model parameters gathered during the human-in-the-loop experiment were in line with the results that were found in literature. With this multimodal identification method now verified and validated, the potential for application in the development of online adaptive support systems for the flight deck can be investigated in future work.

Nomenclature

a_{n_a}	ARX coefficient A polynomial	-	j	Imaginary unit	-
A_n	Forcing function amplitude	deg	I	Identity matrix	-
$A(q)$	ARX model output polynomial	-	K_c	CE gain	-
b_{n_b}	ARX coefficient B polynomial	-	K_e	Visual proportional error gain	-
$B(q)$	ARX model input polynomial	-	$K_{\dot{e}}$	Visual derivative error gain	s
B_r	ARX model bias	-	$K[i]$	ARX RLS gain vector	-
e	Error signal	deg	K_n	Remnant filter gain	-
f	Forcing function signal	deg	K_x	Vestibular feedback gain	-
G	Max rate of change	s^{-1}	K_δ	SAS proportional gain	-
$H_{CE}(s,t)$	Time-varying CE dynamics	-	K_θ	SAS rate gain	-
$H_{HO}(s,t)$	Time-varying HO dynamics	-	n	Remnant signal	deg
i	Sample number	-	N	Number of samples	-

*MSc. Student, Control and Simulation Division, Faculty of Aerospace Engineering, Delft University of Technology, P.O. Box 5058, 2600 GB Delft, the Netherlands; m.j.j.linssen@student.tudelft.nl. Student Member AIAA

†Associate Professor, Control and Simulation Division, Faculty of Aerospace Engineering, Delft University of Technology, P.O. Box 5058, 2600 GB Delft, the Netherlands; d.m.pool@tudelft.nl. Member AIAA

‡Professor, Control and Simulation Division, Faculty of Aerospace Engineering, Delft University of Technology, P.O. Box 5058, 2600 GB Delft, the Netherlands; m.mulder@tudelft.nl. Associate Fellow AIAA

n_a	Number of coefficients $A(q)$	-	τ_e	Visual time delay	s
n_b	Number of coefficients $B(q)$	-	τ_x	Vestibular time delay	s
n_k	Time delay coefficient	-	$\varphi[i]$	Regression vector	-
$P[i]$	ARX RLS Covariance matrix	-	$\Phi[i]$	Regression matrix	-
P_n	Remnant power	-	ϕ_n	Forcing function phase shift	rad
q	discrete-time shift operator	-	ω	Frequency	rad/s
t	Simulation time	s	ω_b	CE break frequency	rad/s
t_M	Time of maximum rate of change	s	ω_m	Forcing function base frequency	rad/s
T_n	Remnant filter time constant	s	ω_{nm}	Neuromuscular natural frequency	rad/s
u	Control signal	deg			
$\hat{u}$	Predicted control signal	deg	**Subscripts**		
w	Gaussian white noise	deg	d	Disturbance forcing function	
x	Output signal	deg	del	Delayed signal	
ϵ	ARX RLS model difference	deg	e	Visual feedback channel	
ζ_{nm}	Neuromuscular damping ratio	-	t	Target forcing function	
θ	ARX coefficient vector	-	x	Vestibular feedback channel	
$\hat{\theta}$	Predicted ARX coefficient vector	-			
λ	ARX RLS forgetting factor	-	**Superscripts**		
Λ	ARX RLS forgetting matrix	-	c	continuous-time	
σ_n^2	Remnant signal variance	deg^2	d	discrete-time	
σ_u^2	Control signal variance	deg^2	m	Model order	

I. Introduction

Since the invention of the first autopilot, automation has been on the rise in aviation. It has replaced many skill-based manual flying tasks and created a safer environment for passengers and crew by mitigating human errors due to fatigue, boredom and complacency during routine work. The reason for still including the pilot in the complex vehicle-controller system is that human operators have a highly adaptable nature [1]. This is an essential characteristic when, for instance, a subsystem breaks down and automation stops working. Pilots must control the aircraft adequately and safely without the aid of automation in these cases, for which proper training is required. To improve aircraft control design and pilot training, knowledge is required on how pilots adapt to changing task demands.

Developing manual control models is essential for understanding how operators control dynamic systems and therefore assist in improving aircraft design and pilot training [2]. The Crossover Model by McRuer and Jex [3] is considered a good foundation, however, this model is only valid for unimodal, linear and time-invariant control tasks. Considering that in most real-life scenarios pilots experience motion feedback, multimodal manual control models with a vestibular feedback loop provide a better representation of the actual situation. Of specific interest are multimodal models which describe how human operators adapt when confronted with a change in the control task [2]. Recursive identification methods allow for an analysis of adaptive manual control behaviour as the models are evaluated at every time step and therefore capture changes in human control behaviour without imposing a priori assumptions [4–9].

Considerable advancements in the use of recursive methods for the identification of time-varying manual control have been made by making use of Kalman Filters [4–7] or ARX identification techniques [8, 9]. Research only focused on manual control in tasks with time-varying system dynamics without vestibular feedback, however. Simultaneously, more research has been done in the field of identifying time-invariant multimodal manual control [10–16]. Zaal and Pool [17] attempted to bridge the gap by developing a time-varying, multimodal human operator model, but did so by making use of a Maximum Likelihood Estimate algorithm for which a priori assumptions on the variations of human operator model parameters were required. To date, no effort has been made to develop a time-varying multimodal human operator identification technique based on recursive methods that does not require any a priori assumptions on the exact nature and dynamics of the control behaviour adaptations.

Previous research has shown that the presence of vestibular feedback, as well as a change in the controlled dynamics each affect human control behaviour in a different way [4–17]. Pool [13] found that when vestibular feedback is presented to the human operator, the visual gain increases and the visual lead time constant decreases compared to runs without motion feedback. When multiple feedback loops are presented, the feedback path that results in the best performance with the least effort will be selected [18]. Plaetinck et al. [9] found that when the control task increases in difficulty during a run, the visual gain slightly decreases and the visual lead time constant increases. It is yet unknown if it is possible to reliably separate human visual and vestibular responses with a time-varying algorithm.

This paper verifies and validates a recursive ARX identification technique for time-varying multimodal human operator identification. For the verification of the method, Monte-Carlo human control model simulations were performed in which the influence of the memory horizon of the recursive identification algorithm and the presence of remnant was evaluated. In addition, validation was performed, based on experimental data that were gathered during a dedicated human-in-the-loop experiment. For this experiment, 16 participants were asked to perform a compensatory tracking task with time-varying controlled element (CE) dynamics, similar to the fast adaptation conditions previously tested by Van Grootheest et al. [8] and Plaetinck et al. [9], expanded to conditions in which vestibular feedback was provided. Finally, the effects of motion feedback on time-varying manual control were explicitly analysed by comparing the results of the newly developed time-varying multimodal method with those of both state-of-the-art time-varying unimodal methods and time-invariant multimodal methods.

This paper is structured as follows. First, the multimodal time-varying compensatory control task is presented in Section II, after which the proposed multimodal ARX identification method will be presented in detail in Section III. Next, the verification of the recursive identification method based on simulation data is given in Section IV. Section V describes the validation of the method based on real human operator data. The identification results of the experiment will be presented in Section VI. A discussion of all findings can be found in Section VII, after which the conclusions are presented in Section VIII.

II. Control Task

In order to develop the time-varying multimodal human operator (HO) identification method, a control task equivalent to the task defined by Zaal [19] was selected. The block diagram of the task is shown in Figure 1. In this block diagram the HO controls the output x of a CE that is augmented with a stability augmentation system (SAS) by providing a control input u and attempts to minimize the error e between the target signal f_t and x. Furthermore, the system output is perturbed by a disturbance signal f_d. The HO perceives visual feedback by means of the error shown on the primary flight display, as well as vestibular feedback perceived by the semi-circular canals.

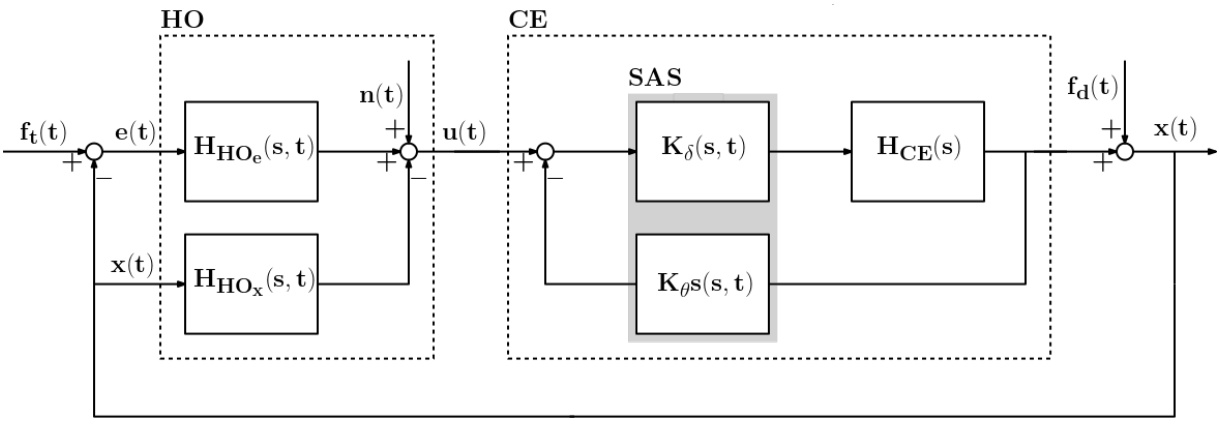

Fig. 1 Block diagram of the multimodal compensatory tracking task

A. Controlled Element Dynamics

To investigate how HO's change their control behaviour in time-varying control tasks, Zaal [19] used a CE block for which the parameters were changed during the run. Although the selected CE dynamics were suitable for the analysis of time-varying HO manual control behaviour, the reasoning behind the change in CE dynamics lacked a physical interpretation. For this research, the change in dynamics is represented by an SAS that is switched "on" or "off" during the experiment runs which results in different closed-loop CE dynamics. The time-invariant basic CE dynamics H_{CE} are given by Equation (1). The stability augmented time-varying CE dynamics $H_{CE_{SAS}}$ including the SAS are given by Equation (2).

$$H_{CE}(s) = \frac{K_c}{s(s+\omega_b)} = \frac{30}{s(s+0.2)} \tag{1}$$

$$H_{CE_{SAS}}(s,t) = \frac{K_\delta(t)H_{CE}(s)}{1 + K_\delta(t)K_\theta(t)sH_{CE}(s)} = \frac{30K_\delta(t)}{s(s+0.2+30K_\delta(t)K_\theta(t))} \tag{2}$$

The SAS consists of a proportional gain K_δ and rate feedback $K_\theta s$ that are changed in a sigmoidal fashion similar to Zaal [19]. The values for the gains K_δ and K_θ are chosen such that the closed-loop dynamics are equal to those used by Zaal [19], leading to a case with approximately single integrator (SI) CE dynamics and one with double integrator (DI) CE dynamics. The sigmoids for both SAS gains are shown in Figure 2. For the sigmoidal change, a rate of change G = 100 s^{-1} is chosen to resemble an instantaneous failure of the SAS, approximating a step-like change. A total run time of 100 seconds was chosen of which the first 10 seconds were discarded as run-in time and the remaining 90 seconds of measurement time were divided over three equal portions, later on referred to as Window 1, Window 2 and Window 3. The three windows are visualized in Figure 2. Window 2 contained the change in the CE dynamics which occurred halfway through the measurement time of the run at t = 55 s, denoted by the red dashed line in Figure 2. The CE dynamics are time-invariant for the initial and final 30 second time spans of Window 1 and Window 3, which are shaded grey, leading to a steady-state HO response. The corresponding Bode plots of the CE dynamics are shown in Figure 3. The Bode plots show that if the SAS is switched "on", the closed-loop CE dynamics in the crossover domain can be considered SI dynamics, and if it is switched "off", the dynamics approximate DI dynamics.

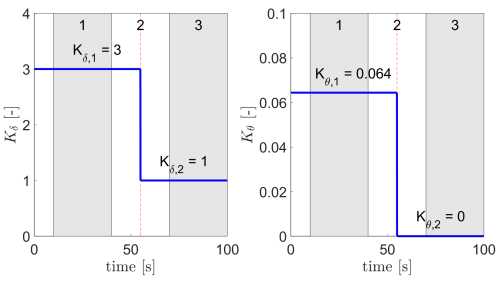

Fig. 2 Change in SAS gains when switched off in the middle of the run

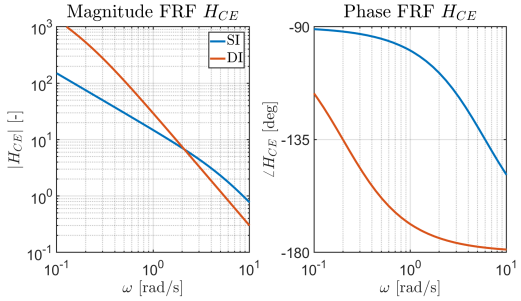

Fig. 3 Bode plot of the steady-state SI and DI CE dynamics

B. Human Operator Model

The multimodal HO model that was used during the identification phase consists of a visual feedback block H_{HO_e}, as shown in Equation (3), and a vestibular feedback block H_{HO_x}, as shown in Equation (4). The visual HO response function, also known as the Extended Crossover Model, was validated by McRuer and Jex [3] for time-invariant control tasks. In later research, this visual HO model was validated for time-varying control tasks by Zaal [19], Van Grootheest et al. [8] and Plaetinck et al. [9]. The vestibular HO response function as used in a parallel multichannel HO model was proposed and validated by Van der Vaart [20] for time-invariant control tasks. Zaal and Pool [17] validated the vestibular HO model for time-varying control tasks. This multimodal HO model has been successfully used in previous research [10–13, 15–17, 21].

$$H_{HO_e}(s,t) = \left(K_e(t) + K_{\dot{e}}(t)s\right)e^{-s\tau_e}H_{nm}(s,t) \tag{3}$$

$$H_{HO_x}(s,t) = K_x(t)se^{-s\tau_x}H_{nm}(s,t) \tag{4}$$

The equalization terms are governed by the visual error gain K_e and visual error rate gain $K_{\dot{e}}$ for the visual HO model and the motion gain K_x for the vestibular HO model. The error rate gain $K_{\dot{e}}$ is equal to the multiplication of the visual gain K_e and lead time T_L in the form of the models used by McRuer and Jex [3], but avoids the identification ambiguities inherent to this form for high T_L [9]. The human operator responses both have their own time delay terms τ_e and τ_x and include the same neuromuscular dynamics H_{nm}, which is parametrized with the neuromuscular natural frequency ω_{nm} and damping ratio ζ_{nm}, as shown in Equation (5).

$$H_{nm}(s,t) = \frac{\omega_{nm}^2(t)}{s^2 + 2\zeta_{nm}(t)\omega_{nm}(t)s + \omega_{nm}^2(t)} \tag{5}$$

Based on earlier work [8, 9], five of the parameters of the model are assumed to vary over time $\left(K_e, K_{\dot{e}}, K_x, \omega_{nm}, \zeta_{nm}\right)$ and are estimated recursively. Both time delays are assumed constant for each of the presented CE dynamics for which they were estimated with a time-invariant ARX estimation algorithm, but can thus change during the experiment run if the dynamics are changed. The time delays are assumed to change in a similar sigmoidal fashion as the CE dynamics for runs with time-varying dynamics. More information on the identification of the HO model is presented in Section III. The remnant is not explicitly modelled and is considered the residue between the measured control input and both the modelled HO outputs [3, 22].

C. Forcing Functions

The target forcing function f_t and disturbance forcing function f_d used in the control task are both multisine signals with the number of sinusoids N_{sin} equal to 10. Each sinusoid, its number denoted by n, has its own amplitude A_n, frequency $k_n\omega_m$ and phase shift ϕ_n, as shown in Equation (6).

$$f(t) = \sum_{n=1}^{N_{sin}} A_n \sin(k_n\omega_m t + \phi_n) \tag{6}$$

To be able to equally compare the HO's steady-state behaviour pre and post transition, no artefacts should arise from the forcing function difficulty, which biased the analysis in Zaal and Pool [17]. It was chosen to repeat the forcing function every 30 seconds as is shown in Figure 4. Hence, the HO's control is independent of the forcing function difficulty for both the windows with time-invariant CE dynamics. For a measurement time of 30 seconds, the base frequency ω_m is equal to 0.2094 rad/s. The numerical properties of both forcing functions are given in Table 1.

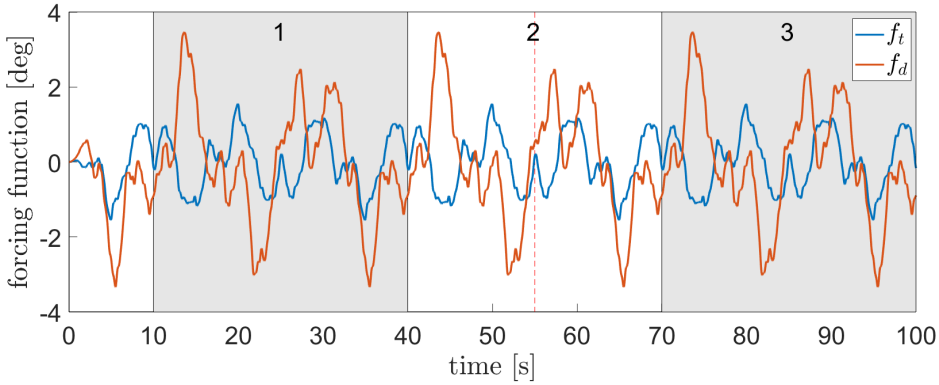

Fig. 4 Time traces of forcing function signals

Table 1 shows that the amplitudes for the target forcing function are approximately half the amplitudes of the disturbance forcing function. This was done to make it predominantly a disturbance-rejection control task [11]. For disturbance-rejection tasks, the forcing function directly influences the system output. Vestibular motion cues are perceived faster than visual motion cues, increasing pilot performance [13]. Four different realizations of both forcing functions are generated by selecting a random phase shift for each of the multisine frequencies. By doing so, participants are presented with different combinations of forcing functions during the experiment phase, preventing them to remember and anticipate a change in dynamics after a certain forcing function dynamism.

Table 1 Frequency, amplitude and phase shift forcing functions

	f_t Parameter Values						
n [-]	$k_{n,t}$ [-]	$\omega_{n,t}$ [rad/s]	$A_{n,t}$ [rad]	$\phi_{n,t,1}$ [rad]	$\phi_{n,t,2}$ [rad]	$\phi_{n,t,3}$ [rad]	$\phi_{n,t,4}$ [rad]
1	3	0.6283	0.0155	1.8008	1.3088	4.2877	4.6594
2	7	1.4661	0.0084	2.7231	4.0056	2.7890	3.5559
3	11	2.3038	0.0047	0.1897	2.3724	3.2533	4.9210
4	17	3.5605	0.0024	0.0507	4.5767	4.4919	5.5860
5	21	4.3982	0.0018	3.9391	3.6275	0.6555	5.9137
6	29	6.0737	0.0011	0.4741	5.8126	0.1391	3.6184
7	41	8.5870	0.0007	5.6030	3.1568	3.5551	3.7204
8	53	11.1003	0.0006	6.2293	4.1400	6.0887	3.4432
9	71	14.8702	0.0005	0.3548	3.5109	2.3544	5.4860
10	87	18.2212	0.0004	0.7741	3.0082	1.6882	5.7340

	f_d Parameter Values						
n [-]	$k_{n,d}$ [-]	$\omega_{n,d}$ [rad/s]	$A_{n,d}$ [rad]	$\phi_{n,d,1}$ [rad]	$\phi_{n,d,2}$ [rad]	$\phi_{n,d,3}$ [rad]	$\phi_{n,d,4}$ [rad]
1	2	0.4189	0.0291	1.9864	4.4771	5.5149	2.8416
2	5	1.0472	0.0192	5.8760	1.3299	6.0377	3.3197
3	9	1.8850	0.0102	0.2433	1.2588	3.2878	0.7182
4	13	2.7227	0.0060	2.7584	2.6748	0.2975	0.7687
5	19	3.9794	0.0034	5.8004	5.3686	4.6609	2.9249
6	27	5.6549	0.0020	0.0668	2.6944	4.3559	5.1453
7	39	8.1681	0.0012	3.5067	4.9951	2.1447	2.0855
8	51	10.6814	0.0009	3.5714	3.5500	4.2549	0.3834
9	67	14.0324	0.0008	2.1492	0.6432	0.8442	0.7629
10	83	17.3835	0.0007	3.0233	5.2846	0.3753	3.2475

D. Test Conditions

For the simulations and the human-in-the-loop experiment a number of test conditions with different CE dynamics were defined. These conditions were chosen to facilitate the explicit analysis of the effects of motion feedback on time-varying manual control and direct comparison with corresponding time-invariant human operator dynamics. This implied that both time-varying and time-invariant closed-loop CE dynamics were needed for the analysis. It was chosen to have two conditions with fully time-invariant CE dynamics, i.e. the SI and DI CE dynamics of Equation 2, and two time-varying conditions with a transition from SI to DI CE dynamics or vice versa. In addition, to be able to verify the effects of added "physical" feedback, all the aforementioned CE dynamics settings were tested with and without the presence of motion feedback. The set of conditions (C1 - C8) is shown in Table 2. The conditions without vestibular feedback (C1 - C4) are identical to those considered by Zaal [19], Plaetinck et al. [9] and Van Grootheest et al. [8].

Table 2 Testing conditions for time-varying, multimodal manual control research

	No Motion		Motion	
	Con	CE	Con	CE
LTI CE	C1	SI	C5	SI
	C2	DI	C6	DI
TV CE	C3	SI $\Rightarrow$ DI	C7	SI $\Rightarrow$ DI
	C4	DI $\Rightarrow$ SI	C8	DI $\Rightarrow$ SI

III. Identification Method

In this paper an ARX model structure is used for the identification of human operator behaviour [23]. To be able to separate identification issues due to the ARX model structure (i.e., a bias [8]) from issues due to recursive parameter estimation, both a time-invariant Ordinary Least Squares (OLS) and time-varying Recursive Least Squares (RLS) algorithm were used to estimate the ARX model coefficients. To obtain estimates of the HO model parameters defined in Section II, the ARX coefficients were converted to HO model parameters.

A. Model Structure

To estimate the ARX coefficients for multimodal HO models a multichannel ARX model structure as used by Nieuwenhuizen et al. [10] is implemented. A block diagram of this multichannel ARX model structure and the corresponding mathematical expressions can be found in Figure 5 and Equation (7). Equations (8) to (10) give an expression for the $A(q)$ and $B(q)$ polynomials with n_a and n_b coefficients in discrete-time (denoted by the superscript d), respectively.

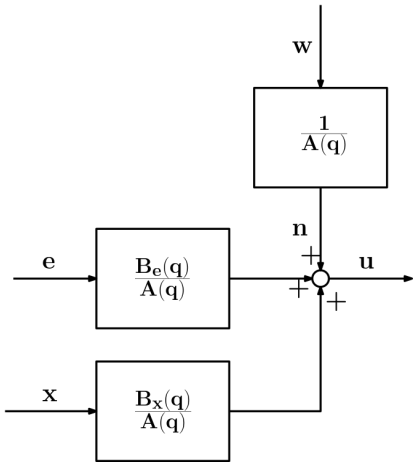

$$u(t) = \frac{B_e(q)}{A(q)} e(t - n_{k_e}) + \frac{B_x(q)}{A(q)} x(t - n_{k_x}) + \frac{1}{A(q)} w(t) \tag{7}$$

$$A(q) = 1 + a_1^d q^{-1} + a_2^d q^{-2} + \cdots + a_{n_a}^d q^{-n_a} \tag{8}$$

$$B_e(q) = b_{0_e}^d q^{-1} + b_{1_e}^d q^{-2} + \cdots + b_{n_{b\,e}}^d q^{-n_{b\,e}} \tag{9}$$

$$B_x(q) = b_{0_x}^d q^{-1} + b_{1_x}^d q^{-2} + \cdots + b_{n_{b\,x}}^d q^{-n_{b\,x}} \tag{10}$$

Fig. 5 Block diagram of ARX model structure

In the multichannel ARX model, the $A(q)$ and both of the $B(q)$ polynomials are a function of a discrete-time shift operator q^{-n} that acts on the error signal e, system output signal x and control signal u according to $q^{-1}u(t) = u(t-1)$. Figure 5 shows that the visual and vestibular HO models are defined by the expressions $\frac{B_e(q)}{A(q)}$ and $\frac{B_x(q)}{A(q)}$, respectively. Here, all ARX polynomials have been assigned a model order of 2 to be able to directly convert the model coefficients to HO model parameters without using model order reduction [8, 9]. The expression for the visual and vestibular ARX HO model structures can be found in Equations (11) and (12). As can be seen in this set of equations, 8 coefficients need to be identified. The 6 ARX coefficients of the $A(q)$ and $B(q)$ polynomials were estimated with the OLS and RLS ARX algorithms, which will be explained in the next two subsections. Afterwards, the discrete-time delay coefficients n_{k_e} and n_{k_x} were determined by means of a model fit. The model fit was based on a comparison of the measured control input and the predicted control input that was generated with the estimated ARX coefficients, which will also be explained in the next subsection.

$$H_{HO_e}(q) = \frac{B_e(q)}{A(q)} q^{-n_{k_e}} = \frac{b_{0_e}^d + b_{1_e}^d q^{-1}}{1 + a_1^d q^{-1} + a_2^d q^{-2}} q^{-n_{k_e}} \tag{11}$$

$$H_{HO_x}(q) = \frac{B_x(q)}{A(q)} q^{-n_{k_x}} = \frac{b_{0_x}^d + b_{1_x}^d q^{-1}}{1 + a_1^d q^{-1} + a_2^d q^{-2}} q^{-n_{k_x}} \tag{12}$$

Note from Figure 5 that the remnant noise is accounted for in the ARX model by means of the inverse of the $A(q)$ polynomial. As the linear ARX model dynamics are also dependent on the $A(q)$ polynomial, the noise is (unfortunately) coupled to the HO models, which leads to a bias in the ARX model coefficient estimation [8, 9]. During the verification of the identification method the magnitude of this bias was inspected.

B. OLS Algorithm

The OLS algorithm is a batch mode method and therefore results in one set of optimized model coefficients over the entire window of data that is used for the analysis. The estimation algorithm makes use of the coefficient vector θ and regression vector $\varphi[i]$, which are shown in Equations (13) and (14).

$$\theta = \begin{pmatrix} a_1^d & a_2^d & b_{0_e}^d & b_{1_e}^d & b_{0_x}^d & b_{1_x}^d \end{pmatrix}^T \tag{13}$$

$$\varphi[i] = \begin{pmatrix} -u[i-1] & -u[i-2] & e[i-n_{k_e}] & e[i-n_{k_e}-1] & -x[i-n_{k_x}] & -x[i-n_{k_x}-1] \end{pmatrix} \tag{14}$$

When the ARX coefficients are estimated with the OLS algorithm, the regression vector $\varphi[i]$ and control input $u[i]$ are replaced by a regression matrix Φ and control input vector U with all individual elements of the complete batch of the measurement time as shown in Equation (15) and (16). For runs with time-invariant CE dynamics, the OLS algorithm is applied to data for Window 1 up to Window 3 (t = 10 s up to t = 100 s), whereas for time-varying CE dynamics the data is analyzed for the steady-state Window 1 (t = 10 s up to t = 40 s) and Window 3 (t = 70 s up to t = 100 s) separately. By discarding the run-in time it is made sure that the HO has achieved a steady-state control situation and all transients have died out, as well as that there are no problems with shifting the error signal and system output signals with n_{k_e} and n_{k_x} steps, respectively as enough data points are available. The coefficient vector θ^{OLS}, containing the ARX coefficient estimates, can be found with Equation (17).

$$\Phi = \begin{pmatrix} \varphi[i] & \varphi[i+1] & \cdots & \varphi[n] \end{pmatrix}^T \tag{15}$$

$$U = \begin{pmatrix} u[i] & u[i+1] & \cdots & u[n] \end{pmatrix}^T \tag{16}$$

$$\theta^{OLS} = \left(\Phi^T \Phi\right)^{-1} \Phi^T U \tag{17}$$

As shown in Equations (11) and (12) and discussed in the previous section, the time delays were estimated separately from the ARX model structure identification algorithms. This is done by running the OLS algorithm for a range of time delays and quantifying the model fit for each combination of n_{k_e} and n_{k_x}. The combination that results in the best model fit is selected as the optimal set of time delays. The quality of fit is calculated with the Variance Accounted For (VAF), as is presented in Equation (18). The VAF is based on the measured control input $u[i]$ and the predicted control $\hat{u}[i]$ input that was reconstructed from the estimated parameter set and corresponds to the percentage of the variation explained by the predicted control input $\hat{u}[i]$. A lower bound of 0% is imposed, meaning that the variation cannot be explained by the predicted control input. First, the VAF is calculated by implementing visual delays starting from n_{k_e} = 11 up until n_{k_e} = 41 and vestibular delays starting from n_{k_e} = 1 up until n_{k_e} = 31, all with increments of 5, resulting in a higher level delay approximation. Afterwards, the time delays that resulted in the best model fit and their adjacent values were selected for estimation of both time delays at the precision of a single time step.

$$\text{VAF} = \max\left(0, \left(1 - \frac{\sum_{i=1}^{N} \left|u[i] - \hat{u}[i]\right|^2}{\sum_{i=1}^{N} \left|u[i]\right|^2}\right) \cdot 100\%\right) \tag{18}$$

C. RLS Algorithm

In contrast to the OLS algorithm, the RLS algorithm implements a recursive least-squares method which implies that the estimated coefficient vector θ^{RLS} is updated at every time step. This makes it possible to track changes in the HO model parameters [8, 9]. The RLS algorithm is visualized in Figure 6 [24].

The RLS algorithm first calculates the predicted control input $\hat{u}[i]$ with Equation (19), which is then compared to the actual control input $u[i]$. The RLS gain $K^{RLS}[i]$ then determines to what extent the difference $\epsilon[i]$ is taken into account for the update of the coefficient vector $\theta^{RLS}[i]$ as can be found in Equation (20). The expression for the RLS gain is given by Equation (21).

$$\hat{u}[i] = \varphi[i]\theta^{RLS}[i-1] \tag{19}$$

$$\hat{\theta}^{RLS}[i] = \hat{\theta}^{RLS}[i-1] + K^{RLS}[i]\epsilon[i] \tag{20}$$

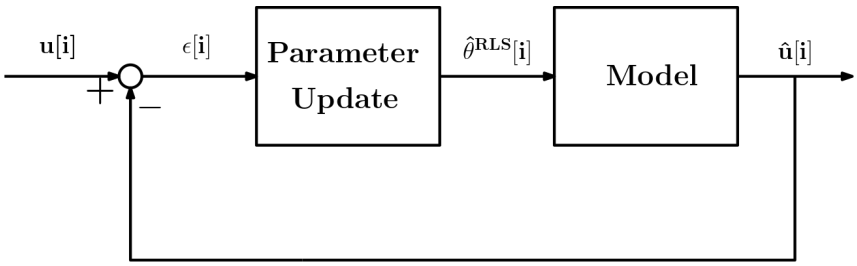

Fig. 6 Block diagram of an RLS algorithm, adapted from [24]

$$K^{RLS}[i] = \frac{\Lambda P[i-1]\Lambda}{1+\varphi[i]\Lambda P[i-1]\Lambda\varphi^T[i]}\varphi[i] \tag{21}$$

Two important variables that define the RLS gain are the covariance matrix $P[i]$ and the forgetting matrix Λ [8, 9]. Here, a forgetting matrix consists of a set of forgetting factors that may vary per ARX coefficient as is shown in Equation (22). The forgetting factor determines the memory horizon T_0 of the recursive algorithm according to Equation (23). This means that for the RLS ARX algorithm the estimation of past coefficient vectors θ^{RLS} affect the estimate of the next coefficient vector estimate. The values for the forgetting factors and corresponding memory horizons for a sampling frequency of 100 Hz that are tested in this research are listed in Table 3.

Table 3 Forgetting factors RLS ARX algorithm

λ	T_0
0.992	125
0.996	250
0.998	500
1	∞

$$\Lambda = \text{diag}\big(\lambda_{a_1},\ \lambda_{a_2},\ \lambda_{b_{0_e}},\ \lambda_{b_{1_e}},\ \lambda_{b_{0_x}},\ \lambda_{b_{1_x}}\big)^{-1/2} \tag{22}$$

$$T_0 = \frac{1}{1-\lambda} \tag{23}$$

$$P[i] = \Lambda P[i-1]\Lambda\big(I - K[i]\varphi[i]\big) \tag{24}$$

For $\lambda = 1$ an infinite memory horizon is used, meaning that all previous samples were used in the estimation procedure, which suppresses quick changes in coefficient values as time progresses. For $\lambda = 0.992$ only the previous 125 samples are taken into account, which means the coefficients are able to change quickly at any point during the estimation process. The forgetting factor implementation can therefore be considered a trade-off between tracking ability and noise suppression. The covariance matrix is updated at every time step as well, as given by Equation (24).

For the RLS algorithm to work, an initial coefficient estimate $\hat{\theta}_0^{RLS}$ and covariance matrix P_0 need to be provided. In this paper, the initial coefficient is based on the coefficients estimated with the OLS algorithm of the same data and the initial covariance matrix is taken similar to Van Grootheest et al. [8] and Plaetinck et al. [9], however, extended for applicability with multimodal HO identification. It was chosen to start the algorithm at $t = 5$ s to ensure that all transients have died out and no identification issues should arise with the inclusion of time shifts n_{k_e} and n_{k_x}.

D. Coefficient Conversion

The last step is to convert the estimated discrete-time ARX model coefficients to continuous-time HO model parameters. In order to do so, the ARX model is first rewritten to a discrete-time transfer function according to the Z-transform property $Z\big[q^{-n}f(i\Delta t)\big] = F(z)z^{-n}$, of which the result for the visual model H_{HO_e} is shown in Equation (25). Next, the discrete-time transfer function is converted to continuous-time (denoted by the superscript c) with a zero-order hold method for which the expression is found in (26). The continuous form of the vestibular HO model can be derived in a similar fashion.

$$H_{HO_e}(z) = \frac{b_{0_e}^d + b_{1_e}^d z^{-1}}{1 + a_1^d z^{-1} a_2^d z^{-2}} z^{-\frac{-\tau_e}{\Delta t}} \tag{25}$$

$$H_{HO_e}(s) = \frac{b^c_{0_e} s + b^c_{1_e}}{s^2 + a^c_1 s + a^c_2} e^{-\tau_e s} \tag{26}$$

By using this expression, together with the retrieved continuous vestibular HO model H_{HO_x}, the model parameters can be directly converted from the ARX model coefficients. The relationships between the ARX model coefficients and HO model parameters can be found in Equation (27). As can be seen in these relationships, the ARX coefficient b_{1_x} was not needed for the estimation of the HO model parameters, but was included nevertheless for the sake of completeness.

$$K_e = \frac{b^c_{1_e}}{a^c_2} \qquad K_{\dot{e}} = \frac{b^c_{0_e}}{a^c_2} \qquad K_x = \frac{b^c_{0_x}}{a^c_2} \qquad \omega_{nm} = \sqrt{a^c_2} \qquad \zeta_{nm} = \frac{a^c_1}{2\sqrt{a^c_2}} \tag{27}$$

IV. Verification: Simulations

A. Verification Goals

The method that was presented in the previous section has, to the best of the author's knowledge, never been used for the identification of time-varying multimodal manual control behaviour. However, earlier work provided the verification and validation of the recursive ARX method for capturing time-varying unimodal manual control in the same scenario [8, 9]. For the verification of this method, the same steps were carried out as done by Van Grootheest et al. [8]. Monte Carlo simulations of the aforementioned control task were performed to check the estimation results of this method. The input parameters for the simulations (i.e. reference data) were compared to the estimated values to find out if the verification of this method for identifying time-varying multimodal manual control behaviour was successful. The goals for the verification are as follows:

[S1] Show that the estimated ARX coefficients θ^{RLS} and θ^{RLS} for remnant-free simulations are exactly the same as the reference values θ^{REF}

[S2] Show that the conversion from ARX coefficients to HO model parameters for remnant-free simulations leads to exactly the input parameters for the HO model

[S3] Show that the multichannel recursive ARX method is able to converge to a new steady-state value after a transition in CE dynamics

[S4] Estimate the expected bias on the ARX coefficients and HO model parameter estimates for different remnant power ratios

[S5] Select the best forgetting matrix setting for the identification of simulation data for time-varying multimodal manual control

B. Simulation Setup

To be able to perform the verification of this identification method, simulations of a HO controlling time-varying CE dynamics were performed. The simulations were set up in discrete-time using state-space representations of the models of Figure 1. The CE dynamics in this simulation were equal to the dynamics described in Section II. The continuous-time state-space representation of the closed-loop CE dynamics is shown in Equation (28), which for the simulation was converted to discrete-time via the MATLAB `c2d`-command.

$$\begin{bmatrix} \dot{m}_1 \\ \dot{m}_2 \end{bmatrix} = \begin{bmatrix} 0 & 1 \\ 0 & -0.2 - 30K_\delta(t)K_\theta(t) \end{bmatrix} \begin{bmatrix} m_1 \\ m_2 \end{bmatrix} + \begin{bmatrix} 0 \\ 1 \end{bmatrix} u \qquad x = \begin{bmatrix} 30K_\delta(t) & 0 \end{bmatrix} \begin{bmatrix} m_1 \\ m_2 \end{bmatrix} \tag{28}$$

The continuous-time state-space representation of the multimodal HO model can be found in Equation (29). The parameters that define the equalization dynamics were taken from an initial test experiment in the SIMONA Research Simulator (SRS) with LTI CE dynamics. A verified OLS multimodal ARX identification technique was used to estimate the equalization parameters [10]. The settings for the equalization parameters for conditions without motion feedback present were in line with the results found by Plaetinck et al. [9]. Furthermore, the change in parameters that originates from adding vestibular feedback, being an increase in the visual gain K_e and motion gain K_x, was as expected [13]. Finally, it was observed that HO's do not use the available motion feedback path for SI CE dynamics conditions as

was found by Shirley and Young [25] and Lu [26]. The time delays for both the HO model blocks were set to values comparable to the ones found in literature [8–10, 13]. An overview of the HO model parameters used for the simulations can be found in Table 4.

Table 4 Parameter values human operator model for different CE dynamics

		HO Parameter Values						
	CE	K_e [-]	$K_{\dot{e}}$ [s]	K_x [-]	τ_e [s]	τ_x [s]	ω_{nm} [rad/s]	ζ_{nm} [-]
No Motion	SI	0.08	0.005	-	0.24	-	7.75	0.125
	DI	0.03	0.0175	-	0.24	-	7.75	0.125
Motion	SI	0.08	0.005	-	0.24	-	7.75	0.125
	DI	0.06	0.02	0.025	0.24	0.12	7.75	0.125

$$\begin{bmatrix} \dot{z}1_e \\ \dot{z}2_e \end{bmatrix} = \begin{bmatrix} 0 & 1 \\ -\omega_{nm}^2(t) & -2\zeta\omega_{nm}(t) \end{bmatrix} \begin{bmatrix} z1_e \\ z2_e \end{bmatrix} + \begin{bmatrix} 0 \\ 1 \end{bmatrix} e \qquad u_e = \begin{bmatrix} K_e(t)\omega_{nm}^2(t) & K_{\dot{e}}(t)\omega_{nm}^2(t) \end{bmatrix} \begin{bmatrix} z1_e \\ z2_e \end{bmatrix} \tag{29}$$

$$\begin{bmatrix} \dot{z}1_x \\ \dot{z}2_x \end{bmatrix} = \begin{bmatrix} 0 & 1 \\ -\omega_{nm}^2(t) & -2\zeta\omega_{nm}(t) \end{bmatrix} \begin{bmatrix} z1_x \\ z2_x \end{bmatrix} + \begin{bmatrix} 0 \\ 1 \end{bmatrix} x \qquad u_x = \begin{bmatrix} 0 & K_x(t)\omega_{nm}^2(t) \end{bmatrix} \begin{bmatrix} z1_x \\ z2_x \end{bmatrix} \tag{30}$$

The state-space representation of Equations (29) and (30) does not take the HO time delays into account directly, but the delays are accounted for by shifting the control signals in time as is shown in Equation (31). Bode plots of the simulated HO models can be found in Figures 7 and 8. Figure 7 clearly shows the lead generation in the frequency region in which HO's operate [1-5 Hz]. Figure 8 shows less difference between SI and DI CE dynamics because the lead generation is accounted for by the motion feedback. No data for the vestibular HO response for SI CE dynamics is shown in Figure 8, because the motion gain for this case is zero.

$$u_{e_{del}}[i] = u_e[i - n_{k_e}] \tag{31}$$

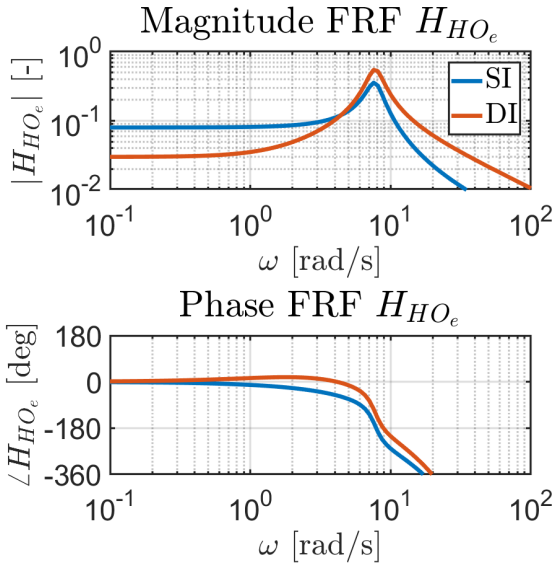

Fig. 7 Bode plot HO simulation without vestibular feedback

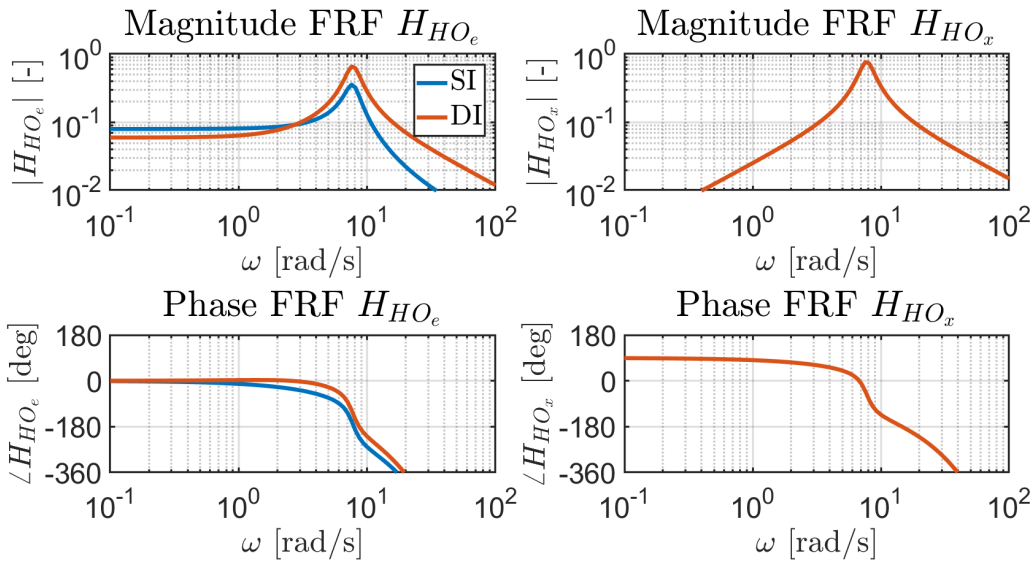

Fig. 8 Bode plot HO simulation with vestibular feedback

The nonlinear part of the HO behaviour is modeled by means of a remnant signal n [3, 22]. For this research, the remnant is modeled as a stand-alone zero-mean unit-variance Gaussian white noise input signal w that is passed through a second-order remnant filter. Van Grootheest et al. [8] found that for remnant filters of order 2 and higher, the bias on the estimated ARX coefficients was acceptably small. The continuous-time state-space representation for the remnant filter dynamics is given by Equation (32).

$$\begin{bmatrix} \dot{v}_1 \\ \dot{v}_2 \end{bmatrix} = \begin{bmatrix} 0 & 1 \\ -\frac{1}{T_n^2} & -\frac{2}{T_n} \end{bmatrix} \begin{bmatrix} v_1 \\ v_2 \end{bmatrix} + \begin{bmatrix} 0 \\ \frac{K_n(t)}{T_n^2} \end{bmatrix} w \qquad n = \begin{bmatrix} 1 & 0 \end{bmatrix} \begin{bmatrix} v_1 \\ v_2 \end{bmatrix} \tag{32}$$

The remnant filter time constant T_n was set to 0.06 seconds, similar to Pool et al. [27]. The filter gain $K_n(t)$ was tuned iteratively to achieve certain power ratios P_n of the remnant as part of the control signal. The remnant power ratio is defined as the fraction of the remnant power σ_n^2 by the control input power σ_u^2 as shown in Equation (33). For the tuning process, the power ratios were calculated for certain values of the remnant gain K_n based on 10 different remnant signals and then averaged. Next, the averaged remnant power ratios were linearly interpolated to find the required gain settings to achieve the desired power ratios. The desired power ratios are a range of 0 (no remnant) to 0.25 with increments of 0.05. The corresponding gains are listed in Table 5. For cases with time-varying CE dynamics the remnant filter gain was changed in a similar sigmoidal fashion as the SAS gains.

$$P_n = \frac{\sigma_n^2}{\sigma_u^2} \tag{33}$$

Table 5 Remnant gain values remnant for different CE dynamics and different remnant power ratios

		Remnant Filter Gain Values				
	CE	$P_n = 0.05$	$P_n = 0.10$	$P_n = 0.15$	$P_n = 0.20$	$P_n = 0.25$
No Motion	SI	0.0088	0.0130	0.0167	0.0201	0.0234
	DI	0.0070	0.0106	0.0136	0.0164	0.0192
Motion	SI	0.0088	0.0130	0.0167	0.0201	0.0234
	DI	0.0130	0.0194	0.0248	0.0302	0.0357

C. Verification Results

With the simulation that was presented in the Section II, simulation data were generated to be used for the verification of the multimodal recursive ARX identification method. It was explained that due to the coupling of the remnant noise and the HO model dynamics a bias will be present in the coefficient estimation [8], so therefore it was opted to first verify the method for simulation cases without any remnant present. The influence of the remnant on the estimation results will then be evaluated in a second step. In addition, first the estimation performance for the LTI conditions is checked before the method is verified for time-varying cases. This verification was performed by comparing the mean of the RLS ARX coefficient vector estimate $\bar{\hat{\theta}}^{RLS}$ with the (known) reference values that were directly converted from the selected HO model settings, by calculating the bias B_r with Equation (34). Furthermore, the OLS ARX identification results, for which the method was verified by Nieuwenhuizen et al. [10], were used as a reference. The verification procedure has been completed with a constant forgetting factor of $\lambda = 0.996$ for conditions C6 and C7 (see Table 2) for all coefficients. All results that follow are shown for forcing function realization 1. Equivalent results were found for the other forcing function realizations.

$$B_r = \frac{\bar{\hat{\theta}}^{RLS} - \theta}{\theta} \tag{34}$$

Time-invariant CE Dynamics

For the remnant-free simulation of condition C6 it can be seen in Figure 9 that the recursive algorithm, denoted by the dark blue line ($P_n = 0$), perfectly overlaps the reference values for parameters ω_{nm}, ζ_{nm} and K_e. Biases of 3% and 0.3% are found for the parameters $K_{\dot{e}}$ and K_x, respectively, even though the simulation is completely deterministic. As discussed in the introduction, this shows that the identification method is not completely able to separate the visual and vestibular HO models as both these parameters have the function to generate lead [12]. For the HO model parameters estimated with the OLS ARX algorithm, equal biases were found, showing that the identification issues are not related to the recursive ARX algorithm. Nevertheless, the bias is very small and therefore the recursive ARX identification method is verified for identifying multimodal human operator models for runs with time-invariant CE dynamics, meeting verification goals **[S1]** and **[S2]**.

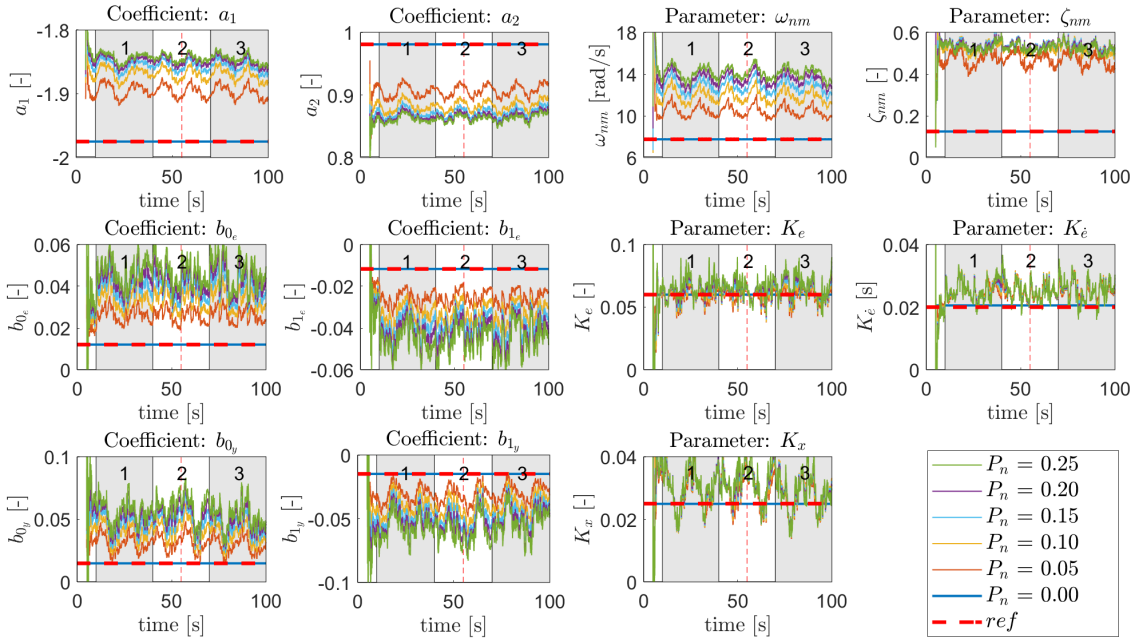

Fig. 9 Average estimation results of ARX coefficients and HO model parameters for 10 realizations of simulation data of condition C6 for different remnant power ratios

Figure 9 shows that when remnant is introduced in the system, the expected bias appears in the coefficient estimates [8]. The magnitude of the bias and its spread for all remnant power ratios and all ARX coefficients and HO model parameters are shown in Figure 10. It can be seen that the bias of the ARX model coefficients increases with increasing remnant power ratios, as expected. Furthermore, the increase in bias between a remnant power ratio of $P_n = 0$ and $P_n = 0.05$ is higher than the additional increments in remnant power. The spread of the bias for the ARX coefficients of the $B(q)$ polynomials is larger than for the $A(q)$ polynomial coefficients. For the neuromuscular HO model parameters, a small spread was found, because these parameters only depend on the coefficients of the $A(q)$ polynomial, see Equation 27. For ω_{nm} a similar increase in bias was found as for the ARX coefficients of the $A(q)$ polynomial as the parameter only depends on one ARX coefficient. For ζ_{nm} no such relationship was found as this HO model parameter depends on more than one ARX coefficient. For the equalization parameter $K_{\dot{e}}$, no clear relationship between remnant power ratio and bias magnitude was found either for the same reasons. It can be seen, however, that the spread for the equalization HO model parameters is larger compared to the neuromuscular HO model parameters, which can be explained by the smaller memory horizon that is applied to these coefficients. Moreover, the equalization parameters amongst others depend on the ARX coefficients of the $B(q)$ polynomial for which a higher spread was found that the ARX coefficients of the $A(q)$ polynomial. For the other conditions with time-invariant CE dynamics similar magnitudes of bias were found.

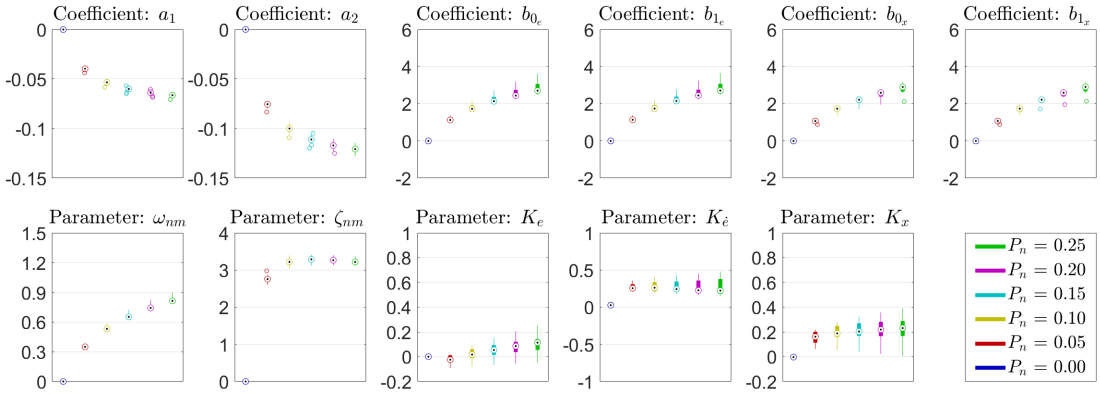

Fig. 10 Boxplot of bias estimation results for ARX coefficients and HO model parameters for 10 realizations of simulation data of condition C6 for different remnant power ratios

Time-varying CE Dynamics

When considering simulations with time-varying CE dynamics equivalent results were found, as can be found in Figure 11. After the transition in CE dynamics at $t = 55$ s, the RLS algorithm shows convergence to the reference value for remnant-free simulations after approximately 10 seconds for all coefficients, which can be seen in a close-up in Figure 12. This convergence shows that the RLS ARX algorithm is able to track the reference value if its current value is not equal to the reference value, therefore meeting verification goal **[S3]**.

Similar to the case with time-invariant CE dynamics, for remnant-free simulations no bias was found for the HO model parameters ω_{nm}, ζ_{nm} and K_e, while a small bias was found for $K_{\dot{e}}$. The bias for the coefficients of the $B_x(q)$ polynomial and corresponding HO model parameter K_x for Window 1 approaches infinity because the reference value is approximately 0. For Window 3, a bias comparable to the case with time-invariant CE dynamics was found. This suggests that also for cases with time-varying CE dynamics the identification method is not able to fully separate the visual and vestibular HO models. As the bias for remnant-free simulation runs is small, the recursive ARX identification method is also verified for simulations with time-varying CE dynamics. Again, for simulations with remnant included, parameter biases were found. Similar to the conditions with time-invariant dynamics, higher remnant power ratios lead to larger biases. The spread for the ARX coefficients of the $B(q)$ polynomials was larger compared to the cases with time-invariant dynamics, hence leading to larger variations in the biases of the HO model parameters. The magnitude of the bias for all remnant power ratios and all HO model parameters for conditions with time-varying CE dynamics is shown in Figure 13. For the other conditions with time-varying CE dynamics similar magnitudes of bias were found, therefore meeting verification goal **[S4]**.

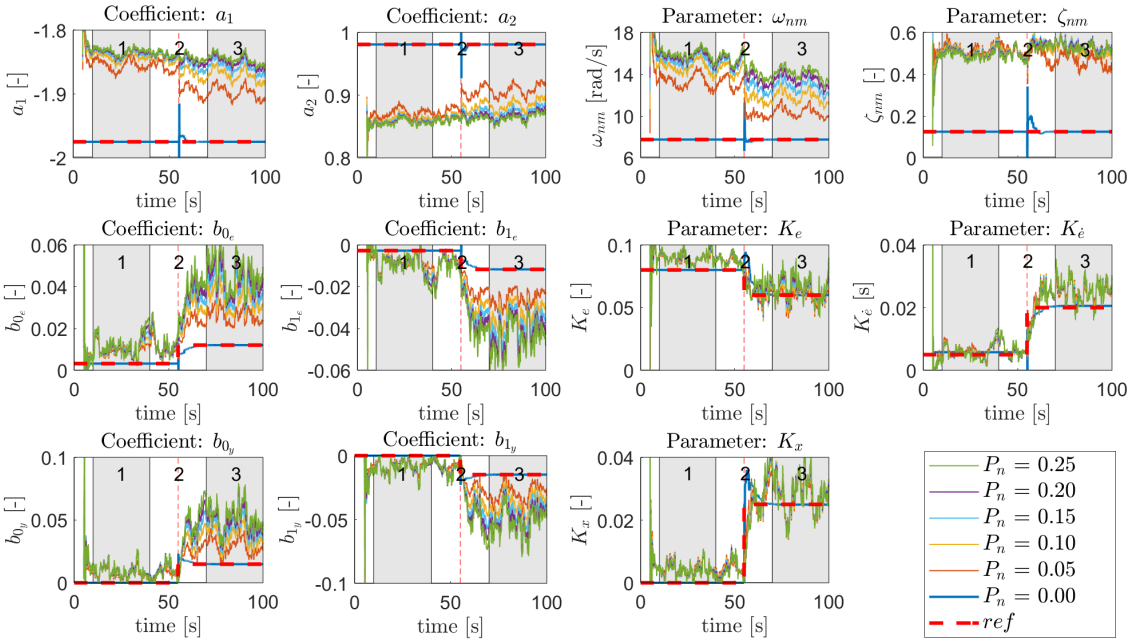

Fig. 11 Average estimation results of ARX coefficients and HO model parameters for 10 realizations of simulation data of condition C7 for different remnant power ratios

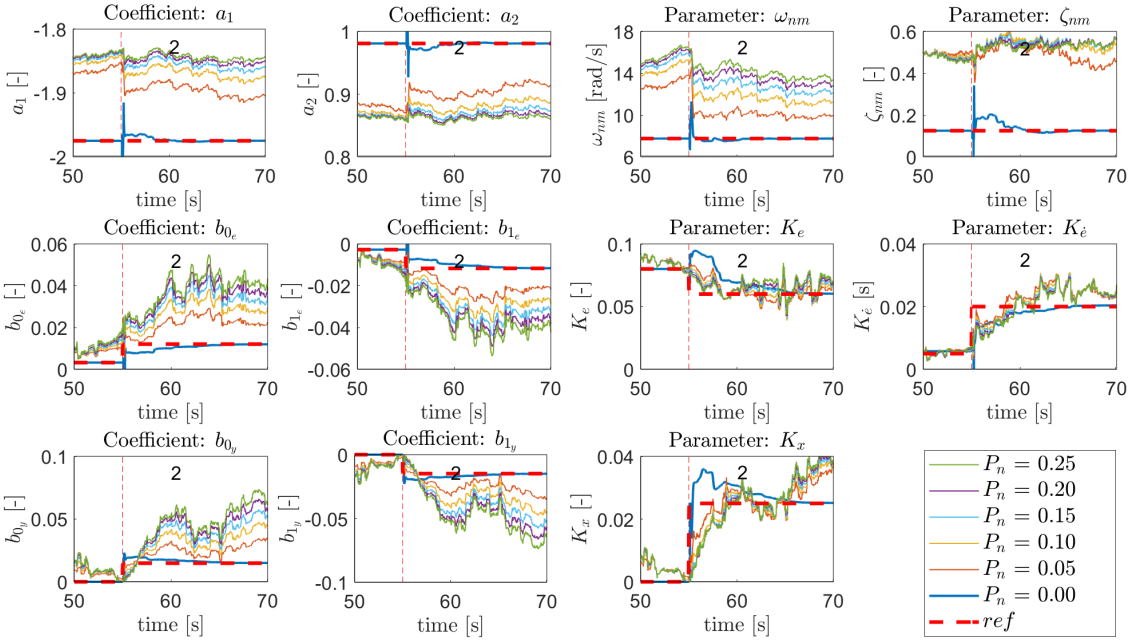

Fig. 12 Average estimation results of ARX coefficients and HO model parameters for 10 realizations of simulation data of condition C7 for different remnant power ratios, close-up transition region

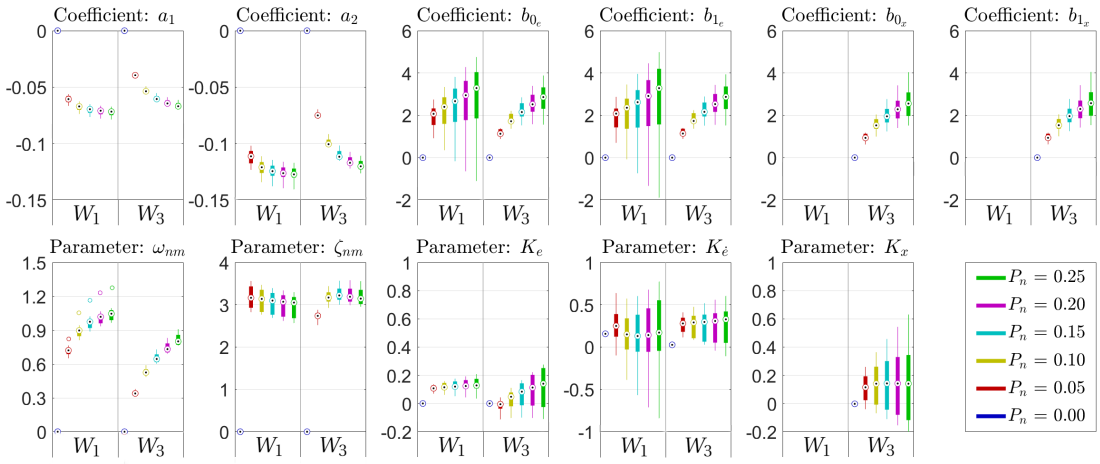

Fig. 13 Boxplot of bias estimation results for ARX coefficients and HO model parameters for 10 realizations of simulation data of condition C7 for different remnant power ratios

D. Sensitivity Analysis for Forgetting Factor

For the identification of time-varying HO behaviour, it is essential to investigate the influence of the memory horizon of the recursive ARX identification algorithm on the identification results. Plaetinck et al. [9] showed that for unimodal time-varying HO models a clear increase in $K_{\dot{e}}$ is visible when transition from SI CE dynamics to DI CE dynamics, due to the need for lead generation. This suggests that a recursive ARX algorithm with infinite memory horizon might not be suitable for identification, as this would suppress any changes the coefficients. Van Grootheest et al. [8] found that for time-varying manual control without the presence of motion feedback the optimal forgetting strategy was to apply an infinite memory horizon to the coefficients of the $A(q)$ polynomial (i.e., constant ω_{nm} and ζ_{nm} parameters) and a memory horizon of 2.56 s for the $B(q)$ polynomial. It is unknown if this forgetting strategy is also the most suitable for the identification of time-varying multimodal manual control.

To find out what the effect is of the selected forgetting strategy on the identification of time-varying multimodal manual control, the multimodal recursive ARX estimation has been performed with different forgetting settings, see Table 6. The memory horizons corresponding to these forgetting settings were introduced in Table 3. For this analysis, the HO model simulation data with a remnant power ratio of 0.25 were used. The estimated parameter traces were averaged for 10 realizations for all conditions. The time traces of the estimated ARX coefficients and HO model parameters for conditions C6 and C7 are shown in Figures 14 and 15.

Table 6 Overview of implemented forgetting strategies and corresponding VAF for simulation data conditions C6 and C7 with P_n = 0.25 averaged over 10 realizations

	Λ_1	Λ_2	Λ_3	Λ_4	Λ_5	Λ_6
λ_A	1	1	1	1	1	1
λ_{B_e}	1	0.996	0.996	0.996	0.998	0.992
λ_{B_x}	1	0.996	0.998	0.992	0.998	0.992
VAF Condition C6	**82.8**%	0%	78.6 %	76.8%	80.7%	70.4%
VAF Condition C7	0%	61.5%	69.2%	55.6%	**74.6**%	51.8%

Figures 14 and 15 show that for simulation data Λ_1 and Λ_5 result in the estimation closest to the reference value for runs with time-invariant and time-varying CE dynamics, respectively. Table 6 confirms that the aforementioned forgetting matrices result in the best model fits for conditions C6 and C7, respectively, because the highest VAF is

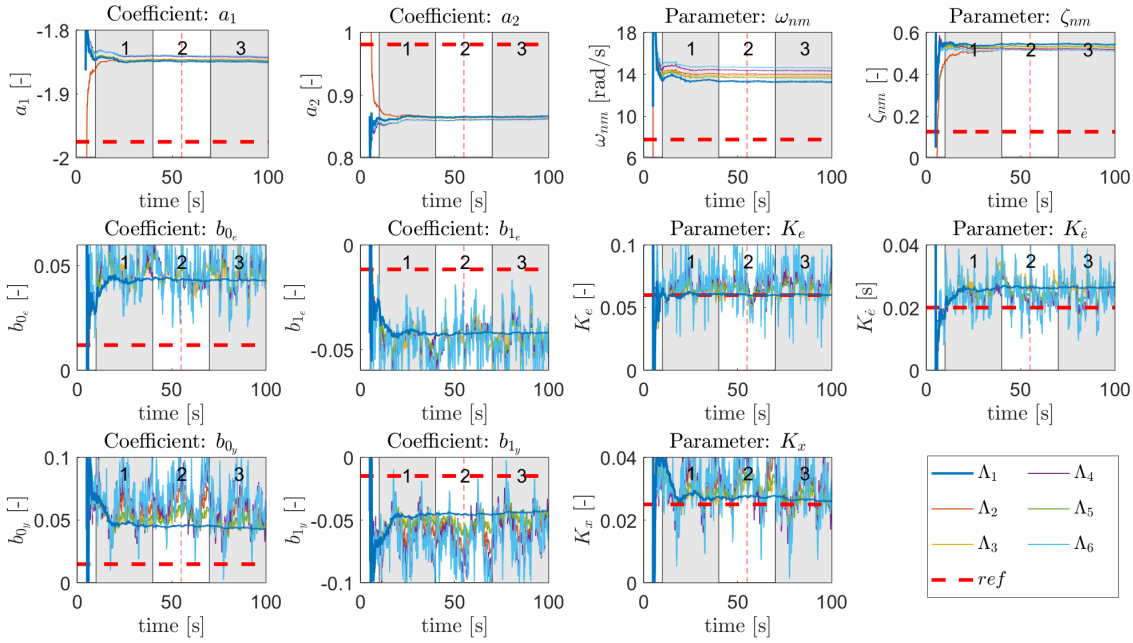

Fig. 14 Average estimation results of ARX coefficients and HO model parameters for 10 realizations of simulation data of condition C6 with a remnant power ratio of P_n = 0.25 for different forgetting strategies

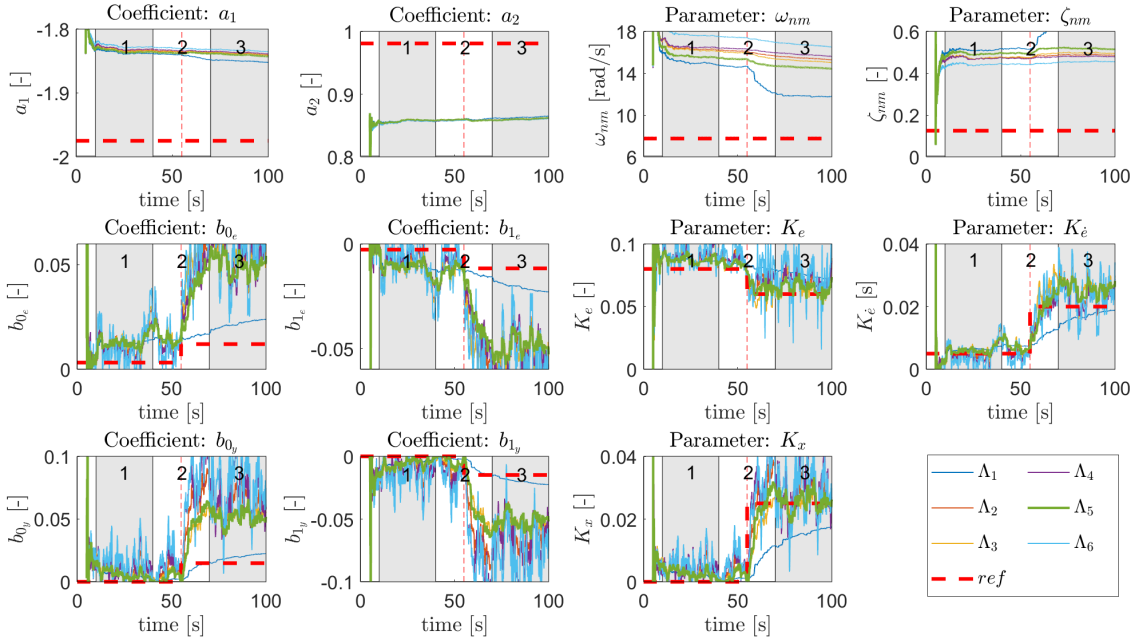

Fig. 15 Average estimation results of ARX coefficients and HO model parameters for 10 realizations of simulation data of condition C7 with a remnant power ratio of P_n = 0.25 for different forgetting strategies

achieved for those forgetting strategies. Therefore the last verification goal **[S5]** is met. Furthermore it can be seen in Figures 14 and 15 that for Λ_6 (i.e. the forgetting matrix with the shortest memory horizon for the $B(q)$ polynomials) the largest oscillations can be found in the estimates of the ARX coefficients of those polynomials and the HO model equalization parameters K_e, $K_{\dot{e}}$ and K_x. Lastly, one can see that for all of the tested forgetting matrices, the estimates of the ARX coefficients of the $A(q)$ polynomial and neuromuscular HO model parameters ω_{nm} and ζ_{nm} show no variation in the estimates over time. This is because an infinite memory horizon is applied for these coefficient estimates.

V. Validation: Experiment

A. Validation Goals

Now that the recursive ARX identification method is verified for the identification of time-varying multimodal manual control behaviour it is important to validate the method. Therefore, similar to Van Grootheest et al. [8] and Plaetinck et al. [9], a human-in-the-loop experiment was conducted. The validation was performed in both the time domain and the frequency domain. In the time domain, the estimated ARX coefficients and corresponding HO model parameters were compared to estimates that were found using the already validated multichannel OLS ARX method as used by Nieuwenhuizen et al. [10]. In the frequency domain, the visual and vestibular responses generated with the estimated HO parameters were compared to the estimated Fourier Coefficients (FC). The goals for the validation are as follows:

[E1] Show that the mean of the recursively estimated ARX coefficients and HO model parameters has comparable magnitudes to the estimates retrieved with the OLS ARX method

[E2] Show that the average steady-state HO dynamics for Window 1 and Window 3 are accurately represented by the mean of the recursively estimated ARX coefficients when compared to the estimated multimodal FC's

[E3] Select the best forgetting method for the identification of HO data for real measurements of time-varying multimodal manual control

B. Experiment Setup

The human-in-the-loop experiment was conducted in the SRS at the Faculty of Aerospace Engineering of Delft University of Technology, see Figure 16. The SRS has a 6 degree-of-freedom hexapod motion system that is capable of providing accurate motion cues to the participants.

Fig. 16 SIMONA Research Simulator

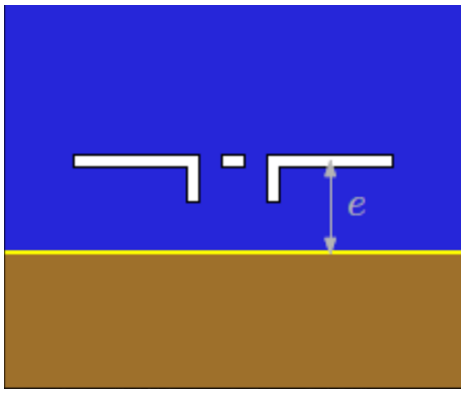

Fig. 17 Compensatory visual display design

For this experiment 16 participants were asked to perform a compensatory pitch tracking task for all selected test conditions, i.e., a within-subject experiment design. The participants were seated in the right cockpit seat and instructed to provide pitch inputs via the electric side-stick (right-handed side) in order to minimize the error between the target signal and system output. The error was presented to the participants via the Primary Flight Display (PFD) using a compensatory display as shown in Figure 17. The arrow in this figure is merely shown as an annotation and was not visible to participants.

The participants provided written informed consent before the start of the experiment and the experiment was approved by the Human Research Ethics Committee of Delft University of Technology. Furthermore, participants were briefed about the safety measures of the simulator and their experimental task, but were given no detailed information about the different test conditions. To get acquainted with the environment and the task, each participant completed a run for all time-invariant conditions (C1, C2, C5 and C6, see Table 2). After this training phase, each participant completed all conditions 8 times according to a balanced Latin square design, to minimize fatigue effects and avoid that participants would anticipate a transition in the CE dynamics. After each run, participants were presented with the RMS of the error signal e for the completed run via the PFD to keep them motivated.

C. Validation Results

The recursive ARX identification method was validated with data gathered during the aforementioned experiment. The runs with time-invariant CE dynamics were validated first before the validation of the runs with time-varying CE dynamics were completed. The validation was done in both the time domain as well as the frequency domain. In the time domain, time traces of the recursively identified ARX coefficients and HO model parameters were plotted against the values estimated with the OLS ARX algorithm. Furthermore, boxplots are provided with an overview of the estimated ARX coefficients for both the OLS and RLS algorithm of which the latter is represented by the mean over the identification window. In the frequency domain, Bode plots were generated with the HO model parameters that were estimated with both the OLS and RLS algorithm, as well as the estimate of the FC's, similar to Nieuwenhuizen [10]. The method is considered validated if the results for the experiment for the OLS and RLS algorithm match in both the time and frequency domain.

For the recursive ARX algorithm the initial conditions were set to the coefficient estimates of the OLS algorithm, to provide a good initial estimate to the recursive algorithm. The list of possible forgetting strategies was expanded to 12 as is shown in Table 7. To select the best forgetting method for runs with time-invariant and time-varying CE dynamics, the VAF was calculated for each complete run. Table 7 shows the median of the VAF results for each forgetting method for all runs of conditions C6 and C7. Forgetting matrix Λ_4 resulted in the best model fit for runs with both time-invariant CE dynamics as well as time-varying CE dynamics with a median of 61.5% for runs with time-invariant CE dynamics and 43.3% for runs with time-varying CE dynamics, thereby completing validation goal **[E3]**. To be able to compare the results for different testing conditions properly, all results that follow are shown for forgetting matrix Λ_4.

Table 7 Overview of implemented forgetting method strategies and corresponding median VAF for all runs of experiment data conditions C6 and C7

	Λ_1	Λ_2	Λ_3	Λ_4	Λ_5	Λ_6	Λ_7	Λ_8	Λ_9	Λ_{10}	Λ_{11}	Λ_{12}
λ_A	1	1	1	1	1	1	0.992	0.996	0.998	0.996	0.996	0.996
λ_{B_e}	1	0.992	0.996	0.998	0.996	0.996	0.992	0.996	0.998	0.992	0.996	0.998
λ_{B_x}	1	0.992	0.996	0.998	0.992	0.998	1	1	1	0.992	0.996	0.998
VAF Condition C6	51.9%	45.9%	53.4%	**55.0**%	53.6%	52.8%	0%	42.9%	50.5%	44.3%	48.8%	41.5%
VAF Condition C7	48.4%	45.0%	52.9%	**54.0**%	52.2%	51.2%	0%	39.8%	50.0%	43.0%	47.2%	40.6%

Time-invariant CE Dynamics

Figure 18 shows the time traces of the ARX coefficients and HO model parameters that were estimated with the multimodal recursive ARX algorithm (solid lines) and their mean values (dash-dotted lines), supported with the values that were estimated with the OLS ARX algorithm (dashed lines) for conditions with time-invariant CE dynamics (C1, C2, C5 and C6, see Table 2). The data has been averaged over all runs of all participants for each condition. From Figure 18 it can clearly be seen that the coefficients of the $B_e(q)$ and $B_x(q)$ polynomials, and the equalization parameters K_e, $K_{\dot{e}}$ and K_x that are dependent on these coefficients, show some small variations in the estimates. This is expected with the choice of Λ_4, as these coefficients have a finite memory horizon of 5 seconds. Opposed to what was found in literature [25, 26], the estimation results for the motion gain K_x suggest that HO's use the motion feedback channel when controlling SI CE dynamics (i.e., condition C5). For the coefficients of the $A(q)$ polynomial and the corresponding HO model parameters that define the neuromuscular dynamics, it can be noted that the ability for small variations over time is suppressed because an infinite memory horizon is applied for these coefficient estimates.

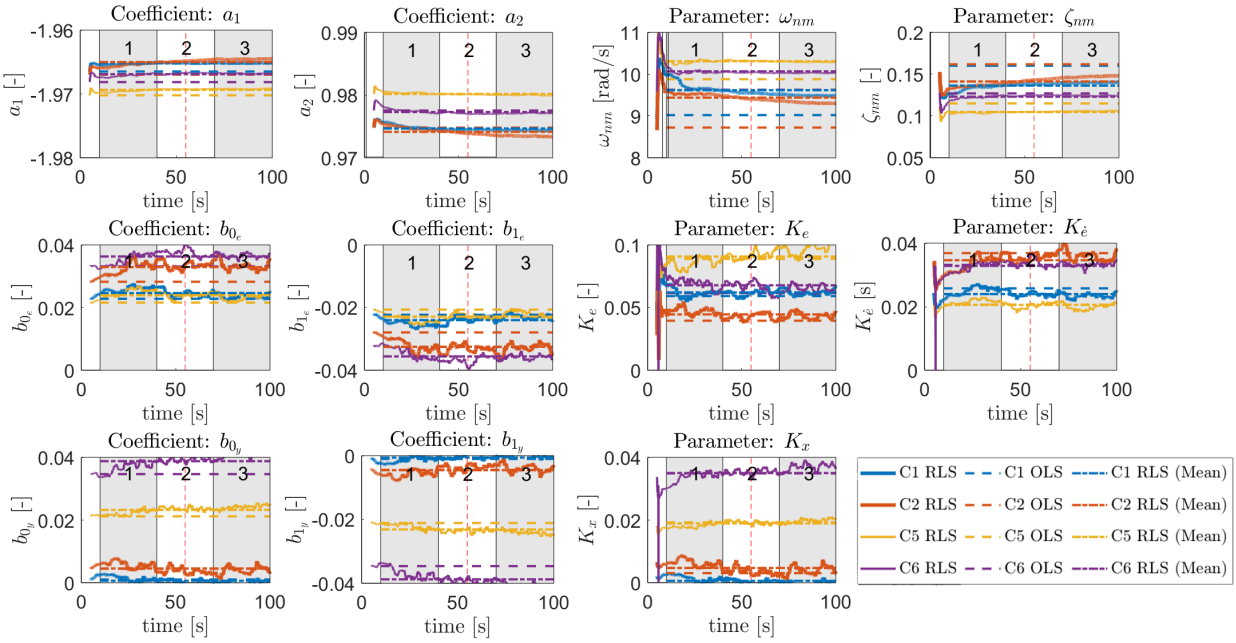

Fig. 18 Average estimation results of ARX coefficients and HO model parameters of all participants for runs with time-invariant CE dynamics for both motion and no-motion conditions

The spread of the ARX coefficients and HO model parameters estimated with the RLS and OLS algorithm for both identification windows for condition C6 is compared using boxplots in Figure 19. For easy comparison, the OLS estimate is shown in blue, whereas the mean of the RLS is shown in red. Figure 19 shows equivalent results for the recursive ARX method and the OLS ARX method, both in terms of the mean values and spread. Therefore, validation goal **[E1]** is met and the method is validated in the time domain for cases with time-invariant CE dynamics.

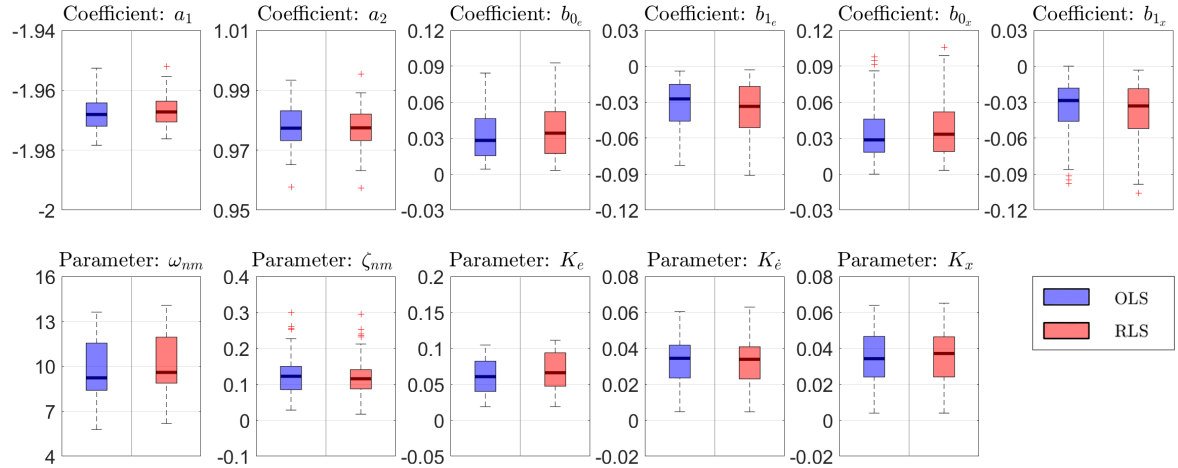

Fig. 19 Boxplot of ARX coefficients and HO model parameters estimated with the OLS and RLS ARX algorithm (RLS ARX represented by its mean) for condition C6 for all runs of all participants

In the frequency domain, the Bode plots that were generated with the mean of the estimates of the RLS ARX identification method and with the OLS ARX algorithm show similar results as can be seen in Figure 20. The model fit (MF) in the frequency domain of the HO responses generated with the RLS ARX estimates, was quantified by comparing the magnitudes of the HO response generated with the average RLS ARX algorithm estimates, H_{HO}^{RLS}, with the HO response generated with the average OLS ARX algorithm estimates, H_{HO}^{OLS}, evaluated at the forcing function frequencies ω_n. An expression for the model fit of the visual HO response, evaluated at the target forcing function frequencies, is shown in Equation (35). The magnitudes were scaled with the inverse of the forcing function frequencies to give more weight to the magnitudes around the region in which HO's operate [1-5 Hz]. The model fit for the vestibular HO response $H_{HO_x}^{RLS}$, as well as the evaluations of both HO responses at the disturbance forcing function frequencies $\omega_{n,d}$ can be found in a similar fashion. The fit values for both the averaged visual and vestibular HO response for condition C6 for all runs of all participants can be found in Table 9. For other conditions similar model fits were found. Furthermore, both the visual and vestibular HO responses show a good fit to the FC's, which therefore validates this identification method for runs with time-invariant CE dynamics and meets the last validation goal **[E2]**.

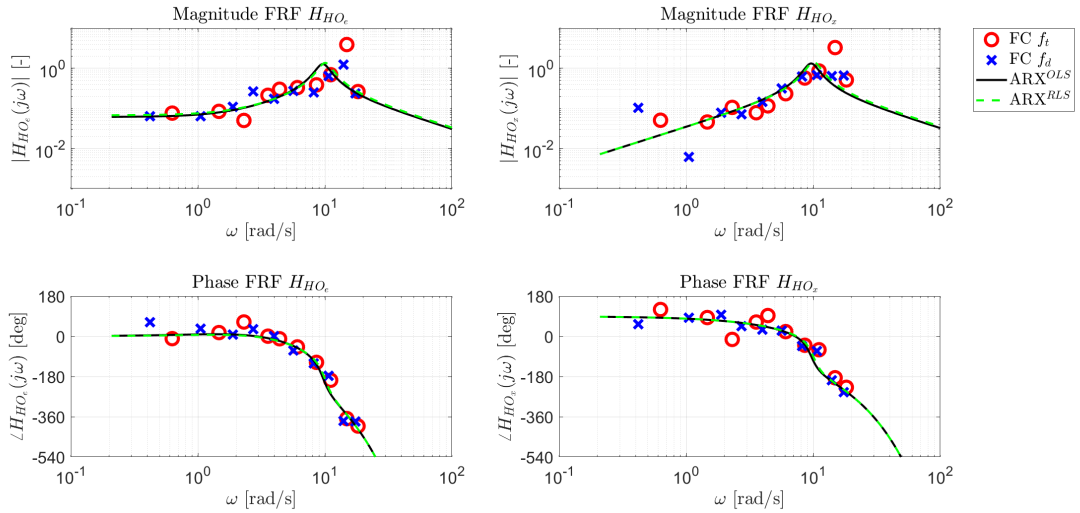

Fig. 20 Bode plots of visual and vestibular HO responses for condition C6 for mean RLS and OLS ARX algorithm and FC estimates of f_t and f_d

$$\text{MF} = \max\left(0, \left(1 - \frac{\sum_{\text{n=1}}^{\text{N}_{\text{sin}}} \left(\frac{1}{\omega_{n,t}}\right) \left|H_{HO_e}^{RLS}(\omega_{n,t}) - H_{HO_e}^{OLS}(\omega_{n,t})\right|^2}{\sum_{\text{n=1}}^{\text{N}_{\text{sin}}} \left(\frac{1}{\omega_{n,t}}\right) \left|H_{HO_e}^{RLS}(\omega_{n,t})\right|^2}\right) \cdot 100\%\right) \tag{35}$$

Table 8 Model fit in the frequency domain for both the visual and vestibular HO response generated with the average RLS ARX estimates for condition C6 for all runs of all participants

	$H_{HO_e}^{RLS}$		$H_{HO_x}^{RLS}$	
	f_t	f_d	f_t	f_d
MF	84.1%	88.6%	83.2%	88.4%

Time-varying CE Dynamics

For the validation of the identification method for the conditions with time-varying CE dynamics (C3, C4, C7 and C8, see Table 2), the estimates of the steady-state parts of each run in Window 1 and Window 3 were compared to the estimates of the OLS ARX algorithm on the data from the corresponding windows. Figure 21 shows the time traces of the ARX coefficients and HO model parameters for the runs with time-varying CE dynamics that were estimated with the recursive ARX algorithm, as well as their mean values, and as reference the OLS ARX estimates. The data has been averaged over all runs of all participants for each condition.

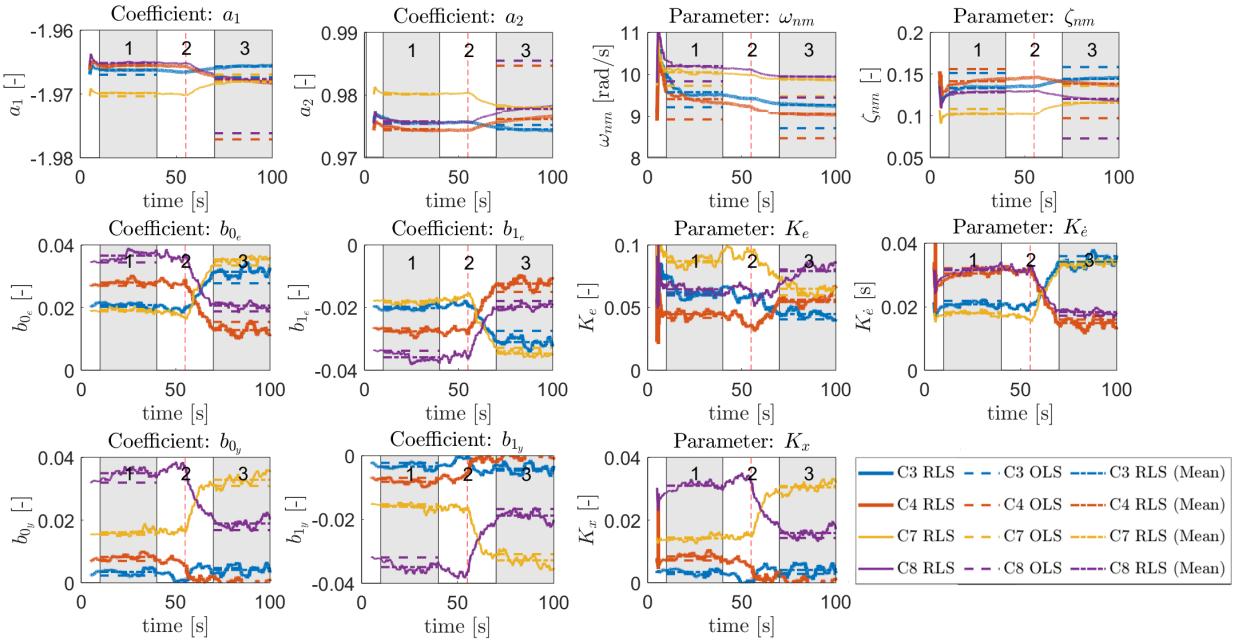

Fig. 21 Average estimation results of ARX coefficients and HO model parameters of all participants for runs with time-varying CE dynamics for both motion and no-motion conditions

For the coefficients of the $B_e(q)$ and $B_x(q)$ polynomials and the resulting equalization parameters K_e, $K_{\dot{e}}$ and K_x, the transitions can be clearly noted after the change in CE dynamics at t = 55 s. Similar to the estimation results for LTI CE dynamics, the estimates for the motion gain K_x suggest that HO's use the motion feedback channel when controlling SI CE dynamics (i.e. condition C7 Window 1 and C8 Window 3), opposed to what was found in literature [25, 26]. As shown in Table 7, forgetting matrix Λ_4 resulted in the best model fit, which implies that an infinite memory horizon is applied to the coefficients of the $A(q)$ polynomial. As a result, the estimates of the coefficients of the $A(q)$ polynomial show larger differences with the OLS ARX coefficient estimates for Window 3 compared to the estimates of Window 1. This difference is best visible in the estimates of the parameters that define the neuromuscular parameters (ω_{nm} and ζ_{nm}) as these are only dependent on the coefficients of the $A(q)$ polynomial.

The spread of the ARX coefficients and HO model parameters estimated with the RLS and OLS algorithm for both identification windows for condition C7 is compared using boxplots in Figure 22. The estimates for both Window 1 and Window 3 show equivalent results for OLS and RLS algorithm. A minor difference between the recursively estimated coefficients of the $A(q)$ polynomial and the estimates retrieved with the OLS ARX algorithm is visible in the estimates of a_2. However, it is only a 0.4% difference between the estimates of the RLS and OLS ARX algorithm.

In the frequency domain, separate Bode plots of the visual and vestibular HO responses were generated for each of the windows with time-invariant CE dynamics with the mean of the estimates of the RLS ARX and OLS ARX algorithm for condition C7 as presented in Figures 23 and 24. For both of the windows and both the visual and vestibular HO responses, a good fit is found with the estimates of the FC's. Similar to the time-invariant CE dynamics, the MF was calculated for time-varying dynamics. For condition C7, a model fit of approximately 92% was found for Window 1 and 87% for Window 3. Although the time-domain estimates showed slight differences between the estimates of the RLS ARX and OLS ARX algorithm for the third window, the Bode plots generated with both the parameter sets are nearly equal. Therefore, this recursive identification method for runs with time-invariant CE dynamics is validated.

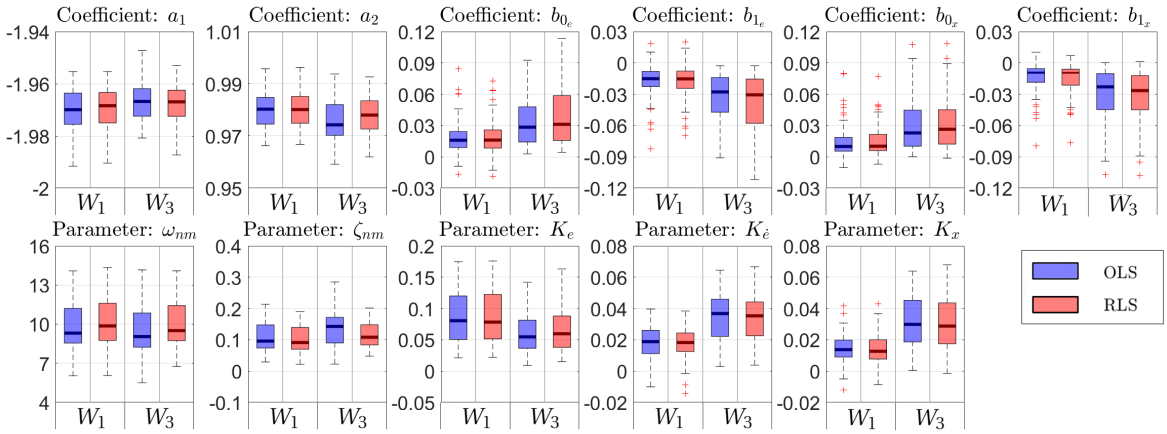

Fig. 22 **Boxplot of ARX coefficients and HO model parameters estimated with the OLS and RLS ARX algorithm (RLS ARX represented by its mean) for condition C7 for all runs of all participants**

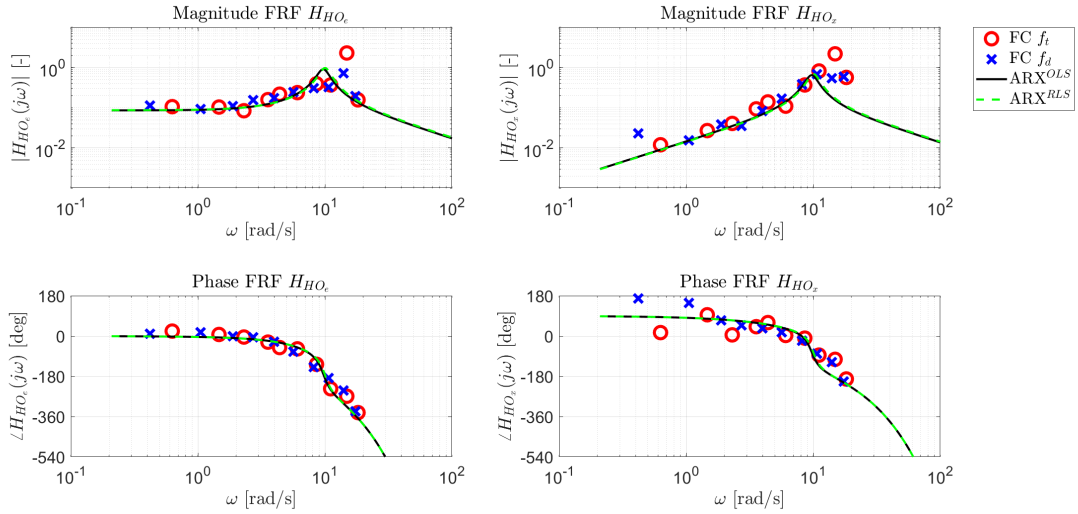

Fig. 23 **Bode plots of visual and vestibular HO responses for condition C7 Window 1 for mean RLS and OLS ARX algorithm and FC estimates of f_t and f_d**

Table 9 **Model fit in the frequency domain for both the visual and vestibular HO response generated with the average RLS ARX estimates for condition C7 Windows 1 and 3 for all runs of all participants**

		$H_{HO_e}^{RLS}$		$H_{HO_x}^{RLS}$	
	Window	f_t	f_d	f_t	f_d
MF	W_1	94.5%	95.4%	88.9%	87.9%
	W_3	88.4%	88.9%	86.6%	86.3%

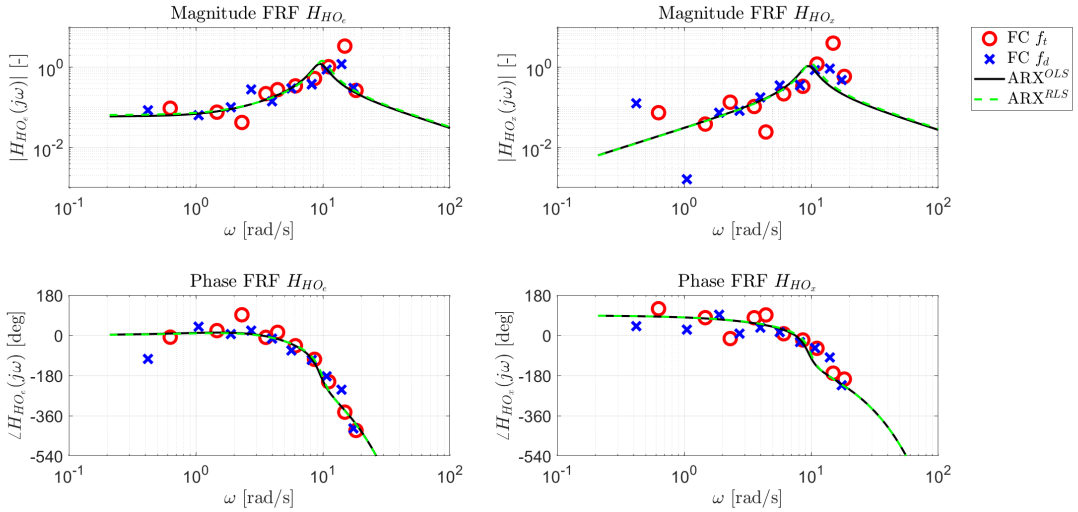

Fig. 24 Bode plots of visual and vestibular HO responses for condition C7 Window 3 for mean RLS and OLS ARX algorithm and FC estimates of f_t and f_d

VI. Results

With the validity of the identification method confirmed, the experimental results will be discussed. The effects of motion feedback are investigated for conditions with time-varying closed-loop CE dynamics. This was done by comparing the estimated HO model parameters for different conditions by using boxplots of all data available. First, the HO model parameters for time-invariant and time-varying CE dynamics cases were compared when motion feedback was present. Afterwards cases were compared for time-varying CE dynamics with and without the presence of vestibular feedback.

Comparing LTI and TV cases

Figure 25 shows the estimates of the HO model parameter estimates for conditions with time-invariant and time-varying CE dynamics and the presence of vestibular feedback. For cases with time-varying dynamics, the estimate results for Window 1 and Window 3 are denoted by W_1 and W_3, respectively. For easy comparison, the results for SI CE dynamics have been shaded in green, and the results for DI CE dynamics have been shaded in yellow. It can clearly be noted that the results for the neuromuscular dynamics show similar outcomes for cases with time-invariant CE dynamics and time-varying CE dynamics. The reason for this can be retraced to the fact that the selected forgetting strategy for the identification of the experiment data applied an infinite memory horizon to the coefficients of the $A(q)$ polynomial and hence less variations could be noted as at the end of the experiment runs.

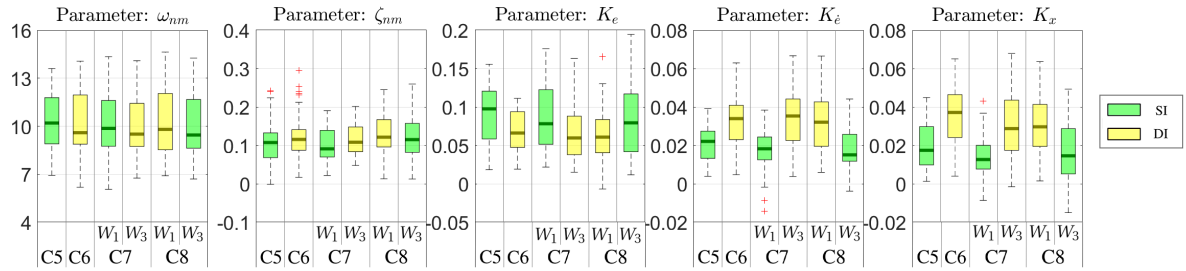

Fig. 25 Boxplot of HO model parameters estimated with the RLS ARX algorithm (represented by its mean) for all conditions with the presence of vestibular feedback for all runs of all participants

For the equalization parameters, distinguishable differences were found for the runs with time-varying CE dynamics between the two steady-state time windows with time-invariant dynamics. The parameter estimates for these windows were similar to the corresponding parameter estimates that were taken for the cases with time-invariant CE dynamics. This suggests that the participants adapted their manual control behaviour to the new CE dynamics within the 15 seconds after the transition before the identification of Window 3 started, which was already shown in Figure 21. The decrease in visual gain K_e when switching from SI CE dynamics to DI CE dynamics is in accordance with the results found by Plaetinck et al. [9]. However, the increase in visual error rate gain $K_{\dot{e}}$ is considerably smaller compared to Plaetinck et al. [9] which can be explained by the fact that participants were able to use the vestibular feedback instead of adopting visual lead [27–29]. This is visualized by the increase in the motion gain K_x when transitioning from SI CE dynamics to DI CE dynamics.

The parameter estimates were used to create the predicted visual and vestibular control inputs $\hat{u}_e$ and $\hat{u}_x$. The absolute value of the control inputs for conditions C5 to C8 (also see Table 2) are shown in Figure 26, together with the VAF for a sliding 5 second centered window for the averaged data of the same conditions. For easy comparison, the control inputs were smoothed by averaging the data points over a 5 second centered window.

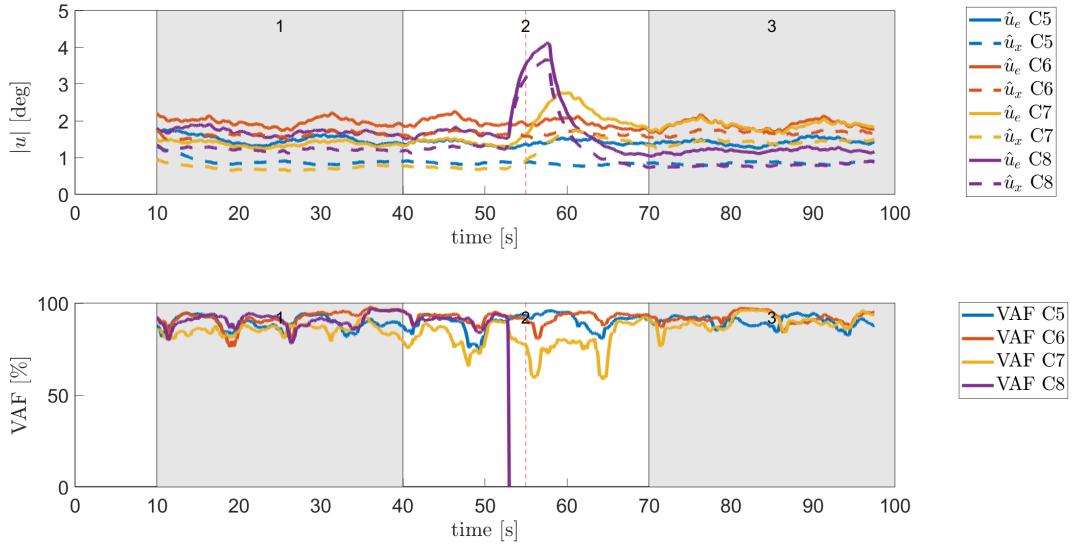

Fig. 26 Average estimated visual and vestibular control input of all participants for all conditions with the presence of vestibular feedback with corresponding sliding VAF

An important observation is that for condition C8, when the CE dynamics switch from DI dynamics to SI dynamics, both the visual and vestibular control input contributions show an increase though the opposite was expected. The explanation for this can be found in the fact that the CE dynamics change instantaneously, while the transition in the estimated parameters show a more gradual change as was shown in Figure 21. Therefore, directly after the transition in dynamics, the HO is controlling SI CE dynamics with an estimated parameter set of HO DI dynamics, leading to an increase in predicted control input. As a result, the VAF has a tremendous drop after the dynamics have changed, because the predicted control input does not match the actual control input.

Furthermore, Figure 26 shows that the new steady-state is achieved faster for condition C7 than condition C8 as it occurs at an earlier moment in time. The reason for this is that for condition C7 the CE dynamics after the transition become DI CE dynamics, which are marginally stable, and therefore the HO has to quickly adapt his or her control strategy to maintain stability. This was already shown in Figure 21, as the estimate of the motion gain K_x reached a new steady-state after approximately 8 seconds after the transition in dynamics, whereas the motion gain for the opposite change in dynamics achieved a steady-state value after approximately 20 seconds.

Comparing unimodal and multimodal feedback models

Figure 27 shows the distribution of the parameter estimation for all time-varying conditions with and without vestibular feedback. The estimate results for Window 1 and Window 3 are again denoted by W_1 and W_3, respectively. Similarly to the previous subsection, no large variations were found between the estimates of the neuromuscular dynamics parameters for both of the windows per condition. When comparing the neuromuscular natural frequencies for the cases with and without vestibular feedback, an increase was found in the parameter estimates when motion feedback was provided to the participants. This increase was in line with results found by Nieuwenhuizen et al. [10] and Pool [13]. According to the aforementioned literature, an increase in the neuromuscular damping ratio was expected for cases where vestibular feedback was provided, but estimates show only a minor decrease for these situations. No apparent reasons could be found for this occurrence.

When considering the visual equalization parameters K_e and $K_{\dot{e}}$, it can be noted that the parameter estimates for both windows of conditions C3 and C7 are similar to the estimates of the windows of conditions C4 and C8 with corresponding dynamics, irrespective of the presence of motion feedback. Furthermore, an increase in the visual gain K_e was found for conditions where motion feedback was provided which is in line with Pool's findings [13]. For $K_{\dot{e}}$ no such increase was found which can be explained by the fact that the need for adopting visual lead is less because of the presence of vestibular cues. This statement is confirmed by the estimates of the motion gain K_x. For the conditions where no vestibular cues were available, the estimates of the motion gain were approximately zero.

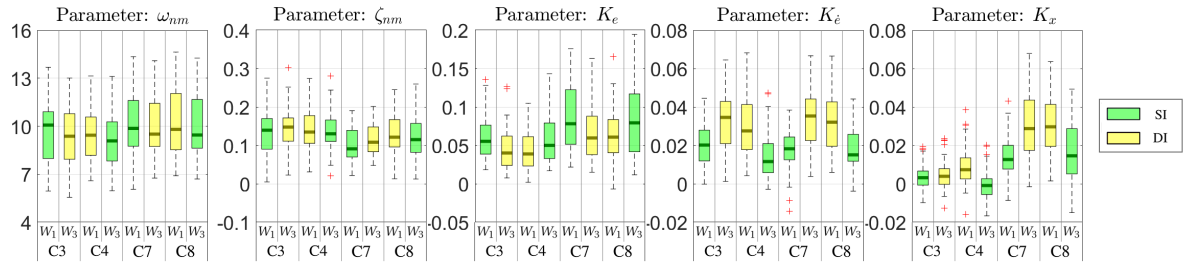

Fig. 27 Boxplot of HO model parameters estimated with the RLS ARX algorithm (represented by its mean) for all conditions with time-varying CE dynamics for all runs of all participants

Also for the comparison of cases with and without the presence of vestibular feedback for time-varying CE dynamics, the predicted visual and vestibular control inputs $\hat{u}_e$ and $\hat{u}_x$ were computed. The absolute values of the control inputs for conditions C3, C4, C7 and C8 (also see Table 2) are shown in Figure 28, together with the VAF for a sliding 5 second centered window for the averaged data of the same conditions. Again, the control input was smoothed by averaging the data points over a 5 second centered window.

When comparing the predicted control inputs for cases with and without the presence of motion cues, it can be seen that irrespective of the presence of vestibular cues, conditions with a transition from DI CE dynamics to SI CE dynamics show a bad model fit. However, the sliding VAF for condition C4 achieves positive VAF values 20 seconds after the transition in dynamics, whereas the sliding VAF for condition C8 does not achieve positive VAF values after the transition. The explanation for this can be found in the fact that the total predicted control input for condition C8 is higher than for condition C4.

VII. Discussion

In this paper a strategy for the identification of time-varying multimodal manual control using recursive ARX identification was presented. Under the assumption that the multimodal HO model that was considered for this research (Equations (3) and (4)) is correct [19], an ARX model structure of order 2 was used which ensures no model order reduction is required, therefore yielding a computationally efficient and fast estimation procedure. Thus, this results in a recursive identification method that can be ran in online and can be used for developing real-time adaptive support systems for the flight deck.

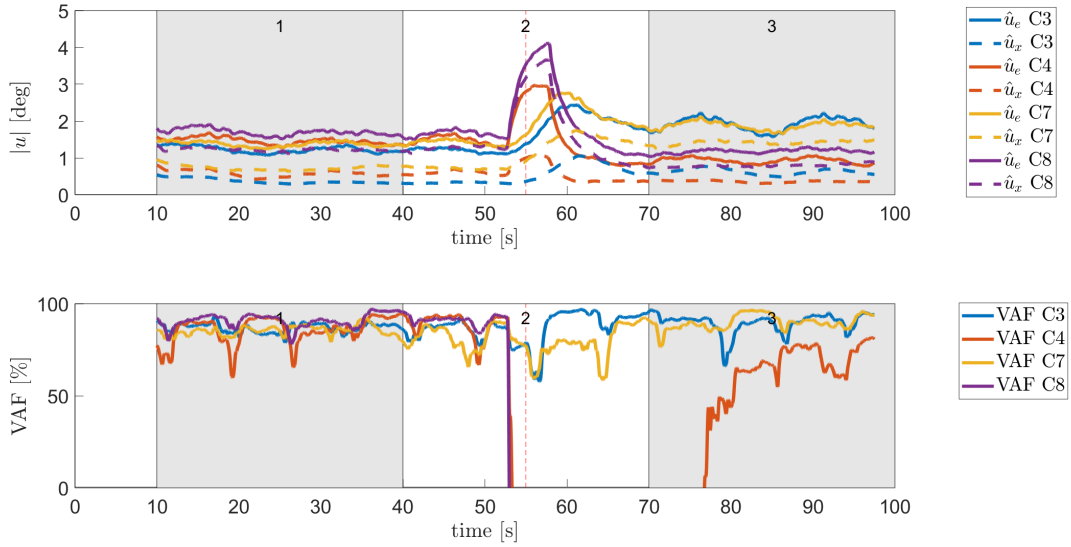

Fig. 28 Average estimated visual and vestibular control input of all participants for all conditions with time-varying CE dynamics with corresponding sliding VAF

One key assumption made in developing the recursive ARX identification method in this research was to use HO time delay estimations performed with an OLS estimation method, therefore assuming the delays to be time-invariant for both Window 1 and Window 3, where the CE dynamics were time-invariant. While this is a reasonable assumption, more research should be carried out to find out whether it is possible to estimate both time-varying time delays, for example, by making use of a sliding window approach or an approach using Kalman Filters [5–7]. For now it is unknown how the time delays are exactly affected by a transition in dynamics at the moment of change, which is essential for understanding time-varying multimodal manual control.

During the performed simulation-based verification of the method it was found that the recursive ARX algorithm was indeed able to converge to a new reference value if the dynamics were changed throughout the run, which showed this method can be used for the identification of time-varying multimodal manual control. However, for simulations without any remnant present the recursive ARX algorithm was not completely able to perfectly separate the contributions of the visual and vestibular feedback channels, as a small bias was found for both the parameters $K_{\dot{e}}$ and K_x, for both time-varying as well as time-invariant CE dynamics. This is a well-known problem for the identification of multimodal manual control [12], as both of these parameters account for a part of the HO lead. The algorithm has difficulty in distinguishing each of the contributions. In fact, since simulations without remnant are deterministic, the estimation can only be considered fully correct if the estimated HO parameters are exactly equal to the reference values. Nevertheless, the percentage difference between the reference value and the estimation results were only 3% and 0.3% for the parameters $K_{\dot{e}}$ and K_x, respectively, and therefore the estimation results can still be considered sufficiently accurate for practical purposes. For simulations with remnant it is unknown, however, what part of the bias is caused by the introduction of noise and what part is due to the inaccurate estimations because of the difficulties in separating the visual and vestibular feedback channel. More investigations should be performed in the future to check the magnitude of the bias caused by possible false separations and if it is possible to avoid these biases.

During the validation of the proposed method with dedicated human-in-the-loop experiment data it was found that in the time domain the mean values of the recursive ARX algorithm estimation results showed equivalent results to the parameters estimated with the OLS ARX algorithm which was validated in earlier research [10]. Moreover, in the frequency domain, the Bode plots that were generated with both the mean of the RLS ARX algorithm had a model fit of approximately 85% for condition C6, when compared with the Bode plots that were generated with the OLS

ARX algorithm results. For Window 1 and Window 3 of condition C7, the model fit was approximately 92% and 87%, respectively. Furthermore a good fit with the Fourier Coefficient estimates was found, therefore validating this recursive ARX identification method.

Both during the verification and validation phase, the recursive estimation algorithm was tested with different forgetting strategies. It was found that for time-varying multimodal manual control the optimal forgetting strategy involved a memory horizon of 5 seconds for the coefficients of the $B(q)$ polynomials, twice as long compared to the optimal memory horizon of the $B(q)$ polynomial previously found for time-varying unimodal control [8]. This can be explained by the fact that a larger number of coefficients needs to be estimated and a short memory horizon results in too much freedom in the estimation of the coefficients, as small memory horizons lead to higher noise sensitivity [8, 9]. The time traces of the recursively estimated neuromuscular HO model parameters ω_{nm} and ζ_{nm} do not show a good fit with the OLS ARX estimates because of the infinite memory horizon that was applied to the coefficients of the $A(q)$ polynomial, however, this still resulted in the best model fit. This suggests that better estimation results might be obtained if the forgetting factors are tuned differently. A promising solution for the identification of time-varying multimodal manual control using a recursive ARX model structure might be the use of time-varying forgetting factors, a method quite similar to Kalman Filtering. If a smaller memory horizon is applied only in the transition region and a larger memory horizon is applied in the regions with steady-state dynamics, the recursive ARX algorithm might converge to the new steady-state value faster and show smaller variations in the estimates for the window with time-invariant dynamics afterwards, hence improving the model fit.

The estimation results that were gathered during the experiment were similar for all windows with equal CE dynamics, being either SI CE dynamics or DI CE dynamics. However, during the transition of the CE dynamics in Window 2, notable differences were observed between the model fits of cases where the CE dynamics change from SI to DI dynamics and vice versa. As explained in Section VI, for conditions C4 and C8, which had a transition from DI to SI CE dynamics, the proposed method resulted in highly unreliable model fits for these conditions directly after the transition in dynamics. The reason for this is that the CE dynamics change nearly instantaneously, whereas the HO model parameter estimates can only adapt at a slower rate. This slower adaptation is partly caused by the fact that a memory horizon of 5 seconds is applied to the coefficient estimation that define the equalization parameters K_e, $K_{\dot{e}}$ and K_x, and an infinite memory horizon to the neuromuscular HO parameters ω_{nm} and ζ_{nm}. This implies that the model fit for cases with a transition from DI to SI CE dynamics will always be worse compared to a transition from SI to DI CE dynamics irrespective of the rate of change of the CE dynamics. The HO model parameter estimates directly after the transition still behave like controlling DI CE dynamics, while the CE dynamics themselves (almost instantaneously) changed to SI CE dynamics, resulting in a high control input predicted by the model. The recursive algorithm will always be lacking behind compared to the actual HO adaptation because of the applied memory horizon.

VIII. Conclusions

For this research a recursive ARX identification method was verified and validated for the identification of time-varying, multimodal manual control behaviour in compensatory tracking tasks. The verification of this method was done by performing simulations of a human operator (HO) performing a control task for which the controlled element (CE) dynamics are changed over time. The influence of the forgetting factor tuning was investigated by calculating the variance accounted for (VAF) for different forgetting matrices. For simulation data the best identification results for time-varying manual control behaviour were found when forgetting factors of $\lambda = 1$ and $\lambda = 0.998$ were selected for the coefficients of the $A(q)$ polynomial and $B(q)$ polynomials, respectively. For a remnant power ratio of 0.25, VAF's of 82.8% and 74.6% were found for the best forgetting method for cases with time-invariant and time-varying CE dynamics, respectively.

For the validation of this identification method, a human-in-the-loop experiment was conducted. It was found that for real human data, the same forgetting factor tuning as for time-varying simulations led to the best identification results, both for cases with time-invariant and time-varying CE dynamics. In addition, the time-averaged values of the estimates of the recursive algorithm were equivalent to the OLS ARX estimates for steady-state HO manual control behaviour. Finally, as expected, the RLS ARX algorithm showed a clear transition in the estimation results for the coefficients of the $B(q)$ polynomials after the transition in CE dynamics.

Overall, this research shows that the recursive ARX identification method is a powerful tool for the identification of time-varying, multimodal manual control. This method can be used in future work for developing adaptive support systems for the flight deck to improve safety in aviation.

References

[1] Young, L. R., "On Adaptive Manual Control," *Ergonomics*, Vol. 12, 1969, pp. 635–674.

[2] Mulder, M., Pool, D. M., Abbink, D. A., Boer, E. R., Zaal, P. M. T., Drop, F. M., Van Der El, K., and Van Paassen, M. M., "Manual Control Cybernetics: State-of-the-Art and Current Trends," *IEEE Transactions on Human-Machine Systems*, Vol. 48, No. 5, 2018, pp. 468–485. https://doi.org/10.1109/THMS.2017.2761342.

[3] D.T. McRuer, and H.R. Jex, "A Review of Quasi-Linear Pilot Models," *IEEE Transactions on Human Factors in Electronics*, Vol. HFE-8 No 3, No. 3, 1967.

[4] Schiess, J. R., and Roland, V. R., "Kalman Filter Estimation of Human Pilot Model Parameters," *Technical Report NASA-TN-D-8024, NASA Langley Research Center, Hampton (VA)*, , No. November 1975, 1975, pp. 1–7.

[5] Boer, E. R., and Kenyon, R. V., "Estimation of Time-Varying Delay Time in Nonstationary Linear Systems: An Approach to Monitor Human Operator Adaptation in Manual Tracking Tasks," *IEEE Transactions on Systems, Man, and Cybernetics Part A:Systems and Humans.*, Vol. 28, No. 1, 1998, pp. 89–99. https://doi.org/10.1109/3468.650325.

[6] Popovici, A., Zaal, P. M. T., and Pool, D. M., "Dual Extended Kalman Filter for the Identification of Time-Varying Human Manual Control Behavior," *Proc. of the AIAA Modeling and Simulation Technologies Conference, Denver (CO), AIAA-2017-3666.*, , No. June, 2017. https://doi.org/10.2514/6.2017-3666.

[7] Rojer, J., Pool, D. M., van Paassen, M. M., and Mulder, M., "UKF-based Identification of Time-Varying Manual Control Behaviour," *IFAC-PapersOnLine*, 2019.

[8] van Grootheest, H. A., Pool, D. M., van Paassen, M. M., and Mulder, M., "Identification of Time-Varying Manual Control Adaptations with Recursive ARX Models," *Proc. of the AIAA Modeling and Simulation Technologies Conference, Kissimmee (FL), AIAA-2018-0188.*, , No. January, 2018. https://doi.org/10.2514/6.2018-0118.

[9] Plaetinck, W., Pool, D. M., van Paassen, M. M., and Mulder, M., "Online Identification of Pilot Adaptation to Sudden Degradations in Vehicle Stability," *IFAC-PapersOnLine*, Vol. 51, No. 34, 2019, pp. 347–352. https://doi.org/10.1016/j.ifacol.2019.01.020.

[10] Nieuwenhuizen, F. M., Zaal, P. M. T., Mulder, M., Van Paassen, M. M., and Mulder, J. A., "Modeling Human Multichannel Perception and Control Using Linear Time-Invariant Models," *Journal of Guidance, Control, and Dynamics*, Vol. 31, No. 4, 2008, pp. 999–1013. https://doi.org/10.2514/1.32307.

[11] Zaal, P. M. T., Pool, D. M., Mulder, M., and Van Paassen, M. M., "Multimodal Pilot Control Behavior in Combined Target-Following Disturbance-Rejection Tasks," *Journal of Guidance, Control, and Dynamics*, Vol. 32, No. 5, 2009, pp. 1418–1428. https://doi.org/10.2514/1.44648.

[12] Zaal, P. M. T., Pool, D. M., Chu, Q. P., Mulder, M., Van Paassen, M. M., and Mulder, J. A., "Modeling Human Multimodal Perception and Control Using Genetic Maximum Likelihood Estimation," *Journal of Guidance, Control, and Dynamics*, Vol. 32, No. 4, 2009, pp. 1089–1099. https://doi.org/10.2514/1.42843.

[13] Pool, D. M., *Objective Evaluation of Flight Simulator Motion Cueing Fidelity Through a Cybernetic Approach*, 2012.

[14] Pool, D. M., Zaal, P. M. T., Damveld, H. J., Van Paassen, M. M., Van Der Vaart, J. C., and Mulder, M., "Modeling Wide-Frequency-Range Pilot Equalization for Control of Aircraft Pitch Dynamics," *Journal of Guidance, Control, and Dynamics*, Vol. 34, No. 5, 2011, pp. 1529–1542. https://doi.org/10.2514/1.53315.

[15] van Paassen, M. M., and Mulder, M., "Identification of Human Operator Control Behaviour in Multiple-Loop Tracking Tasks," *IFAC Proceedings Volumes*, Vol. 31, No. 26, 1998, pp. 455–460. https://doi.org/10.1016/s1474-6670(17)40135-2.

[16] Pool, D. M., Zaal, P. M. T., Van Paassen, M. M., and Mulder, M., "Identification of Multimodal Pilot Models Using Ramp Target and Multisine Disturbance Signals," *Journal of Guidance, Control, and Dynamics*, Vol. 34, No. 1, 2011, pp. 86–97. https://doi.org/10.2514/1.50612.

[17] Zaal, P. M. T., and Pool, D. M., "Multimodal Pilot Behavior in Multi-Axis Tracking Tasks with Time-Varying Motion Cueing Gains," *Proc. of the AIAA Modeling and Simulation Technologies Conference, National Harbor (MD), AIAA-2014-0810.*, , No. January, 2014. https://doi.org/10.2514/6.2014-0810.

[18] Stapleford, R. L., McRuer, D. T., and Magdaleno, R. E., "Pilot Describing Function Measurements in a Multiloop Task," , No. 2, 1967.

[19] Zaal, P. M. T., "Manual Control Adaptation to Changing Vehicle Dynamics in Roll–Pitch Control Tasks," *Journal of Guidance, Control, and Dynamics*, Vol. 39, No. 5, 2016, pp. 1046–1058. https://doi.org/10.2514/1.g001592.

[20] Van der Vaart, J. C., *Modelling of Perception and Action in Compensatory Manual Tracking Tasks*, 1992.

[21] Zaal, P. M. T., Pool, D. M., Mulder, M., Van Paassen, M. M., and Mulder, J. A., "Identification of Multimodal Pilot Control Behavior in Real Flight," *Journal of Guidance, Control, and Dynamics*, Vol. 33, No. 5, 2010, pp. 1527–1538. https://doi.org/10.2514/1.47908.

[22] Levison, W. H., Baron, S., and Kleinman, D. L., "A Model for Human Controller Remnant," *IEEE Transactions on Man-Machine Systems*, Vol. 10, No. 4, 1969, pp. 101–108. https://doi.org/10.1109/TMMS.1969.299906.

[23] Ljung, L., *System Identification Theory for the User*, Vol. 25, 1987. https://doi.org/10.1016/S0959-1524(01)00020-8, URL http://linkinghub.elsevier.com/retrieve/pii/0005109889900198.

[24] Tangirala, A. K., *Principles of System Identification: Theory and Practice*, 2015.

[25] Shirley, R. S., and Young, L. R., "Motion Cues in Man-Vehicle Control – Effects of Roll-Motion Cues on Human Operator's Behavior in Compensatory Systems with Disturbance Inputs," *IEEE Transactions on Man-Machine Systems*, , No. 9(4), 1968, pp. 121–128. https://doi.org/10.1109/TMMS.1968.300016.

[26] Lu, T., *Objective evaluation of human manual control adaptation boundaries using a cybernetic approach* , 2018.

[27] Pool, D. M., Pais, A. R. V., De Vroome, A. M., Van Paassen, M. M., and Mulder, M., "Identification of nonlinear motion perception dynamics using time-domain pilot modeling," *Journal of Guidance, Control, and Dynamics*, Vol. 35, No. 3, 2012, pp. 749–763. https://doi.org/10.2514/1.56236.

[28] Hosman, R. J. A. W., *Pilot's Perception and Control of Aircraft Motions*, 1996.

[29] Zaal, P. M. T., Pool, D. M., De Bruin, J., Mulder, M., and Van Paassen, M. M., "Use of Pitch and Heave Motion Cues in a Pitch Control Task," *Journal of Guidance, Control, and Dynamics*, Vol. 32, No. 2, 2009, pp. 366–377. https://doi.org/10.2514/1.39953.

II

Preliminary Thesis Report

To be graded for AE4020 Literature Study

1 Introduction

Since the invention of the first autopilot, automation has been on the rise in aviation. Automation in aviation has provided a safer situation for passengers and crew since it has mitigated human errors due to fatigue, boredom and complacency when performing routine work. Pool indicated that some say that in the future skill-based manual control tasks such as manually landing the aircraft will be completely replaced by rule-based and knowledge-based supervisory control tasks [1].

However, as Young already pointed out in 1969, the main reason for including a human operator in the complex vehicle-controller loop is its adaptability, a statement that is still deemed valid today [2]. For instance, when a subsystem of the aircraft breaks down, the automation generally stops working and the pilot must control the aircraft adequately without the aid of automation. Proper aircraft design and pilot training is vital for ensuring safe flight under these circumstances. To improve aircraft control design and develop fitting pilot training, models have to be made how pilots react to changing dynamics.

For over 50 years researchers have tried to model manual control behaviour. Developing these models helps in understanding how humans control dynamic systems and can therefore assist in improving aircraft design and pilot training. The models developed by McRuer and Jex [3] have been considered as a good foundation in the field of cybernetics. They set several guidelines for their models based on their experimental findings that originated from a simple single-axis compensatory tracking task. Since then, models have been expanded and improved, and new research topics within the field of manual control for the upcoming years have been addressed by Mulder et al. [4].

A topic that has gained a lot of attention is the modeling of time-varying manual control. The field of time-varying manual control is of interest because it can be applied to many real-life situations such as a pilot reacting to a failure or modified task constraint. McRuer and Jex already proved that the human operator has an adaptive nature if presented with a different task [3]. Recently, more research is conducted to investigate the adaptive ability of the human operator during a single run [4–11]. By using recursive identification methods, researchers have been able to examine how human operators react to the change in dynamics [5–7].

The aforementioned research was conducted for a unimodal manual control task in which participants only were presented with visual feedback. In real-life scenarios such as flying an aircraft, the pilot is presented with motion feedback as well. It is expected that the presence of motion feedback has an influence on how the pilots react to a change in the system dynamics as this was proven for time-invariant control tasks. This thesis research is an attempt to quantify the effects of motion feedback on time-varying pilot control behaviour.

This research objective will be completed by performing a simulation and a human-in-the-loop experiment. The simulation will be used to verify the multichannel time-varying identification method and the effect of important parameters of this identification method. The data that will be gathered during the human-in-the-loop experiment will be used to develop multimodal human operator models in order to validate the identification framework and draw conclusions on the effects of motion feedback on time-varying dynamics.

This preliminary thesis report forms the foundation to this research. First, an extensive literature survey is presented in Chapter 2 to show what previous research in the same cybernetics fields have found. Chapter 3 discusses the main research question that is based on the presented literature and the roadmap to answer the research question. Afterwards, the simulation setup and identification method will be elaborated upon in Chapters 4 and 5. Preliminary thesis results that consider important investigations for the identification method will be presented in Chapter 6. Afterwards, considerations for the human-in-the-loop experiment that will be conducted in the future will be dealt with in Chapter 7. Lastly, the preliminary thesis research will be concluded in Chapter 8.

2

Literature Study

In the introduction of this report, the importance of establishing multimodal human operator models for time-varying dynamics was made clear. To be able to create these models it is meaningful to understand what the past and current developments have been in this research field. This chapter highlights essential discoveries in the different topics of which this thesis project is composed of. In Section 2.1, the general human operator model will be explained. Section 2.2 will elaborate upon the multimodal human operator model, an extended version of the general, unimodal human operator model. Afterwards, the important properties of time-varying dynamics will be made clear in Section 2.3. The identification of such models will be presented in Section 2.4. Finally, the literature study will be summarized in a concise synthesis in Section 2.5 that highlights important elements in this research field that will be used throughout this research.

2.1. General Human Operator Models

The first human operator models were developed in the 60's by McRuer and Jex [3]. In their research they were able to conclude that the human operator has an adaptive nature: the pilot changed his control action when presented with a new, different task. Although that they found that the human operator has a non-linear behaviour, they were able to separate the control actions in a part that was directly and equivalently related to the perceived error and a residu that accounted for the difference between the aforementioned linear input and actual control action which is called the remnant. The linear relation between the perceived error and the equivalent control action could be modeled in the frequency domain. This breakthrough was followed by efforts to extend and improve these models [12–15]. McRuer and Jex found these results after conducting a compensatory closed-loop experiment for which the control scheme is shown in Figure 2.1.

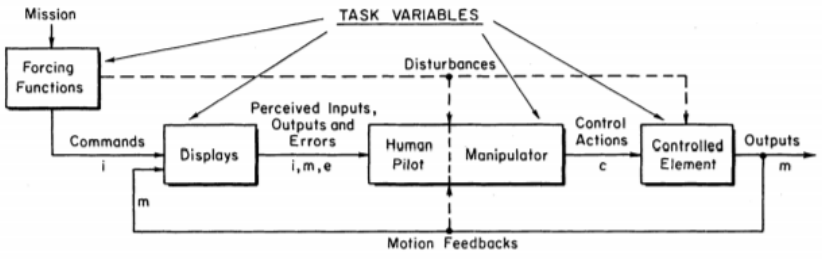

Figure 2.1: Overview of a unimodal control scheme, adapted from McRuer [3]

The most important variables of this research that affect the performance of the pilot are the task variables, which include for instance the forcing function, displays, manipulator and controlled element. However, McRuer and Jex also noted three other important type of variables that influence the performance of the human operator, being environmental variables such as vibration and temperature, operator-centered variables such as fatigue and workload and finally procedural variables such as instructions and practice.

The first human operator model developed by McRuer and Jex is the Crossover Model. A vital part to this model is that the human operator adapts his behaviour according to the controlled element such that the closed-loop response is stable. The open-loop transfer function which is valid in the crossover region (1 - 5 rad/s) is shown in Equation 2.1. The gain of the open loop system $|H_{ol}|$ around crossover frequency can be approached by multiplying the gain of the human operator $|H_{HO}|$ and controlled element $|H_{CE}|$. The phase of the open loop system $\angle H_{ol}$ around crossover frequency can be approached by summing the phase of the human operator $\angle H_{HO}$ and controlled element $\angle H_{CE}$. For an open-loop system to be stable when closing the feedback loop, the gain and phase margin need to be positive. The gain margin is defined as the additional gain that is required to bring the closed-loop system on the verge of instability. The phase margin is defined as the additional phase lag that is required to bring the closed-loop system on the verge of instability. One of the biggest limitations of human operators is the time delay because the time delay has an exponential effect on the decrease of phase for increasing frequencies, hence resulting in smaller phase margins, which brings the closed-loop system closer to instability.

$$H_{ol}(j\omega) = H_{HO}(j\omega)H_{CE}(j\omega) \tag{2.1}$$

The adaptation of the human operator is such that around the crossover region single integrator dynamics is achieved for the open loop system, which means that the slope of the open loop gain is approximately -20 dB per decade. This implies that if the human operator is instructed to perform acceleration control, which is double integrator dynamics, the operator has to generate lead, denoted by the lead time constant T_L. However, if the human operator has to perform position control, the operator has to generate lag compensation, denoted by the lag time constant T_I. Furthermore, McRuer and Jex concluded that there is a static gain K_e which is part of the model to adjust the crossover frequency of the human operator. Finally, a time delay τ_e was added to the model to account for the processing time of the inputs as provided to the human operator. Altogether, the open-loop Crossover Model for visual feedback can be described as shown in Equation (2.2).

$$H_{HO_e}(j\omega) = K_e \frac{T_L j\omega + 1}{T_I j\omega + 1} e^{-j\omega\tau_e} \tag{2.2}$$

In later research, McRuer extended the Crossover Model with an additional term that accounted for the neuromuscular limitations of the human operator [13]. A pilot is unable to provide high frequency inputs to the manipulator. The limitations of the neuromuscular dynamics are modeled as a second order filter including the undamped natural frequency ω_{nm} and damping ratio ζ_{nm}. The updated Crossover Model is shown in Equation (2.3).

$$H_{HO_e}(j\omega) = K_e \frac{T_L j\omega + 1}{T_I j\omega + 1} e^{-j\omega\tau_e} \frac{\omega_{nm}^2}{(j\omega)^2 + 2\zeta_{nm}\omega_{nm} j\omega + \omega_{nm}^2} \tag{2.3}$$

As touched upon in the first paragraph of this section, the non-linearities of the human operator are accounted for by the remnant. The remnant signal is part of the control action that the human operator exerts on the manipulator. Different opinions can be formed on how to model the remnant. Levison was one of the first to model the remnant and included the control signal in front of the visual control block [16].The research that forms this basis injects the remnant control signal after the visual human operator block [5, 6]. The remnant signal is low-pass filtered zero-mean, unit variance Gaussian white noise. However, again no unanimous point of view exists on how to model the filter dynamics exactly. Van Grootheest et al. investigated the effect of the filter order on the bias of the estimation results for all pilot parameters by means of a simulation [5]. He developed an m-th order filter ranging from first to fourth order as shown in Equation (2.4).

$$H_n^m(j\omega, t) = \frac{K_n(t)}{(T_n j\omega + 1)^m} \tag{2.4}$$

In this low-pass filter the time constant T_n is set to 0.06 s [5, 17] and the gain K_n is used to iteratively tune the remnant signal to achieve the desired power level. The remnant filter gain is a function of time as van Grootheest et al. investigated time-varying manual control behaviour and the remnant needed to attain certain power levels irregardless of the controlled element dynamics. He tuned the remnant such that the power fractions of the control action accounted for by the remnant ranged from 0.00 to 0.30 with increments of 0.05. The results showed that for all power levels the first order filter had the highest bias and that the second, third and fourth order have similar bias levels and are suitable for remnant modeling.

The Crossover Model consists out of easily interpretable parameters which makes it easily applicable in manual control research. Furthermore the model has been validated by McRuer for single axis compensatory tracking tasks. Consequently this model will be used throughout this research.

2.2. Multimodal Human Operator Models

The Crossover Model as presented in the previous section was developed after conducting a compensatory, unimodal tracking task in which the human operator was only presented with visual feedback, being the error difference between the system output and target forcing function. In the years after, research has expanded by including more task variables in the control scheme such as an additional feedback loop [9, 12, 18–22] or feedforward loop [23]. For this research, the motion feedback loop is the main focus. This section will elaborate upon the model structure of control schemes that use motion feedback loops in Section 2.2.1. Afterwards, the effects of motion feedback on human operators will be presented in Section 2.2.2.

2.2.1. Model Structure

Stapleford et al. were the first to conduct research in the field of multimodal feedback systems [24]. One of the conclusions from this study stated that the quasi-linear pilot model as developed by McRuer and Jex [3] is also applicable for multimodal control tasks. The model structure for a multimodal control scheme is an extended version of the unimodal control scheme as shown in Figure 2.1. For unimodal control schemes in compensatory tracking tasks the system output is fed back to the human operator together with the target forcing function as the difference between the two. However, when motion feedback is present, the system output is also directly perceived by the human operator. The control scheme for compensatory tracking tasks with vestibular feedback is shown in Figure 2.2.

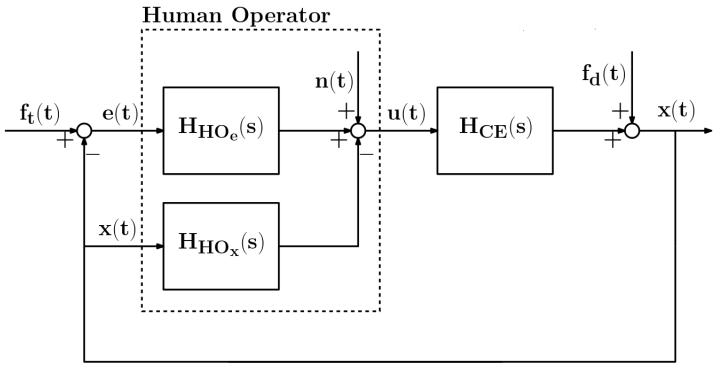

Figure 2.2: Control scheme for compensatory tracking tasks with vestibular feedback, adapted from Nieuwenhuizen et al. [18]

Motion perception can be divided over two different types of motion, being translational motion and rotational motion. Translational motion is perceived by the otolith organs, whereas rotational motion is perceived by the semicircular canals. Since most of the previous research on which this research is based has examined rotational motion, only the semicircular canals will be elaborated upon [5, 6].

The semicircular canals form an organ that is located in the inner ear. As the name suggests, the organ exists out of three semicircular canals that are placed perpendicularly to one another, thereby creating a three dimensional axis system. A fluid flows through these canals that accelerates or decelerates depending on the rotational motion of the head. Sensors inside the canals perceive this acceleration or deceleration and send that information to the brain. The perception of rotational motion is modeled as a first order lag-lead filter and is shown in Equation (2.5) [25].

$$H_{ves}(j\omega) = \frac{\tau_{v1} j\omega + 1}{\tau_{v2} j\omega + 1} \tag{2.5}$$

The break frequencies that correspond to the lag and lead filters are 0.1667 rad/s and 10 rad/s, respectively [18]. This implies that the sensor dynamics behave like single integrator dynamics in the complete crossover region, which is the region of interest in manual control research. Next to that, the semicircular

canals do not perceive the pitch angle as an input, but rather the rotational acceleration as explained in the previous paragraph. Therefore, the sensor dynamics can be simplified to a single differentiator term.

Next to the sensor dynamics, the vestibular human operator model also has a gain term denoted by K_x. Finally, the motion feedback channel has its own motion time delay, denoted by τ_x. The neuromuscular limitation term for the vestibular feedback path is equal to that of the visual feedback path. The human operator model for processing the motion feedback is given by Equation (2.6) [12, 18].

$$H_{HO_x}(j\omega) = K_x j\omega e^{-j\omega\tau_x} \frac{\omega_{nm}^2}{(j\omega)^2 + 2\zeta_{nm}\omega_{nm} j\omega + \omega_{nm}^2} \tag{2.6}$$

Both Equations (2.3) and (2.6) have to be identified separately to provide a complete, multimodal human operator model. The identification process will be elaborated upon in Section 2.4.

2.2.2. Effects of Motion Feedback

Presenting a human operator with motion feedback has several effects on the performance and model parameters of the human operator. One of the first studies by Stapleford et al. that involved multimodal manual control tasks concluded that when a human operator is provided with more than one feedback loop, the human operator selects the feedback path that results in the best performance with the least effort [24]. This suggests that when a human operator is presented with vestibular feedback, not only the pilot parameters of the vestibular feedback path will change, but also the parameters of the visual feedback path, when compared to the same situation without motion feedback.

This suggestion was confirmed by Pool after conducting an experiment in which the motion filter gain of the moving base simulator was changed in between runs [1]. By changing the motion filter gain, the perceived motion by the participants was varied from feeling no motion at all to a full motion simulator. As a result he found that participants' model parameters changed as follows (full motion with respect to no motion):

- Increased visual gain (+ 23%)
- Decreased visual lead time constant (− 22%)
- Increased visual time delay (+ 7%)
- Decreased motion gain (− 8%)
- Decreased motion time delay (− 9%)
- Increased neuromuscular system natural frequency (+ 6%)
- Increased neuromuscular system damping ratio (+ 13%)

However, the actual change of the pilot parameters is not only dependent on the motion filter gain, but all other task variables and other key parameters as identified by McRuer and Jex as explained in Section 2.1 [3]. Nevertheless, the trend of increasing or decreasing parameters is not expected to change. The most consistent trend is found in the decrease in visual lead time constant. More studies have concluded that the presence of vestibular feedback results in a decrease in the lead that needs to be generated [17, 25, 26]. The reason for this can be found in the fact that the rotational velocity of the simulator can be felt instantaneously, hence diminishing the need to adopt visual lead.

Next to the pilot model parameters, Pool also investigated the effect of the motion filter gain on the open-loop crossover frequency and phase margin. The crossover frequency is a measure of effort, whereas the phase margin is a measure of stability. He did so for disturbance rejection tracking tasks as well as target following tracking tasks. The open-loop parameters changed as follows (full motion with respect to no motion):

Disturbance rejection tracking tasks
- Crossover frequency (+ 29%)
- Phase margin (− 9%)

Target following tracking tasks
- Crossover frequency (− 4%)
- Phase margin (+ 12%)

Lastly, Pool was also able to draw conclusions on the effect of motion feedback on the error signal and control signal after conducting a multimodal manual control experiment [19]. When presented with motion feedback, participants achieved a considerable performance increase that was found statistically significant. The setup of the experiment resulted in different conclusions for the control signal: when the participants were instructed to complete a disturbance-rejection task, their control action increased if they perceived the motion feedback, but if they were instructed to complete a target-following task, their control action decreased when they perceived motion.

For this research it is expected that the effects of the motion feedback are similar to what the aforementioned studies have found in case no variation in the dynamics in the controlled element is implemented. However, as will be discussed in the next section, the variation in controlled element dynamics also will have an effect on the model parameters. Section 2.5 elaborates on the difficulty of the identification problem.

2.3. Time-varying Human Operator Models

In Section 2.1 it was explained that McRuer and Jex had concluded that the human operator has an adaptive nature [3]. When presented with a different task, participants adapted their control strategy which could be visualized by the change in the parameters of the human operator models. McRuer's and Jex' conclusions were based on experiments with controlled elements that were linear and time-invariant (LTI). Since the development of the first LTI human operator models, the focus of manual control slowly extended to the field of time-varying dynamics [4–11, 15, 27, 28]. After all, the human operator is proven to be an adaptive controller, so it is of great interest to investigate how the human operator behaves when sudden changes in the task or environment are imposed, such as changes in the controlled element (for instance failure modeling) or modified task constraints (for instance decreased tunnel-in-the-sky dimensions). This section will discuss the modeling of such an adaptation.

The way the adaptation needs to be modeled is dependent on the testing conditions, the type of research question and corresponding hypotheses that need to be answered and the technical limitations of the simulator. Recent efforts in the field of time-varying dynamics that form the foundation for this research considered a change in the controlled element dynamics [5, 6, 8]. Other possibilities to induce a change in multimodal control dynamics is to modify the motion cueing for the simulator as was done by Zaal and Pool [9]. Since previous research on which this research is built focused on a change in the controlled element dynamics, only changes in the controlled element dynamics are considered from here onwards.

The actual change that is modeled can take various forms. A widely used model shape is that of a sigmoid function [5, 6, 8, 9]. A sigmoid function consists of two linear parts that are connected with a gradual, smooth curve as can be seen in Figure 2.3. The expression for a generic sigmoid function of variable p is presented in Equation (2.7). The parameters of a sigmoid function that can be tuned are the initial and final value, p_i and p_f respectively, as well as the maximum rate of transition G and the moment at which this occurs t_M.

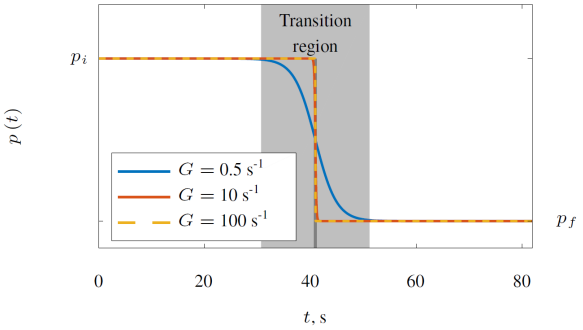

Figure 2.3: Generic sigmoid function, obtained from van Grootheest et al. [5]

$$p(t) = p_i + \frac{p_f - p_i}{1 + e^{-G(t-t_M)}} \tag{2.7}$$

The main advantage of using a sigmoid function is that there is a clear distinction between the initial and final steady-state setting that enables researchers to compare the results from both LTI parts easily. Moreover, in the part where the transition between the two types of dynamics occurs, the adaptation of the human op-

erator is clearly visible. Lastly, the use of a sigmoid allows the researcher to either choose a slow and gradual change in dynamics for values of G below 1 s^{-1}, or go with an approximation of a step input when the maximum rate of change is over 10 s^{-1} [5].

Other options for model shapes are ramp functions. Zaal and Sweet used this type of transition to model the change of the pilot parameters and controlled element dynamics in their simulations [29]. Linear transitions allow for selecting the initial and final values similarly to the sigmoidal shape to easily compare the results. However, the transition between the LTI parts and the actual change is less smooth. Another option for a model change is a sinusoidal shape. This shape is not used often, since it doesn't allow for the comparison of two steady-state human operator models.

Plaetinck et al. successfully identified unimodal time-varying human operator data gathered from an experiment using autoregressive models [6]. He found that when transitioning from single integrator controlled element dynamics to double integrator dynamics there is a clear increase in the lead that is adopted by the human operators. Furthermore there is a minor decrease in the visual gain, and the parameters related to the neuromuscular dynamics remained constant.

For this thesis research, the change in dynamics is expected to have similar effects on the visual feedback model if no vestibular cues are provided. It is unknown, however, if the presence of motion feedback results in a coupled effect on the time-varying model parameters. As discussed at the end of Section 2.2.2, the combination of both effects proves a challenge for the identification of the model, something that will be elaborated upon in Section 2.5.

2.4. Identifying Human Operator Models

To be able to develop human operator models, simulation and experiment data need to be analyzed. Different methods have been developed to perform the identification step and estimate the parameters of the human operator model. This section will elaborate upon these methods and provide advantages and disadvantages. First, more detailed information is given on parametric system identification in Section 2.4.1. Afterwards, some identification methods involving a priori model assumption will be discussed in Section 2.4.2, followed by an explanation on recursive identification methods in Section 2.4.3.

2.4.1. Parametric Identification

As explained in Section 2.1 and 2.2.1, the human operator model consists of several parameters. The parameters can be identified using the time traces of the error signal, control signal and system output signal. Within the branch of parametric identification three different types of identification techniques exist: black-box modeling, white-box modeling and grey-box modeling. Black-box model identification only requires knowledge about the input and output of a system and is therefore an easy and fast model identification technique. No prior model knowledge about the system is required because the model will be established by the relation between input and output. The parameters of the system will be estimated from the experiment data. White-box model identification also estimates the parameters from experiment data, but can only be applied if the model structure is known in advance. Grey-box model identification is a hybrid version that does not need a complete model structure to be known in advance, but is more time-consuming than black-box model identification. Within the domain of grey-box modeling, there is the possibility to fit the data to an a priori assumed model shape or use recursive fitting methods. Each of these methods will be addressed shortly hereafter.

2.4.2. A Priori Model Assumption

If the data is fitted to an a priori assumed model structure, the estimation of the parameters can only be completed after a complete experiment or simulation run is finished. A possible fitting method is Linear Parameter Varying (LPV). A global LPV approach was used by Duarte et al. to estimate single loop, time-varying human operator data [30]. LPV models assume that solely the equalization parameters are allowed to vary and do not include delay estimation. Analytically and experimentally determined sigmoids are compared to estimate the parameters of the human operator. To find the most suitable delay, the model fit is calculated for a range of appropriate time delay values. The time delay that results in the highest Variance Accounted For (VAF) is selected.

Another identification method with a priori model assumption is the Maximum Likelihood Estimation (MLE). Zaal et al. used this method to perform parameter estimation of LTI multimodal control schemes [21, 22], as well as a time-varying multimodal manual control task [9] together with Pool. This identification method works in the time domain. Sigmoidal shapes are fitted to the pilot parameters of the experimental results for which the motion filter gains were also changed in a sigmoidal way.

The advantage of using these identification methods is that these methods require only a low computational load and the identification process can be completed fairly quickly. However, the main downside is that fitting the data to an a priori defined curve constraints the research outcome, for that the pilot parameters may change differently. Moreover, variations in the human operator parameters during the steady-state parts of the experiment runs are not visible when the data is fitted to a sigmoidal curve. Lastly, the identification process can only be completed after a complete run is performed. Hence the change in pilot parameters cannot be tracked in real time.

2.4.3. Recursive Identification Methods

Recursive fitting methods calculate the pilot parameters at every time step based on previous data. An example of a recursive identification method is Kalman Filtering. In contrast to the batch identification methods, no assumption on the shape of the variation of the parameters has to be made prior to the analysis. Different type of Kalman Filters exist to perform parameter estimation. Mandal and Gu [31] used an Unscented Kalman Filter to identify the human operator dynamics. In their research all parameters were free to vary except for the parameters linked to the neuromuscular dynamics, that were taken out of account and assumed to be constant. More recently, Rojer et al. also used an Unscented Kalman Filter in which also the time delay was estimated recursively [32]. Popovici et al. used a Dual Extended Kalman Filter to identify time-varying human operator dynamics [7]. The Dual Extended Kalman Filter made it possible to estimate all pilot parameters. A state filter was used to estimate the pilot equalization dynamics, and a parameter filter was used to estimate the time delay and the neuromuscular dynamics parameters. The disadvantage of both of the aforementioned Kalman Filters is that convergence of the filter heavily relies on the chosen initial condition [7].

A different recursive identification method is Autoregressive Exogenous (ARX) modeling. This method estimates the parameters by means of linear regression using a time shift operator that acts on the time traces of the signals in the control scheme as shown in Figure 2.2. The method was developed by Lennart Ljung [33], but its application to identify manual control behaviour was proven at a later stage [5, 6, 18, 23, 34]. ARX models have been used for modeling multimodal LTI human operator behaviour [18] as well as modeling unimodal time-varying human operator behaviour [5, 6]. In the aforementioned research all pilot parameters except the time delay could be estimated with the ARX models. The time delay was estimated by checking what combination of time delay and estimated pilot parameters resulted in the highest VAF and therefore best model fit, similarly to Duarte et al. [30]. The downside of using ARX models to identify human operator data is that the remnant noise creates a bias in the estimation of the parameters [5] due to the coupling of the remnant noise model and human operator model.

Recursive methods in general have numerous advantages, with the most prominent one being that these methods allow for updating the parameters in real time. As a result, no assumptions have to be made on the shape of the parameter variation prior to the identification process. Furthermore, small behavioral variations in the steady-state parts of the experiment runs are still visible. Besides, for time-varying manual control tasks, the actual change between the initial and final conditions can be studied, which is of high interest. Lastly, the estimation process can be performed during the run since it relies only on past values and/or predictions and not a complete data set. The disadvantage of recursive methods, next to the downsides that are inherent to the methods mentioned above, is a higher computational load.

2.5. Synthesis Literature Study

This chapter has presented valuable research efforts and the corresponding findings in the fields that are of importance to this research. Much effort has been put into investigating these topics separately, however, extensive research on the combination of all the topics considered in the sections before could be beneficial to the improvement of manual control research. The challenge in this thesis research lies in the fact that both the presence of vestibular feedback as well as the change in controlled element dynamics each have an effect on

the model parameters in their own way. If both of these independent variables are implemented it is unknown if the recursive ARX model is able to distinguish the control input between the visual feedback block and the vestibular feedback block. The multichannel time-varying identification method first needs to be verified.

As presented in Section 2.1, the Crossover Model as developed by McRuer and Jex forms a good foundation when investigating manual control tasks [3]. One of the aims of this research is to identify multimodal manual control. As proven by Pool, the parameters of the equalization term of the visual human operator block, as well as the neuromuscular parameters and visual time delay, change if participants are presented with motion feedback, so it is of vital importance to include these parameters in the human operator model as shown in Equation (2.3) [1].

The vestibular human operator block as discussed in Section 2.2 will be modeled with the sensor dynamics as shown in Equation (2.6). The neuromuscular parameters for the vestibular human operator block are equal to those of the visual human operator block, however, the motion gain term and motion time delay will be estimated separately. The trends that were found by Pool regarding change in pilot parameters are expected to occur too for this research. To be able to identify the LTI parts of an experiment run in a simple fashion using a Frequency Response Function (FRF) as a means of verification, two forcing functions will be included. The experiment will therefore not be just a disturbance-rejection or target-following task only.

This research focuses on time-varying dynamics as was elaborated upon in Section 2.3. To model the variation of the dynamics, the same strategy as Plaetinck et al. and van Grootheest et al. will be used [5, 6]. In this way, the results found by them can be compared to the results of this research. This prior research on which this research will be founded has used sigmoidal shapes to model a change in the controlled element dynamics, so this variation will be used throughout this research as well. By using a sigmoidal change, the change in the parameters corresponding to the two time-invariant parts of the experiment can be studied. The exact modeling of the controlled element dynamics and other key-elements of the simulation will be elaborated upon in Chapter 4. As Plaetinck et al. concluded for a unimodal manual control experiment, the parameters of the equalization term for time-varying dynamics change depending on the dynamics that participants are controlling. The same trends will be expected to occur for this research.

The identification of the results that will be gathered from simulation and experiment data is a vital part to answer the research questions. Section 2.4 shed a light on different identification methods. Recursive identification methods allow for tracking changes in the human operator model parameters without making a priori assumptions on the shape of the change, which makes them suitable candidates for identifying time-varying human operator behaviour. To be able to compare the results with Plaetinck's et al. and van Grootheest's et al. findings, the same ARX method is used [5, 6]. The application of the ARX identification method on this time-varying multimodal manual control research will be further explained in Chapter 5.

With the literature survey complete it is important to emphasize the research question and subquestions that will be examined. The next chapter presents the objectives of this research.

3

Research Objectives

In the previous two chapters it was made clear why this research is valuable and what previous research in relevant fields have found. Although much research has been conducted in the fields of time-varying dynamics, as well as the field of multimodal human operator analysis, not much effort has been done to model the combination of these two topics. The findings of the aforementioned research pave the way to make an effort to model this time-varying multimodal human operator dynamics. This chapter presents the research question and objectives that are established for this research in Section 3.1 as well as the roadmap to answer the research questions in Section 3.2.

3.1. Research Questions

The goal of this research is to draw conclusions on the effects of motion feedback on human operator behaviour for time-varying dynamics. This will be achieved by developing a real time, time-varying human operator model with both visual and vestibular feedback loops. The synthesis of the literature study as presented in Section 2.5 elaborated upon a suitable method to model the time-varying dynamics as well as a suitable method to identify the control behaviour. The time-varying dynamics will be modeled as a sigmoidal change of the controlled element dynamics. The identification process will be completed by means of a multichannel ARX model structure.

To develop these models a human-in-the-loop experiment will be conducted as well as a simulation of this experiment. The simulation is meant to verify the the multichannel recursive ARX identification method. Section 2.5 discussed that it is yet unclear if the identification method is able to distinguish between the visual and vestibular feedback blocks as both the vestibular feedback as the change in dynamics have their own effect on the model parameters. Furthermore, the simulation aids in investigating the effect of several parameters of the identification algorithm on time-varying multimodal manual control. These results can be used to make design choices for the actual human-in-the-loop experiment and its identification that will be conducted in later stages of this research. The experiment serves as a validation of the multichannel ARX method for the identification of multimodal time-varying manual control. The research question is constructed as follows:

"What are the effects of motion feedback on pilot control behaviour in time-varying controlled element compensatory tracking tasks identified using ARX models?"

This main research question can be split up in five subquestions that each help to answer the main question. The first subquestion concerns the identification method. The other four subquestions are grouped based on whether the answer can be found by comparing multimodal human operator models with each other, or by comparing multimodal and unimodal human operator models with each other. The five important questions to the main question are:

- Verifying the multimodal time-varying identification procedure in a simulation
    1. *Is it possible to identify both of the time-varying human operator blocks separately in a correct manner using recursive ARX models when motion feedback is present?*
- Comparing multimodal human operator models from experimental data
    2. *Do the time-invariant sections of the experiments with time-varying controlled elements and motion feedback yield the same pilot model parameters as experiments with a corresponding linear time-invariant controlled element dynamics and comparable literature?*
    3. *Do the pilot model parameters change equally fast for controlled elements with decreasing and increasing stability when motion feedback is present?*
- Comparing multimodal human operator models with unimodal human operator models from experimental data
    4. *By how much do the model parameters increase or decrease for time-varying conditions when human operators are presented with vestibular feedback?*
    5. *Do the pilot model parameters change equally fast for controlled elements with decreasing and increasing stability when human operators are presented with vestibular feedback?*

If the ensemble of the subquestions can be answered positively, this means that a verified recursive ARX model can be used to identify time-varying multimodal manual control behaviour. As discussed in Chapter 1, real-time time-varying human operator models would be of great value. The recursive algorithm gives an in-depth insight in how humans adapt their manual control behaviour when the task changes. Moreover, the effects of vestibular feedback can be analyzed for time-varying manual control. This information can be used to improve pilot training or aircraft control design for instance.

3.2. Roadmap

As presented in the previous section, a simulation will be performed to verify the recursive identification method. Besides, a human-in-the-loop experiment will be conducted to develop the real-time time-varying multichannel human operator models and validate the identification method. The research questions can only be answered if the correct testing conditions are implemented in the simulation and experiment. First, each subquestion will be dealt with separately, after which an overview of conditions is given in Table 3.1.

The first subquestion can be answered by means of a bilateral verification step using the cross spectral densities of the signals as presented in Figure 2.2 for the time-invariant parts of the time-varying conditions with vestibular feedback. The subquestion can be considered to be answered positively if multimodal FRF estimates of the human operator model overlap with the human operator model that is generated with the estimated parameters for both the LTI conditions as well as the corresponding time-invariant part of the time-varying dynamics conditions. Since the recursive algorithm does not provide one single parameter value for the conditions with time-varying dynamics, an Ordinary Least Squares (OLS) ARX model structure will be used for the time-invariant parts of those conditions instead of Recursive Least Squares (RLS).

The second and third subquestion considered multimodal human operator models only. To be able to answer the first subquestion, it is necessary to have two different LTI conditions and two time-varying conditions for which the dynamics change from the first LTI condition to the second LTI condition and vice versa, all with motion feedback present. These conditions were chosen to be similar to Zaal [8], being an LTI single integrator dynamics and LTI double integrator dynamics and the transition between the two LTI conditions in both directions. In this way, the parameter values for the time-invariant parts of the conditions with changing dynamics can be compared to the parameters found for conditions with solely LTI dynamics. The second subquestion which considers the adaptation speed of human operators can be answered with only the two time-varying conditions as mentioned in the previous paragraph. The time it takes for the parameters to attain a steady-state after the transition of the controlled element dynamics gives insight in the rate at which human operators accommodate to the new dynamics.

The last two subquestions considered the difference between unimodal and multimodal human operator models. Both of these subquestions can be answered in a similar fashion as the second and third subquestion.

However, considering the second subquestion, instead of comparing the parameters for time-varying dynamics with the corresponding LTI conditions, the parameter values should be compared with the same conditions for unimodal human operator models. This gives the opportunity to check how parameter values change when motion feedback is added to the control task. For the fourth subquestion, the time it takes until a new steady-state value is attained should be compared to the settling time for the same conditions for unimodal human operator models. Conclusively, to answer the third and fourth question, two additional time-varying conditions should be included, however without vestibular feedback.

Altogether, to answer the five questions as discussed in this section, six testing conditions need to be implemented in the simulation, being four time-varying conditions and two LTI conditions, of which four include vestibular feedback and two only have visual feedback. For the sake of completeness, two LTI conditions without motion feedback are included to the list. The conditions that do not involve vestibular feedback are similar to van Grootheest et al. [5], Plaetinck et al. [6] and Zaal [8]. The total set of conditions (C1 - C8) is as follows:

Table 3.1: Testing conditions for time-varying multimodal manual control research

		No Motion		Motion	
		Con	CE	Con	CE
LTI CE		C1	SI	C5	SI
		C2	DI	C6	DI
TV CE		C3	SI ⇒ DI	C7	SI ⇒ DI
		C4	DI ⇒ SI	C8	DI ⇒ SI

First, the simulation setup and its verification will be explained in Chapter 4. The implementation of the identification procedure and verification will be clarified in Chapter 5. The preliminary thesis results involving the effects of the recursive identification algorithm parameters will be presented in Chapter 6. For this preliminary thesis report, only the simulation will be considered, however the important considerations for the experiment and updates to the simulation will be elaborated upon in Chapter 7.

4

Human Operator Simulation

As explained in the previous chapter, a simulation of a human-in-the-loop experiment can aid in verifying the identification framework and making design choices for the actual experiment. This simulation is performed using MATLAB R2017b and is based on the research in the field of time-varying dynamics by van Grootheest et al., Plaetinck et al. and Zaal [5, 6, 8].

All the important components of the block diagram such as the visual and vestibular model need to be taken into account for simulating a human operator. Each of the components will be addressed in this chapter separately. First, information on the simulation run time will be discussed in Section 4.1. Section 4.2 will explain the state-space representation that is used to model the time-varying dynamics. Next, Section 4.3 will deal with the simulation and tuning of the remnant signal. Finally, both of the forcing functions will be elaborated upon in Section 4.4. The correctness of the simulation computations is done by means of a simulation verification step that is presented in Section 4.5. This chapter will be concluded in Section 4.6.

4.1. Simulation Run Information

The simulation will be executed in discrete time using a state-space representation of the task depicted in Figure 2.2. The time step that will be used for this discrete time simulation is 0.01 s. From the total run time of 100 s the first 10 seconds were discarded and therefore not used for identification. With the `fft`-command in MATLAB there is no strict requirement anymore to have the number of samples as power of 2 for correct and efficient analysis. For the runs with time-varying conditions the maximum rate of change was modeled exactly in the middle of the measurement time at 55 s. To properly evaluate the LTI parts of the time-varying runs, the remaining measurement time was divided over three equal pieces of 30 s as is shown in Figure 4.1. Section 4.4 will further elaborate on the consequences of this partitioning of the measurement time.

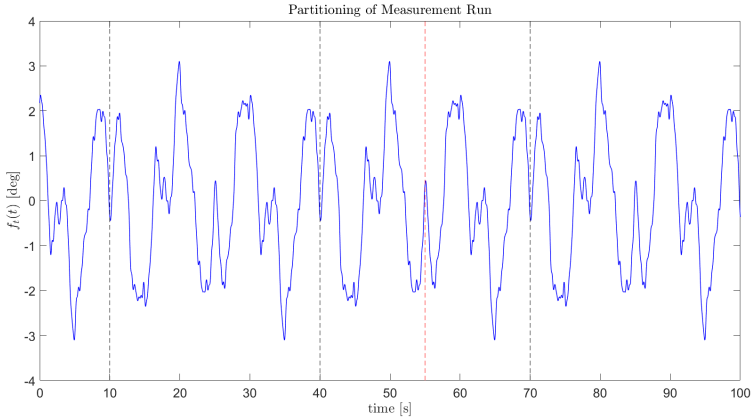

Figure 4.1: Partitioning of the run time in 3 windows

4.2. State-Space Representation

With the conditions defined and information on the simulation runs provided, it is important to implement the conditions correctly into the simulation. The conditions do not only affect the controlled element dynamics, but also the human operator model. Both of these will be discussed in the following Subsections 4.2.1 and 4.2.2 respectively.

4.2.1. Controlled Element Model

In the synthesis of the literature study in Section 2.5 it was proposed to model the time-varying dynamics by using a sigmoidal change to create the transition from single integrator dynamics to double integrator dynamics and vice versa. In this way, the results from this research can be compared to results found in the unimodal time-varying manual control research as done by Zaal which had a similar setup [8]. Zaal used a controlled element for which the parameters varied over time. The dynamics are presented in Equation (4.1).

$$H_{CE}(j\omega) = \frac{K_c(t)}{j\omega\big(j\omega + \omega_b(t)\big)} \tag{4.1}$$

One can see that by varying the break frequency ω_b the dynamics in the crossover region can be either single integrator dynamics for high values of ω_b or double integrator dynamics for low values of ω_b. Furthermore, the controlled element gain K_c can be varied to achieve a desirable gain for the gain in the crossover region. Zaal used a gain of 90 and break frequency of 6 rad/s for single integrator dynamics and a gain of 30 and break frequency of 0.2 rad/s for double integrator dynamics [8]. The corresponding Bode plots are shown in Figure 4.2.

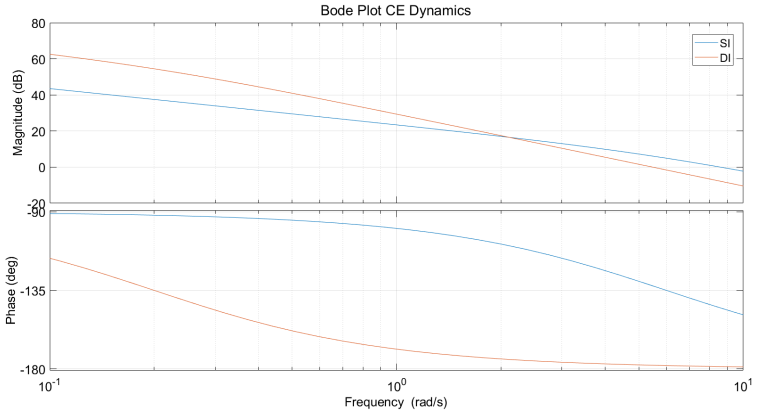

Figure 4.2: Bode plot of controlled element dynamics

Although the transition from single integrator to double integrator dynamics is suitable for capturing time-varying human operator behaviour as demonstrated by Plaetinck et al., the reasoning for this specific change in the controlled element block is lacking [6]. The intention was to model a failure, but the explanation for doing so by changing the gain and break frequency was not provided in earlier studies. To be able to provide a better motivation for the modeling of the failure, a different controlled element structure is implemented. The revised control scheme is shown in Figure 4.3.

In this block diagram the controlled element is expanded with a stability augmentation system (SAS). The SAS consists of a proportional gain K_δ and rate feedback $K_\theta\, j\omega$. The controlled element transfer function is linear and time-invariant and equal to the "double integrator" dynamics from Zaal [8]. By implementing the SAS and tuning it properly, the closed-loop controlled element dynamics can behave like single integrator dynamics. To still be able to compare the results from this research to the results that are found by Plaetinck et al. and van Grootheest et al., the SAS will be tuned such that the closed-loop controlled element dynamics are equal to the single integrator dynamics from Plaetinck et al. and van Grootheest et al. [5, 6]. The closed-loop controlled element dynamics are presented in Equation (4.2).

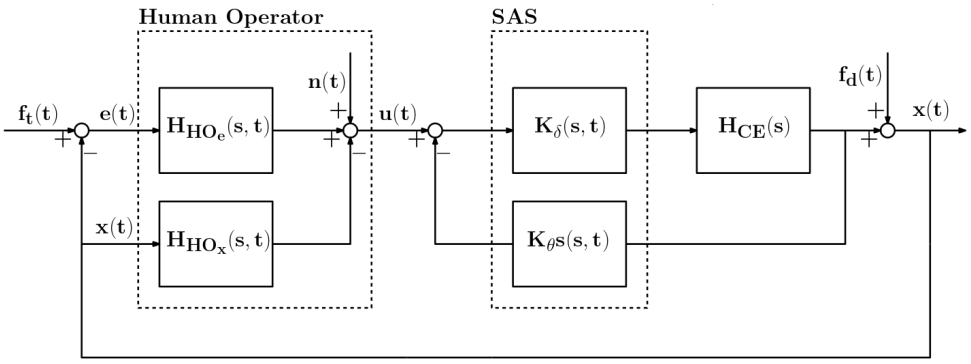

Figure 4.3: Block diagram for controlled element with stability augmentation system

$$H_{CE_{cl}}(j\omega) = \frac{K_\delta H_{CE}}{1 + K_\delta K_\theta j\omega H_{CE}} = \frac{K_\delta \frac{30}{j\omega(j\omega+0.2)}}{1 + K_\delta K_\theta \frac{30}{j\omega(j\omega+0.2)}} = \frac{30K_\delta}{j\omega(j\omega + 0.2 + 30K_\delta K_\theta)} = \frac{90}{j\omega(j\omega+6)} \tag{4.2}$$

With the expression for the closed-loop controlled element dynamics and the desired single integrator dynamics known, it is possible to tune the gain terms of the SAS in such a way that the same dynamics is achieved. The final values for the gain terms can be found hereafter.

$$K_\delta = \frac{90}{30} = 3 \qquad\qquad K_\theta = \frac{6 - 0.2}{30K_\delta} = \frac{5.8}{90} \approx 0.0644$$

The time-varying dynamics thus in fact model a failure of the SAS. In case the SAS fails, the feedback loop is deactivated and the proportional gain reduces to unity. As a result, the "closed-loop" dynamics after a failure occurs is the original controlled element double integrator dynamics. In this way, the same dynamics as Zaal have been achieved, however the reasoning behind the failure modeling has improved [8].

As explained in the previous section, for both the motion and non-motion conditions, two out of four conditions should exhibit LTI controlled element dynamics. For the single integrator dynamics the SAS is active and for the double integrator dynamics the SAS is inactive. For the time-varying conditions, the SAS is suddenly deactivated when trying to model a change from single integrator dynamics to double integrator dynamics, or suddenly activated when modeling the opposite change. The corresponding values for the gain terms of the SAS are listed in Table 4.1. Table 4.1 shows that the failure of the SAS is irrespective of the presence of motion feedback since the gain values are equal for both the motion and non-motion conditions.

Table 4.1: Gain values SAS for controlled element dynamics

	CE	K_δ	K_θ
No Motion	SI	3	0.0644
	DI	1	0
Motion	SI	3	0.0644
	DI	1	0

The activation or deactivation of the SAS during the simulation runs is still modeled as a sigmoidal change of the gain terms, however, with a rate of change of 100 s^{-1}. As can be seen in Figure 2.3, this rate of change results in an abrupt transition and can therefore be considered as an instant failure of the SAS. This instantaneous change in dynamics forces the human operator to directly change his or her manual control behaviour to adapt to the new task quickly.

Two steps need to be taken before the controlled element dynamics can be implemented into the simulation run as defined in Section 4.1. First, the continuous time transfer function as shown in Equation (4.1) should be converted to a continuous time state-space system. The state-space form of this transfer function is given in Equation (4.3).

$$\begin{bmatrix}\dot{x}_1\\ \dot{x}_2\end{bmatrix} = \begin{bmatrix}0 & 1\\ 0 & -0.2-30K_\delta(t)K_\theta(t)\end{bmatrix}\begin{bmatrix}x_1\\ x_2\end{bmatrix} + \begin{bmatrix}0\\ 1\end{bmatrix}u \qquad y = \begin{bmatrix}30K_\delta(t) & 0\end{bmatrix}\begin{bmatrix}x_1\\ x_2\end{bmatrix} \tag{4.3}$$

As explained before, the addition of the SAS does not change anything to the actual controlled element dynamics compared to the controlled element dynamics as used by van Grootheest et al., Plaetinck et al. and Zaal and is only used to provide a better explanation for the failure modeling. [5, 6, 8]. Although the state-space representation looks different from the aforementioned research, the simulated input-output dynamics are equal. In this state-space representation, the gain terms are time-dependent, which is required to model time-varying dynamics as was shown in Table 4.1.

Afterwards, the state-space representation should be converted to the discrete time domain with the MATLAB `d2c` command. With this step being completed, the controlled element model can be inserted into the simulation.

4.2.2. Human Operator Model

Next to the controlled element model, the synthesis of the literature study in Section 2.5 also presented a proposal for a suitable human operator model. Both the visual feedback block and vestibular feedback block need to be modeled.

To model the visual feedback human operator block, the Crossover Model with the neuromuscular limitation term as presented in Equation (2.3) will be used. This model will be simplified by removing the lag term, because with the chosen testing conditions human operators are not expected to adopt lag equalization [3]. Furthermore, Plaetinck et al. stated that replacing the gain K_p and lead constant T_L by two error gains of which one is proportional and one is derivative avoided ambiguity during the identification step [6]. The transfer function of the model that will be implemented in the simulation is shown in Equation (4.4).

$$H_{HO_e}(j\omega,t) = \left(K_e(t) + K_{\dot{e}}(t)\,j\omega\right)e^{-j\omega\tau_e}\frac{\omega_{nm}^2(t)}{(j\omega)^2 + 2\zeta_{nm}(t)\omega_{nm}(t)\,j\omega + \omega_{nm}^2(t)} \tag{4.4}$$

In Section 2.4 it was explained that with the ARX identification method all parameters except the time delay could be estimated recursively. The time delay would be estimated by means of a model fit that is carried out for different sets of time delay values. Therefore, all model parameters except the visual time delay are assumed to be time-variant as is visualized by their time dependency in Equation (4.4). The vestibular feedback model will not be simplified further compared to the transfer function that was presented in Equation (2.6). However, due to the time-varying nature of this research, the motion feedback model parameters are expected to change over time just like the visual feedback model parameters. The time-dependent vestibular feedback model is given by Equation (4.5).

$$H_{HO_x}(j\omega,t) = K_x(t)\,j\omega e^{-j\omega\tau_x}\frac{\omega_{nm}^2(t)}{(j\omega)^2 + 2\zeta_{nm}(t)\omega_{nm}(t)\,j\omega + \omega_{nm}^2(t)} \tag{4.5}$$

Just as with the controlled element model, the continuous time transfer functions need to be converted to a state-space representation first. The time delay parameters will not be directly included in the state-space equations, but will be treated differently as will be explained hereafter. The continuous time state-space representations for the visual and vestibular human operator blocks are given by Equations (4.6) and (4.7), respectively.

$$\begin{bmatrix}\dot{z}_{1_e}\\ \dot{z}_{2_e}\end{bmatrix} = \begin{bmatrix}0 & 1\\ -\omega_{nm}^2(t) & -2\zeta\omega_{nm}(t)\end{bmatrix}\begin{bmatrix}z_{1_e}\\ z_{2_e}\end{bmatrix} + \begin{bmatrix}0\\ 1\end{bmatrix}e \qquad u_e = \begin{bmatrix}K_e(t)\omega_{nm}^2(t) & K_{\dot{e}}(t)\omega_{nm}^2(t)\end{bmatrix}\begin{bmatrix}z_{1_e}\\ z_{2_e}\end{bmatrix} \tag{4.6}$$

$$\begin{bmatrix}\dot{z}_{1_x}\\ \dot{z}_{2_x}\end{bmatrix} = \begin{bmatrix}0 & 1\\ -\omega_{nm}^2(t) & -2\zeta\omega_{nm}(t)\end{bmatrix}\begin{bmatrix}z_{1_x}\\ z_{2_x}\end{bmatrix} + \begin{bmatrix}0\\ 1\end{bmatrix}x \qquad u_x = \begin{bmatrix}0 & K_x(t)\omega_{nm}^2(t)\end{bmatrix}\begin{bmatrix}z_{1_x}\\ z_{2_x}\end{bmatrix} \tag{4.7}$$

These state-space representations need to be discretized afterwards to be compatible with the discrete time simulation setup. This is done similarly to the discretization of the controlled element state-space representation by means of the MATLAB `d2c`.

The time delay for both the visual and vestibular feedback blocks is modeled by shifting the control signals that are the output of the human operator models. The signals are shifted by the number of time steps that

correspond to the estimated time delay and the sampling time as is shown in Equation (4.8). In this way, the signal values are delayed by a similar magnitude as would have been the case for a real human-in-the-loop experiment. It has to be noted that the input signal can only be shifted by an integer multiple of the sampling time due to the discretization and therefore could be rounded off.

$$u_{e_{del}}[i] = u_e[i - int\left(\frac{\tau_e}{\Delta t}\right)] \tag{4.8}$$

To be able to perform simulations with the human operator model, parameter values are needed as input to the model simulation. Similarly to the controlled element dynamics, the parameter values change in a sigmoidal shape when transitioning from single integrator to double integrator dynamics or vice versa. The values were first taken from Plaetinck et al. [6] and later updated with values after the identification of a preliminary human-in-the-loop test experiment. The retrieval of the experimentally obtained values is explained in Appendix A. The final, updated values can be found in Table 4.2 and will be used throughout the remainder of this research.

Table 4.2: Parameter values human operator model for different controlled element dynamics

		HO Parameter Values						
	CE	K_e	$K_{\dot{e}}$	K_x	τ_e	τ_x	ω_{nm}	ζ_{nm}
No Motion	SI	0.08	0.0050	-	0.24	-	7.75	0.125
	DI	0.03	0.0175	-	0.24	-	7.75	0.125
Motion	SI	0.08	0.0050	-	0.24	-	7.75	0.125
	DI	0.06	0.0200	0.025	0.24	0.12	7.75	0.125

Table 4.2 shows that the human operator is expected to control the single integrator dynamics controlled element the same irrespective of the presence of vestibular feedback cues. This is expected because performing velocity control is considered a fairly easy task. However, different human operator models are defined for the motion and non-motion conditions when the controlled element dynamics behave like double integrator dynamics. As discussed in the literature study in Section 2.2.2, Pool found that when participants controlled double integrator dynamics, human operator models differed for cases where vestibular feedback cues were provided compared to cases where these cues were not provided [1]. Note that these parameter values hold for continuous time and are inserted in the state-space representation before the discretization step.

The Bode plots for the human operator dynamics are shown in Figures 4.4 to 4.6. As there are no vestibular dynamics when no motion feedback is presented, no Bode plot is shown for the vestibular feedback model. Furthermore, the visual human operator dynamics for single integrator dynamics controlled elements is equal irrespective of the presence of motion feedback as was explained before. Lastly, there are no vestibular dynamics for single integrator dynamics controlled elements even with motion feedback present, as the assumption was made that because of the easy control task participants do not use the feedback.

4.3. Remnant Modeling and Tuning

As was explained in Chapter 2 the nonlinear part of the human operator is modeled by means of the remnant. For the MATLAB simulations, the remnant will be included in this research by filtering zero-mean unit-variance Gaussian white noise with a second order filter, as van Grootheest et al. proved that the bias for filter orders from two and upwards showed similar results with acceptable accuracy [5]. Similarly to the human operator model blocks and controlled element dynamics, the filter dynamics of the remnant are converted to a state-space representation and then discretized. The continuous time state-space representation is presented in Equation (4.9).

$$\begin{bmatrix} \dot{v}_1 \\ \dot{v}_2 \end{bmatrix} = \begin{bmatrix} 0 & 1 \\ -\frac{1}{0.06^2} & -\frac{2\cdot 0.06}{0.06^2} \end{bmatrix} \begin{bmatrix} v_1 \\ v_2 \end{bmatrix} + \begin{bmatrix} 0 \\ \frac{K_n(t)}{0.06^2} \end{bmatrix} w \qquad n = \begin{bmatrix} 1 & 0 \end{bmatrix} \begin{bmatrix} v_1 \\ v_2 \end{bmatrix} \tag{4.9}$$

The remnant has a big influence on the identification process for reasons that will be elaborately discussed in Chapter 5. For human-in-the-loop experiments, the remnant is simply the residue between the control sig-

nal and the human operator model output. Since participants are part of a closed-loop system, the remnant noise will be forwarded into the closed-loop and therefore influence the identification and hence model output, which results in a different residue.

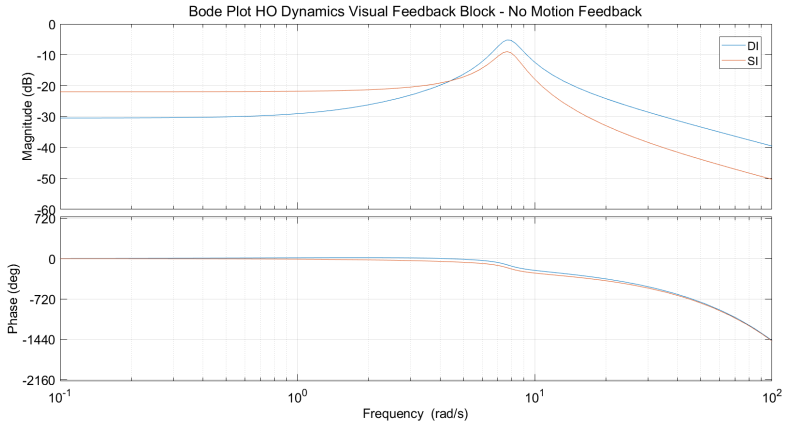

Figure 4.4: Bode plot of simulated human operator visual dynamics without motion feedback

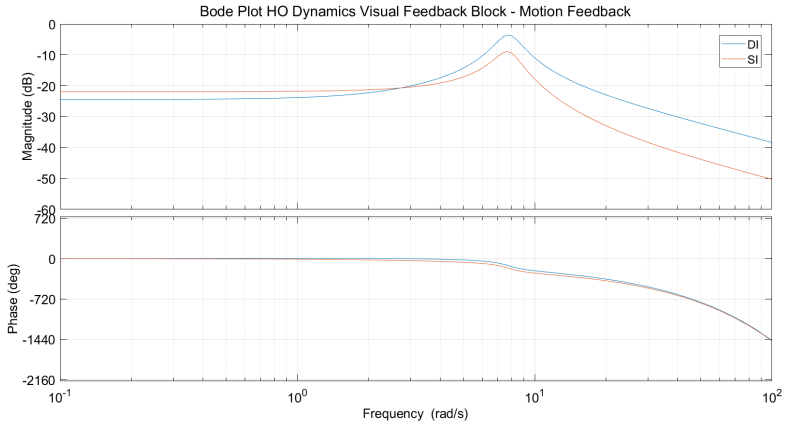

Figure 4.5: Bode plot of simulated human operator visual dynamics with motion feedback

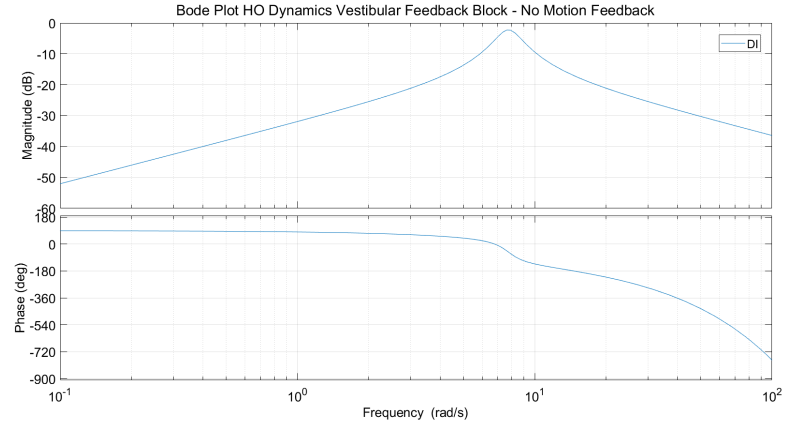

Figure 4.6: Bode plot of simulated human operator vestibular dynamics with motion feedback

For simulations, the remnant is generally modeled as a stand-alone noise input signal. The actual contribution of the remnant to the control action can therefore be modeled as desired. Hence, the influence of the remnant on the identification process can be investigated. As van Grootheest et al. pointed out however, the remnant introduces a bias in the estimation of the parameters [5]. To find out how large this bias actually is for multimodal human operator models, the filter gain $K_n(t)$ is tuned to achieve certain remnant power ratios P_n as is shown in Equation (4.10).

$$P_n = \frac{\sigma_n^2}{\sigma_u^2} \tag{4.10}$$

As can be seen in this equation, the power ratio is determined by calculating the variance of the filtered remnant signal over the variance of the control signal. As explained before, the remnant is part of the control signal in a closed feedback loop. Therefore, the filter gain $K_n(t)$ has to be tuned iteratively. For the tuning process the power ratios were calculated for certain values of the gain based on 10 different remnant signals and then averaged. Next, the filter gains were linearly interpolated to find the required gain settings to achieve the desired power ratios. The desired power ratios are a range of 0.00 (no remnant) to 0.25 with increments of 0.05. The corresponding gains are presented in Table 4.3. By resetting the seed of the random number generator before every simulation is started, the same remnant signals can be generated which allows for repeatability of the simulation.

Table 4.3: Gain values remnant for different controlled element dynamics

		Remnant Filter Gain Values				
	CE	$P_n = 0.05$	$P_n = 0.10$	$P_n = 0.15$	$P_n = 0.20$	$P_n = 0.25$
No Motion	SI	0.0088	0.0130	0.0167	0.0201	0.0234
	DI	0.0070	0.0106	0.0136	0.0164	0.0192
Motion	SI	0.0088	0.0130	0.0167	0.0201	0.0234
	DI	0.0130	0.0194	0.0248	0.0302	0.0357

Since the human operator models for single integrator dynamics are equal irrespective of the presence of motion feedback, it is not strange to see that the remnant signals are equal too. The considerable increase in the remnant filter gain value for the double integrator dynamics with motion feedback present can be explained by the fact that the control action for this condition also increases as was explained in Section 2.2.2 [19]. The change in gain values for time-varying conditions is again realized by means of the same sigmoidal shape as discussed in previous sections. The identification results with different power ratios are discussed in Chapter 6.

4.4. Forcing Functions

The last important parts of the simulation are the two forcing functions. As can be seen in the block diagram in Figure 4.3, the simulations is a combined target-following and disturbance-rejection task. For disturbance-rejection tasks, the vestibular cues and visual cues work in parallel because they are driven by the same output, whereas for target-following tasks the vestibular cues are directly related to the control input of the pilot because that is the only input to the system [22]. For this research a Fourier analysis is required as was presented in Chapter 3, so two forcing functions are necessary to evaluate both the visual and vestibular feedback model. A downside of using two forcing functions is that the coherence between the cues is decreased, but this effect is mitigated by increasing the power of one of the two forcing functions [22]. For this research, the power of the target-following function is halved, making it predominantly a disturbance-rejection control task. The reason for this is that for disturbance-rejection tasks the forcing function directly influences the system output. Vestibular motion cues are perceived faster, hence increasing pilot performance, as was discussed in Section 2.2.2 [1].

The target forcing function and disturbance forcing function are denoted by f_t and f_d, respectively. Both of the forcing functions are multisine signals with each sinusoid having a different frequency, amplitude and phase shift. The selected frequencies are all integer multiples k_n of the base frequency ω_m. The base frequency

is the lowest measurable frequency and depends on the measurement time. The equation for the multisine signal is given by Equation (4.11).

$$f(t) = \sum_{n=1}^{N_{sin}} A_n \sin(k_n \omega_m t + \phi_n) \tag{4.11}$$

To be able to properly compare the human operator models for single integrator dynamics and double integrator dynamics it is of utmost importance to mitigate any effects that can cause differences in the task. Therefore, it is opted to have equal forcing functions realizations for both the time windows with LTI parts for time-varying conditions. As discussed in Section 4.1, the total simulation time of 100 s will be split into a run-in time of 10 s that will be discarded and 90 s of identifiable data, that consist out of 3 equal portions of 30 s. This implies that the forcing functions have to repeat itself every 30 s. The advantage of the repetitive forcing function is that the forcing functions are equal for all windows of the measurement run, leading to parameter estimations that are independent of the forcing function characteristics.

Although this forcing function design allows for equal comparison of the different human operator models, a disadvantage arises. As explained in the previous paragraph, the base frequency depends on the measurement time with a relation as given by Equation (4.12). By decreasing the measurement time, the base frequency increases. This means that the human operator behaviour cannot be identified in the very low frequency region. However, for a measurement time of 30 s, the base frequency is 0.209 rad/s, which is still outside of the crossover region (1 - 5 rad/s), which is the frequency range in which the human operators perform their control.

$$\omega_m = \frac{2\pi}{T_m} = \frac{2\pi}{30} \approx 0.209 rad/s \tag{4.12}$$

Another consideration regarding the forcing function design are the selected phase shifts. During the human-in-the-loop experiment participants might memorize the forcing function after several runs which affects the data. To avoid this experimental confound, 4 different forcing function realizations are generated by changing the randomly generated phase shifts per realization as shown in Tables 4.4 and 4.5 as also done by van der El et al. [35]. In this way, the participants are exposed to different combinations of forcing functions, while still maintaining the same frequency content for the data identification for all conditions and participants. Just as with the decreased measurement time window, this design consideration introduces a downside to the identification process too. Since the time traces of the forcing functions are different, the data cannot be averaged in the time domain. This implies that different methods have to be used to visualize the results compared to [6]. Because of high computational loads, all results as shown in Chapter 6 are based on only one realization, namely realization 1. Although the forcing function is not considered a dependent measure, it could well be the case that the forcing function properties around the transition point of the dynamics have an influence on the identification algorithm. Therefore, it is strongly advised to investigate the effect of the different forcing function realizations for future research.

Table 4.4: Frequency, amplitude and phase shift target forcing function

	f_t Parameter Values						
n	$k_{n,t}$	$\omega_{n,t}$	$A_{n,t}$	$\phi_{n,t,1}$	$\phi_{n,t,2}$	$\phi_{n,t,3}$	$\phi_{n,t,4}$
1	3	0.6283	0.0155	1.8008	1.3088	4.2877	4.6594
2	7	1.4661	0.0084	2.7231	4.0056	2.7890	3.5559
3	11	2.3038	0.0047	0.1897	2.3724	3.2533	4.9210
4	17	3.5605	0.0024	0.0507	4.5767	4.4919	5.5860
5	21	4.3982	0.0018	3.9391	3.6275	0.6555	5.9137
6	29	6.0737	0.0011	0.4741	5.8126	0.1391	3.6184
7	41	8.5870	0.0007	5.6030	3.1568	3.5551	3.7204
8	53	11.1003	0.0006	6.2293	4.1400	6.0887	3.4432
9	71	14.8702	0.0005	0.3548	3.5109	2.3544	5.4860
10	87	18.2212	0.0004	0.7741	3.0082	1.6882	5.7340

Table 4.5: Frequency, amplitude and phase shift disturbance forcing function

	f_d Parameter Values						
n	$k_{n,d}$	$\omega_{n,d}$	$A_{n,d}$	$\phi_{n,d,1}$	$\phi_{n,d,2}$	$\phi_{n,d,3}$	$\phi_{n,d,4}$
1	2	0.4189	0.0291	1.9864	4.4771	5.5149	2.8416
2	5	1.0472	0.0192	5.8760	1.3299	6.0377	3.3197
3	9	1.8850	0.0102	0.2433	1.2588	3.2878	0.7182
4	13	2.7227	0.0060	2.7584	2.6748	0.2975	0.7687
5	19	3.9794	0.0034	5.8004	5.3686	4.6609	2.9249
6	27	5.6549	0.0020	0.0668	2.6944	4.3559	5.1453
7	39	8.1681	0.0012	3.5067	4.9951	2.1447	2.0855
8	51	10.6814	0.0009	3.5714	3.5500	4.2549	0.3834
9	67	14.0324	0.0008	2.1492	0.6432	0.8442	0.7629
10	83	17.3835	0.0007	3.0233	5.2846	0.3753	3.2475

4.5. Simulation Verification

To be able to draw valid conclusions based on the results of the identification phase, the simulation needs to be verified. The verification phase ensures that the implementation of the simulation is done correctly. For verification, the simulated responses need to be checked with a different, independent method. If the same simulation results are found, the verification procedure is deemed a success. The verification will be done in both the frequency domain in Subsection 4.5.1 and the time domain in Subsection 4.5.2.

4.5.1. Verification Frequency Domain

The additional method that will be used for verification of the human operator models in the frequency domain is the Fourier coefficient method as used by van Paassen and Mulder [12]. By using the cross spectral densities of the block diagram signals an estimate of the human operator transfer function at the forcing function excitation frequencies can be made. The relationship between these signal in the frequency domain is given by Equation (4.13).

$$U_1(\omega_{n,d_1}) = H_{HO_e}(\omega_{n,d_1})E_1(\omega_{n,d_1}) - H_{HO_x}(\omega_{n,d_1})X_1(\omega_{n,d_1}) + N_1 \tag{4.13}$$

In this equation, U_1, E_1 and X_1 are the Fourier coefficients of the block diagram signal in the frequency domain. N_1 denotes the Fourier coefficient for the remnant, but it will not be taken into account as the remnant has a low signal-to-noise ratio at the excitation frequencies compared to the control signal, error signal and output signal [12]. In the relation one can see that there are two unknowns for only equation and therefore will not provide just one solution. To solve this problem, another relationship needs to be defined. This is done by finding the Fourier coefficients for the other forcing functions, and then interpolating the values to find the coefficient values for the excitation frequencies of the first forcing function. When interpolating one must not forget to correct for the phase angle. This yields a set of equations that can be solved as is shown in Equation (4.14).

$$\begin{bmatrix} U_1(\omega_{n,d_1}) \\ \hat{U}_1(\omega_{n,d_1}) \end{bmatrix} = \begin{bmatrix} E_1(\omega_{n,d_1}) & -X_1(\omega_{n,d_1}) \\ \hat{E}_1(\omega_{n,d_1}) & -\hat{X}_1(\omega_{n,d_1}) \end{bmatrix} \begin{bmatrix} H_{HO_e}(\omega_{n,d_1}) \\ H_{HO_x}(\omega_{n,d_1}) \end{bmatrix} \tag{4.14}$$

This system of equations can be rewritten to expressions for the estimates of the human operator models as is presented in Equations (4.15) and (4.16). Since these expressions consist of known values, the estimate of the human operator model can be calculated as well. This step can be executed for all the excitation frequencies of the forcing functions to get estimates for the human operator models over a broad frequency range.

$$H_{HO_e}(\omega_{n,d_1}) = \frac{\hat{U}_1(\omega_{n,d_1})X_1(\omega_{n,d_1}) - U_1(\omega_{n,d_1})\hat{X}_1(\omega_{n,d_1})}{\hat{E}_1(\omega_{n,d_1})X_1(\omega_{n,d_1}) - E_1(\omega_{n,d_1})\hat{X}_1(\omega_{n,d_1})} \tag{4.15}$$

$$H_{HO_x}(\omega_{n,d_1}) = \frac{\hat{U}_1(\omega_{n,d_1})E_1(\omega_{n,d_1}) - U_1(\omega_{n,d_1})\hat{E}_1(\omega_{n,d_1})}{\hat{E}_1(\omega_{n,d_1})X_1(\omega_{n,d_1}) - E_1(\omega_{n,d_1})\hat{X}_1(\omega_{n,d_1})} \tag{4.16}$$

For the estimates of the human operator models the gain and phase can be calculated. These results can then be plotted together with the simulated human operator model. If the simulation has been performed correctly, both plots should overlap perfectly for a remnant free, completely deterministic simulation. To check that the verification is a success, this method has been applied to a single integrator controlled element dynamics condition with only visual feedback which is shown in Figure 4.7. To show the verification is a success for the multimodal control diagram as well, the Bode plots of the simulated human operator for double integrator controlled element dynamics is presented in Figure 4.8.

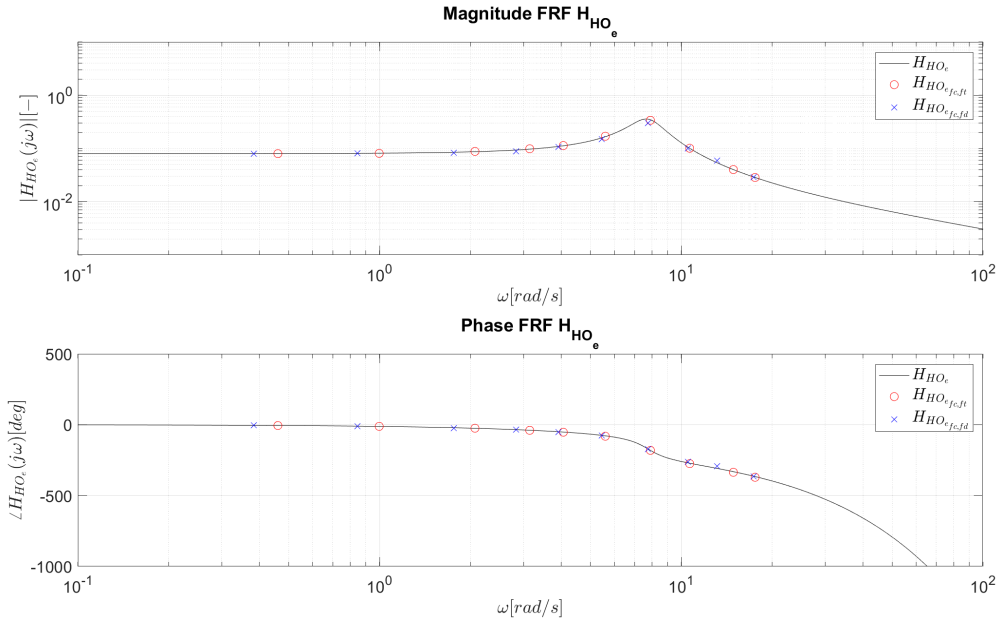

Figure 4.7: Verification of unimodal SI CE dynamics

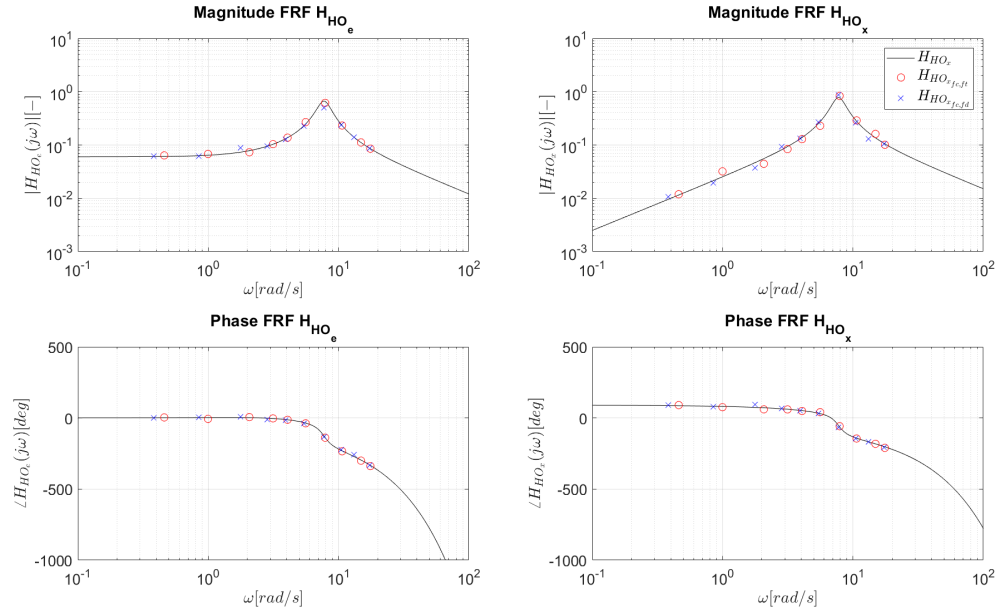

Figure 4.8: Verification of multimodal DI CE dynamics

The verification of the remnant signal in the frequency domain will be done by calculating the auto-power spectrum of the filtered noise signal and comparing that to the power spectrum of the analytical model. The power spectral densities are shown in Figure 4.9. This figure shows that for the complete frequency range the analytical model perfectly overlaps the power spectrum of the filtered noise signal. Therefore, the implementation of the remnant is considered verified.

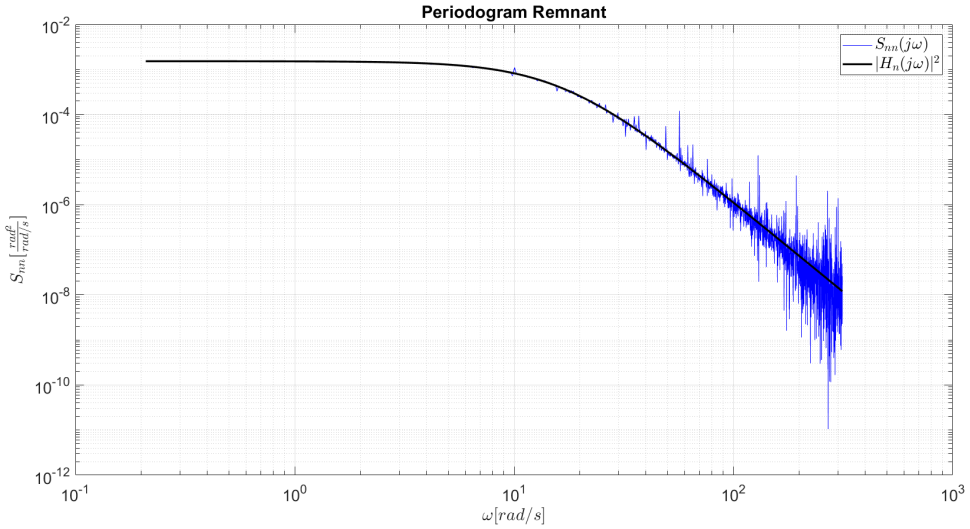

Figure 4.9: Verification of remnant signal

4.5.2. Verification Time Domain

For verification in the time domain, the time traces of the error signal, control signal and system output signal will be compared for different conditions. If there is no remnant present, the simulation should be completely deterministic and therefore the signals for the LTI parts of the time-varying condition should be equal to the signals of the corresponding LTI conditions. For this comparison, conditions C5, C6 and C7 will be used. The overview of the time traces of the signals is given in Figure 4.10.

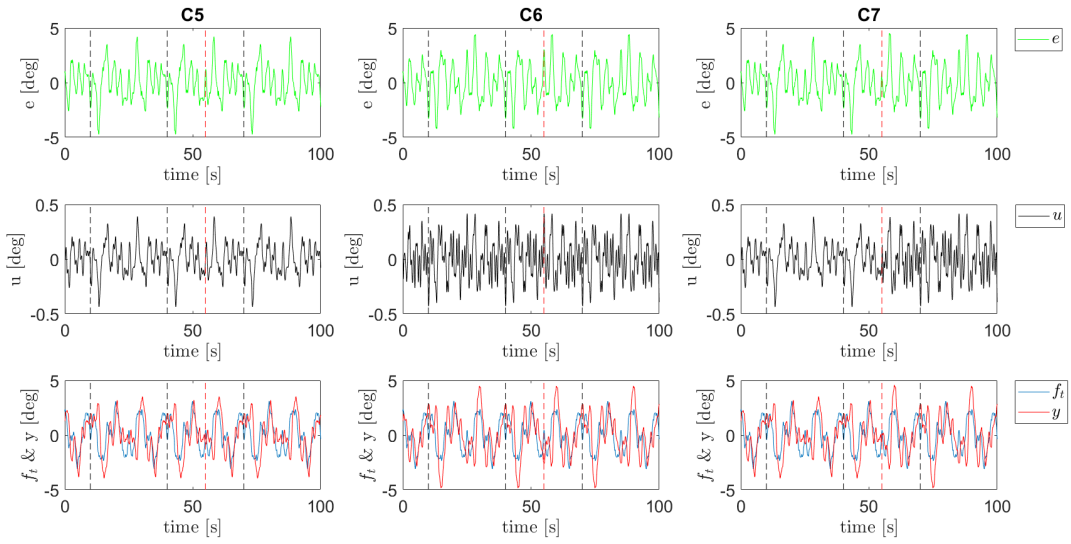

Figure 4.10: Time traces of the block diagram signals for different conditions

Figure 4.10 shows that the time signals in the right column, which correspond to the time-varying condition, have both single and double integrator dynamics properties. Before the transition, the time-varying condition has equal dynamics with the time signals in the left column, which is a single integrator dynamics case. After the transition, the time-varying condition has equal dynamics with the middle column, which is a double integrator dynamics condition. The verification is deemed complete, because condition C7 contains a transition from single integrator to double integrator controlled element dynamics as was presented in Table 3.1.

The remnant will be verified in the time domain by analyzing the prefiltered noise signal, as previous section already showed that the implementation of the noise filter was successful. Section 4.3 discussed that the remnant would be modeled as a filtered zero-mean unit-variance Gaussian white noise signal. One realization of the noise signal has been analyzed as is presented in Figure 4.11. The mean and standard deviation of this prefiltered noise signal are 0 and 10, respectively. Note that the white noise signal has been divided by the square root of the time step. As a result, all the values are scaled by a factor of 10, hence leading to the fact that the mean and standard deviation in this graph are 10 times higher than the original input values of 0 for the mean and 1 for the standard deviation. Therefore, the white noise signal can be considered verified.

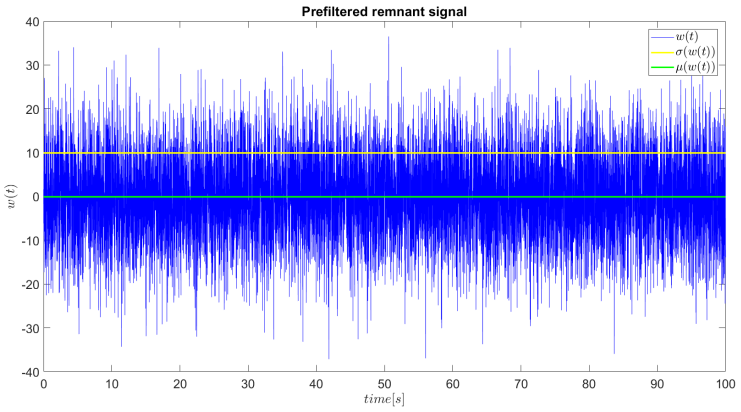

Figure 4.11: Time traces of the prefiltered white noise signal with mean and standard deviation values

4.6. Concluding Remarks on the Simulation

This chapter presented all the important aspects of the setup of a manual control simulation. The goal of this simulation is to verify the recursive multichannel ARX identification method and find investigate the effects of important experiment design considerations for the human-in-the-loop experiment. The simulation is run in discrete time and is propagated by means of a state-space representation of the controlled element and human operator model. The controlled element is represented by double integrator dynamics, supported by an SAS that results in single integrator closed loop controlled element dynamics. The SAS is either switched off or on halfway through the measurement to model time-varying dynamics. The transition is governed by a sigmoidal change in the parameters with a high rate of change, making it feel like an instantaneous failure of the SAS. The human operator is modeled with a set of parameters that is found from a preliminary human-in-the-loop experiment. The time delay in discrete time is modeled as an input-output delay by shifting the time signal by a number a samples that corresponds to the actual time delay. The remnant of the human operator is included after filtering zero-mean unit variance Gaussian white noise through a second order filter. The remnant gain is tuned in such a way that various remnant power ratios can be attained. The forcing functions that excite the closed-loop system are multisine signals that repeat themselves every 30 seconds to ensure that participants are presented with the same forcing functions for the LTI parts of the dynamics that will be identified. Furthermore, different phase shifts are assigned to prevent a participant from memorizing the signal and hence avoiding possible experiment confounds. Verification showed that all parts had been implemented correctly.

With all important elements of the control scheme discussed, the identification procedure can be explained. Chapter 5 elaborates on the implementation of the recursive multichannel time-varying ARX identification method.

5

Human Operator Identification

The previous chapter presented all the details of the simulations that will be performed to provide data used to verify the multichannel recursive ARX identification method. This chapter discusses all important aspects of the identification phase. As introduced in Chapter 3, the identification method will be a recursive ARX model, supported by an additional ordinary least squares ARX model for which the need was explained in Section 3.2. The aim of this chapter is to verify the time-varying multichannel ARX identification method.

The ARX model structure will first be explained in Section 5.1. Both the RLS and OLS identification procedures will be discussed in detail. Afterwards, the conversion from ARX coefficients to human operator model parameters will be reviewed in Section 5.1. Next, the influence of the remnant which results in a bias in the estimation results as announced in Section 2.4.3 will be considered in Section 5.3. Finally, a verification for the identification procedure will be done in Section 5.4. This chapter will be concluded in Section 5.5.

5.1. ARX Model Structure

The ARX model belongs to a class of linear models as developed by Ljung [33]. The foundation of this model structure consists out of a discrete time shift operator q and two polynomials which are a function of this time shift operator, namely the $A(q)$ and $B(q)$ polynomial. The time shift operator works on the time domain signals in the block diagram following the relation as defined in Equation (5.1).

$$\begin{aligned} q^{-1}e(t) &= e(t-1) \\ q^{-2}e(t) &= e(t-2) \end{aligned} \tag{5.1}$$

This relation is similar for the control signal $u(t)$ and system output signal $x(t)$ and can be expanded for higher orders of the time shift operator q. The polynomial order is still undefined for now, so the equations are given for a generic number of coefficients n_a and n_b respectively in Equations (5.2) and (5.3).

$$A(q) = 1 + a_1 q^{-1} + a_2 q^{-2} + ... + a_{n_a} q^{-n_a} \tag{5.2}$$

$$B(q) = b_0 + b_1 q^{-1} + b_2 q^{-2} + ... + b_{n_b} q^{-n_b} \tag{5.3}$$

This model structure was applied by Nieuwenhuizen et al. on a human operator model for the identification of LTI multimodal manual control [18]. For the analysis of multimodal manual control, two different $B(q)$ polynomials need to be defined for each of the feedback channels, being $B_e(q)$ and $B_x(q)$. The dependencies of the polynomials and block diagram signals are given by Equation (5.4) and visualized in Figure 5.1.

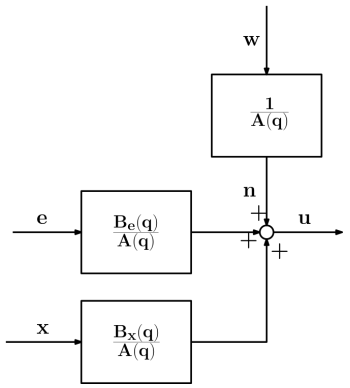

Figure 5.1: Block diagram of ARX model structure

$$\begin{aligned} A(q)\,u(t) &= B_e(q)e(t-n_{k_e}) + B_x(q)x(t-n_{k_x}) + w(t) \\ u(t) &= \frac{B_e(q)}{A(q)}e(t-n_{k_e}) + \frac{B_x(q)}{A(q)}x(t-n_{k_x}) + \frac{1}{A(q)}w(t) \end{aligned} \tag{5.4}$$

To be able to model the human operator the polynomial coefficients need to be estimated. This estimation process is done with both a RLS algorithm and OLS algorithm that will be discussed in the next two subsections. Both algorithms are based on the one-step-ahead predictor as defined by Ljung [33]. The predictor is given by Equation (5.5).

$$\hat{u}(t|t-1) = [1 - A(q)]\,u(t) + B_e(q)e(t) - B_x(q)x(t) \tag{5.5}$$

The first term on the right of this predictor processes past outputs, whereas the second and third terms process current inputs. Because all of these terms are known, the model can predict the control signal. The predictor can be rewritten in the form of a linear regression format as the multiplication of a regression vector φ and a coefficient vector θ, which is shown in Equation (5.6).

$$\hat{u}[i|i-1,\theta] = \varphi[i]\theta \tag{5.6}$$

The equation is given in discrete time since the analysis will be done in discrete time as well. The coefficient vector in this linear regression format consists out of the polynomial coefficients from Equations (5.2) and (5.3).

$$\theta = \begin{pmatrix} a_1^d & a_2^d & \cdots & a_{n_a}^d & b_{0_e}^d & b_{1_e}^d & \cdots & b_{n_{b_e}}^d & b_{0_x}^d & b_{1_x}^d & \cdots & b_{n_{b_x}}^d \end{pmatrix}^T \tag{5.7}$$

The regression vector $\varphi[i]$ consists out of the time shifted block diagram signals and is set up as such that the correct time shift corresponds to the correct ARX coefficient in the linear regression format. The regression vector is given by Equation (5.8).

$$\begin{aligned} \varphi[i] = \big(&-u[i-1] \quad -u[i-2] \quad \cdots \quad -u(t-n_a) \quad e[i-n_{k_e}] \quad e[i-n_{k_e}-1] \quad \cdots \quad e[i-n_{k_e}-n_{b_e}] \quad \cdots \\ &\cdots \quad -x[i-n_{k_x}] \quad -x[i-n_{k_x}-1] \quad \cdots \quad -x[i-n_{k_x}-n_{b_x}] \big) \end{aligned} \tag{5.8}$$

As can be seen in Equation (5.4), the error signal $u(t)$ and system output signal $x(t)$ are shifted in time by n_{k_e} and n_{k_x} instances, respectively. These time shifts correspond to the delay of the signals that cannot be included in the polynomials and have to be estimated with the regression as shown in Equation (5.8). The discrete time delays are modeled similarly to the human operator delay as shown in Equation (4.8). Plaetinck et al. proposed that a parallel time delay processing strategy would be suitable for the estimation of the time delay [6]. The parallel delay estimation calculates the model parameters and corresponding model fit for a series of delays and selects the delay for which the model error is minimal. The model fit is based on the VAF calculation as shown in Equation (5.9). Although his findings were based on unimodal manual control, the assumption is made that parallel delay estimation also works well for multimodal manual control since the addition of a new, independent vestibular time delay does not require drastic changes to the estimation method. Since the estimation of the time delay is only based on the model fit and not on the ARX model structure which is of interest for this report, it is decided for computational reasons to only focus on the coefficient estimation in this preliminary thesis report. The time delays were set constant and equal to Zaal for this preliminary thesis research [21].

$$VAF = max\left(0, \left(1 - \frac{\sum_{i=1}^{N} \left|u[i] - \hat{u}[i]\right|^2}{\sum_{i=1}^{N} \left|u[i]\right|^2}\right) \cdot 100\%\right) \tag{5.9}$$

5.1.1. Recursive Least Squares ARX Coefficient Estimation

The most important and complex algorithm that will be used for the identification procedure is the RLS ARX coefficient estimation. Since the nature of this algorithm is recursive, it updates the ARX model coefficients at every time step and therefore allows for tracking time-varying changes in the model parameters. The RLS procedure is visualized in Figure 5.2 [36].

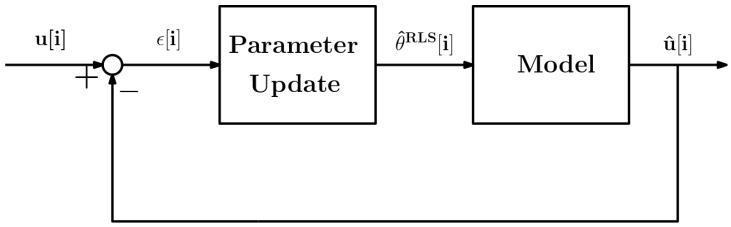

Figure 5.2: Block diagram of RLS algorithm, adapted from Tangirala [36]

For the first time step, the model output $\hat{u}[i]$ needs to be calculated. This is done by providing an initial coefficient vector θ_0^{RLS} that will be multiplied with the regression vector. For the RLS identification procedure, an initial identification start time of 2 seconds is chosen to ensure that transients have died out. In this way, also the problem of not having a complete regression vector (of which some of the signal values are delayed by n_{k_e} or n_{k_x} samples) is mitigated. The model output $\hat{u}[i]$ is then compared to the actual control signal. Based on the difference, the coefficients are then updated again, which results in a new model output $\hat{u}[i]$. This process is iterated until the total simulation run has been analyzed. The algorithm is given by Equations (5.10) to (5.12).

$$\hat{u}[i] = \varphi[i]\theta^{RLS}[i-1] \tag{5.10}$$

$$\epsilon[i] = u[i] - \hat{u}[i] \tag{5.11}$$

$$\theta^{RLS}[i] = \theta^{RLS}[i-1] + K[i]\epsilon[i] \tag{5.12}$$

The rate at which parameters are updated depends on the gain vector $K[i]$. The gain vector is a function of the regression vector φ, the forgetting factor λ and the covariance matrix $P[i]$ [33]. Their relationship is given by Equations (5.13) to (5.15).

$$K[i] = Q[i]\varphi[i] \tag{5.13}$$

$$Q[i] = \frac{P[i-1]}{\lambda + \varphi[i]P[i-1]\varphi^T[i]} \tag{5.14}$$

$$P[i] = \frac{P[i-1]}{\lambda}\big(I - K[i]\varphi[i]\big) \tag{5.15}$$

Next to the coefficient vector θ^{RLS}, the covariance matrix $P[i]$ also needs an initial estimate to make the RLS algorithm work. The initial values for the coefficient vector θ^{RLS} were based on the results found after performing an OLS identification procedure. However, it has to be checked that independently of the OLS procedure, the RLS algorithm converges to the correct coefficient values for different initial conditions since each run of each participant results in different initial values. The convergence for different initial conditions will be checked in this preliminary thesis research and is documented in Chapter 6. The initial values for the covariance matrix $P[i]$ are equal to Plaetinck et al., however, adapted to a larger matrix to account for the multimodal manual control situation compared to Plaetinck's et al. unimodal manual control research [6]. The initial covariance matrix is given in Equation (5.16).

$$P_0 = 10^4 I_{6x6} \tag{5.16}$$

The forgetting factor λ determines the memory horizon of the algorithm. For the algorithm above, the forgetting factor is assumed to be a constant which results in the same memory horizon for all ARX model coefficients. The memory horizon T_0 is defined in Equation (5.17) and visualized in Figure 5.1.1.

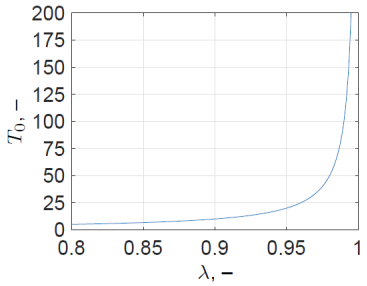

Figure 5.3: Relationship between forgetting factor and memory horizon for $\Delta t = 0.01s$, obtained from Van Grootheest et al. [5]

$$T_0 = \frac{1}{1-\lambda} \tag{5.17}$$

The figure shows that for lower values of λ, old data are discounted quicker in the RLS algorithm. The relationship between the forgetting factor and the number of samples of the memory horizon is given by Table 5.1.

Table 5.1: Relationship between forgetting factor and memory horizon

λ	T_0
0.99219	128
0.99609	256
0.99805	512
1	∞

The forgetting factor was tuned by van Grootheest et al. to be $\lambda = 0.99609$ [5]. λ is most commonly set to values ranging between 0.98 and 0.995 [33]. The forgetting factor can be considered a trade-off between the suppression of noise for values close to $\lambda = 1$ and the ability to track changes for values close to $\lambda = 0.99$.

Van Grootheest et al. also used a forgetting matrix Λ to estimate the ARX model coefficients in which different forgetting factors were applied to the coefficients [5]. The forgetting matrix has its coefficient-specific forgetting factors on the diagonal axis. The definition of the forgetting matrix is shown in Equation (5.18).

$$\Lambda = diag\left(\lambda_{a_1}, \lambda_{a_2}, \ldots, \lambda_{a_{n_a}}, \lambda_{b_{0_e}}, \lambda_{b_{1_e}}, \ldots, \lambda_{b_{n_{b_e}}}, \lambda_{b_{0_x}}, \lambda_{b_{1_x}}, \ldots, \lambda_{b_{n_{b_x}}}\right)^{-1/2} \tag{5.18}$$

Parameters that were expected to be independent of the controlled element dynamics are assigned a value of $\lambda = 1$, whereas parameters that are expected to change with different dynamics were assigned a value lower than $\lambda = 1$. Van Grootheest et al. set the coefficients of the $A(q)$ polynomial to $\lambda = 1$ and varied the values for λ for the $B(q)$ polynomials. By changing the forgetting matrix entries, different values for the VAF were obtained. Equations (5.14) and (5.15), adapted for using forgetting matrices, are displayed hereafter.

$$Q[i] = \frac{\Lambda P[i-1]\Lambda}{1 + \varphi[i]\Lambda P[i-1]\Lambda\varphi^T[i]} \tag{5.19}$$

$$P[i] = \Lambda P[i-1]\Lambda\big(I - K[i]\varphi[i]\big) \tag{5.20}$$

Van Grootheest et al. performed this research for unimodal manual control tasks, so the influence of the forgetting method on multimodal manual control remains unknown [5]. The differences between using a forgetting factor and forgetting matrix will therefore be examined in Chapter 6.

5.1.2. Ordinary Least Squares ARX Coefficient Estimation

The ARX model structure can also be used with an OLS algorithm. Similar to the time delay estimation, the OLS algorithm aims to find a set of coefficients for which the squared difference of the actual control signal and modeled control signal is minimal as presented in Equation (5.9). However, instead of updating the coefficient

vector at every time step, just one coefficient vector is calculated over the entire measurement time. This means that for the LTI conditions, the total run can be identified with the OLS algorithm, and for the time-varying conditions the LTI parts of the run can be identified with the OLS algorithm. The coefficient vector can be computed using Equation (5.21).

$$\theta^{OLS}[i] = \left(\Phi[i]^T \Phi[i]\right)^{-1} \Phi[i]^T U[i] \tag{5.21}$$

Note that in this equation, the regression vector and control signal vector contain all the entries for the entire measurement window. Since $\varphi[i]$ was already a vector, $\Phi[i]$ becomes a matrix. The complete regression matrix is given by Equation (5.22) and the control signal vector is given by Equation (5.23). Similarly to the RLS algorithm, the identification procedure starts at sample i_{start} after all the transients have died out.

$$\Phi = \begin{pmatrix} \varphi[i_{start}]^T & \varphi[i_{start}+1]^T & \cdots & \varphi[i_{start}+N]^T \end{pmatrix}^T \tag{5.22}$$

$$U = \begin{pmatrix} u[i_{start}] & u[i_{start}+1] & \cdots & u[i_{start}+N] \end{pmatrix}^T \tag{5.23}$$

5.2. ARX Coefficient Conversion to Model Parameters

For both algorithms, the ARX model coefficients can be calculated with the methods explained in the previous sections. After estimating the ARX model coefficients, the conversion to human operator model parameters needs to be done.

The rewritten form of Equation (5.4) that is visualized in Figure 5.1 shows a similar input-output relation like the human operator models that were defined in Chapter 4. Up until now, the coefficient vector as shown in Equation (5.7) that defines this input-output relation for the ARX models had an undefined number of coefficients. The number of coefficients determines the model order of the ARX polynomials as displayed in Equations (5.2) and (5.3).

To allow for easy conversion from ARX model coefficients to human operator model parameters, an ARX model of matching order to the human operator model is chosen. This means that the $A(q)$ polynomial and both the $B_e(q)$ and $B_x(q)$ polynomial are all second order equations which results in each polynomial having 2 coefficients. The corresponding expression for the control signal as presented in Equation (5.4) is shown hereafter.

$$u(t) = \frac{b_{0_e}^d + b_{1_e}^d q^{-1}}{1 + a_1^d q^{-1} a_2^d q^{-2}} q^{-n_{k_e}} e(t) + \frac{b_{0_x}^d + b_{1_x}^d q^{-1}}{1 + a_1^d q^{-1} a_2^d q^{-2}} q^{-n_{k_x}} x(t) + \frac{1}{1 + a_1^d q^{-1} a_2^d q^{-2}} w(t) \tag{5.24}$$

This results in a set of 6 discrete time coefficients that need to be estimated, and these coefficients are put together in the coefficient vector θ. The discrete time ARX model transfer functions for visual and vestibular feedback are given by Equations (5.25) and (5.26).

$$H_{HO_e}(q) = \frac{b_{0_e}^d + b_{1_e}^d q^{-1}}{1 + a_1^d q^{-1} a_2^d q^{-2}} q^{-n_{k_e}} \tag{5.25}$$

$$H_{HO_x}(q) = \frac{b_{0_x}^d + b_{1_x}^d q^{-1}}{1 + a_1^d q^{-1} a_2^d q^{-2}} q^{-n_{k_x}} \tag{5.26}$$

To be able to retrieve the human operator parameters, two steps need to be taken. First, the discrete time ARX model needs to be converted to a discrete time transfer function. This step can be explained with one of the Z-transform properties of the discrete time transfer functions: $Z[q^{-n}(i\Delta t)] = z^{-n}F(z)$. This derivation will be shown for the visual feedback human operator block, the vestibular feedback human operator model can be derived in a similar fashion. The discrete time transfer function for the visual feedback model is presented in Equation (5.27).

$$H_{HO_e}(z) = \frac{b_{0_e}^d + b_{1_e}^d z^{-1}}{1 + a_1^d z^{-1} a_2^d z^{-2}} z^{-\frac{\tau_e}{\Delta t}} \tag{5.27}$$

The second step requires a conversion from the discrete time transfer function to the continuous time transfer function. This step is vital because the human operator parameters are also defined in the continuous time domain. The conversion is easily performed with the zero-order hold MATLAB `d2c`-command. The continuous time FRF for the visual with ARX model coefficients is given by Equation (5.28).

$$H_{HO_e}(j\omega) = \frac{b^c_{0_e} j\omega + b^c_{1_e}}{(j\omega)^2 + a^c_1 j\omega + a^c_2} e^{-\tau_e j\omega} \tag{5.28}$$

The newly found continuous time FRF for the human operator models has the same form as the human operator models that were defined in Chapters 2 and 4 as is displayed in Equations (5.29) and (5.30).

$$\begin{aligned} H_{HO_e}(j\omega) = \frac{b^c_{0_e} j\omega + b^c_{1_e}}{(j\omega)^2 + a^c_1 j\omega + a^c_2} e^{-\tau_e j\omega} &= \left(K_e + K_{\dot{e}} j\omega\right) e^{-j\omega\tau_e} \frac{\omega^2_{nm}}{(j\omega)^2 + 2\zeta_{nm}\omega_{nm} j\omega + \omega^2_{nm}} \\ &= \frac{K_e\omega^2_{nm} + K_{\dot{e}}\omega^2_{nm} j\omega}{(j\omega)^2 + 2\zeta_{nm}\omega_{nm} j\omega + \omega^2_{nm}} e^{-j\omega\tau_e} \end{aligned} \tag{5.29}$$

$$\begin{aligned} H_{HO_x}(j\omega) = \frac{b^c_{0_x} j\omega + b^c_{1_x}}{(j\omega)^2 + a^c_1 j\omega + a^c_2} e^{-\tau_x j\omega} &= \left(K_x j\omega\right) e^{-j\omega\tau_x} \frac{\omega^2_{nm}}{(j\omega)^2 + 2\zeta_{nm}\omega_{nm} j\omega + \omega^2_{nm}} \\ &= \frac{K_x\omega^2_{nm} j\omega}{(j\omega)^2 + 2\zeta_{nm}\omega_{nm} j\omega + \omega^2_{nm}} e^{-j\omega\tau_x} \end{aligned} \tag{5.30}$$

The human operators can be derived from the ARX model coefficients individually. The derivation for each of the parameters is presented with Equations (5.31) till including (5.35). With these relations found, the complete identification step can be considered complete.

$$K_e = \frac{b^c_{1_e}}{a^c_2} \tag{5.31}$$

$$K_{\dot{e}} = \frac{b^c_{0_e}}{a^c_2} \tag{5.32}$$

$$K_x = \frac{b^c_{0_x}}{a^c_2} \tag{5.33}$$

$$\zeta_{nm} = \frac{a^c_1}{2\sqrt{a^c_2}} \tag{5.34}$$

$$\omega_{nm} = \sqrt{a^c_2} \tag{5.35}$$

For the conversion to human operator model parameters, the $b^c_{1_x}$ coefficient does not necessarily have to be estimated as is shown with the relations above. It is nevertheless included in the identification procedure because it can aid as verification of the estimation of the $b^c_{0_x}$ coefficient as will be shown in the next section.

5.3. Remnant Influence

When the ARX model identification method was discussed as a suitable option for analysis in Section 2.4.3, a disadvantage that is inherent to this method was mentioned. When identifying manual control behaviour with an ARX model structure, a bias in the estimation results is introduced. This bias arises because both the human operator model blocks and the remnant are governed by the same $A(q)$ polynomial as can be seen in Figure 5.1. The stochastic noise that is injected in the closed-loop system affects not only the estimation of the ARX coefficients a_1 and a_2, but the coefficients of the $B(q)$ polynomials as well.

Van Grootheest et al. investigated the magnitude of this bias for simulations of unimodal control loops [5]. He found that this bias depends on both the order of the remnant filter as well as the power ratio of the remnant noise. In Section 2.5 it was discussed that a second-order remnant filter showed results with acceptable accuracy [5]. In this case, the remnant filter order is equal to the ARX model order.

The bias in the estimation of the ARX coefficients is visualized in Figure 5.4. It can quickly be noted that the first-order remnant filter results in the largest bias and higher order filters result in comparable magnitudes of bias. As expected, higher remnant power ratios lead to a larger bias. Van Grootheest et al. also included a remnant filter that had dynamics equal to the neuromuscular dynamics, denoted by the filter order nm. This filter resulted in the smallest bias due to the perfect match of the noise and process dynamics [5]. However, as the authors pointed out, it is not realistic to assume that the remnant can be modeled equally to the neuromuscular dynamics. Comparable results can be found when investigating the influence of the remnant on the time delay estimation. Van Grootheest's et al. results for time delay estimation can be found in Figure 5.5. Again, the first-order remnant filter proves to be inaccurate, and filter orders of two and upwards show similar results. Again, the remnant filter with neuromuscular dynamics shows the smallest bias. The same trends are

expected for multimodal human operator models because both of the human operator blocks are coupled to the same $A(q)$ polynomial.

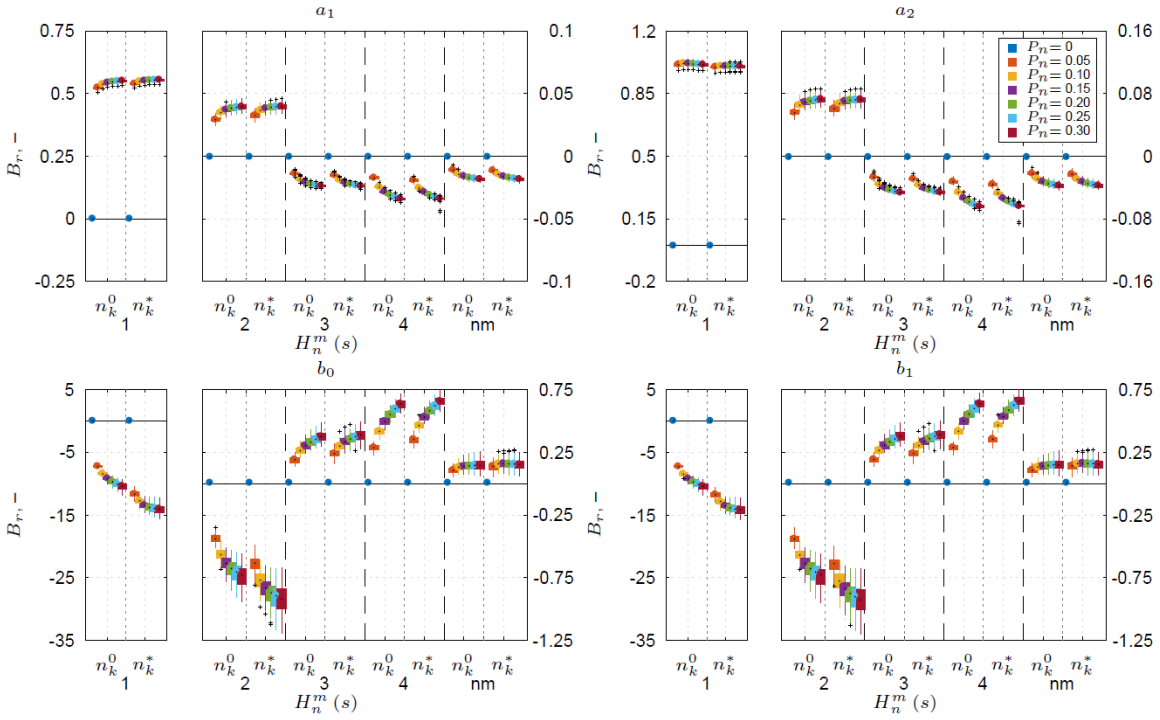

Figure 5.4: Magnitude bias ARX coefficients unimodal control loops with SI CE dynamics for different remnant filter orders and remnant power ratios, obtained from van Grootheest et al. [5]

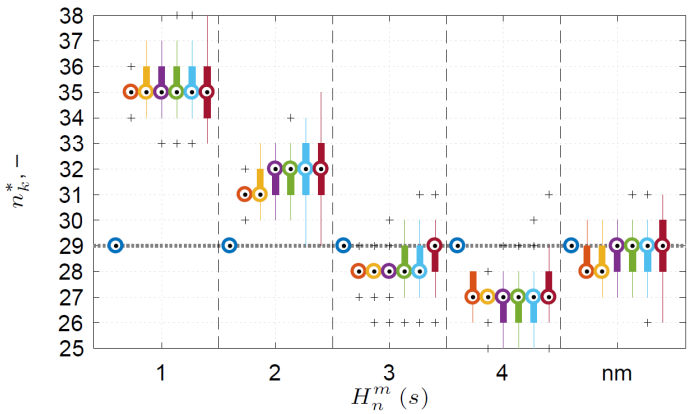

Figure 5.5: Magnitude bias time delay unimodal control loops with SI CE dynamics for different remnant filter orders and remnant power ratios, obtained from van Grootheest et al. [5]

5.4. Verification Identification

Just as with the simulation setup, the identification procedure needs to be verified as well. The verification of the identification step is necessary to ensure that the parameters that have been estimated are correct. As explained in the previous section, the presence of a stochastic signal in the form of a remnant creates a bias in the identification results. To be completely sure that the parameters are estimated correctly, the verification step will be performed without the remnant signal present. Although this is not a realistic situation, it allows to

assure that the implementation is done correctly and that later on, if the remnant signal is present, the parameter values found can be deemed correctly. The verification phase for the identification step will be completed for both the ARX model coefficients and the human operator model parameters.

The RLS algorithm is considered verified if the remnant-free time trace of the retrieved ARX model coefficient overlap with the values that are directly retrieved from converting the input values that are fed to the simulation. The verification is done for a time-varying condition with both visual and vestibular feedback. As support, the values retrieved with the OLS algorithm for the LTI parts of the condition are included as well. The ARX model coefficient values are presented in Figure 5.6, with a close-up of the transition region in Figure 5.7.

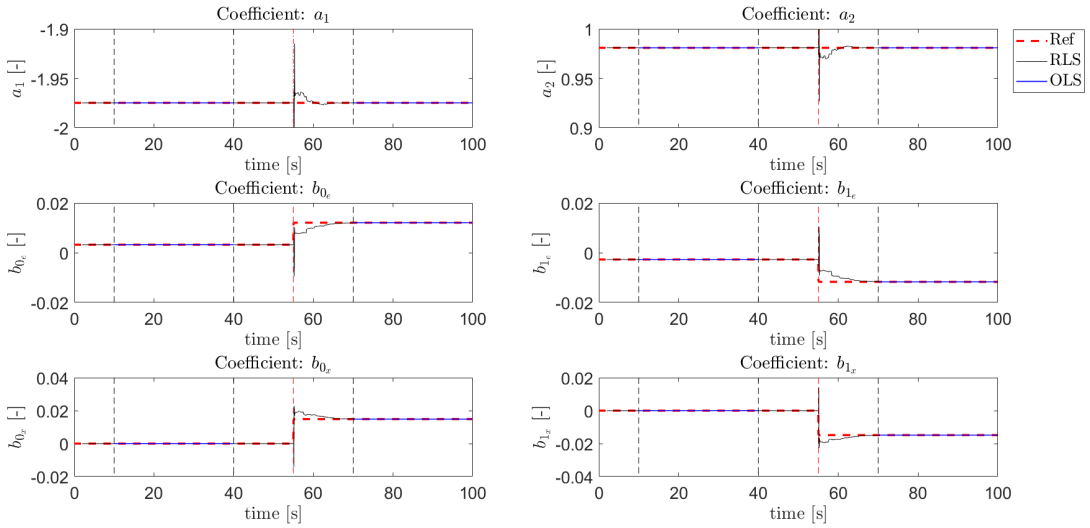

Figure 5.6: Verification identification ARX model coefficients

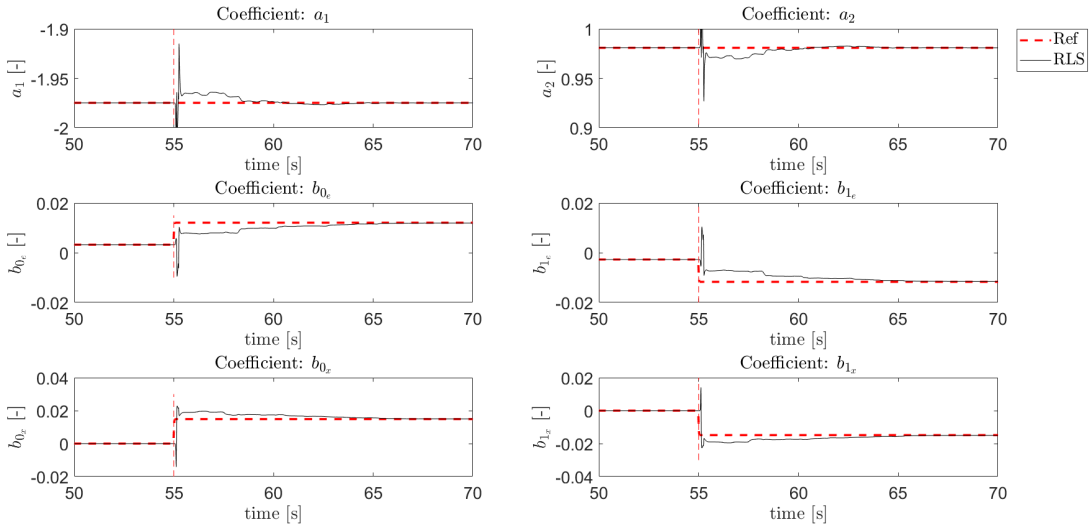

Figure 5.7: Close-up of transition region identification ARX model coefficients

This figure shows that all six of the estimated ARX model coefficients overlap with the directly converted ARX model coefficients of the remnant-free simulation. This means that the estimation process is coded correctly and the RLS identification algorithm can be deemed verified.

The OLS identification algorithm is considered verified if the bias that stems from the difference between the estimated values and directly converted values for the ARX model coefficients is negligibly small. Because a remnant-free simulation is a deterministic process, only the same condition as with the RLS identification algorithm has to be reviewed, as it includes both controlled element dynamics. The bias will be calculated with Equation (5.36). The bias values are stored in Table 5.2.

$$B_r = \frac{\hat{\theta} - \theta}{\theta} \tag{5.36}$$

Table 5.2: Magnitude bias estimated ARX model coefficients for conditions C3 and C7 in a single remnant-free simulation realization

	C3		C7	
	1^{st} window	2^{nd} window	1^{st} window	2^{nd} window
a_1	$1.03 \cdot 10^{-12}$	$-1.35 \cdot 10^{-13}$	$1.03 \cdot 10^{-12}$	$-2.18 \cdot 10^{-13}$
a_2	$2.06 \cdot 10^{-12}$	$-2.28 \cdot 10^{-13}$	$2.06 \cdot 10^{-12}$	$-4.19 \cdot 10^{-13}$
b_{0_e}	$4.55 \cdot 10^{-11}$	$-9.61 \cdot 10^{-12}$	$4.55 \cdot 10^{-11}$	$-1.49 \cdot 10^{-11}$
b_{1_e}	$5.44 \cdot 10^{-11}$	$-1.02 \cdot 10^{-11}$	$5.44 \cdot 10^{-11}$	$-2.03 \cdot 10^{-11}$
b_{0_x}	-	-	-	$3.35 \cdot 10^{-11}$
b_{1_x}	-	-	-	$3.34 \cdot 10^{-11}$

As can be seen in this table, the bias values are ranging in the order of 10^{-11} to 10^{-13} which can be considered negligibly small. Therefore, the OLS identification algorithm is considered to be coded correctly.

Finally, the conversion from ARX model coefficients to human operator parameters needs to be verified. This verification step is done in a similar fashion as the RLS algorithm verification. The recursively estimated pilot model parameters are compared to the parameter values that were used in the propagated state-space representation. For the remnant-free simulation, the parameter values should overlap. The time traces of the human operator parameters are visualized in Figure 5.8, with a close-up of the transition region in Figure 5.9.

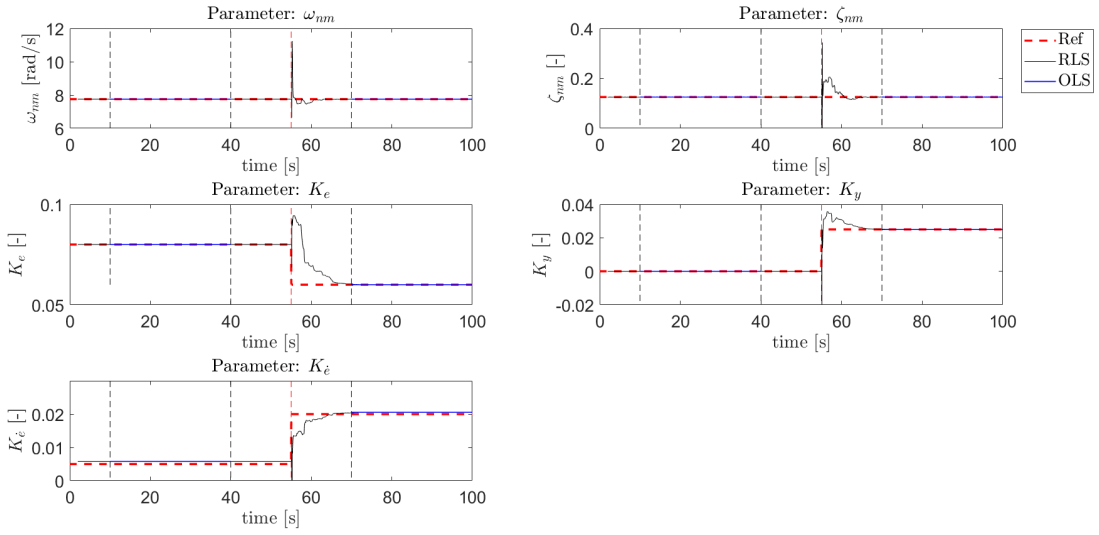

Figure 5.8: Verification ARX model coefficient conversion

Figure 5.8 shows a good overlap between the estimated human operator parameter values and the parameters used to simulate the data. Therefore, one can conclude that the implementation of the conversion of the ARX model coefficients to human operator parameters is done correctly. With this last step completed, one can confirm that all parts of the simulation have been verified.

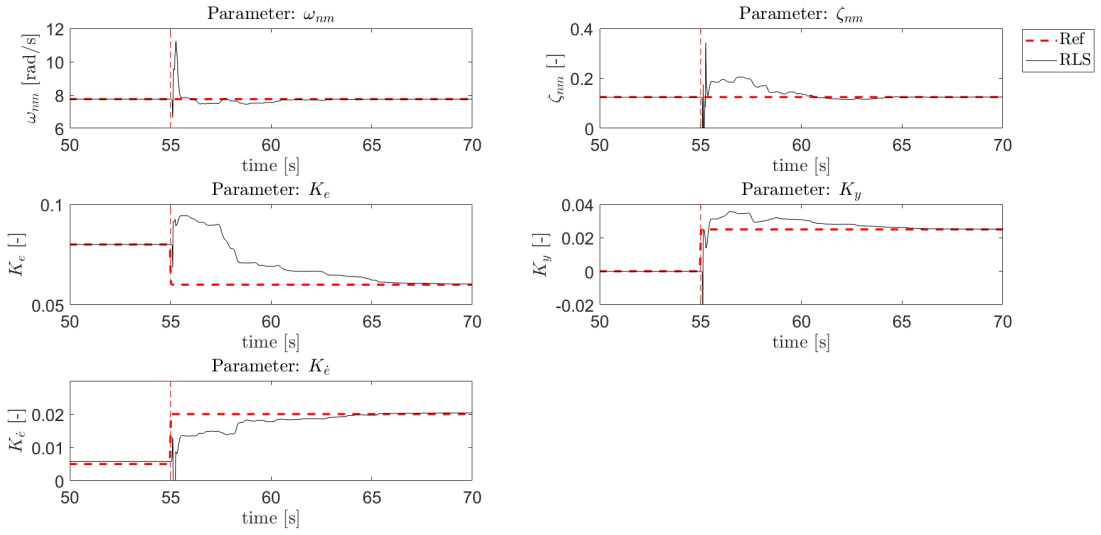

Figure 5.9: Close-up of transition region ARX model coefficient conversion

5.5. Concluding Remarks on the Identification

This chapter elaborately discussed the method that will be used for identifying the simulation data and human-in-the-loop data to develop the human operator models. The selected ARX model structure works both for an OLS algorithm as well as an RLS algorithm. The OLS ARX method results in a single parameter value that can be used to properly develop the human operator models for all LTI conditions or LTI parts of the time-varying conditions. The recursive fitting ARX method computes the human operator model parameter values at every time step and can therefore track changes in the human operator behaviour.

The ARX method works on the basis of a discrete time shift operator q that acts on the block diagram signals and three polynomials that define the ARX model order. A model order of two is selected to allow for easy conversion from ARX polynomial coefficients to human operator parameters. A disadvantage of the ARX identification method is that due to the coupling of the remnant model and the human operator model by means of one of the polynomials a bias is introduced.

The influence of this bias on unimodal systems has been investigated by van Grootheest et al., but the effect of the bias on multimodal systems needs to be researched [5]. Furthermore, the initial conditions that are applied to the RLS algorithm will be different for each run of the human-in-the-loop experiment, so the convergence for different sets of initial conditions will be checked as well. Lastly, the use of a constant forgetting factor or coefficient-specific forgetting matrix results in different parameter estimations and therefore different VAFs. The effect of both memory horizon variables will be investigated too. The results for these preliminary research objectives can be found in Chapter 6. Because the identification procedure has been verified, the results in the next chapter will be considered correct.

6

Preliminary Results

Section 5.5 concluded the explanation of the identification procedure with three important investigations that might affect the human-in-the-loop experiment setup. The results considering these investigations are presented in this chapter. First of all the influence of different remnant power ratios on the estimation results will be researched in Section 6.1. Afterwards the convergence of different initial conditions will be examined in Section 6.2. Lastly, the differences between using a forgetting factor or forgetting matrix will be analyzed in Section 6.3. This chapter will be concluded with some concluding remarks on the results that are found in Section 6.4.

6.1. Influence of the Remnant

In the previous chapter the influence of the remnant on the ARX model coefficient estimation was explained. To investigate the bias for multimodal human operator models, the estimation procedure is conducted for all remnant power ratios for both the OLS algorithm and the RLS algorithm. Although that this assumption might not hold for future research, the time delays are assumed to be estimated correctly for this analysis even with remnant present. In later stages of this research the sensitivity of the time delay estimation will be investigated.

The results for the OLS algorithm have been documented by calculating the bias for all ARX model coefficients and human operator model parameters. This estimation process is completed for all conditions. The results are put together in Tables B.1 and B.2 for the ARX model coefficient bias and human operator parameter bias, respectively. Reference values have been provided as well. Because of its extensiveness, the results have been put in Appendix B. The discussion on the results shown in the appendices will be presented hereafter.

As can bee seen in Table B.1, one can see that for both unimodal and multimodal manual control the bias increases for higher remnant power, independent of the selected condition. This result is expected because as explained in Section 5.3 the introduction of remnant creates a bias in the result. For higher remnant power, a larger component of the control signal consists out of the stochastic remnant, hence creating a higher bias. In this Table it can also be noted that when no remnant is present, not only for the verification case from Section 5.4, but all conditions the bias is negligibly small.

When comparing the found biases for unimodal and multimodal manual control, the result of implementing an additional feedback loop is that the bias for the original feedback loop increases. The bias for the vestibular feedback path is smaller than for the visual feedback path, however, in the same order of magnitude.

Another fact that stands out is that the bias for the coefficients of the $B(q)$ polynomials is over an order of magnitude higher than the bias for the coefficients of the $A(q)$ polynomial. The reason for this can be ascribed to the fact that the values for the coefficients of the $B(q)$ polynomials are over an order of magnitude smaller than the coefficients of the $A(q)$ polynomial and therefore the percentage difference increases more with the same offset in values. These findings are in correspondence with van Grootheest et al. [5]. These results are found when the forgetting factor is kept constant. Section 5.1.1 already hinted that by applying different forget-

ting factors to different coefficients, changes in the balance between the suppression of noise and the ability to track changes in coefficient values could be achieved. Section 6.3 will check this change in bias.

When inspecting the bias for the human operator model parameters not so many clear relationships were found as with the ARX model coefficients. This is true because almost all human operator model parameters are dependent on more than one ARX model coefficient as was shown in Equation (5.31) to (5.35). The neuromuscular frequency ω_{nm}, which only depends on one ARX model coefficient, shows an increasing bias with increasing power remnant ratio, however. The bias for the neuromuscular damping ratio is higher than the equalization parameters.

The results for the RLS algorithm have been visualized by showing the variation in the parameter values for different remnant power ratios. This algorithm too has been used to evaluate the bias for both the ARX model coefficients and the human operator parameters as shown for condition C7 in Figures 6.1 and 6.2, respectively. Also the reference values have been provided. The initial conditions and forgetting factor have been kept constant throughout the estimation process. The complete set of plots can be found in Figures B.1 to B.16.

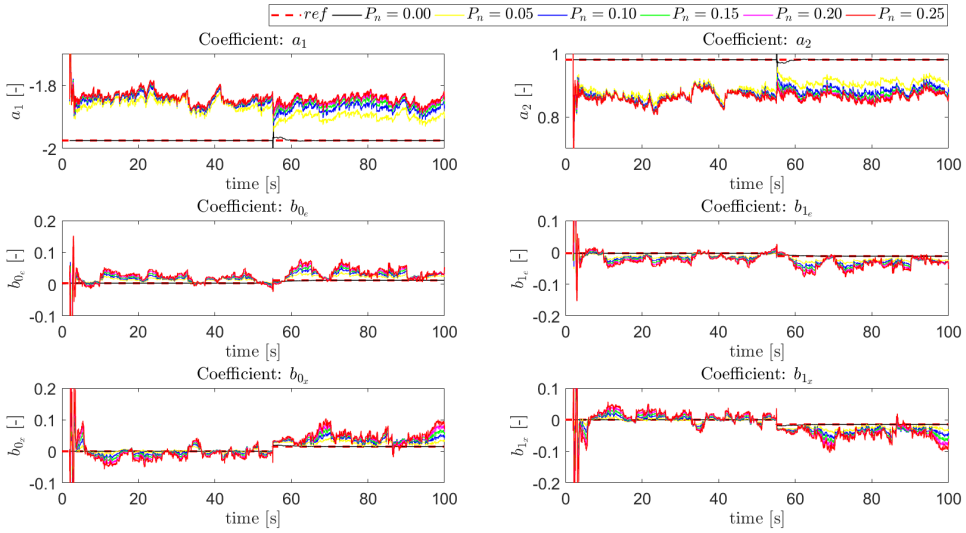

Figure 6.1: Time traces ARX model coefficient estimation with RLS algorithm for condition C7 and different remnant power ratios

For all conditions the simulations without any remnant show perfect overlap with the reference values, showing that also for the RLS algorithm the identification procedure is performed as expected. Similar to the OLS algorithm, a higher bias is found for higher ratios of remnant power. The bias values that were found using the OLS algorithm correspond to the values that can be found in the time traces using the RLS algorithm.

6.2. Influence of the Initial Conditions

Another preliminary research objective that was mentioned in Chapter 5 is the influence of the selected initial conditions on the convergence of the recursive estimation analysis. It was pointed out that an initial condition for the coefficient vector is required for the estimation procedure. It was chosen to have the initial condition similar to the estimated OLS ARX coefficient as proposed by van Grootheest et al. [5]. However, if this value would be biased the RLS algorithm should be able to converge to a different value quickly without ending up in a local minimum.

To test this convergence, 10 different initial conditions have been applied to the same estimation procedure. Each of the estimated OLS coefficients has been multiplied with randomly generated numbers with the MATLAB `randn()`-command and then fed to the RLS algorithm as initial coefficient vector. For this investigation, a constant forgetting factor was used in the RLS algorithm. The convergence of the 10 realizations for a remnant free simulation are shown in Figure 6.3, with a close-up of the first few seconds in Figure 6.4.

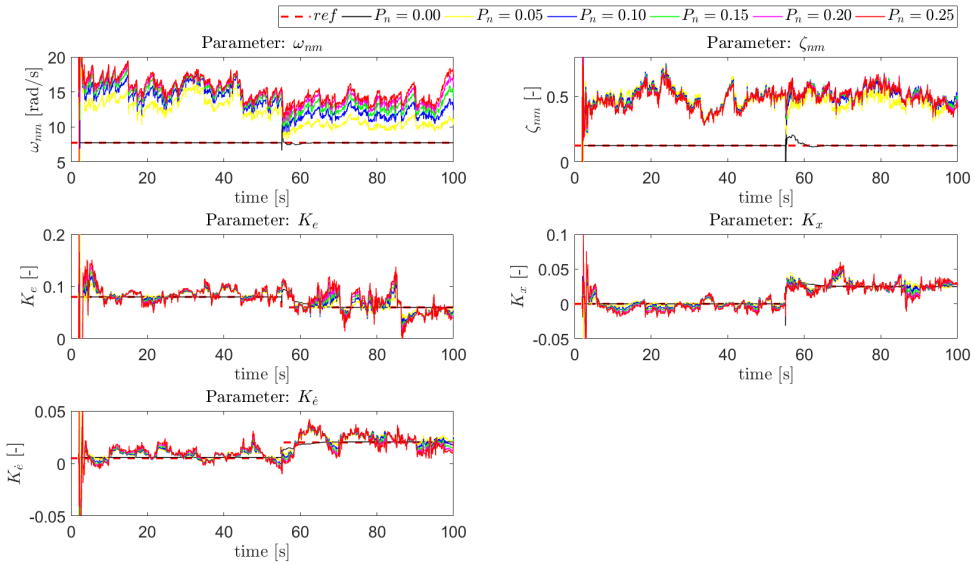

Figure 6.2: Time traces human operator model parameter estimation with RLS algorithm for condition C7 and different remnant power ratios

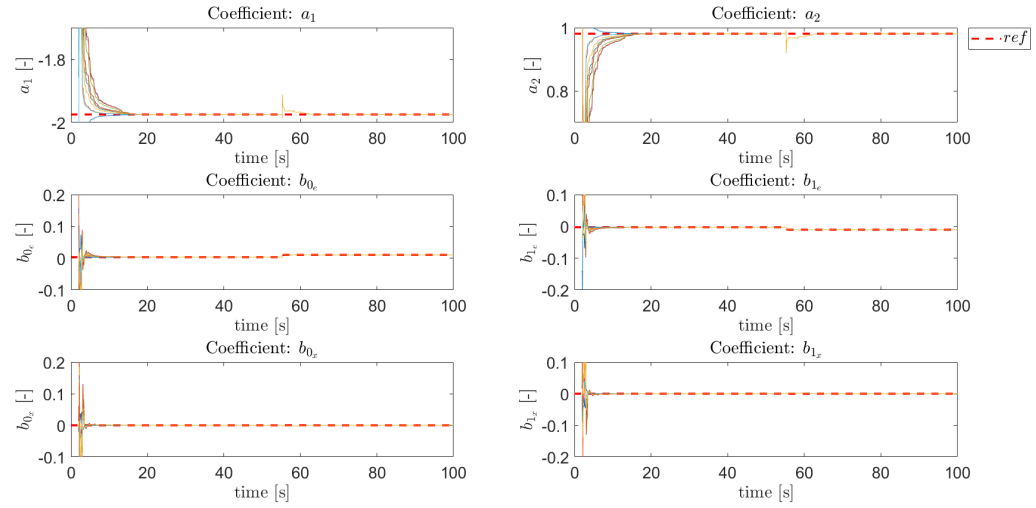

Figure 6.3: Convergence of RLS algorithm for different initial conditions for a remnant-free simulation of condition C3

The figure shows that irrespective of the selected initial conditions all of the parameter estimations return to the same, correctly estimated value for the remnant-free simulation. The coefficients of the $A(q)$ polynomial and $B(q)$ polynomials have converged to the reference values after 20 seconds and 6 seconds respectively. This implies that for a remnant-free simulation the chosen initial conditions have no effect on the estimation procedure.

The same check is applied to a more realistic simulation in which a remnant signal is inserted. The results have been visualized in Figures 6.5 and 6.6. Compared to a remnant-free simulation, the figures show that for simulations with remnant all coefficient estimates have converged to the same value after 6 seconds. The bias that is found for the estimation of the coefficients is similar to the bias as presented in Figure B.5, so it can be concluded that also for simulations with remnant the initial conditions do not strongly affect the estimation results.

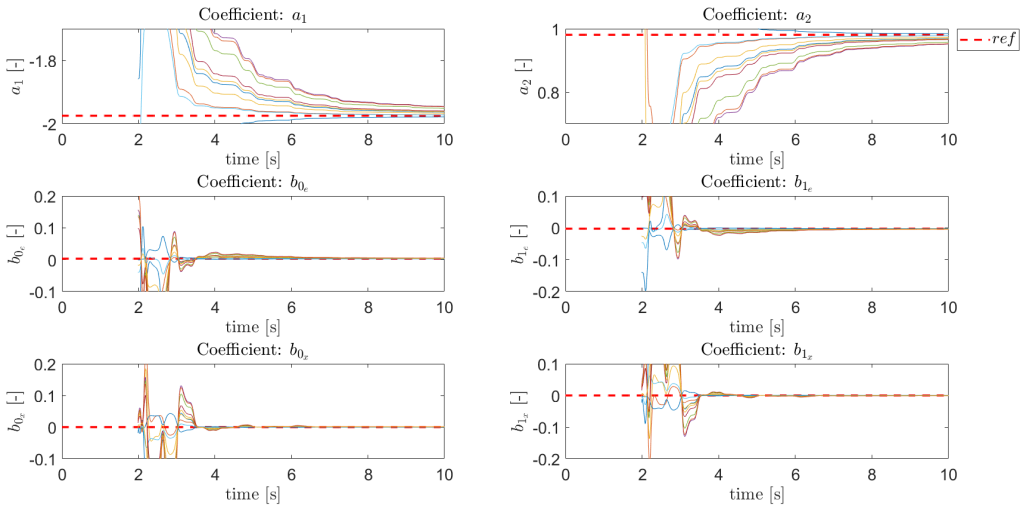

Figure 6.4: Close-up of initial convergence of RLS algorithm for different initial conditions for a remnant-free simulation of condition C3

It was explained in Chapter 5 that the convergence rate is amongst others dependent on the forgetting factor of the RLS algorithm [33]. The next section will elaborate on the different convergence rates that are found for a forgetting factor and forgetting matrix.

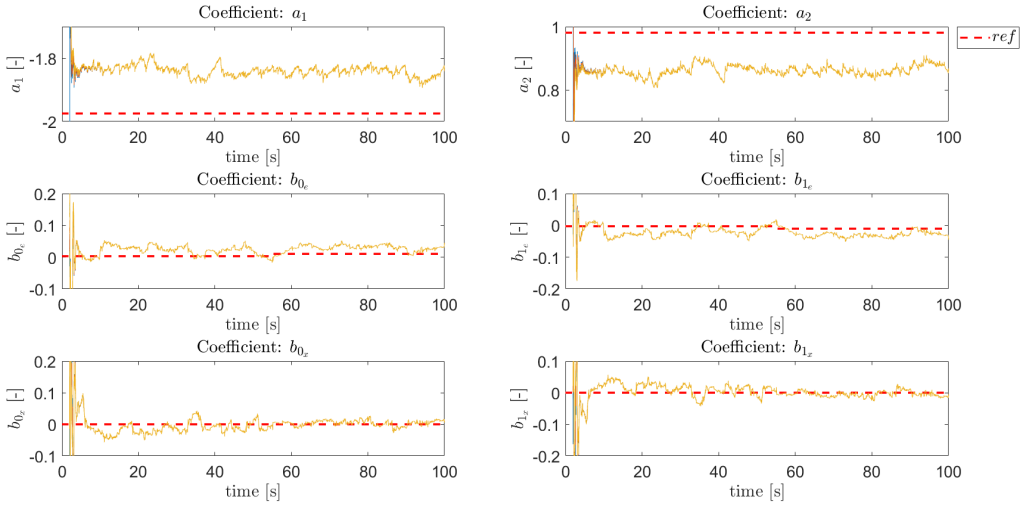

Figure 6.5: Convergence of RLS algorithm for different initial conditions for a simulation of condition C3 with $P_n = 0.25$

6.3. Influence of the Forgetting Factor and Forgetting Matrix

The last parameter influencing the results that is up for investigation is the forgetting factor λ. Section 5.1.1 explained that the forgetting factor determines the rate at which old data is discounted for the estimation of the ARX model coefficients. The forgetting factor can also be replaced by a forgetting matrix Λ in which specific forgetting factors can be applied to individual ARX model coefficients.

Van Grootheest et al. used a forgetting matrix with an infinite memory horizon for the coefficients of the $A(q)$ polynomial [5]. They found that there was no significant increase in the VAF when using a forgetting matrix. However, lower standard deviations were found, especially for the $A(q)$ polynomial coefficients.

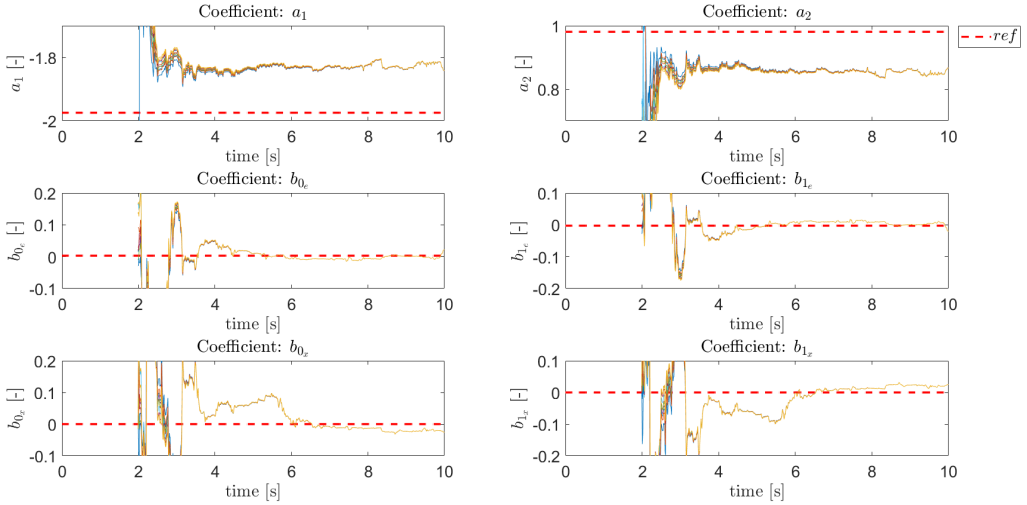

Figure 6.6: Close-up of initial convergence of RLS algorithm for different initial conditions for a simulation of condition C3 with $P_n = 0.25$

In this section, the estimation procedure for a remnant-free simulation as well as a simulation with remnant will be completed for RLS algorithms with both a forgetting factor and a forgetting matrix. It was chosen to keep the values for the forgetting factor and forgetting matrix similar to van Grootheest et al. [5], denoted respectively by λ and Λ_1. Next to that, four additional forgetting matrices were developed with varying forgetting factors for the $B(q)$ polynomials. The forgetting factor for the $A(q)$ polynomial was kept constant since it is inspected that the parameters connected to these coefficients change less drastically compared to the parameters that are connected to the $B(q)$ polynomials [5]. It was opted to create two matrices in which different forgetting factors were applied to the coefficients of the $B_x(q)$ polynomial. The forgetting factors for the $B_x(q)$ polynomial for Λ_2 and Λ_3 have memory horizons that are twice and half as long compared to the memory horizons for the $B_e(q)$ polynomial, respectively. The two other matrices have equal forgetting factors for the coefficients of both the $B(q)$ polynomials, however different to Λ_1. In these cases, the memory horizon for Λ_4 and Λ_5 is twice and half as long as compared to the memory horizon as used by van Grootheest et al., respectively [5]. For clarity, the relationship between the forgetting factors and memory horizons is repeated in Table 6.1, and the complete set of forgetting matrices is given by Equation (6.1).

Table 6.1: Relationship between selected forgetting factors and memory horizon

λ	T_0
0.99219	126
0.99609	256
0.99805	512
1	∞

$$
\begin{aligned}
\Lambda_1 &= diag\big(1,1,0.99609,0.99609,0.99609,0.99609\big)^{-1/2} \\
\Lambda_2 &= diag\big(1,1,0.99609,0.99609,0.99805,0.99805\big)^{-1/2} \\
\Lambda_3 &= diag\big(1,1,0.99609,0.99609,0.99219,0.99219\big)^{-1/2} \\
\Lambda_4 &= diag\big(1,1,0.99805,0.99805,0.99805,0.99805\big)^{-1/2} \\
\Lambda_5 &= diag\big(1,1,0.99219,0.99219,0.99219,0.99219\big)^{-1/2}
\end{aligned} \tag{6.1}
$$

The time traces for the parameter estimation for all three methods in a remnant-free simulation can be found in Figure 6.7. The plots correspond to simulation condition C7 and the initial conditions are set similar to the retrieved coefficient values with the OLS algorithm.

The same results for the estimation of the coefficients are found for all forgetting factor methods for the steady-state parts of the simulation. Λ_4 shows a slightly slower convergence after the transition in dynamics for the $B_e(q)$ polynomial coefficients and Λ_5 shows a slightly slower convergence after the transition in dynamics for the $B_x(q)$ polynomial coefficients. It can be seen that there is no convergence at the start of the simulation. The reason for this can be ascribed to the fact that the initial conditions are already similar to

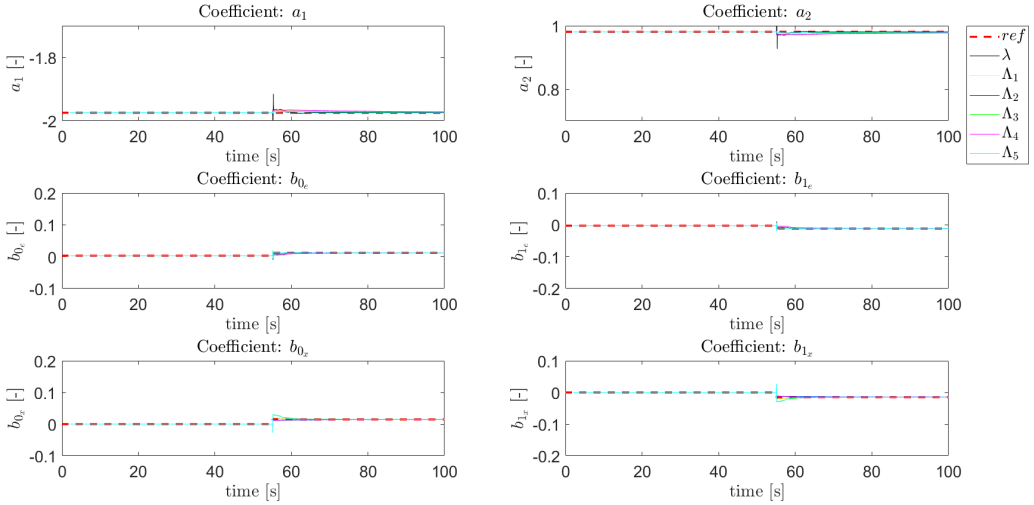

Figure 6.7: RLS ARX model coefficient estimation with all forgetting methods for remnant-free simulation of condition C7

the perfectly estimated values with the OLS algorithm since there is no remnant. Therefore, it is interesting to examine the effect of having different initial conditions on the convergence with different forgetting methods. Section 6.2 discussed that the forgetting factor has an influence on the convergence rate of the RLS algorithm. To check this statement, the three forgetting methods will be used to estimate the ARX model coefficients in a remnant-free simulation of which the initial conditions are 10 times as large as the coefficients estimated with the OLS algorithm. The results can be found in Figure 6.8.

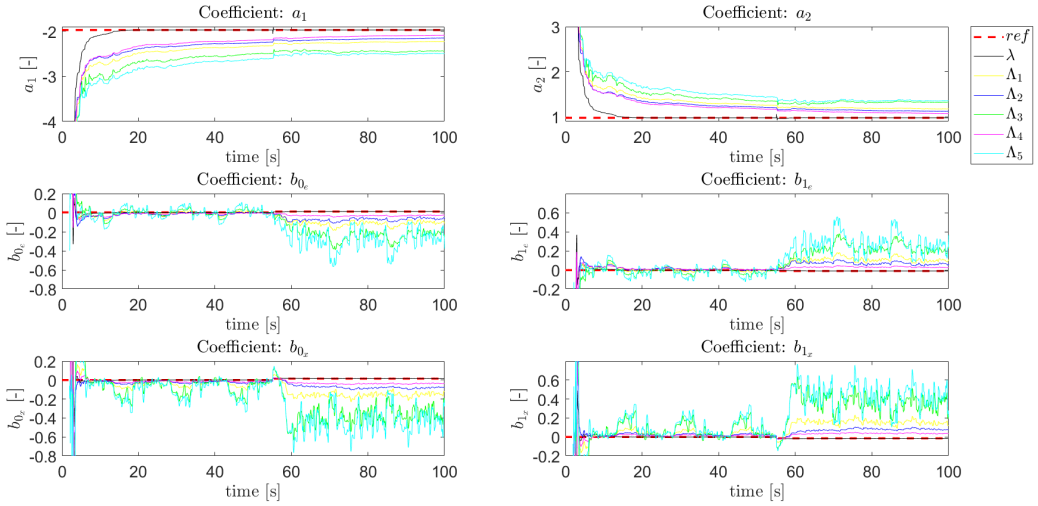

Figure 6.8: Convergence RLS algorithm of a remnant-free simulation for all forgetting methods with initial conditions 10 times the value of the OLS algorithm

From this figure it can be concluded that the selected forgetting method has a drastic impact on the estimation on the parameters. For the coefficients of the $A(q)$ polynomial it can be seen that for remnant-free simulations with initial estimates that are 10 times as high as the reference value an infinite horizon for the memory horizon leads to a convergence rate that is insufficient to attain the correct reference value. If a constant forgetting factor of $\lambda = 0.99609$ is applied, the algorithm has converged after approximately 15 seconds. For the convergence of the coefficients of the $B(q)$ polynomials something remarkable happens. The RLS al-

gorithm converges to the reference in less than 10 seconds for all forgetting methods, however, afterwards the algorithm keeps oscillating around the reference value and after the transition an inexplicable bias is introduced. The oscillation and bias are unexpected because the system is fully deterministic. The forgetting matrices for which the oscillation and bias is present the strongest, are the forgetting matrices with the smaller memory horizons. Note that the axes needed to be enlarged to display all the plots. The code has been verified to ensure that all data is correct. It was also checked with condition C6 that the bias is independent of the controlled element dynamics. A final check considered initial conditions with 5 and 15 times the estimated coefficients with the OLS algorithm. The retrieved time traces of the coefficients for initial conditions 15 times the value that was estimated with the OLS algorithm are shown in Figure 6.9. Note that the axes have been reduced to their original size again.It was found that both of these time traces do not show the earlier observed oscillations and bias, so this might hint that the recursive ARX algorithm is unable to properly distinguish between the visual feedback block and vestibular feedback block for this case as was explained in Chapter 2. Due to planning constraints it is not investigated any further in this preliminary thesis report, but it is strongly recommended to investigate this in future research.

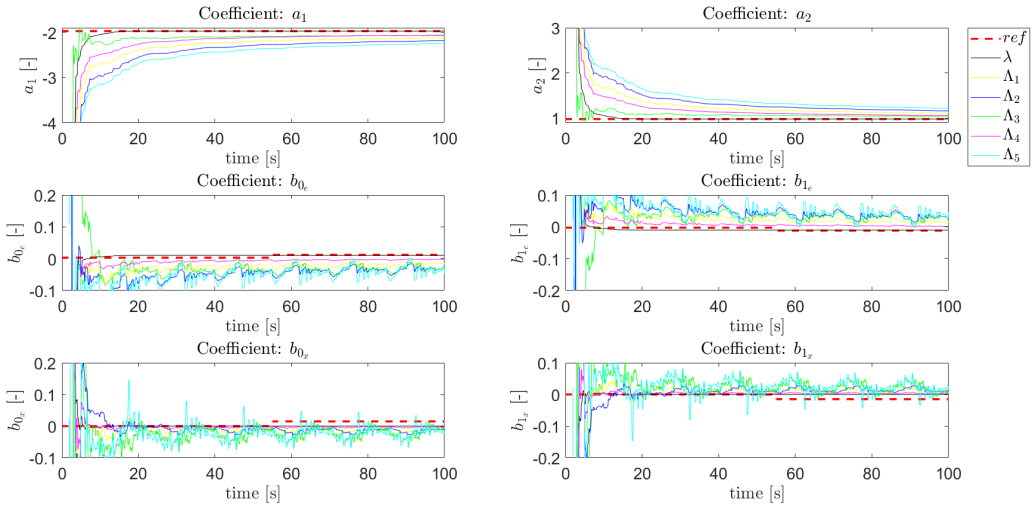

Figure 6.9: Convergence RLS algorithm of a remnant-free simulation for all forgetting methods with initial conditions 15 times the value of the OLS algorithm

Lastly it is of great interest to find the influence of the remnant on the RLS algorithm with different forgetting methods. A remnant power ratio of $P_n = 0.25$ is chosen, while keeping all the other simulation conditions the same. The results are visualized in Figure 6.10.

Figure 6.10 shows that there is very little variation in the coefficients of the $A(q)$ polynomial for all forgetting matrices. This result was expected because an infinite memory horizon was assigned to these coefficients. When comparing the time traces of the coefficients found with the constant forgetting factor with those presented in Figure 6.8 one can see that the remnant introduces the familiar bias as shown in this chapter. For the coefficient of the $B(q)$ polynomial the variation is highest for Λ_5 and smallest for Λ_4, which was also expected because the smallest and largest memory horizon were assigned to these coefficients, respectively. Compared to Figure 6.8, no bias is present after the transition in dynamics.

6.4. Concluding Remarks on Results

In this Chapter, the influence of three important aspects of the identification algorithms were investigated. The influence of the remnant was examined for both the OLS and RLS algorithms for different remnant power ratios if the forgetting factor is kept constant. It was found that with increasing ratio of remnant power the estimation bias increased for all ARX model coefficients in all conditions. The estimation bias was highest for

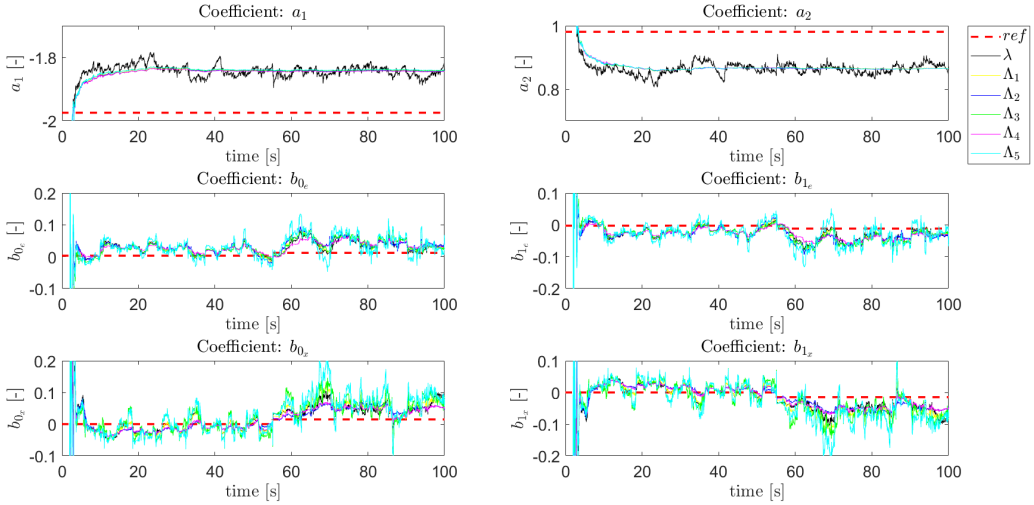

Figure 6.10: Convergence RLS algorithm of a simulation with remnant for all forgetting methods with initial conditions 10 times the value of the OLS algorithm

the coefficients of the $B_e(q)$ polynomial, followed by the coefficients of the $B_x(q)$ polynomial. The bias for the coefficients of the $A(q)$ polynomial was lowest, mainly due to the fact that the values for the coefficients were over an order of magnitude higher. No clear relationship was found between remnant power ratios and human operator model parameter bias because almost all model parameters are calculated with more than one ARX model coefficient.

Furthermore, the influence of the selected initial conditions were researched. It was found that the initial conditions of the RLS algorithm had no influence on the ARX model coefficient value after the convergence for remnant-free simulations as well as simulations with remnant present. The coefficient values for the $B(q)$ polynomials converged after 6 seconds for both remnant-free simulations as well as simulations with remnant present. Coefficient values for the $A(q)$ polynomial converged faster if remnant was implemented in the simulation. The retrieved values for simulations with remnant resulted in equally biased time traces as found in Section 6.1 after convergence.

Lastly the difference between using a constant forgetting factor or forgetting matrix was considered. Results showed that if the same initial conditions were applied that were estimated with the OLS algorithm in a remnant-free simulation, almost equal results were found for all forgetting methods. If a different initial condition was applied and the RLS algorithm had to converge to a steady-state value, results showed that for some of the cases the algorithm remained oscillatory for a deterministic system which was unexpected. Since no clear relationship was found between the offset of the initial condition and the reference value and the presence of the aforementioned bias, it is assumed that for those cases the recursive ARX algorithm is unable to properly distinguish between the visual feedback block and vestibular feedback block. It is highly recommended for future research to examine this further. The best identification results for simulations without and with remnant were found to be Λ_1 and Λ_4, respectively. If remnant is introduced in the simulation, it is indeed proven that small memory horizons lead to large variation in the estimation process and large memory horizons lead to small variations in the estimation process.

7

Future Research

In Chapter 3 the research objectives for this thesis project were made clear. The goal is to develop multimodal human operator models for time-varying dynamics in order to draw valid conclusions on the effect of motion feedback. These models are generated from data gathered in a human-in-the-loop experiment. To be able to investigate the influence of several parameters of the ARX identification algorithm prior to this human-in-the-loop experiment, a simulation of this experiment was set up as a preliminary research. This chapter discusses several key takeways from the results from this simulation that are found in the previous chapter in Section 7.1, as these have an impact on the human-in-the-loop identification that will be conducted in the future. The experimental setup will be discussed in Section 7.2.

7.1. Review Preliminary Thesis Research

During this investigation it was found that the remnant introduced a bias in the estimation of the coefficients for all conditions. As explained in Chapter 2, human operator behaviour always consists out of a nonlinear remnant. Therefore, when analyzing the experiment data, a bias is expected as well. The estimation procedure was repeated for different remnant power ratios to examine the magnitude of this bias. Results showed that the difference in coefficient estimation between no remnant and a remnant power ratio of $P_n = 0.05$ was much higher than the differences between the subsequently higher remnant power ratios. However, in contrast to the simulations, the real remnant power is unknown for human operator data. Moreover, human operators are not likely to be completely time-invariant in their control behaviour in contrast to what was simulated. This will prove an identification challenge for the human-in-the-loop experiment.

Furthermore, from simulations it could be concluded that the selected initial conditions for the RLS algorithm have little impact on the results if the forgetting factor is kept constant for all coefficients. In a remnant-free simulation, all estimations converged to the same value within 20 and 6 seconds for the coefficients of the A and B polynomials respectively. If remnant is added to the system, convergence for the A polynomial coefficients is also achieved in 6 seconds. Although that the final coefficient value is attained quicker it has to be noted that this is biased as explained in the previous paragraph. If it is opted to use a constant forgetting factor for the human-in-the-loop data, the selected initial condition has little influence on the estimation results. It is advised though to use the values estimated with the OLS algorithm since the convergence is completed the quickest.

The last check that was performed with the simulation is the influence of the selected forgetting method. If the initial conditions for the recursive algorithm are taken similarly to the estimation results of the OLS algorithm, the algorithm showed almost exactly the same results, independent of the forgetting method. However, if initial conditions were chosen that were multiple times larger than the reference value, the coefficients of the A polynomial did not completely converge to the reference value for infinite memory horizons, even for remnant-free simulations. In addition, for several initial conditions, a bias was introduced after the transition in dynamics. Because this bias was not present for initial conditions that were even further off as well as initial conditions that were closer to the reference value, the extent to which the initial conditions differ from the

reference value do not influence this bias. Nevertheless, it is of utmost importance for the human-in-the-loop experiment analysis to use the coefficients that were estimated with the OLS algorithm as initial conditions to ensure that the data is as close to the reference value as possible. The best forgetting method that was found for initial conditions equal to the coefficient values found with the OLS algorithm is a forgetting matrix with an infinite memory horizon for the coefficient of the A polynomial and the same memory horizon for both B polynomials, however twice as long as compared to van Grootheest et al. used in his unimodal manual control analysis [5].

7.2. Experimental Setup

Chapter 3 discussed that the validation of the multichannel time-varying ARX identification method will be done by means of a human-in-the-loop experiment. With the results from this preliminary thesis research in mind, the experiment setup can be drafted. The experiment will be conducted in the SIMONA Research Simulator (SRS) at the faculty of Aerospace Engineering of Delft University of Technology. The SRS has a 6 degree-of-freedom hexapod motion base that is capable of providing accurate pitch motion cues to participants. Participants will be seated in the right cockpit seat and are asked to provide pitch inputs to the manipulator to minimize the error between the target output and system output. They perceive the error on the primary flight display in front of them as is shown in Figure 7.1.

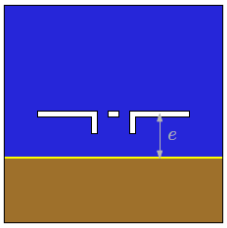

Figure 7.1: Compensatory display as will be used in the human-in-the-loop experiment

16 participants will be asked to participate in the experiment to gather enough data while still maintaining a well balanced Latin square schedule, considering the eight testing conditions as defined in Chapter 3. Each participant will complete all conditions eight times in order to ensure that the learning curve has leveled off and they are completely familiar with the task and environment. The four forcing function realizations as presented in Chapter 4 are balanced between the participants as well.

The experimental data will be analysed with the multichannel time-varying ARX model as presented in Chapter 5. The human operator models that will be developed based on the results will be compared to the results found in the simulations to validate the identification method.

The results that are found in this preliminary thesis report do not include the estimation of both the visual time delay and vestibular time delay, since the main focus of this report is the correct implementation of the ARX model structure for multimodal manual control analysis, as well as the influence of several parameters of the identification algorithms. However, the estimation of these two variables is an important part for the identification of the real human operator data. The time delays will be estimated by calculating the model fit for each possible combination of the delays for both of the measurement windows for time-varying dynamics. The delays are assumed to be constant over the time windows itself, but can change between the two time windows. The change is modeled with the same sigmoidal parameters as the controlled element dynamics. An additional, interesting research topic for the time delay analyses is the sensitivity of the estimation procedure. The sensitivity will be measured by means of a VAF calculation for all time delay combinations.

Furthermore, the recursive estimation of the human operator model parameters will be performed for different forgetting method strategies. For simulation data it was found that forgetting matrices Λ_1 and Λ_4 resulted in the best estimations. However, this does not guarantee that actual human operator data result in the best coefficient estimations with these forgetting strategies as well.

8

Conclusion

This chapter provides a conclusion to this preliminary thesis report. The topic of this thesis is an investigation into the effects of motion feedback on time-varying pilot control behaviour. The goal of this thesis is to develop time-varying multimodal human operator models from experimental data using a multichannel recursive ARX identification method. The report consists out of an overview of the literature study, the research objective, an explanation on the simulation that was used to verify the multichannel time-varying ARX identification method and results of the simulation data that consider important parameters of the identification process and need to be taken into account for the actual human-in-the-loop experiment.

During the literature phase it was found that the human operator models that were developed by McRuer and Jex form a good foundation for developing human operator models [3]. Although that their models were based on unimodal LTI tracking tasks, the models have been used and verified for multimodal time-varying tracking tasks as well [9, 21, 22]. When human operators are presented with motion feedback, both the visual and vestibular model parameters will change, so in order to quantify the effects of motion feedback human operator models with and without vestibular feedback need to be compared. For time-varying dynamics it was found that human operator parameters change during the simulation run depending on the change in the dynamics. It was chosen to model a change in the controlled element dynamics as a sigmoid so two steady-state models could be compared easily. Because the transition in dynamics is of interest, recursive identification methods are selected for analysis since they are able to capture variations in the parameters. The results are supported by an additional batch identification method to capture the pilot model parameters for the two LTI windows of a run in one value.

Prior to the human-in-the-loop experiment a simulation was developed to set up the identification procedure and examine the influence of several parameters of this identification procedure on the results. The simulation is run in discrete time and contains 8 different testing conditions that allow for gathering all the data needed to draw conclusions on the research question. The human operator and controlled element are modeled with a state-space representation for which the input parameters are taken from literature and a preliminary test experiment respectively [5]. The remnant of the human operator model is zero-mean unit variance Gaussian white noise passed through a second order filter, for which the remnant filter gain is tuned such that it can attain different pre-set remnant power ratios. Both a target following forcing function and disturbance forcing function are used in the simulation that are repetitive over a window of 30 seconds to ensure that the identified human operator models are independent of the forcing function properties. The base frequency is still found outside of the crossover region, so no difficulties in the parameter estimation are expected. The simulation has been verified in both the frequency domain and time domain.

The identification procedure will be completed with an ARX model structure. The ARX model structure relies on a discrete time shift operator that acts on the control signal, error signal and system output signal, as well as three polynomials for which relations can be set up that describe the human operator models. The coefficients of these polynomials are estimated with the algorithm and then converted to human operator model parameters. The time delays cannot be estimated with this algorithm and will be determined by means of a model fit. The ARX model structure allows for both recursive estimation and batch estimation. A disadvantage

of using the ARX model structure is that both the visual and vestibular human operator model are dependent on the same polynomial that models the stochastic remnant signal, hence creating a bias in the identification results. The identification procedure has been verified by identifying a remnant-free simulation that resulted in an unbiased coefficient estimation as expected.

To be sure that the identification of real human operator data produces valuable results, the influence of several algorithm parameters have been investigated prior to the experiment data analysis. First of all the bias that is introduced with the ARX model structure is examined. Higher remnant power ratios lead to higher biases in the ARX model coefficients. Furthermore, it was found that a forgetting matrix with infinite memory horizon for the A polynomial and equal, but higher forgetting factors compared to van Grootheest et al. for the coefficients of both B polynomials lead to the best identification results for multimodal manual control. Lastly, the selected initial conditions for the RLS algorithm have no influence on the convergence if a constant forgetting factor is used similar to van Grootheest et al. [5]. However, the convergence of the algorithm depends on the selected initial conditions if the aforementioned, preferred forgetting matrix is used. It was found that if the initial conditions are similar to the values estimated with the OLS algorithm, the best results are found. It is therefore opted to use a forgetting matrix instead of a constant forgetting factor for the RLS algorithm, with initial conditions similar to the estimated coefficient values with the OLS algorithm. For the identification of the human-in-the-loop experiment data, the visual and vestibular time delay will be estimated by means of a model fit, something that was not considered in the preliminary research.

The goal of this preliminary thesis research was to verify a multichannel time-varying ARX model for the identification of multimodal manual control. With this method now verified, it is possible to evaluate how human operators adapt their manual control behaviour if they are presented with motion feedback. As pilots are presented with motion feedback in-flight in real life, this method will prove useful for the improvement of pilot training and aircraft control design.

A

Simulation Model Parameters Retrieval

This appendix provides the identification results to a preliminary test experiment that was conducted to find reasonable values that were used as input parameters for the simulation of the human operator. The time traces for the ARX model coefficients and human operator model parameters are found in Figures A.1 and A.2 respectively. For the RLS algorithm, the initial conditions are set similar to the retrieved coefficients with the OLS algorithm and a constant forgetting factor of $\lambda = 0.99609$ is used. The human operator parameter values are stored in Table 4.2.

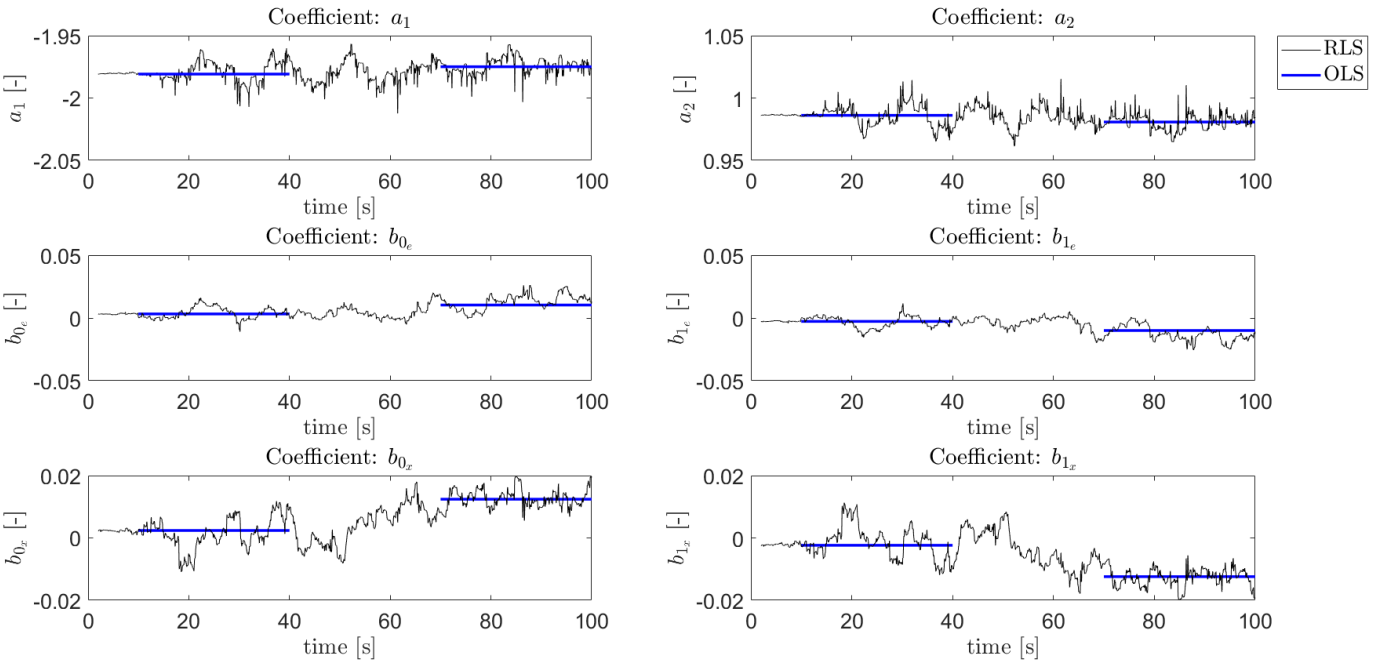

Figure A.1: Retrieved ARX model coefficients from preliminary test experiment

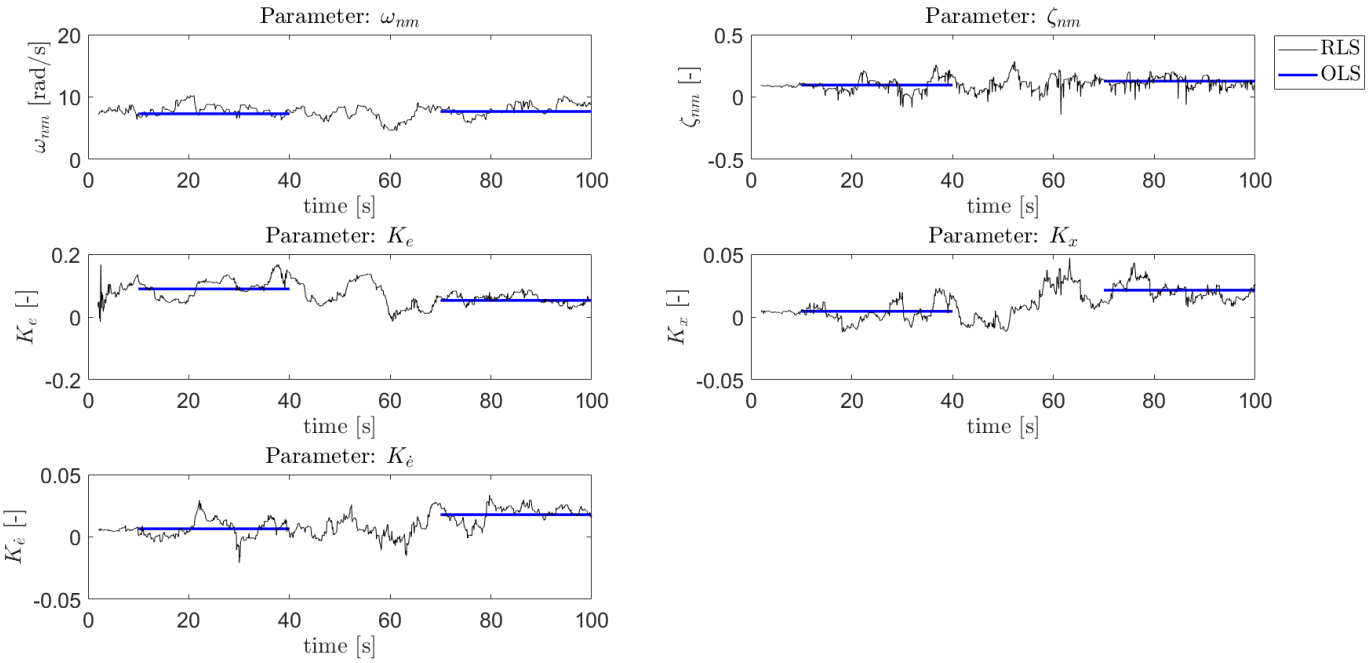

Figure A.2: Retrieved human operator parameters from preliminary test experiment

B

Results Influence Remnant on Estimation Process

This appendix provides the complete results for Chapter 6. As discussed in Section 6.1, the influence of the remnant power ratio on the estimation process of both the ARX model coefficients and the human operator parameters has been examined with both an OLS algorithm as well as RLS algorithm. The bias for the ARX model coefficients can be found in Table B.1 and the corresponding bias for the human operator model parameters can be found in Table B.2. The time traces of the ARX model coefficients and human operator model parameters estimated with the RLS algorithm are grouped for every condition. The results can be found in Figures B.1 till including B.16. The discussion on these tables and figures can be found in Chapter 6.

Table B.1: Magnitude bias ARX model coefficients for different power levels remnant

		C1						C2					
	P_n	0.00	0.05	0.10	0.15	0.20	0.25	0.00	0.05	0.10	0.15	0.20	0.25
	a_1	-1.99 E^{-14}	-0.06	-0.06	-0.07	-0.07	-0.07	1.27 E^{-13}	-0.04	-0.05	-0.06	-0.06	-0.06
	a_2	-6.64 E^{-14}	-0.11	-0.12	-0.12	-0.12	-0.12	2.70 E^{-13}	-0.08	-0.10	-0.11	-0.11	-0.12
	b_{0_e}	6.16 E^{-11}	2.61	3.16	3.56	3.93	4.30	8.22 E^{-14}	0.91	1.39	1.73	2.00	2.24
	b_{1_e}	7.44 E^{-11}	2.77	3.32	3.75	4.17	4.59	6.11 E^{-14}	0.92	1.40	1.73	2.01	2.24
	b_{0_e}	-	-	-	-	-	-	-	-	-	-	-	-
	b_{1_x}	-	-	-	-	-	-	-	-	-	-	-	-

		C3						C4					
	P_n	0.00	0.05	0.10	0.15	0.20	0.25	0.00	0.05	0.10	0.15	0.20	0.25
First Window	a_1	1.03 E^{-12}	-0.06	-0.06	-0.07	-0.07	-0.07	-2.93 E^{-13}	-0.04	-0.05	-0.06	-0.06	-0.06
	a_2	2.06 E^{-12}	-0.11	-0.11	-0.12	-0.12	-0.12	-5.25 E^{-13}	-0.07	-0.10	-0.11	-0.11	-0.11
	b_{0_e}	4.55 E^{-11}	3.36	4.39	5.20	5.97	6.72	4.12 E^{-11}	1.03	1.59	2.02	2.38	2.71
	b_{1_e}	5.44 E^{-11}	3.65	4.76	5.68	6.55	7.43	4.18 E^{-11}	1.03	1.60	2.03	2.40	2.73
	b_{0_x}	-	-	-	-	-	-	-	-	-	-	-	-
	b_{1_x}	-	-	-	-	-	-	-	-	-	-	-	-
Second Window	a_1	-1.35 E^{-13}	-0.04	-0.05	-0.06	-0.06	-0.07	-1.17 E^{-13}	-0.06	-0.07	-0.07	-0.07	-0.07
	a_2	-2.28 E^{-13}	-0.08	-0.10	-0.11	-0.12	-0.12	-1.81 E^{-13}	-0.11	-0.12	-0.12	-0.13	-0.13
	b_{0_e}	-9.61 E^{-12}	0.85	1.27	1.55	1.77	1.94	-5.68 E^{-11}	2.04	2.25	2.40	2.53	2.67
	b_{1_e}	-1.02 E^{-11}	0.85	1.27	1.55	1.77	1.94	-6.95 E^{-11}	2.06	2.23	2.37	2.51	2.67
	b_{0_x}	-	-	-	-	-	-	-	-	-	-	-	-
	b_{1_x}	-	-	-	-	-	-	-	-	-	-	-	-

		C5						C6					
	P_n	0.00	0.05	0.10	0.15	0.20	0.25	0.00	0.05	0.10	0.15	0.20	0.25
	a_1	-1.99 E^{-14}	-0.06	-0.06	-0.07	-0.07	-0.07	6.56 E^{-13}	-0.04	-0.05	-0.06	-0.06	-0.06
	a_2	-6.64 E^{-14}	-0.11	-0.12	-0.12	-0.12	-0.12	1.33 E^{-12}	-0.07	-0.09	-0.11	-0.11	-0.12
	b_{0_e}	6.16 E^{-11}	2.61	3.16	3.56	3.93	4.30	-4.37 E^{-11}	1.20	1.86	2.33	2.71	3.04
	b_{1_e}	7.44 E^{-11}	2.77	3.32	3.75	4.17	4.59	-4.59 E^{-11}	1.22	1.89	2.36	2.75	3.08
	b_{0_e}	-	-	-	-	-	-	5.04 E^{-11}	0.61	0.91	1.06	1.13	1.14
	b_{1_x}	-	-	-	-	-	-	5.05 E^{-11}	0.61	0.91	1.06	1.13	1.14

		C7						C8					
	P_n	0.00	0.05	0.10	0.15	0.20	0.25	0.00	0.05	0.10	0.15	0.20	0.25
First Window	a_1	1.03 E^{-12}	-0.06	-0.06	-0.07	-0.07	-0.07	-6.09 E^{-13}	-0.04	-0.05	-0.05	-0.06	-0.06
	a_2	2.06 E^{-12}	-0.11	-0.11	-0.12	-0.12	-0.12	1.23 E^{-12}	-0.07	-0.09	-0.10	-0.11	-0.11
	b_{0_e}	4.55 E^{-11}	3.36	4.39	5.20	5.97	6.72	-3.78 E^{-11}	1.36	2.16	2.28	3.30	3.80
	b_{1_e}	5.44 E^{-11}	3.65	4.76	5.68	6.55	7.43	-3.96 E^{-11}	1.38	2.20	2.82	3.36	3.87
	b_{0_x}	-	-	-	-	-	-	4.18 E^{-11}	0.56	0.79	0.88	0.90	0.90
	b_{1_x}	-	-	-	-	-	-	4.18 E^{-11}	0.56	0.79	0.89	0.90	0.90
Second Window	a_1	-2.18 E^{-13}	-0.04	-0.05	-0.06	-0.06	-0.06	-1.15 E^{-12}	-0.06	-0.07	-0.07	-0.07	-0.07
	a_2	-4.19 E^{-13}	-0.07	-0.10	-0.11	-0.11	-0.12	-2.24 E^{-12}	-0.11	-0.12	-0.12	-0.13	-0.13
	b_{0_e}	-1.94 E^{-11}	1.14	1.72	2.09	2.35	2.55	-6.68 E^{-11}	2.04	2.27	2.41	2.55	2.69
	b_{1_e}	-2.03 E^{-11}	1.16	1.74	2.11	2.38	2.58	-8.32 E^{-11}	2.07	2.25	2.39	2.53	2.69
	b_{0_x}	3.35 E^{-11}	0.70	1.05	1.24	1.33	1.35	-	-	-	-	-	-
	b_{1_x}	3.34 E^{-11}	0.70	1.05	1.24	1.33	1.35	-	-	-	-	-	-

Table B.2: Magnitude bias human operator parameters for different power levels remnant

		C1						C2					
	P_n	0.00	0.05	0.10	0.15	0.20	0.25	0.00	0.05	0.10	0.15	0.20	0.25
	K_e	-7.82 E^{-12}	0.05	0.05	0.04	0.03	0.02	-1.11 E^{-12}	-0.05	-0.03	-3.12 E^{-3}	0.01	0.03
	$K_{\dot{e}}$	0.16	0.59	0.52	0.54	0.59	0.66	0.01	0.17	0.16	0.15	0.14	0.15
	K_x	-	-	-	-	-	-	-	-	-	-	-	-
	ω_{nm}	-2.16 E^{-12}	0.65	0.81	0.89	0.93	0.96	-1.14 E^{-12}	0.31	0.48	0.59	0.68	0.74
	ζ_{nm}	5.60 E^{-12}	3.16	3.11	3.06	3.02	2.98	-1.51 E^{-11}	2.85	3.28	3.34	3.33	3.29

		C3						C4					
	P_n	0.00	0.05	0.10	0.15	0.20	0.25	0.00	0.05	0.10	0.15	0.20	0.25
First Window	K_e	-3.24 E^{-12}	0.04	0.03	0.02	0.01	-0.01	-5.60 E^{-12}	-0.08	-0.07	-0.06	-0.05	-0.05
	$K_{\dot{e}}$	-0.93	-0.88	-0.88	-0.87	-0.86	-0.86	-0.41	-0.29	-0.27	-0.27	-0.26	-0.24
	K_x	-	-	-	-	-	-	-	-	-	-	-	-
	ω_{nm}	-1.73 E^{-12}	0.66	0.83	0.91	0.95	0.98	5.55 E^{-12}	0.32	0.49	0.60	0.68	0.75
	ζ_{nm}	-1.05 E^{-10}	3.07	2.97	2.90	2.85	2.81	2.15 E^{-11}	2.80	3.19	3.24	3.21	3.16
Second Window	K_e	1.51 E^{-11}	-0.04	-0.02	-8.06 E^{-4}	0.01	0.02	6.90 E^{-12}	0.06	0.04	0.03	0.02	- 2.83 E^{-4}
	$K_{\dot{e}}$	-0.41	-0.35	-0.37	-0.39	-0.40	-0.41	-0.93	-0.92	-0.93	-0.93	-0.93	-0.93
	K_x	-	-	-	-	-	-	-	-	-	-	-	-
	ω_{nm}	3.65 E^{-12}	0.32	0.50	0.61	0.70	0.77	4.58 E^{-12}	0.70	0.86	0.93	0.96	0.99
	ζ_{nm}	8.11 E^{-12}	2.89	3.30	3.35	3.33	3.28	4.78 E^{-12}	3.15	3.11	3.06	3.03	3.00

		C5						C6					
	P_n	0.00	0.05	0.10	0.15	0.20	0.25	0.00	0.05	0.10	0.15	0.20	0.25
	K_e	-7.82 E^{-12}	0.05	0.05	0.04	0.03	0.02	2.48 E^{-11}	-0.07	-0.07	-0.07	-0.07	-0.07
	$K_{\dot{e}}$	0.16	0.59	0.52	0.54	0.59	0.66	0.03	0.34	0.39	0.40	0.42	0.44
	K_x	-	-	-	-	-	-	-2.98E^{-3}	-0.05	-0.10	-0.15	-0.20	-0.26
	ω_{nm}	-2.16 E^{-12}	0.65	0.81	0.89	0.93	0.96	4.46E^{-13}	0.32	0.49	0.60	0.68	0.74
	ζ_{nm}	5.60 E^{-12}	3.16	3.11	3.06	3.02	2.98	-6.91 E^{-11}	2.54	3.08	3.21	3.23	3.21

		C7						C8					
	P_n	0.00	0.05	0.10	0.15	0.20	0.25	0.00	0.05	0.10	0.15	0.20	0.25
First Window	K_e	-3.24 E^{-12}	0.04	0.03	0.02	0.01	-0.01	2.18 E^{-11}	-0.08	-0.09	-0.09	-0.09	-0.09
	$K_{\dot{e}}$	-0.93	-0.88	-0.88	-0.87	-0.86	-0.86	-0.66	-0.53	-0.49	-0.47	-0.45	-0.43
	K_x	-	-	-	-	-	-	2.98 E^{-3}	-0.08	-0.16	-0.23	-0.29	-0.36
	ω_{nm}	-1.73 E^{-12}	0.66	0.83	0.91	0.95	0.98	2.40 E^{-14}	0.32	0.49	0.60	0.68	0.74
	ζ_{nm}	-1.05 E^{-10}	3.07	2.97	2.90	2.85	2.81	-6.35 E^{-11}	2.46	2.96	3.08	3.09	3.07
Second Window	K_e	9.79 E^{-12}	-0.07	-0.08	-0.09	-0.11	-0.12	1.42 E^{-11}	0.06	0.04	0.03	0.01	-6.60 E^{-4}
	$K_{\dot{e}}$	-0.66	-0.58	-0.58	-0.59	-0.59	-0.60	-0.93	-0.92	-0.93	-0.93	-0.93	-0.93
	K_x	2.98 E^{-3}	-0.02	-0.07	-0.12	-0.17	-0.23	-	-	-	-	-	-
	ω_{nm}	1.72 E^{-12}	0.34	0.52	0.64	0.72	0.79	7.24 E^{-12}	0.70	0.86	0.93	0.96	0.99
	ζ_{nm}	1.99 E^{-11}	2.62	3.12	3.22	3.22	3.19	1.08 E^{-10}	3.14	3.10	3.06	3.02	3.00

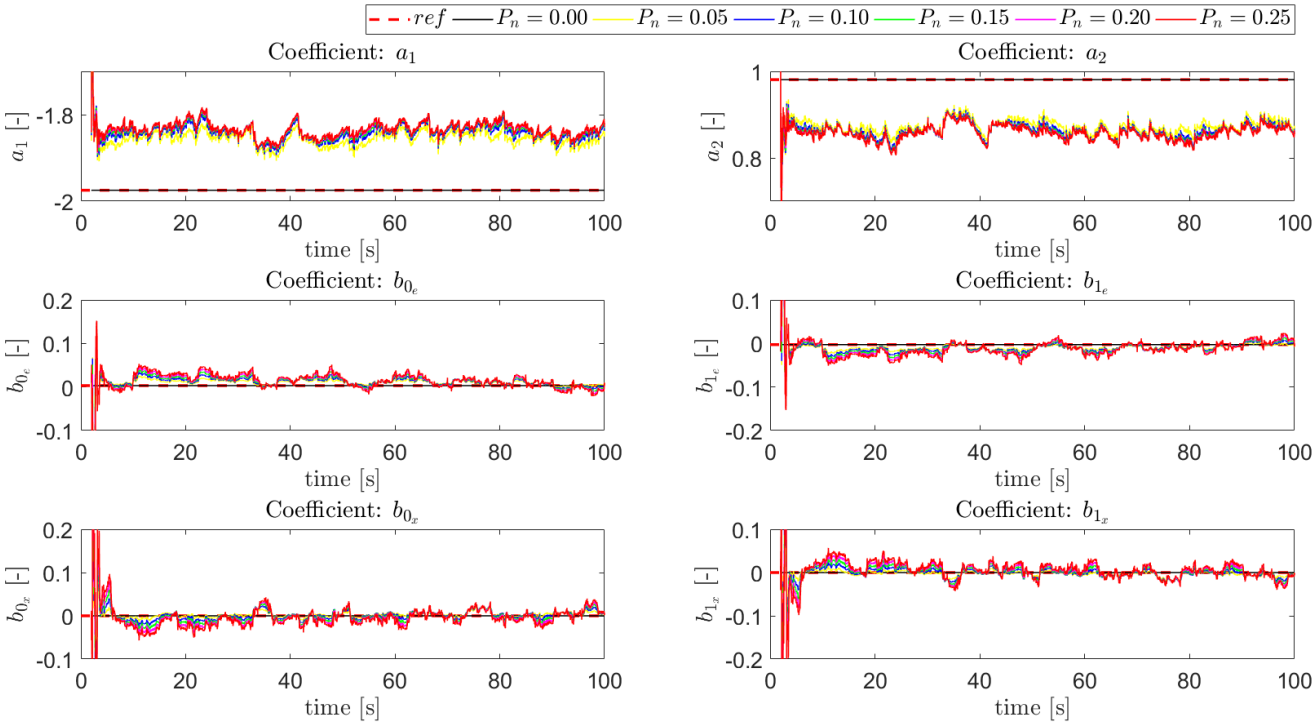

Figure B.1: Time traces ARX model coefficient estimation with RLS algorithm for condition C1 and different remnant power ratios

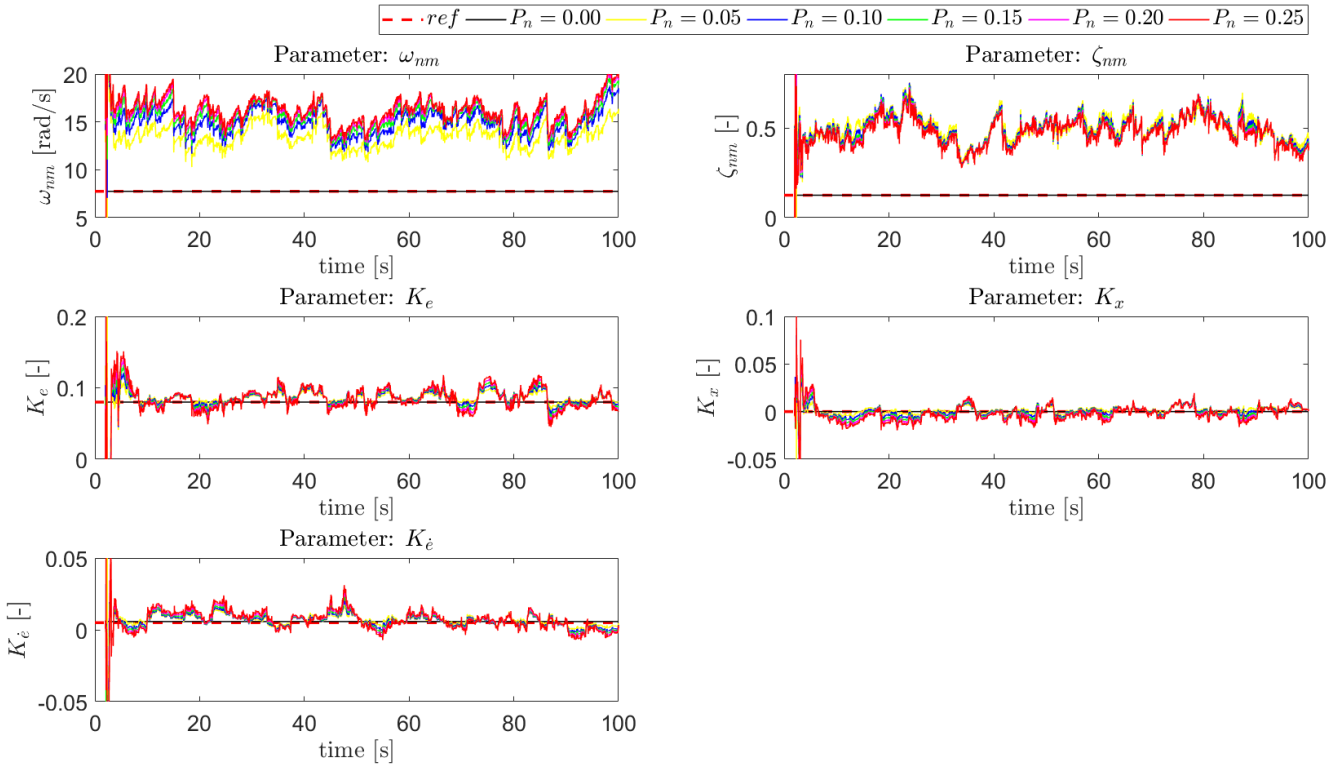

Figure B.2: Time traces human operator model parameter estimation with RLS algorithm for condition C1 and different remnant power ratios

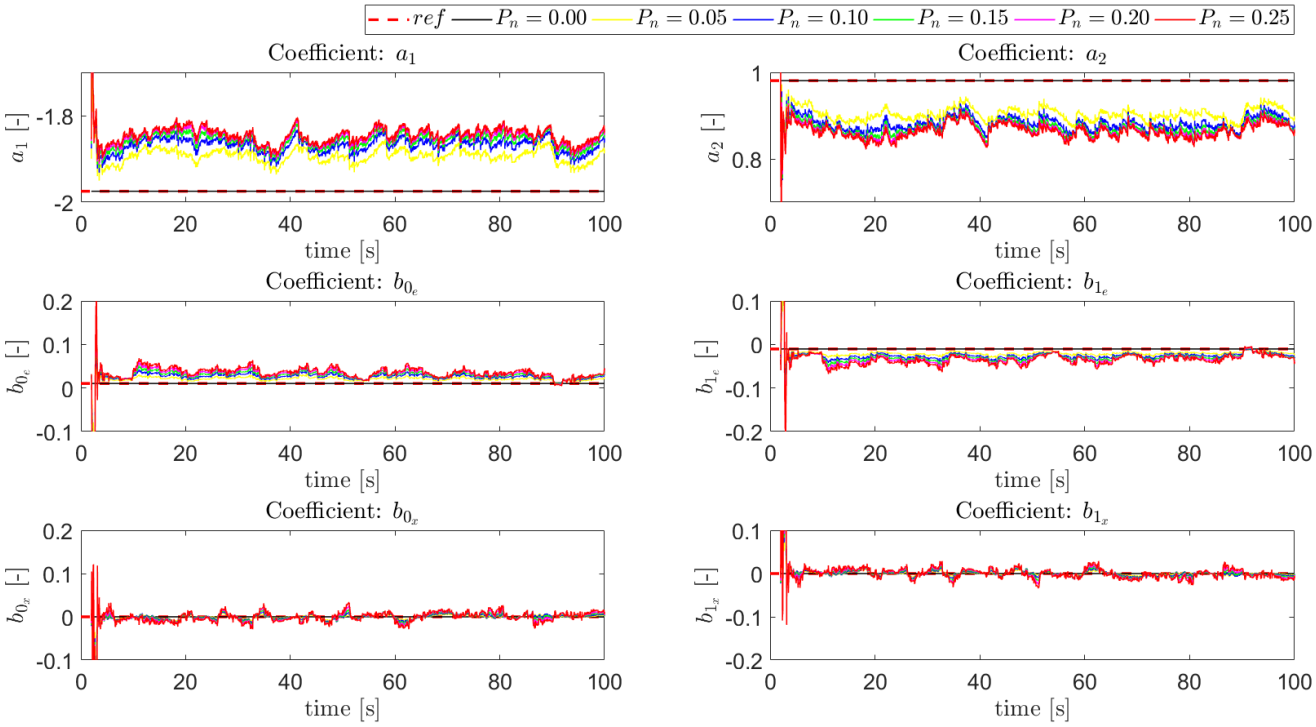

Figure B.3: Time traces ARX model coefficient estimation with RLS algorithm for condition C2 and different remnant power ratios

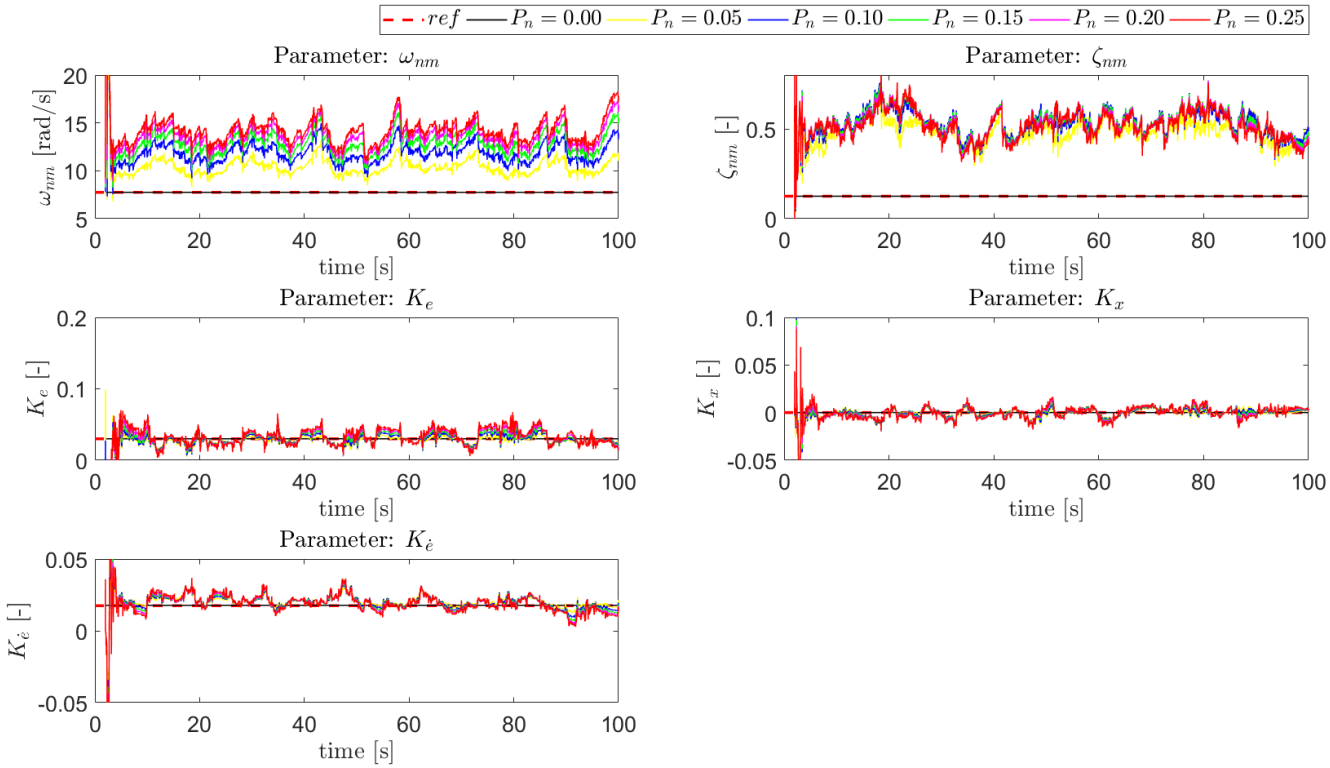

Figure B.4: Time traces human operator model parameter estimation with RLS algorithm for condition C2 and different remnant power ratios

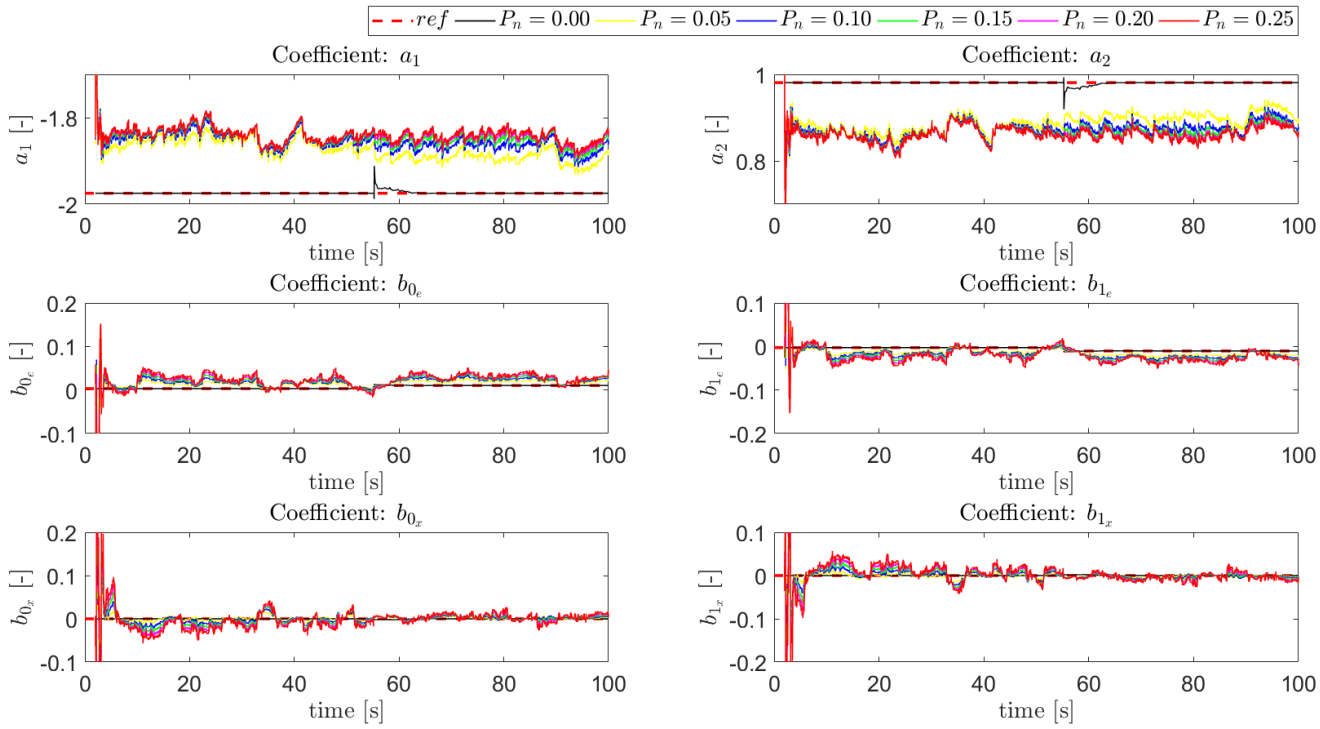

Figure B.5: Time traces ARX model coefficient estimation with RLS algorithm for condition C3 and different remnant power ratios

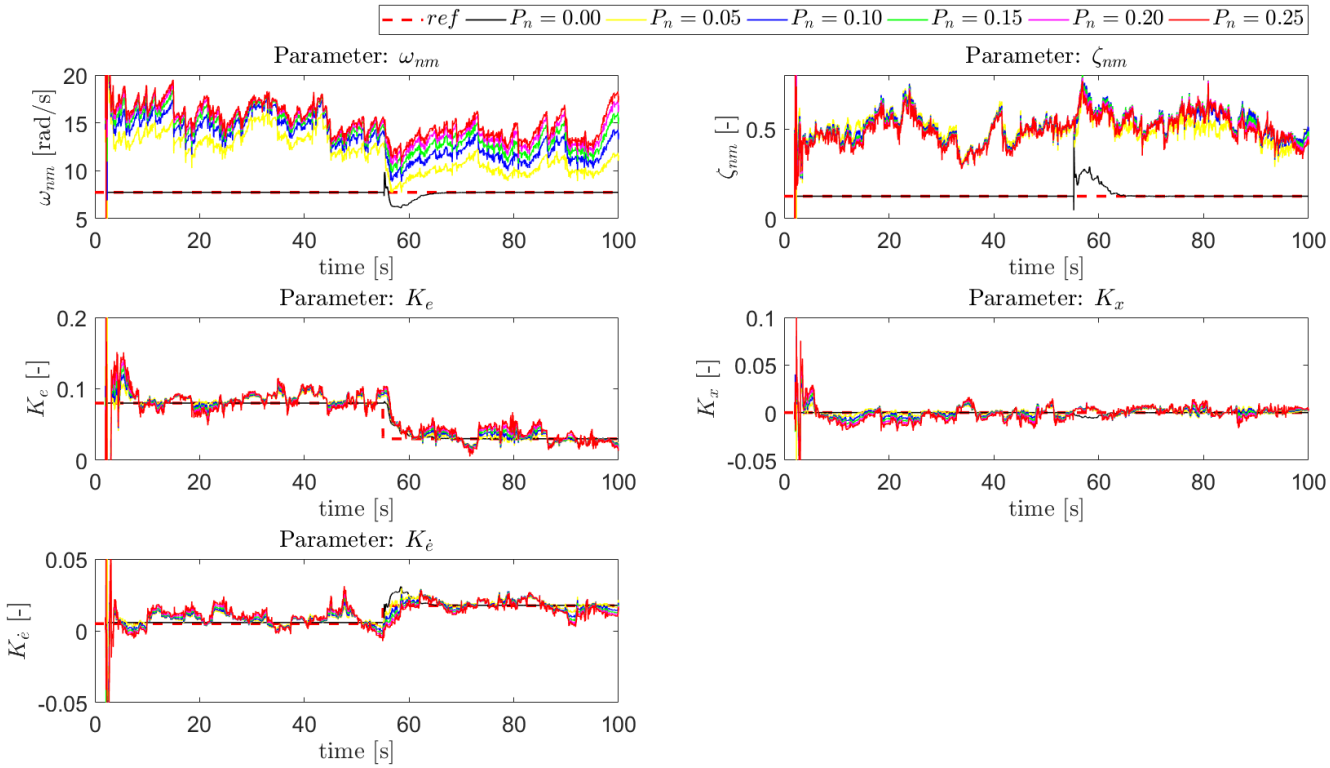

Figure B.6: Time traces human operator model parameter estimation with RLS algorithm for condition C3 and different remnant power ratios

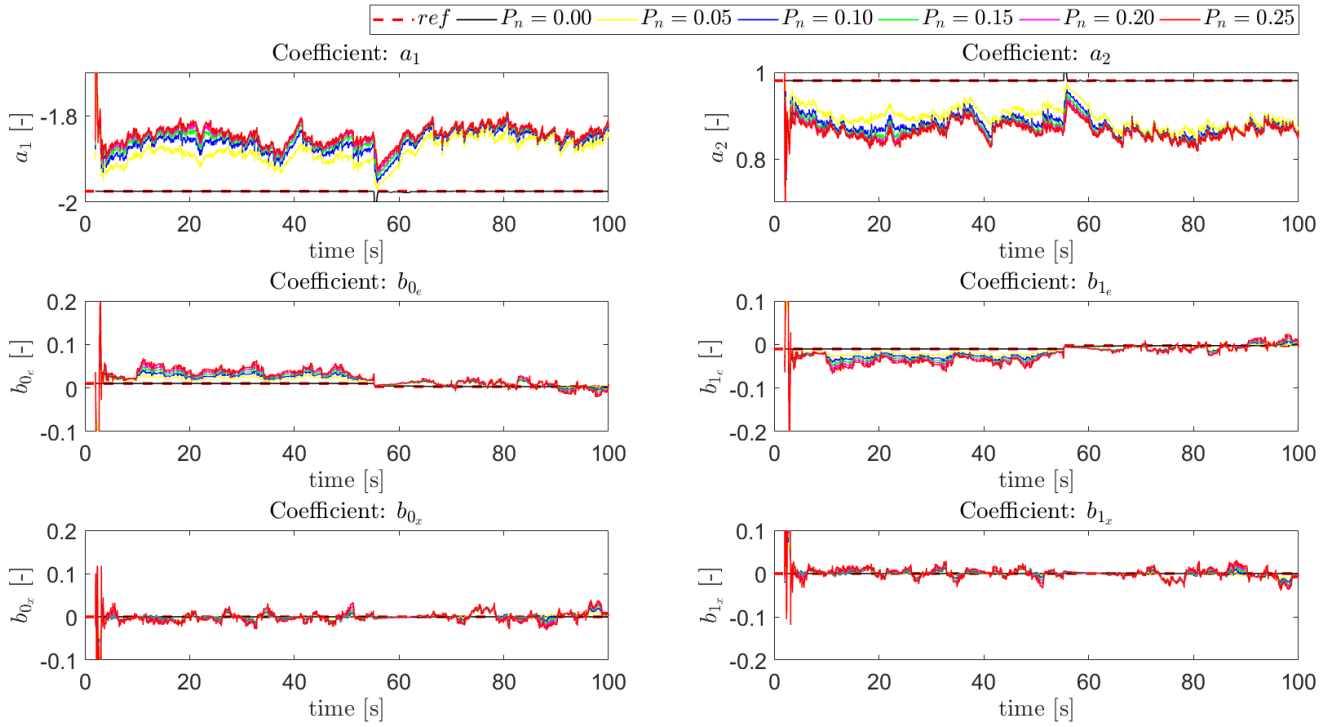

Figure B.7: Time traces ARX model coefficient estimation with RLS algorithm for condition C4 and different remnant power ratios

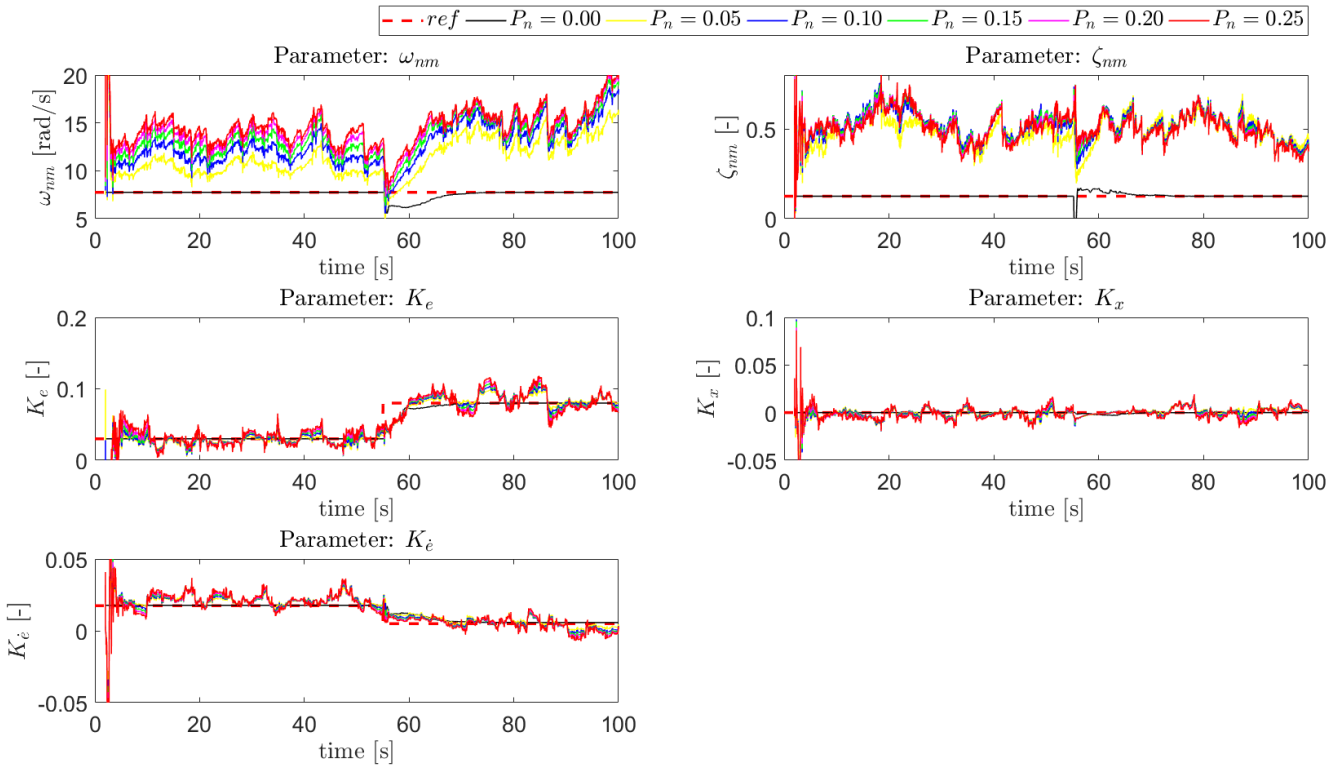

Figure B.8: Time traces human operator model parameter estimation with RLS algorithm for condition C4 and different remnant power ratios

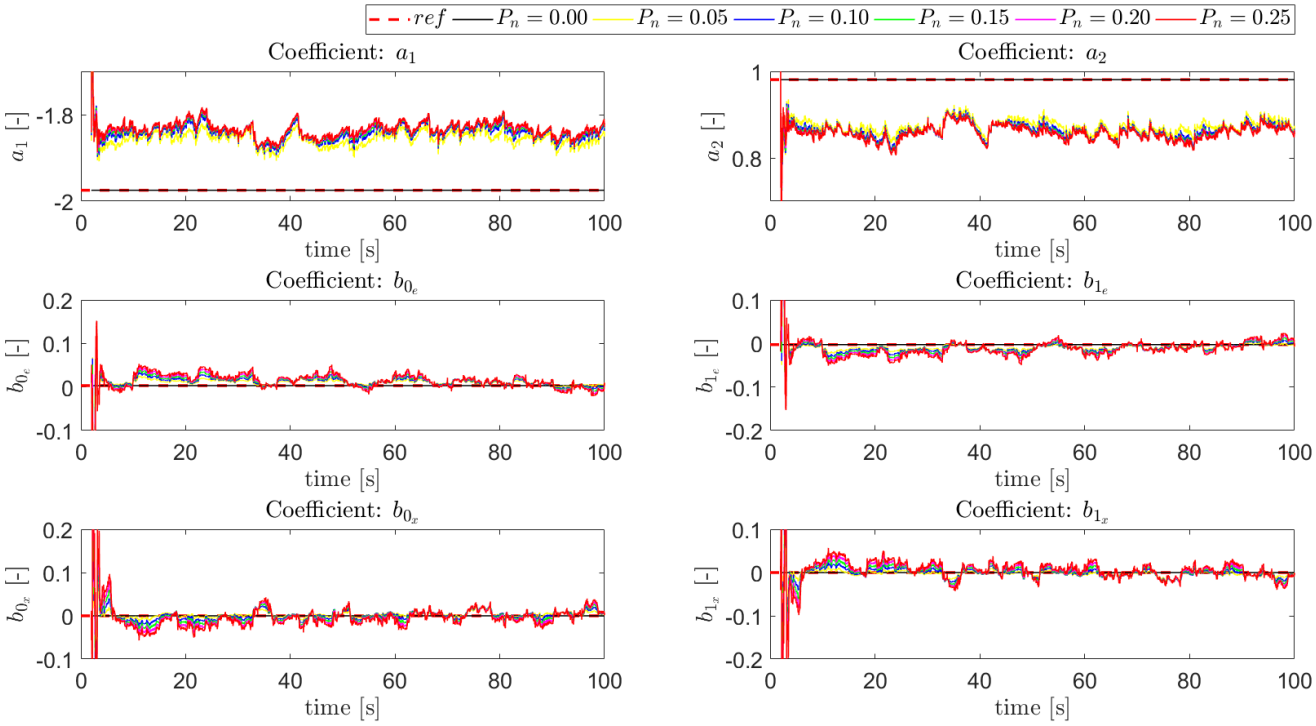

Figure B.9: Time traces ARX model coefficient estimation with RLS algorithm for condition C5 and different remnant power ratios

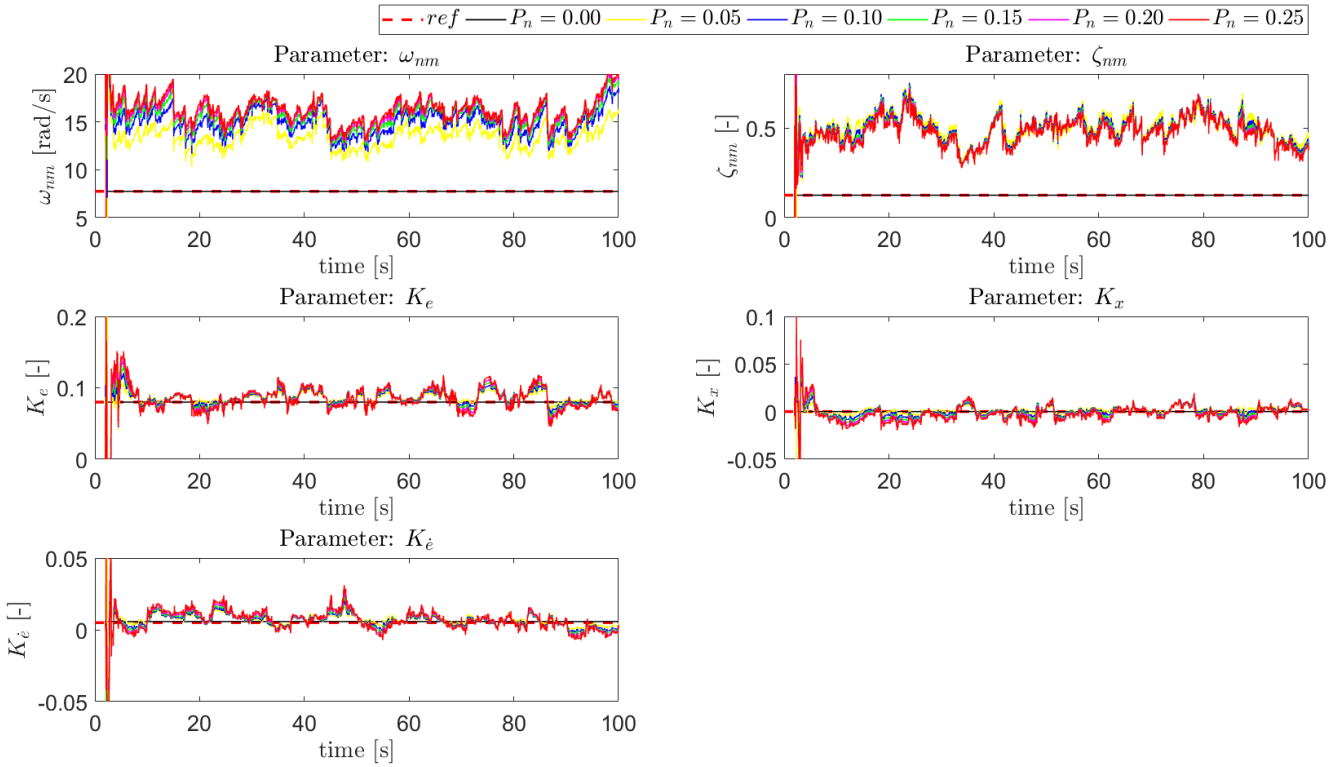

Figure B.10: Time traces human operator model parameter estimation with RLS algorithm for condition C5 and different remnant power ratios

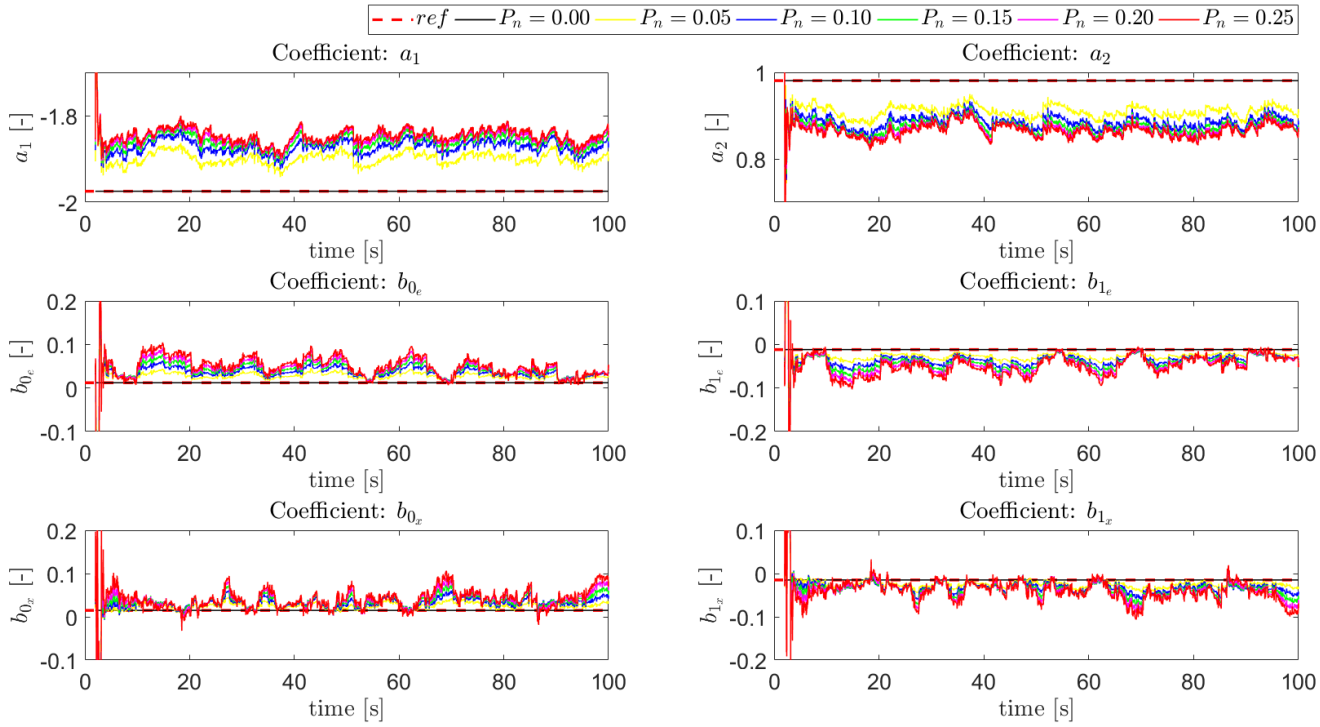

Figure B.11: Time traces ARX model coefficient estimation with RLS algorithm for condition C6 and different remnant power ratios

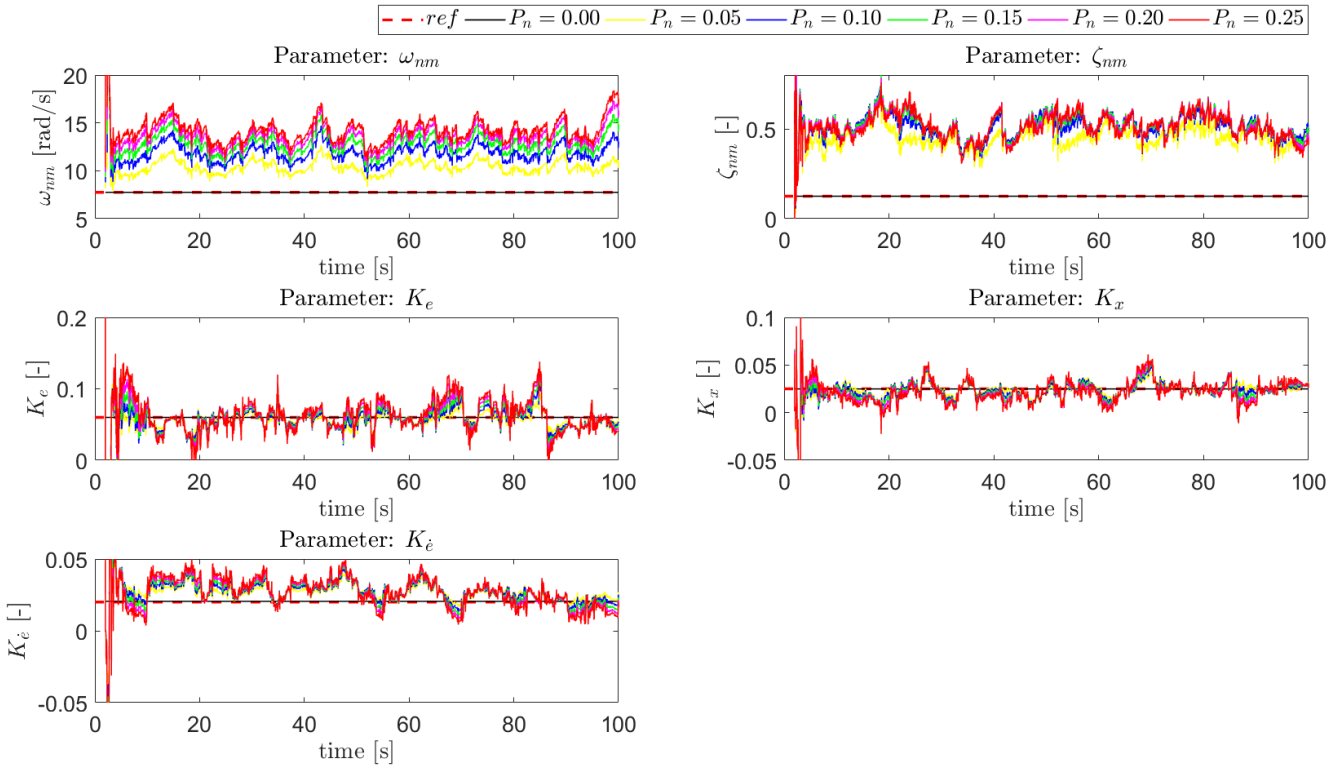

Figure B.12: Time traces human operator model parameter estimation with RLS algorithm for condition C6 and different remnant power ratios

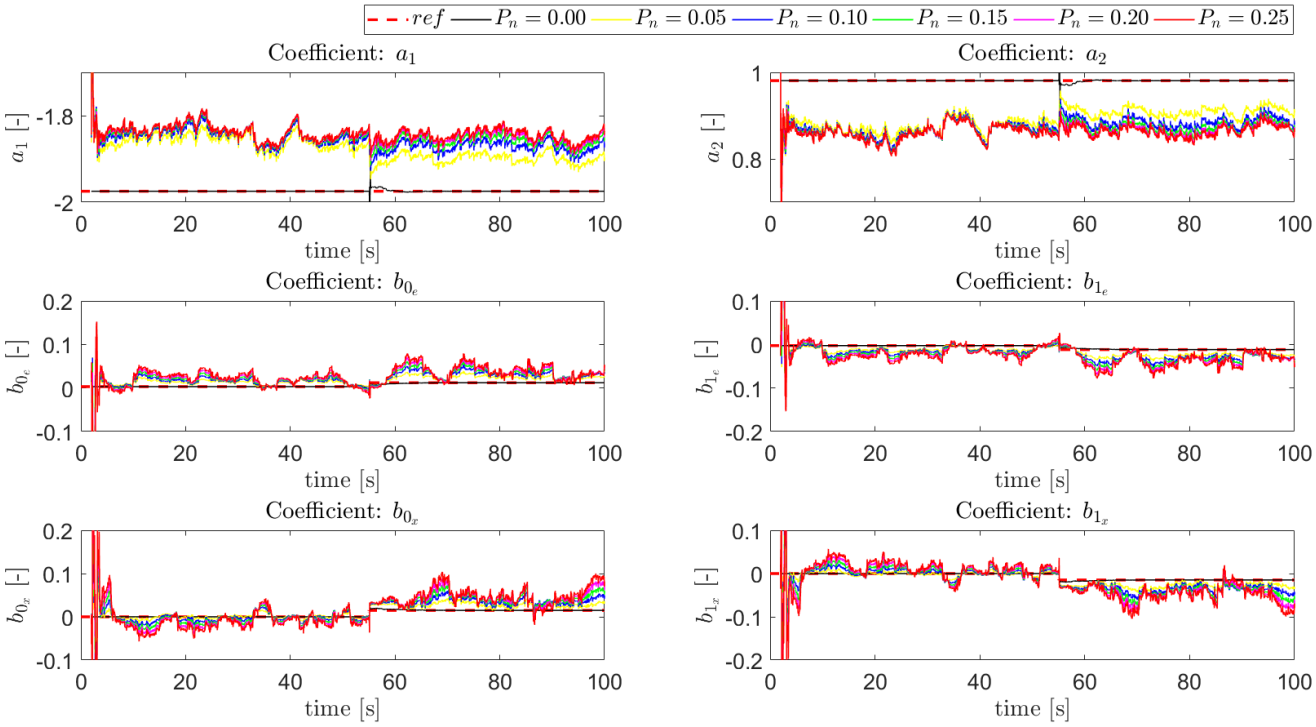

Figure B.13: Time traces ARX model coefficient estimation with RLS algorithm for condition C7 and different remnant power ratios

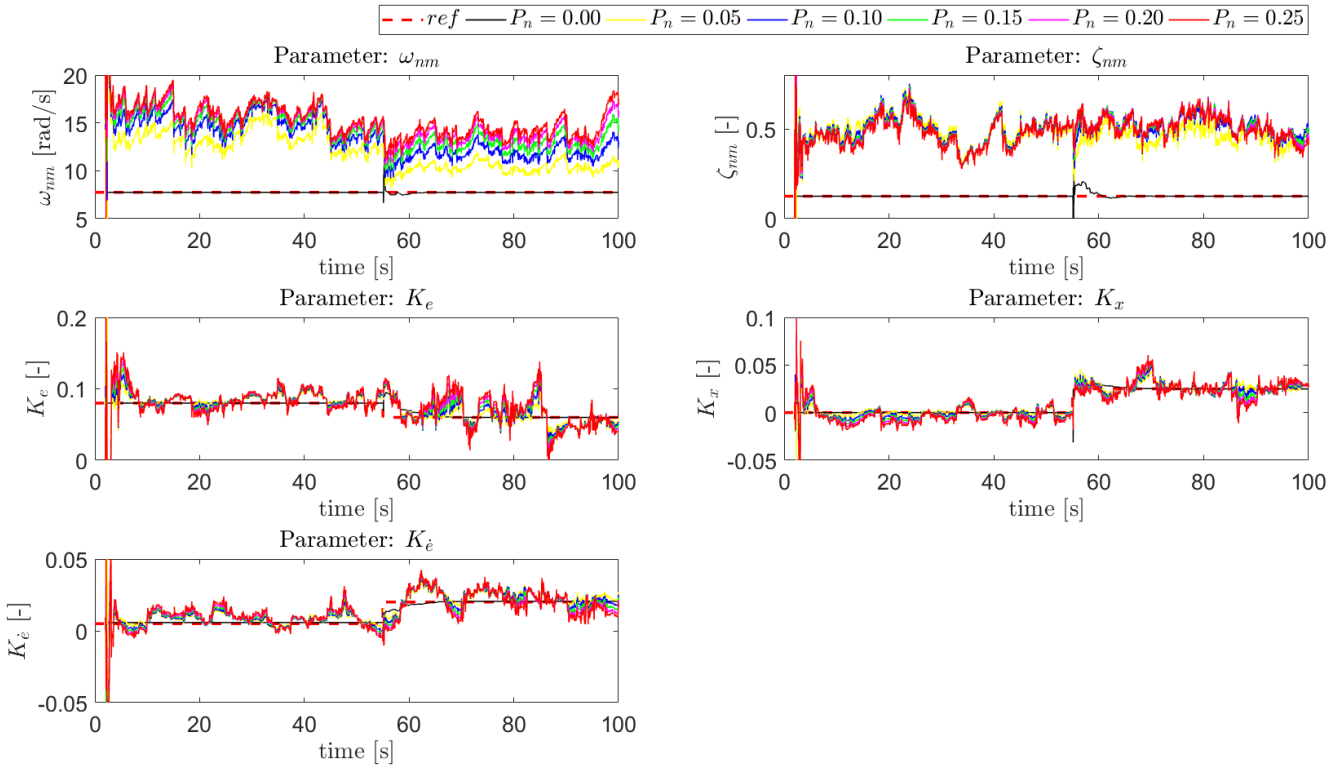

Figure B.14: Time traces human operator model parameter estimation with RLS algorithm for condition C7 and different remnant power ratios

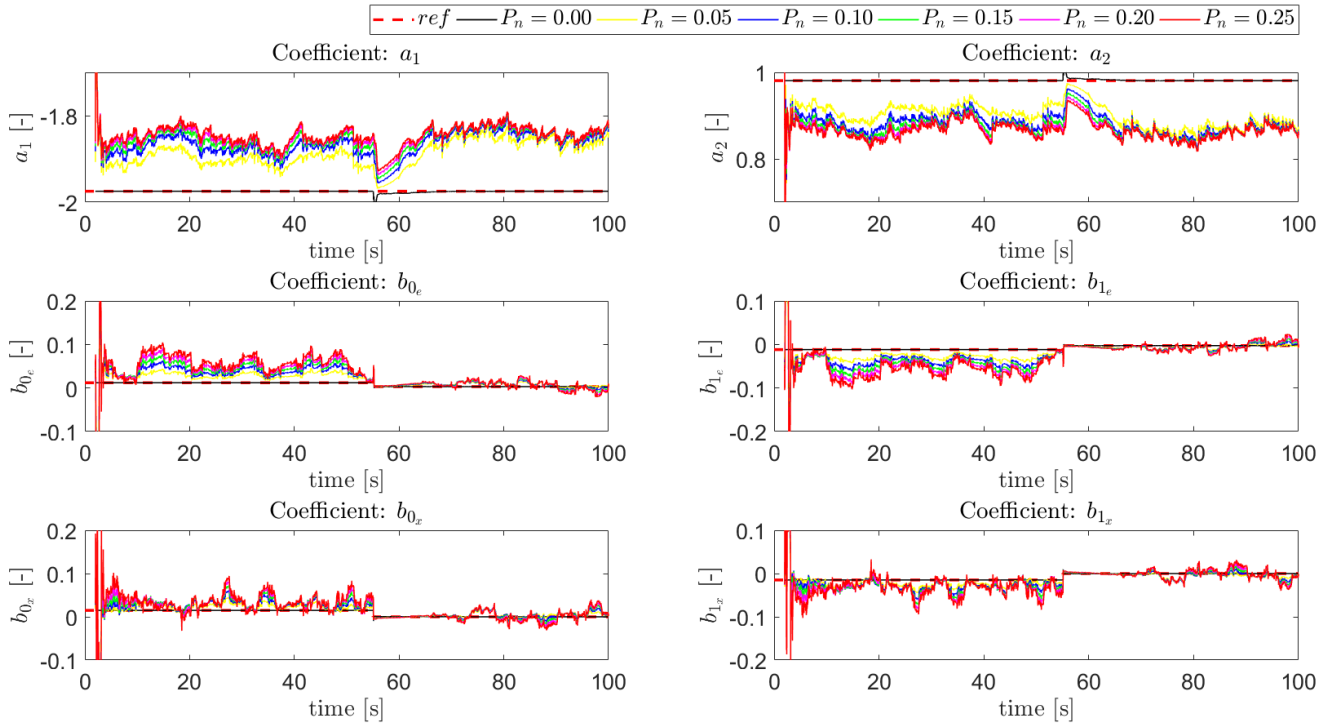

Figure B.15: Time traces ARX model coefficient estimation with RLS algorithm for condition C8 and different remnant power ratios

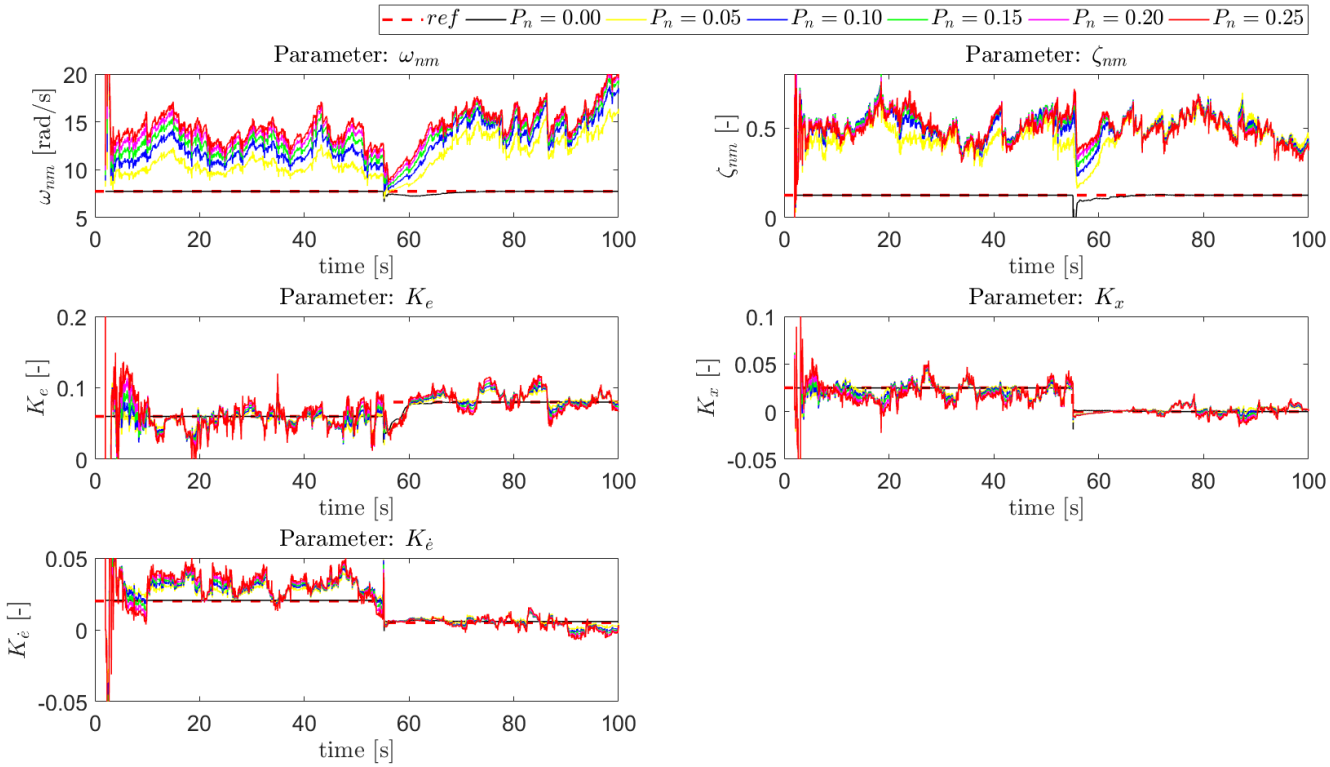

Figure B.16: Time traces human operator model parameter estimation with RLS algorithm for condition C8 and different remnant power ratios

III

Final Thesis Report Appendices

To be graded for AE5310 Final Thesis

C

Time Traces Estimated ARX Coefficients and HO Model Parameters

This appendix contains all the time traces of the estimated ARX coefficients and HO model parameters that were estimated with the multimodal recursive ARX algorithm (solid lines) and their mean values (dash-dotted lines), supported with the values that were estimated with the OLS ARX algorithm (dashed lines). The data has been averaged over all runs of all participants for each condition. All time traces can be found on the next 4 pages.

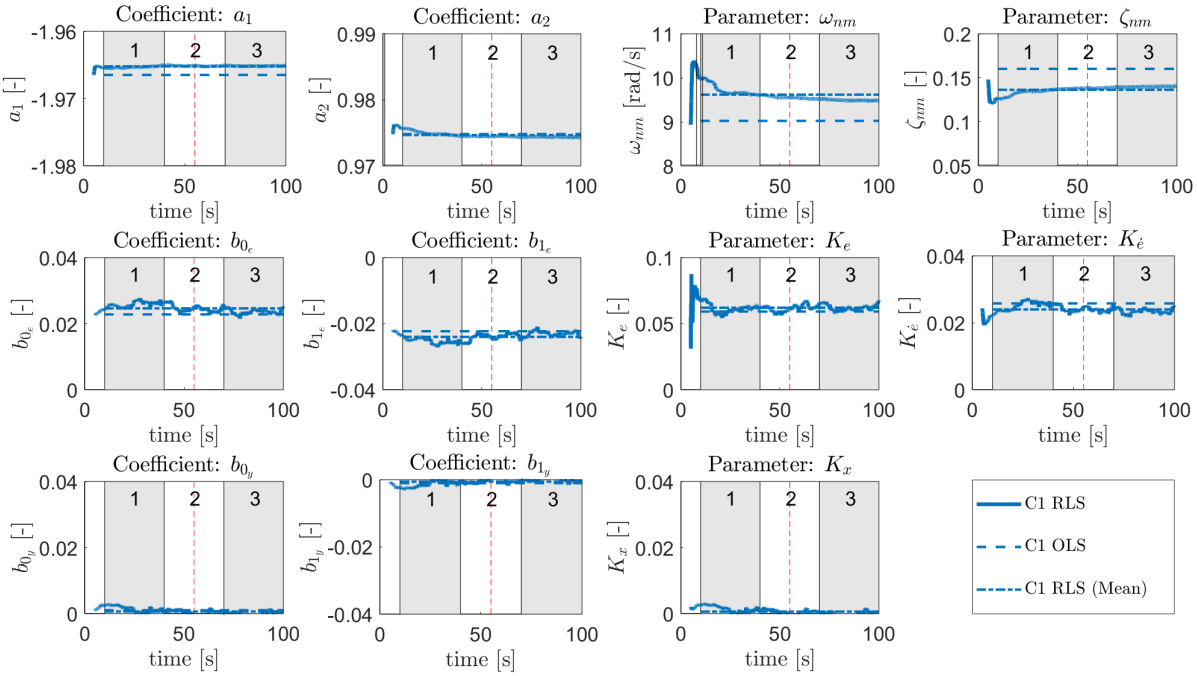

Figure C.1: Average estimation results of ARX coefficients and HO model parameters of all participants and all runs of condition C1

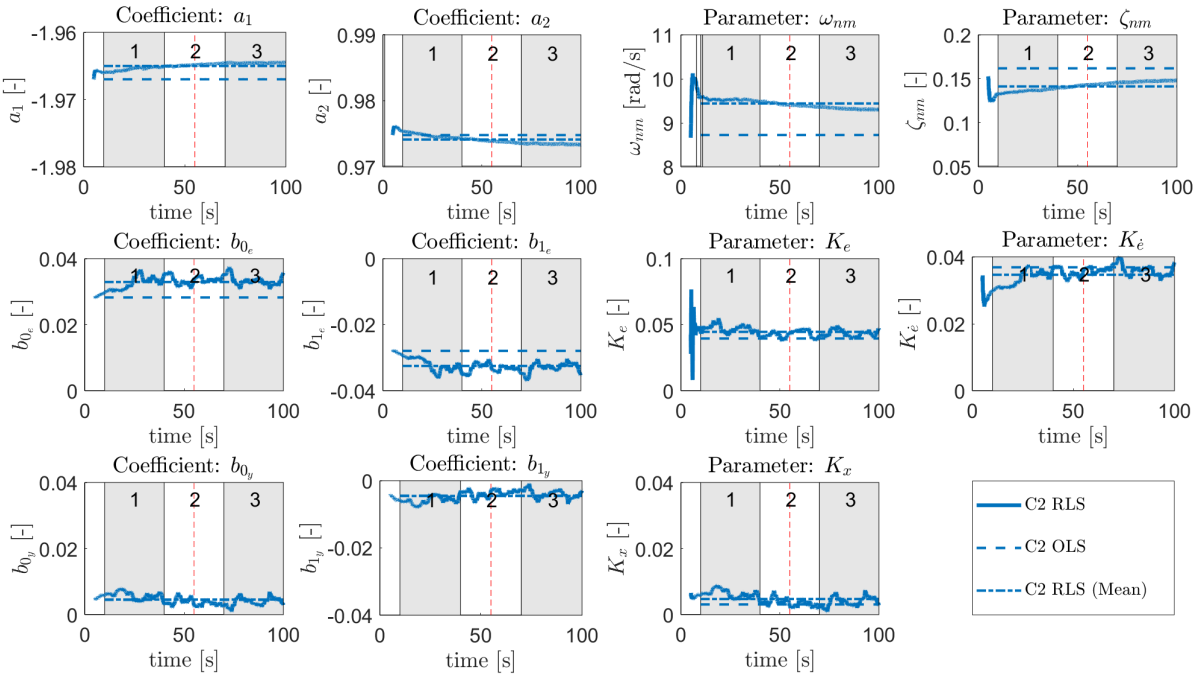

Figure C.2: Average estimation results of ARX coefficients and HO model parameters of all participants and all runs of condition C2

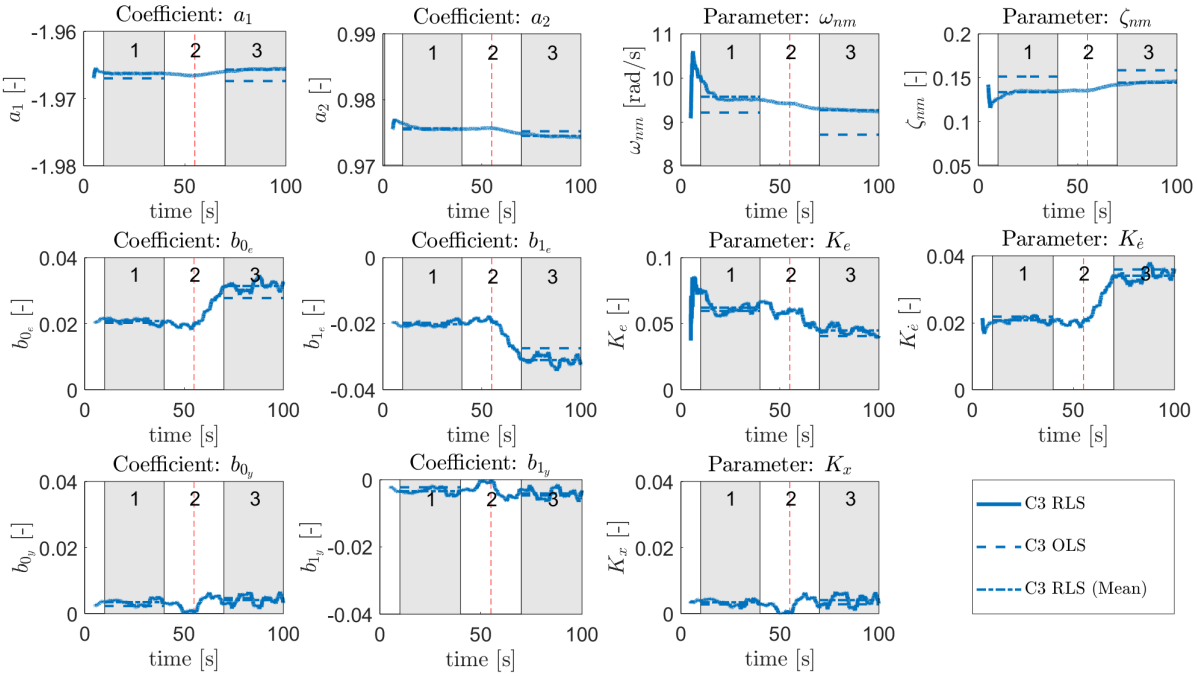

Figure C.3: Average estimation results of ARX coefficients and HO model parameters of all participants and all runs of condition C3

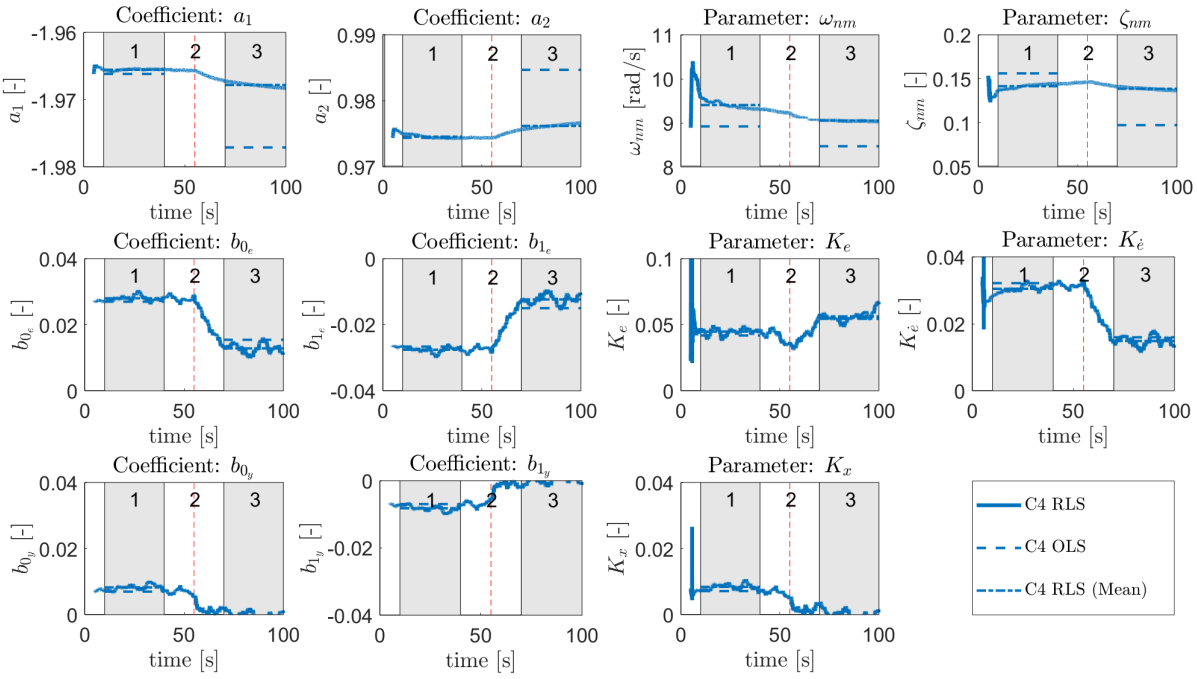

Figure C.4: Average estimation results of ARX coefficients and HO model parameters of all participants and all runs of condition C4

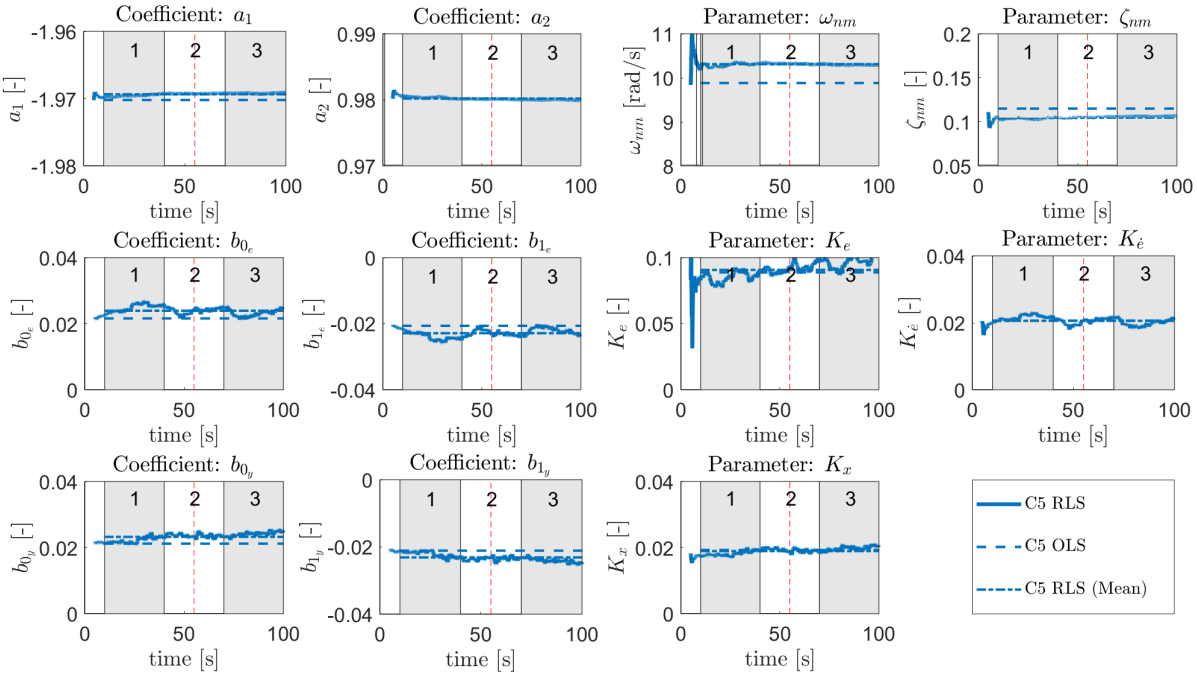

Figure C.5: Average estimation results of ARX coefficients and HO model parameters of all participants and all runs of condition C5

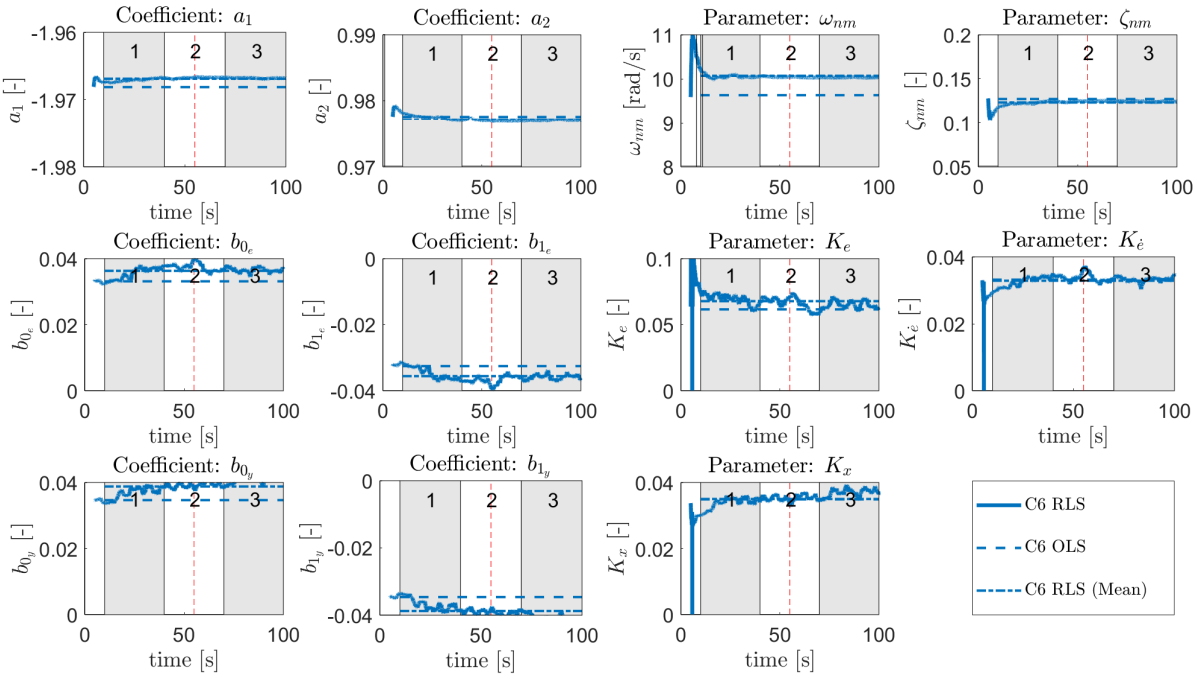

Figure C.6: Average estimation results of ARX coefficients and HO model parameters of all participants and all runs of condition C6

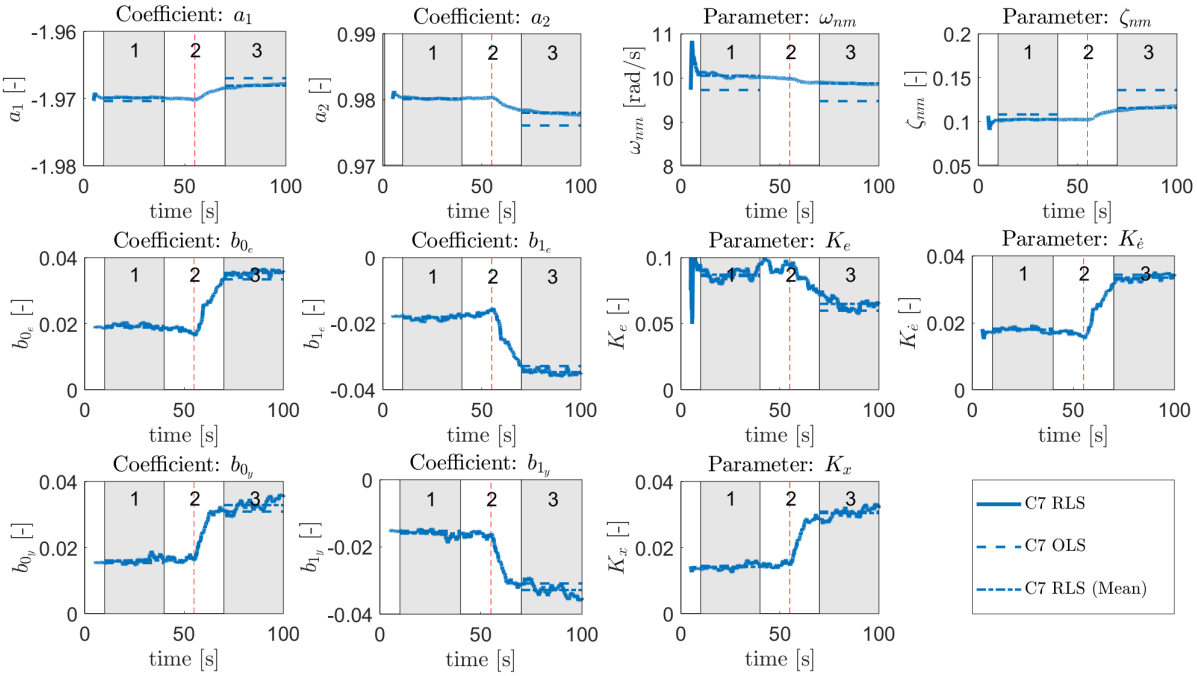

Figure C.7: Average estimation results of ARX coefficients and HO model parameters of all participants and all runs of condition C7

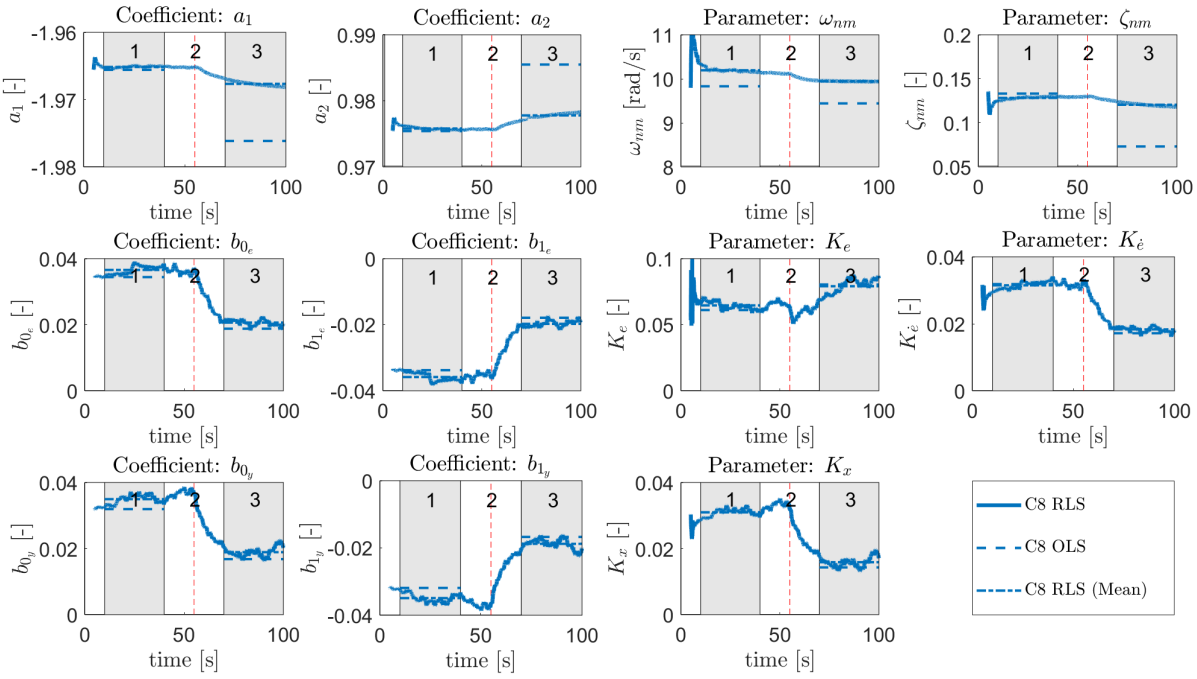

Figure C.8: Average estimation results of ARX coefficients and HO model parameters of all participants and all runs of condition C8

D

Boxplots Estimated ARX Coefficients and HO Model Parameters

This appendix contains the boxplots of all the estimates of the ARX coefficients and HO model parameters for all conditions and all runs. The RLS ARX estimate is represented by the mean value of the measurement run. All boxplots can be found on the next 4 pages.

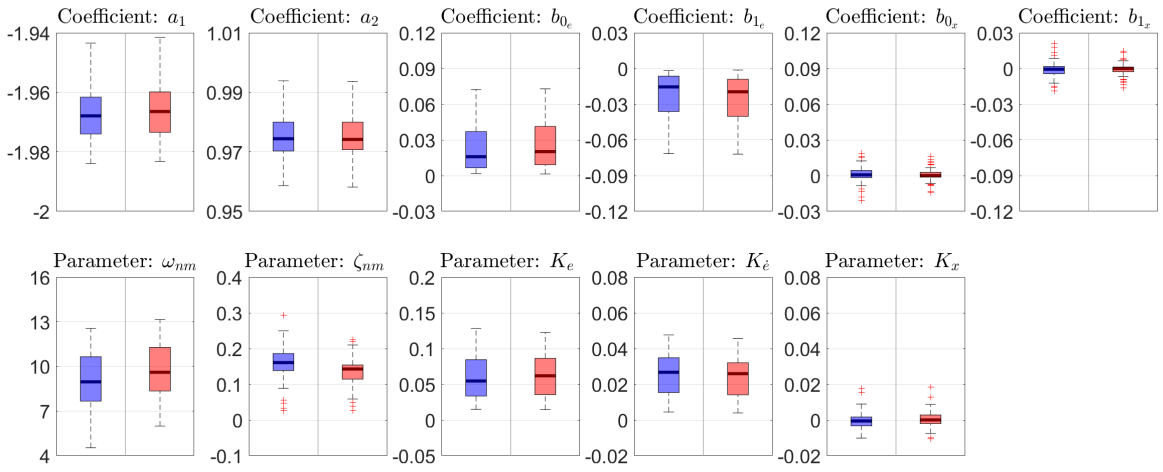

Figure D.1: Boxplot of ARX coefficients and HO model parameters estimated with the OLS and RLS ARX algorithm (RLS ARX represented by its mean) for condition C1 for all runs of all participants

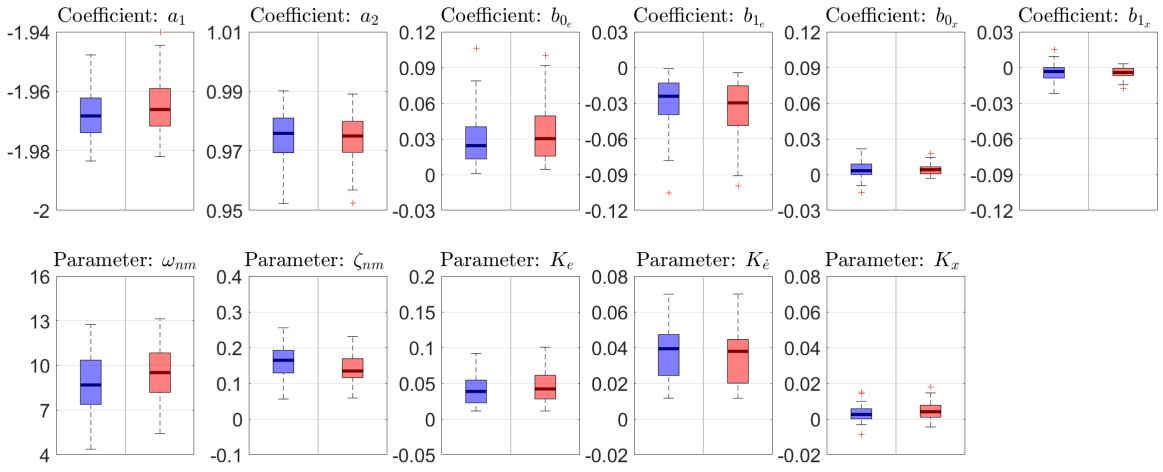

Figure D.2: Boxplot of ARX coefficients and HO model parameters estimated with the OLS and RLS ARX algorithm (RLS ARX represented by its mean) for condition C2 for all runs of all participants

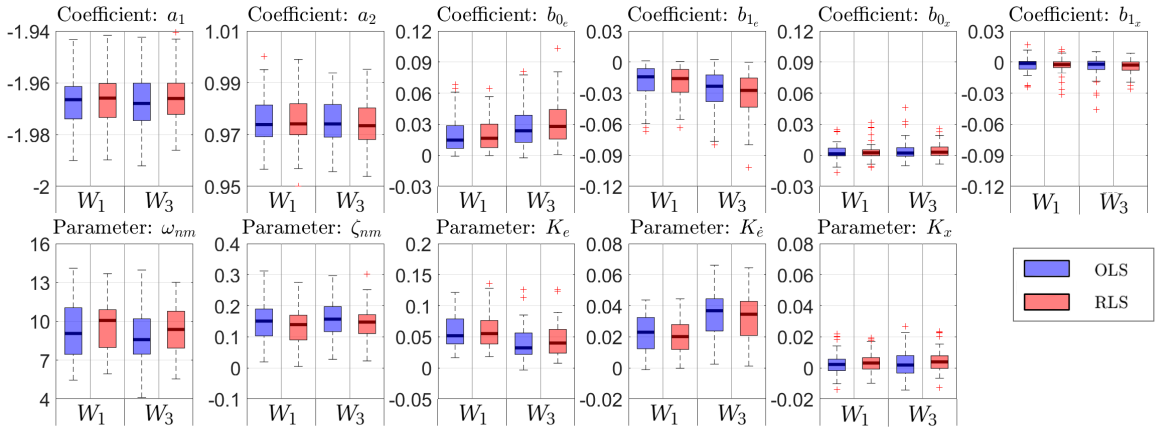

Figure D.3: Boxplot of ARX coefficients and HO model parameters estimated with the OLS and RLS ARX algorithm (RLS ARX represented by its mean) for condition C3 for all runs of all participants

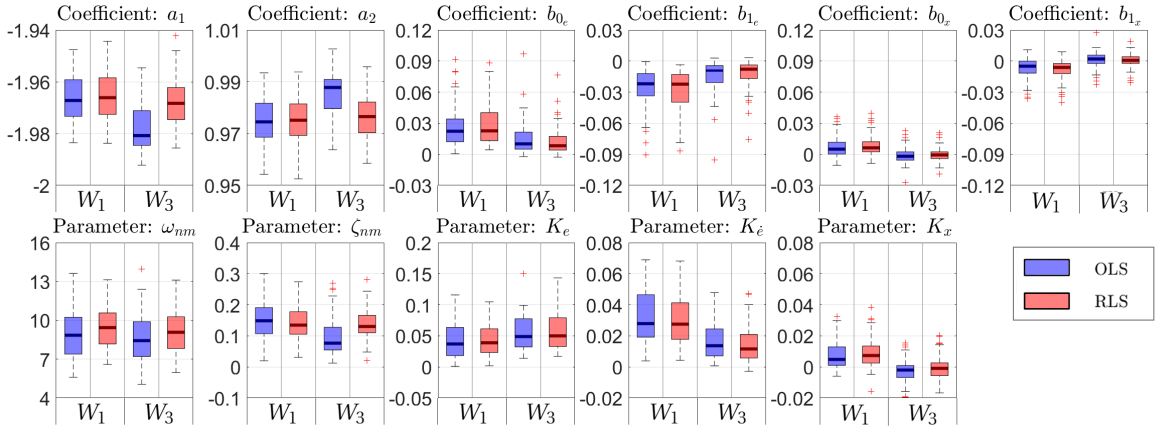

Figure D.4: Boxplot of ARX coefficients and HO model parameters estimated with the OLS and RLS ARX algorithm (RLS ARX represented by its mean) for condition C4 for all runs of all participants

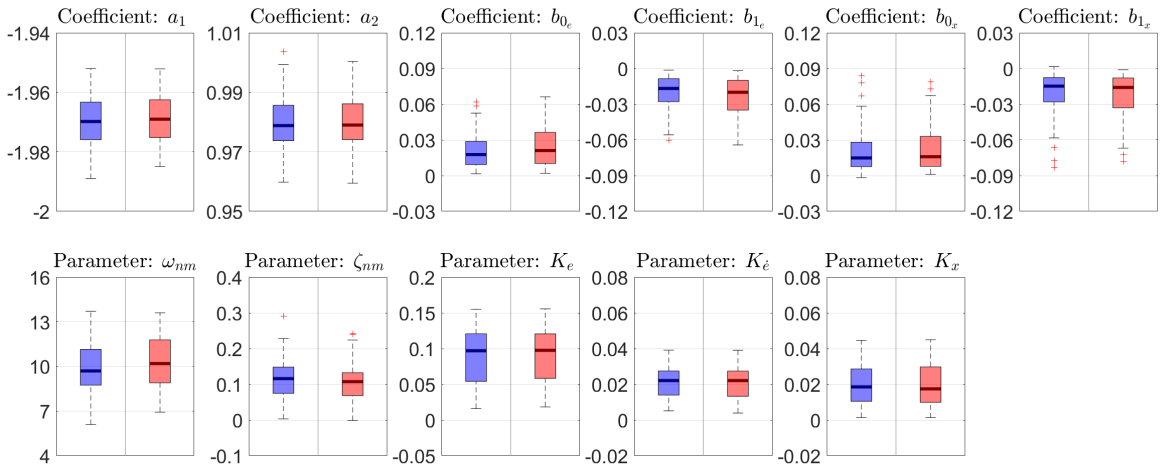

Figure D.5: Boxplot of ARX coefficients and HO model parameters estimated with the OLS and RLS ARX algorithm (RLS ARX represented by its mean) for condition C5 for all runs of all participants

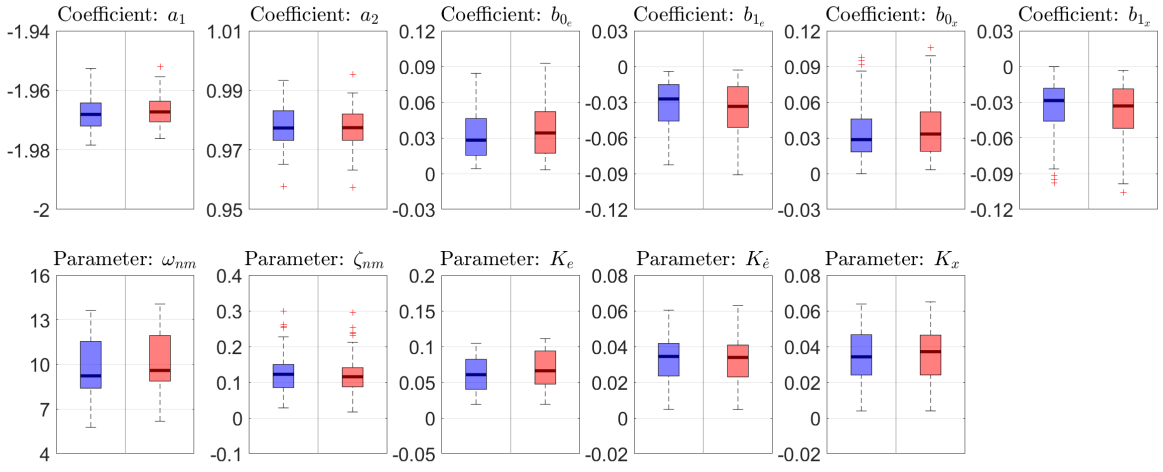

Figure D.6: Boxplot of ARX coefficients and HO model parameters estimated with the OLS and RLS ARX algorithm (RLS ARX represented by its mean) for condition C6 for all runs of all participants

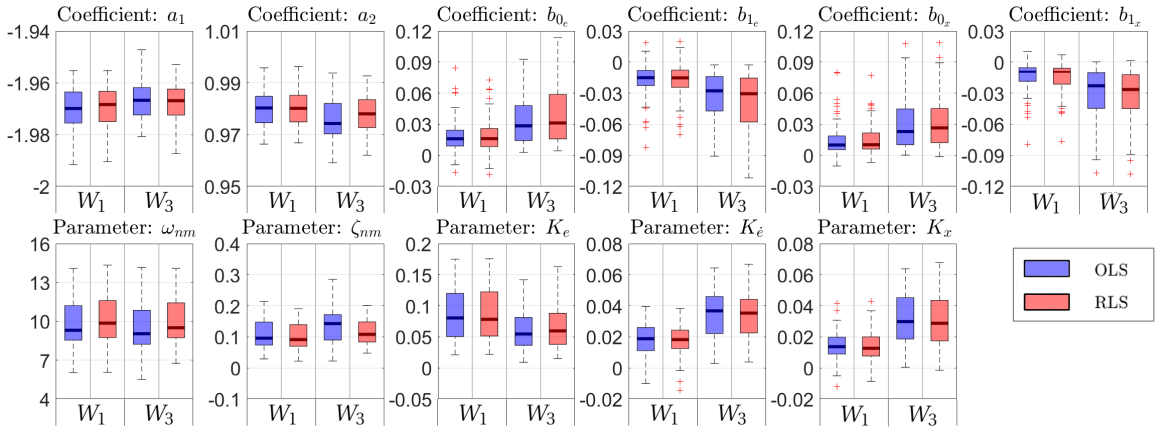

Figure D.7: Boxplot of ARX coefficients and HO model parameters estimated with the OLS and RLS ARX algorithm (RLS ARX represented by its mean) for condition C7 for all runs of all participants

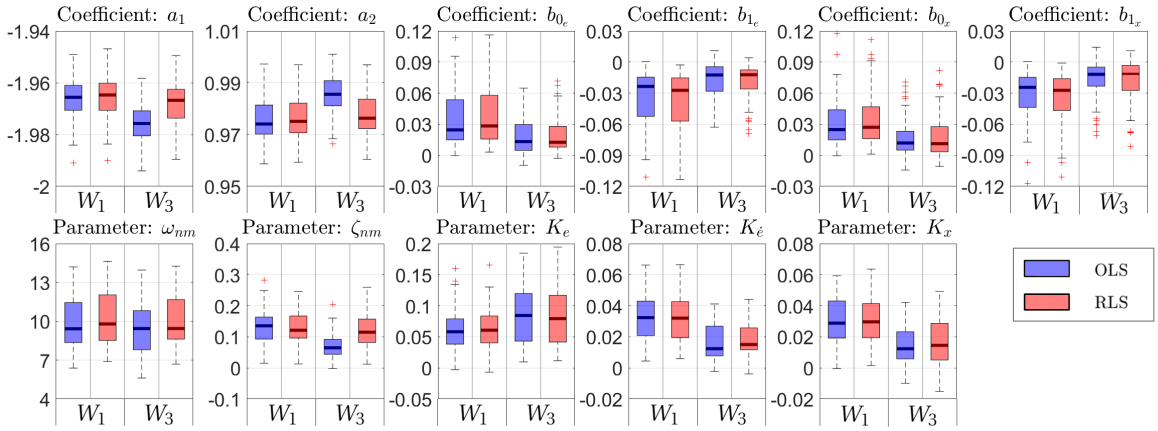

Figure D.8: Boxplot of ARX coefficients and HO model parameters estimated with the OLS and RLS ARX algorithm (RLS ARX represented by its mean) for condition C8 for all runs of all participants

E

Bode Plots Visual and Vestibular HO Responses

This appendix contains all the Bode plots of the visual and vestibular HO responses for all conditions. The data was averaged over all participants and all runs. The Bode plots were generated with both the mean value of the RLS ARX estimate and with the OLS ARX estimate. The Bode plots have been overlayed with the FC estimates of both the target forcing function f_t and the disturbance forcing function f_d to show the model fit in the frequency domain. All Bode plots can be found on the next 6 pages.

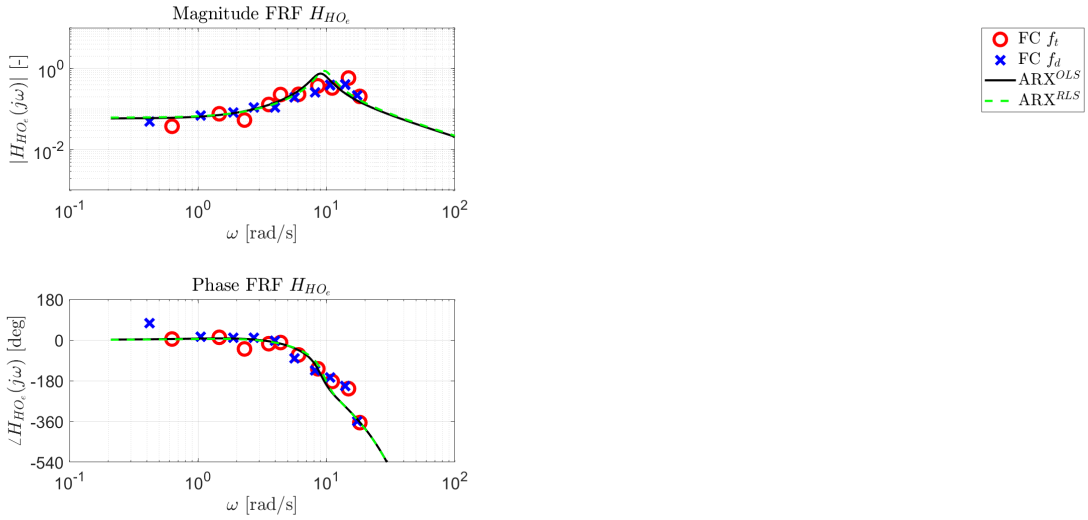

Figure E.1: Bode plots of visual HO response for condition C1 for mean RLS and OLS ARX algorithm and FC estimates of f_t and f_d

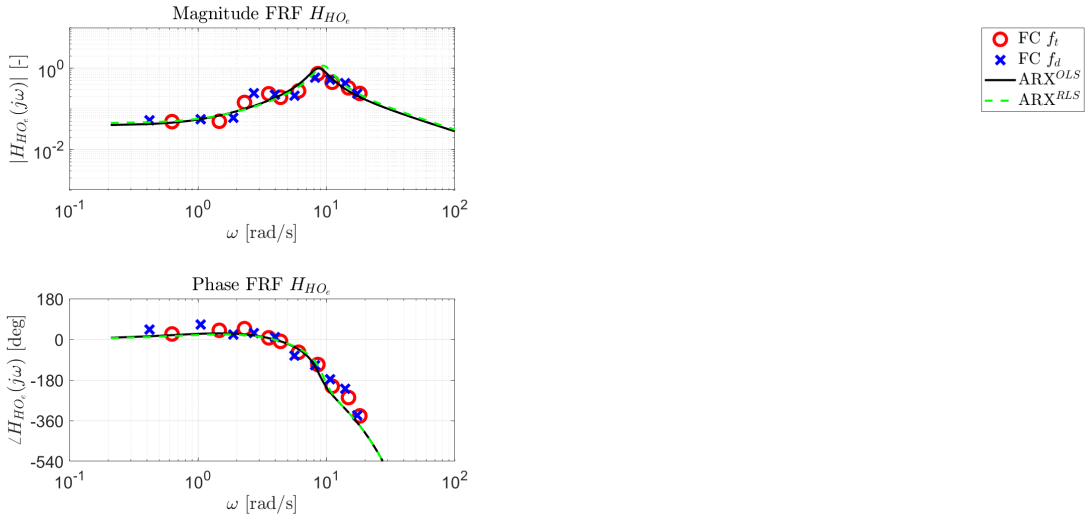

Figure E.2: Bode plots of visual HO response for condition C2 for mean RLS and OLS ARX algorithm and FC estimates of f_t and f_d

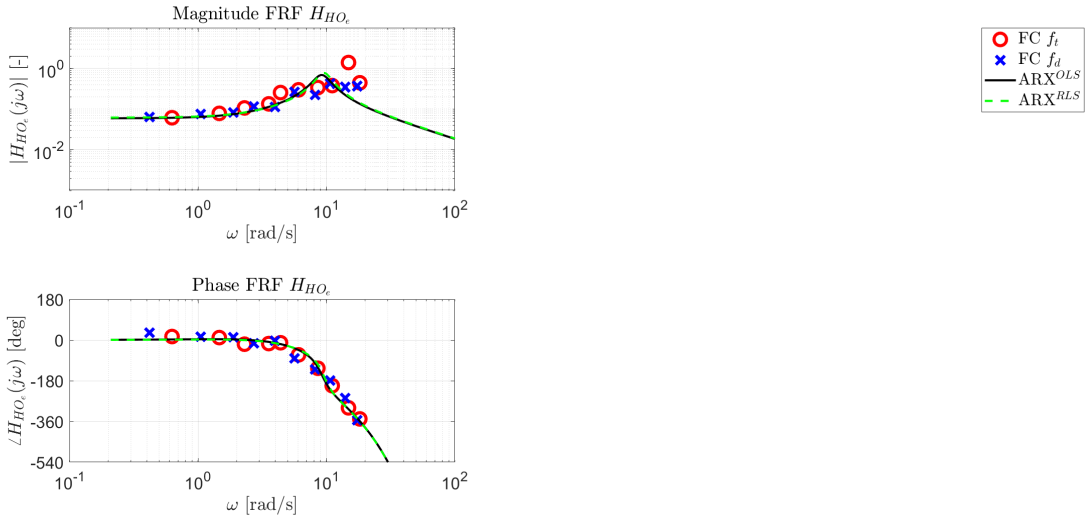

Figure E.3: Bode plots of visual HO response for condition C3 Window 1 for mean RLS and OLS ARX algorithm and FC estimates of f_t and f_d

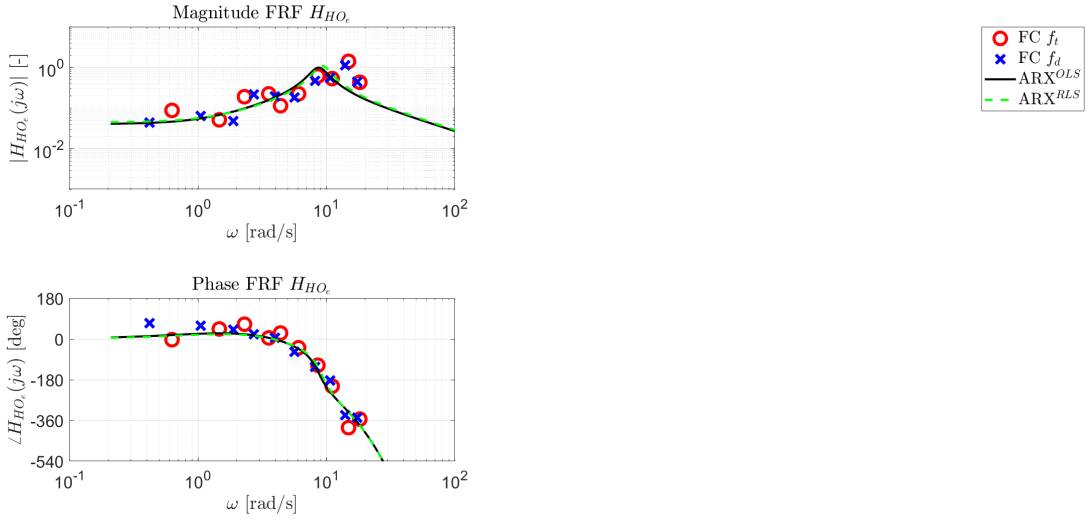

Figure E.4: Bode plots of visual HO response for condition C3 Window 3 for mean RLS and OLS ARX algorithm and FC estimates of f_t and f_d

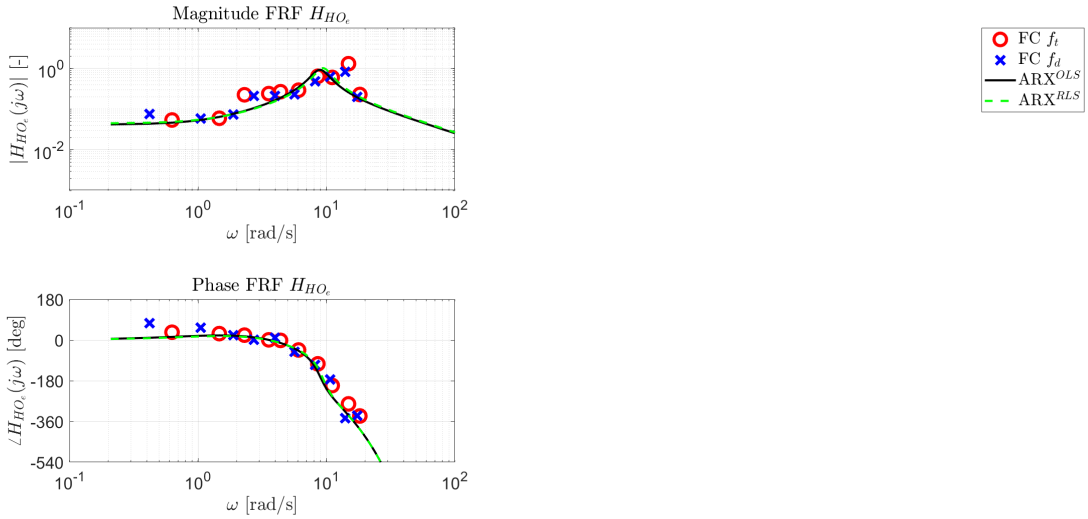

Figure E.5: Bode plots of visual HO response for condition C4 Window 1 for mean RLS and OLS ARX algorithm and FC estimates of f_t and f_d

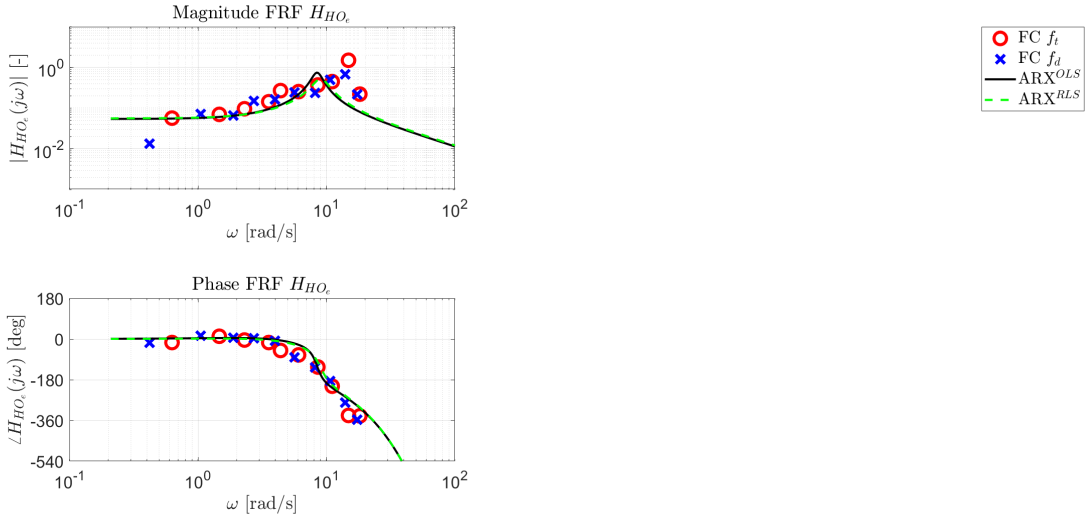

Figure E.6: Bode plots of visual HO response for condition C4 Window 3 for mean RLS and OLS ARX algorithm and FC estimates of f_t and f_d

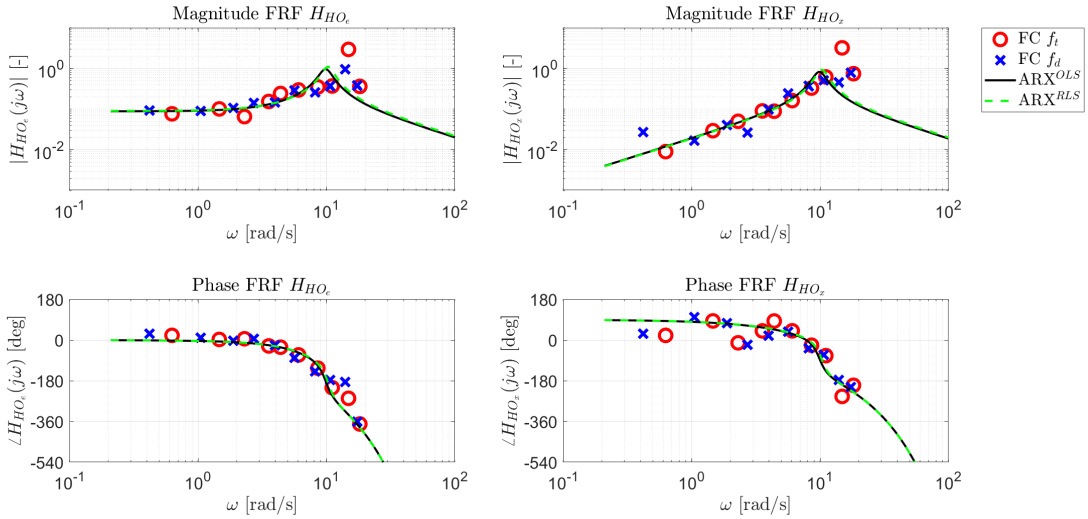

Figure E.7: Bode plots of visual and vestibular HO responses for condition C5 for mean RLS and OLS ARX algorithm and FC estimates of f_t and f_d

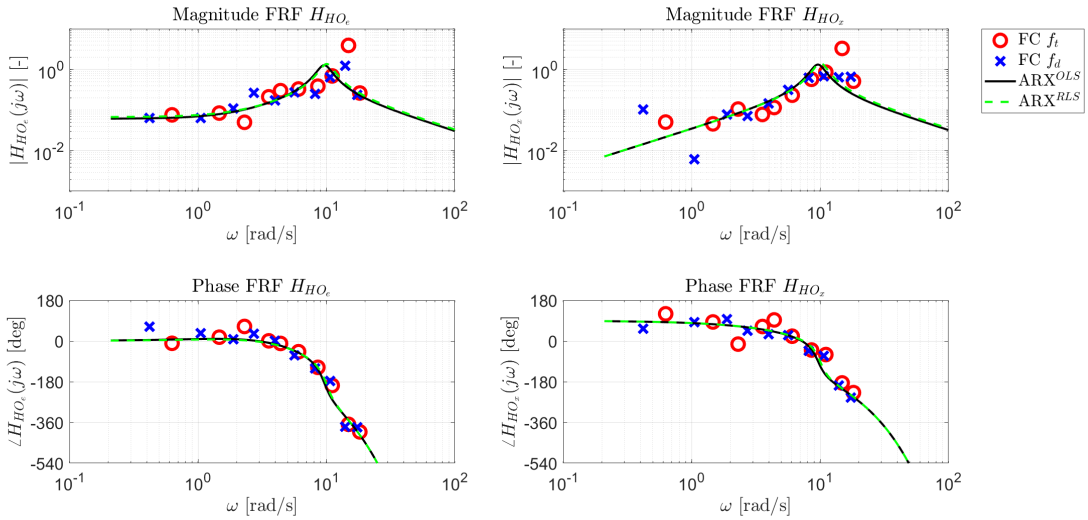

Figure E.8: Bode plots of visual and vestibular HO responses for condition C6 for mean RLS and OLS ARX algorithm and FC estimates of f_t and f_d

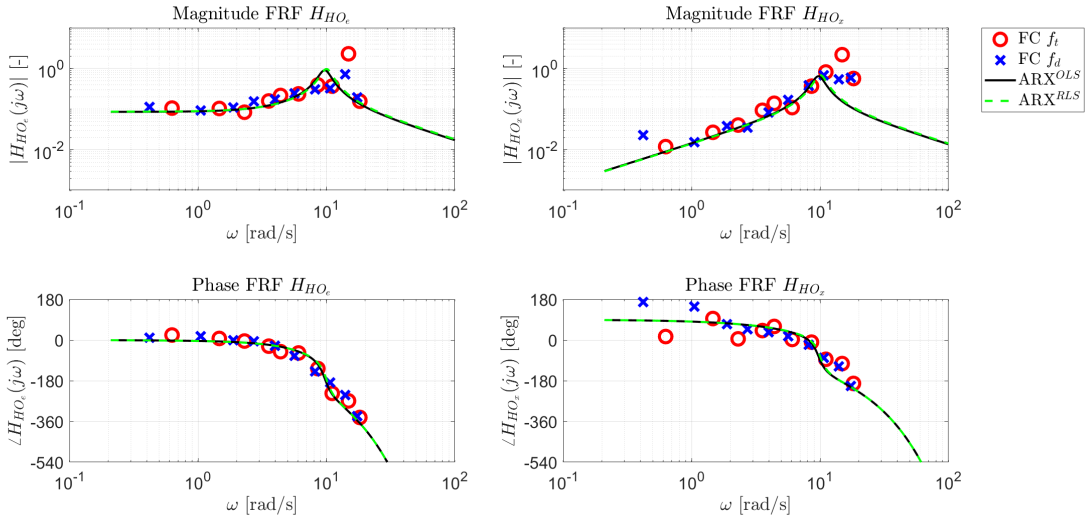

Figure E.9: Bode plots of visual and vestibular HO responses for condition C7 Window 1 for mean RLS and OLS ARX algorithm and FC estimates of f_t and f_d

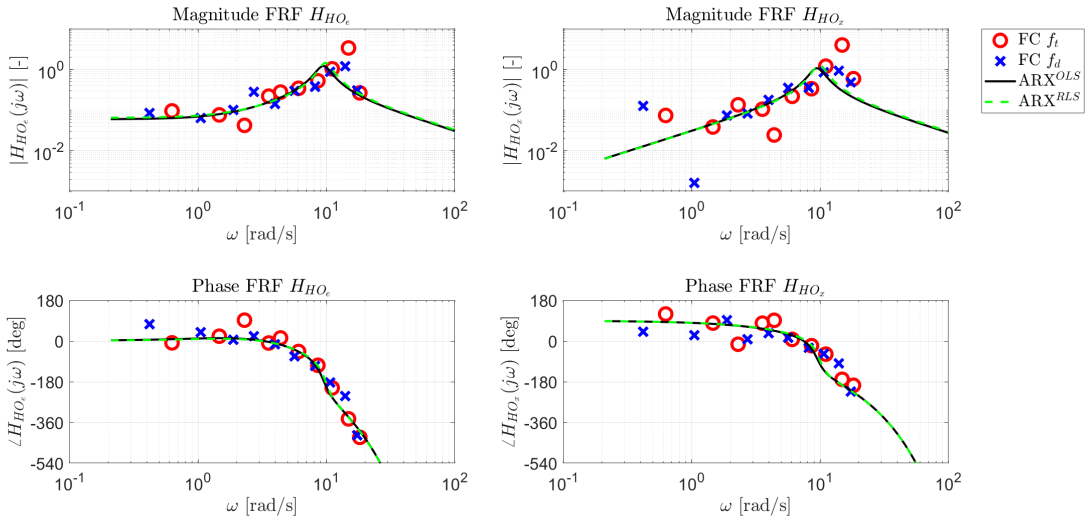

Figure E.10: Bode plots of visual and vestibular HO responses for condition C7 Window 3 for mean RLS and OLS ARX algorithm and FC estimates of f_t and f_d

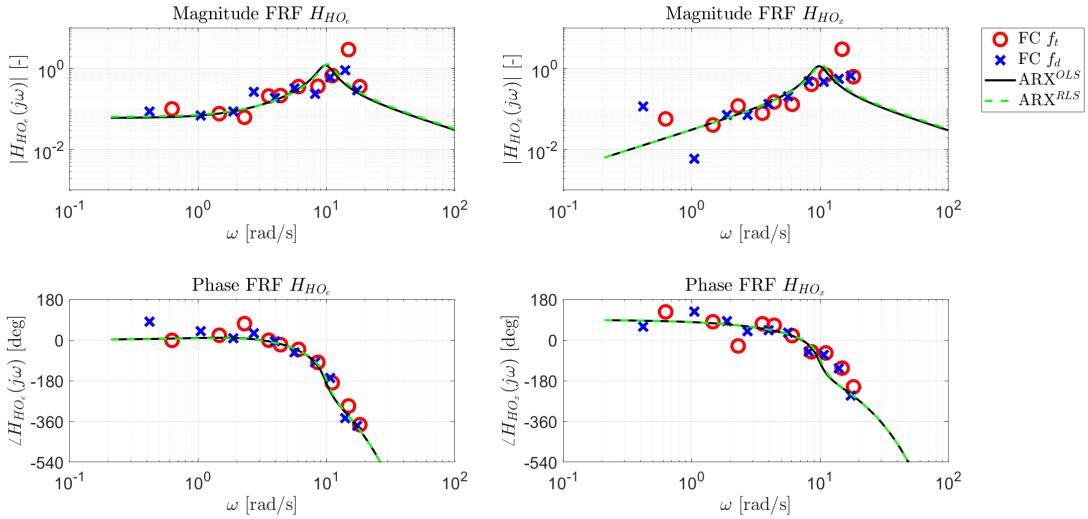

Figure E.11: Bode plots of visual and vestibular HO responses for condition C8 Window 1 for mean RLS and OLS ARX algorithm and FC estimates of f_t and f_d

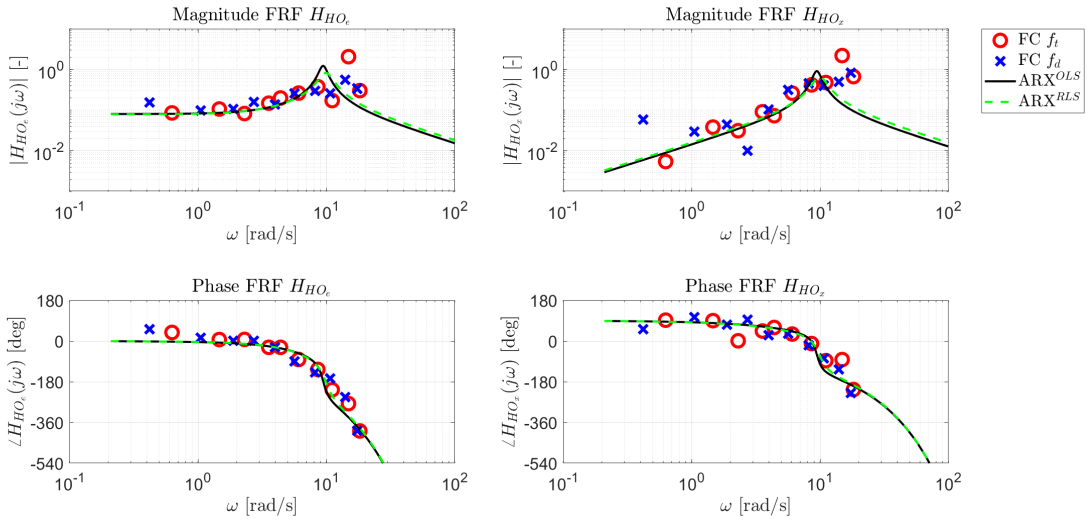

Figure E.12: Bode plots of visual and vestibular HO responses for condition C8 Window 3 for mean RLS and OLS ARX algorithm and FC estimates of f_t and f_d

F

Estimated Control Input and Corresponding VAF

This appendix contains all the time traces of the predicted control input $\hat{u}$ that was generated with the estimated HO model parameters, compared with the measured control input u. Below the plot, the VAF over time is visualized. For the VAF a 5 second centered window was used. The data has been averaged over all runs of all participants for each condition. All time traces can be found on the next 4 pages.

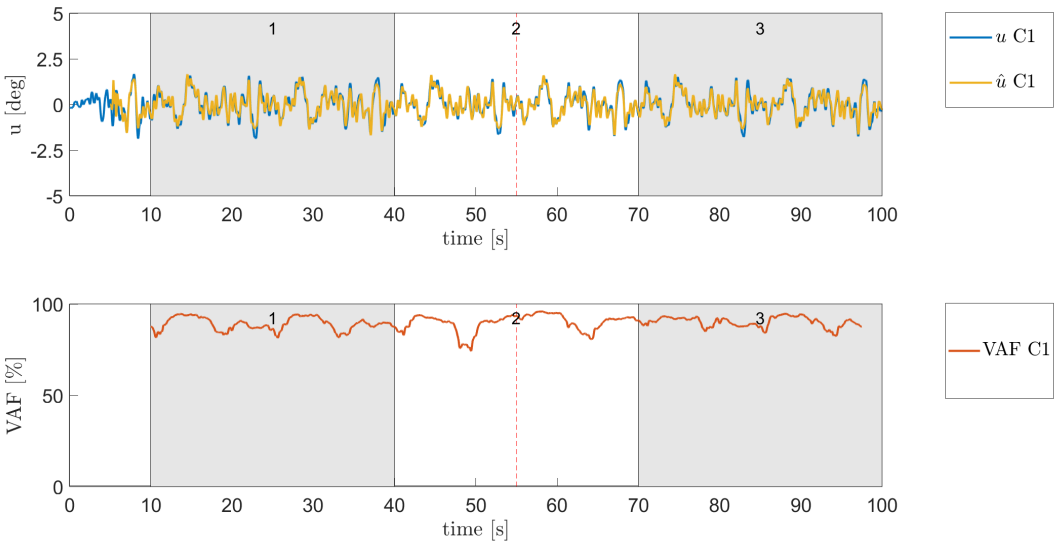

Figure F.1: Predicted control input $\hat{u}$ and measured control input u with corresponding VAF for condition C1

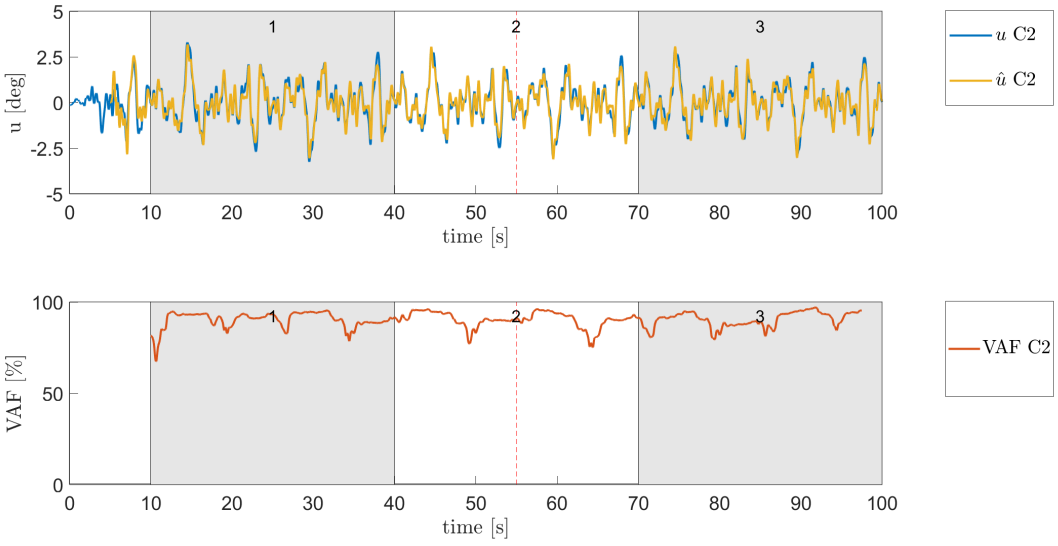

Figure F.2: Predicted control input $\hat{u}$ and measured control input u with corresponding VAF for condition C2

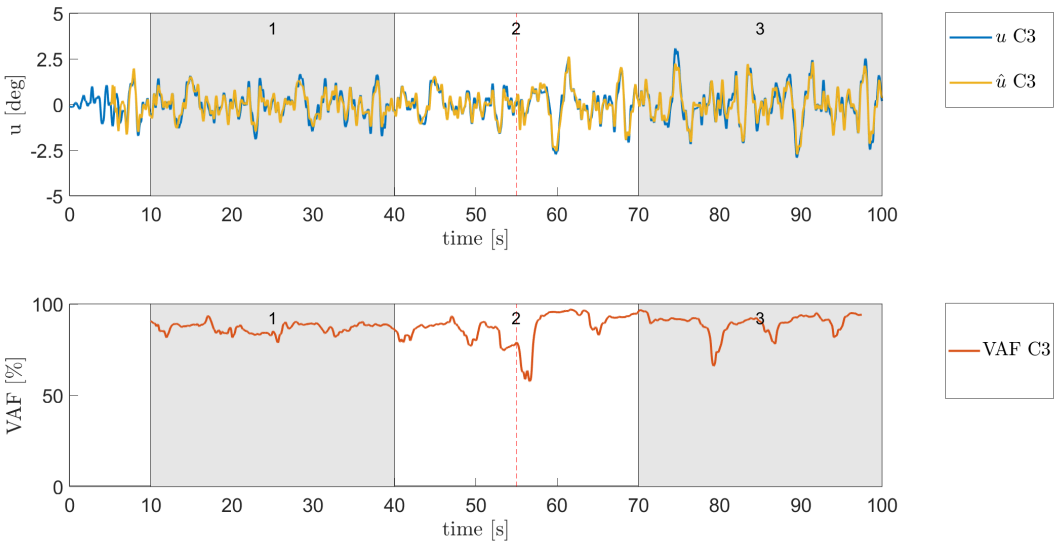

Figure F.3: Predicted control input $\hat{u}$ and measured control input u with corresponding VAF for condition C3

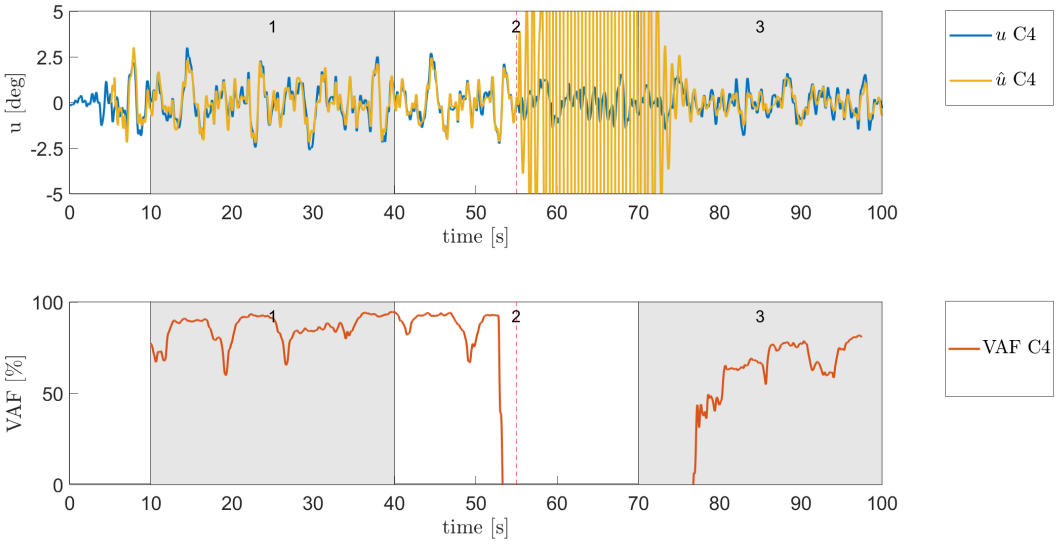

Figure F.4: Predicted control input $\hat{u}$ and measured control input u with corresponding VAF for condition C4

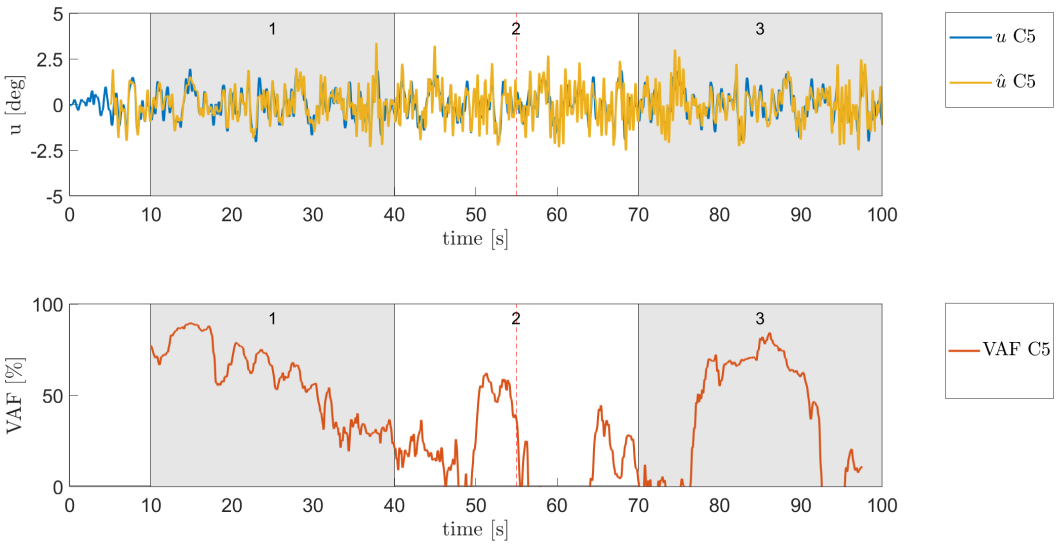

Figure F.5: Predicted control input $\hat{u}$ and measured control input u with corresponding VAF for condition C5

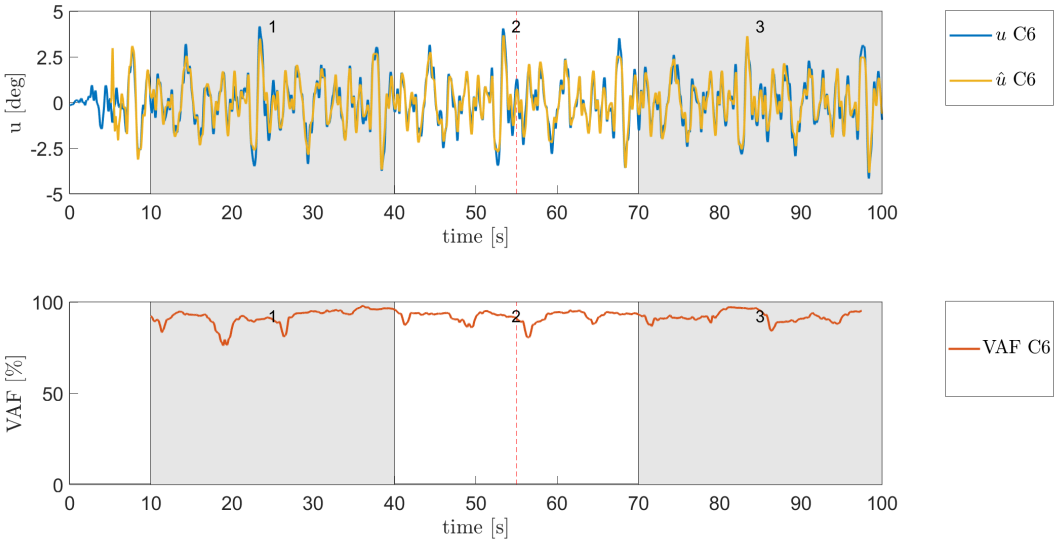

Figure F.6: Predicted control input $\hat{u}$ and measured control input u with corresponding VAF for condition C6

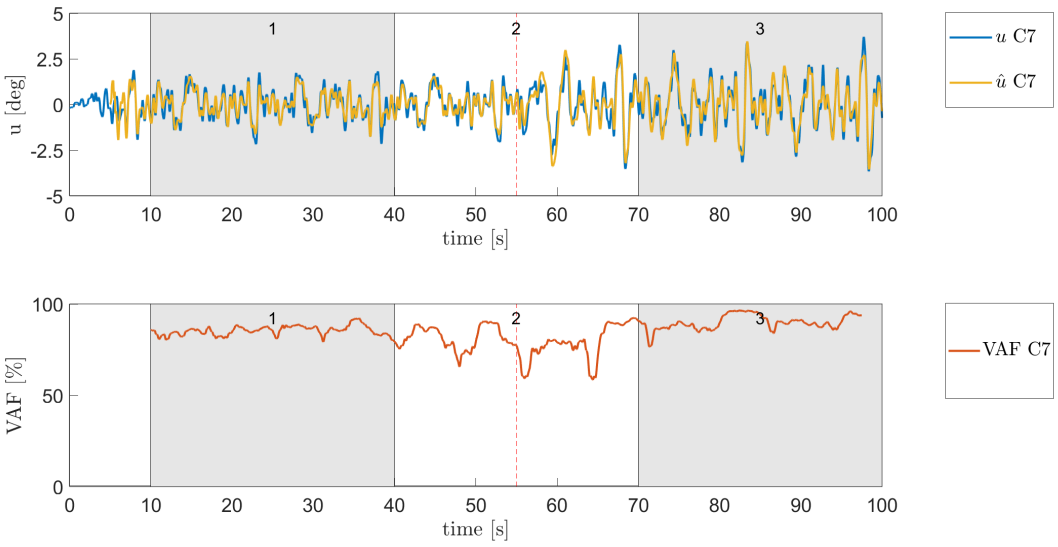

Figure F.7: Predicted control input $\hat{u}$ and measured control input u with corresponding VAF for condition C7

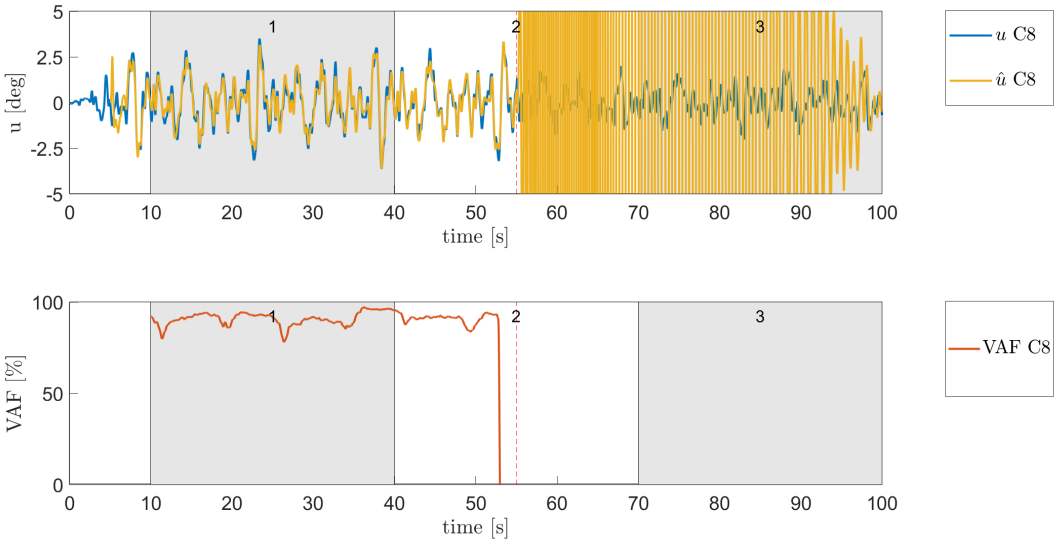

Figure F.8: Predicted control input $\hat{u}$ and measured control input u with corresponding VAF for condition C8

G

Human Research Ethics Committee Checklist

As the experiment involved the cooperation of human participants, the Human Research Ethics Committee (HREC) of Delft University of Technology had to approve of the experiment and its design. New experiments have to be applied for by filling out a checklist provided by the HREC. As the SRS was built in-house, an extensive device report had to be included on the safety of the simulator. The HREC approved of this experiment without demanding any modifications to the experiment. The HREC Checklist can be found on the next 2 pages.

Delft University of Technology
ETHICS REVIEW CHECKLIST FOR HUMAN RESEARCH
(Version 01.02.2019)

This checklist should be completed for every research study that involves human participants and should be submitted before potential participants are approached to take part in your research study.

In this checklist we will ask for additional information if need be. Please attach this as an Annex to the application.

Please upload the documents (go to this page for instructions).

Thank you and please check our website for guidelines, forms, best practices, meeting dates of the HREC, etc.

I. Basic Data

Project title:	**Investigating the effects of motion feedback on time-varying controlled element dynamics in compensatory tracking tasks**
Name(s) of researcher(s):	**M.J.J. (Menno) Linssen**
Research period (planning)	**September-October 2019**
E-mail contact person	**m.j.j.linssen@student.tudelft.nl**
Faculty/Dept.	**Aerospace Engineering/Control & Simulation**
Position researcher(s):[1]	**MSc Student**
Name of supervisor (if applicable):	**Dr. ir. D.M. (Daan) Pool**
Role of supervisor (if applicable):	**Assistant Professor**

II. A) Summary Research

The goal of this experiment is to investigate the effects of physical motion feedback on time-varying adaptation of human manual control skills. This is investigated in a compensatory pitch tracking task, where participants have to use a side stick to perform continuous control of a simulated aircraft's pitch (nose up/down) attitude, as shown on a head-down visual display. The experiment will be conducted in the SIMONA Research Simulator at the Faculty of Aerospace Engineering at TU Delft, which will provide participants with physical pitch motion feedback of their controlled aircraft. Participants will perform the task for four different conditions with different controlled aircraft dynamics that either stay constant or change from single integrator dynamics (easy to control) to double integrator dynamics (difficult to control) and vice versa during an experiment run. In total, 8-16 people will participate in the experiment and will be recruited from the student/PhD student population of TU Delft. The participants behaviour in response to sudden changes in the controlled aircraft dynamics will be compared across the different experiment conditions, especially between matching conditions with and without physical motion feedback. The adopted control dynamics will be analysed and quantified by using human control behaviour identification and modelling techniques on the recorded control task data.

B) Risk assessment

No true risks are foreseen for the participants in the experiment. Three potential risk factors are fully dealt with, as described below:

[1] For example: student, PhD, post-doc

1. All stored data is anonymized and stored under a numeric subject ID. In addition, only objective human control data is collected, no sensitive personal data is analysed.

2. The experiment is performed in the SIMONA Research Simulator and the simulator's hydraulic motion system (which was built in-house) is used to provide participants with a physical sensation of the movement of their controlled vehicle. While a potentially dangerous device, with extensive hardware, software, and operational safety measures the SIMONA Research Simulator is fully safe for use in human subject experiments (see attached signed Device Report and Operator Manual).

3. Though unlikely for this experiment due to minimal visual stimulation, a potential risk could be that participants get nauseous (simulator sickness) while performing the experiment. In case the first symptoms of simulator sickness (warm/sweating, stomach awareness, etc.) are reported by a participant, his/her participation in the experiment will be aborted. Participants will be briefed on this prior to the experiment (see attached Experiment Briefing).

III. Checklist

Question	Yes	No
1. Does the study involve participants who are particularly vulnerable or unable to give informed consent? (e.g., children, people with learning difficulties, patients, people receiving counselling, people living in care or nursing homes, people recruited through self-help groups).		**X**
2. Are the participants, outside the context of the research, in a dependent or subordinate position to the investigator (such as own children or own students)?[2]		**X**
3. Will it be necessary for participants to take part in the study without their knowledge and consent at the time? (e.g., covert observation of people in non-public places).		**X**
4. Will the study involve actively deceiving the participants? (For example, will participants be deliberately falsely informed, will information be withheld from them or will they be misled in such a way that they are likely to object or show unease when debriefed about the study).		**X**
5. Personal data • Will the study involve discussion or collection of confidential (sensitive) personal data? (e.g., BSN number, location, sexual activity, drug use, mental health)?		**X**
If ' yes': Did the data steward approve your data management plan? Please upload proof.		
6. Will drugs, placebos, or other substances (e.g., drinks, foods, food or drink constituents, dietary supplements) be administered to the study participants?		**X**
7. Will blood or tissue samples be obtained from participants?		**X**
8. Is pain or more than mild discomfort likely to result from the study?		**X**

[2] **Important note concerning questions 1 and 2.** Some intended studies involve research subjects who are particularly vulnerable or unable to give informed consent .Research involving participants who are in a dependent or unequal relationship with the researcher or research supervisor (e.g., the researcher's or research supervisor's students or staff) may also be regarded as a vulnerable group . If your study involves such participants, it is essential that you safeguard against possible adverse consequences of this situation (e.g., allowing a student's failure to complete their participation to your satisfaction to affect your evaluation of their coursework). This can be achieved by ensuring that participants remain anonymous to the individuals concerned (e.g., you do not seek names of students taking part in your study). If such safeguards are in place, or the research does not involve other potentially vulnerable groups or individuals unable to give informed consent, it is appropriate to check the NO box for questions 1 and 2. Please describe corresponding safeguards in the summary field.

Question	Yes	No
9. Does the study risk causing psychological stress or anxiety or other harm or negative consequences beyond that normally encountered by the participants in their life outside research?		X
10. Will financial inducement (other than reasonable expenses and compensation for time) be offered to participants?		X
Important: if you answered 'yes' to any of the questions mentioned above, please submit a full application to HREC (see: website for forms or examples).		
11. Will the experiment collect and store videos, pictures, or other identifiable data of human subjects? [3] If "yes", please fill in Annex 1 and make you sure you follow all requirements of the applicable data protection legislation. In addition, please provide proof by sending us a copy of the informed consent form.		X
12. Will the experiment involve the use of devices that are not 'CE' certified? *Only, if 'yes': continue with the following questions:*	X	
➢ Was the device built in-house?	X	
➢ Was it inspected by a safety expert at TU Delft? (*Please provide device report, see: HREC website*)	X	
➢ If it was not built in house and not CE-certified, was it inspected by some other, qualified authority in safety and approved? *(Please provide records of the inspection).*		
13. Has or will this research be submitted to a research ethics committee other than this one? (*if so, please provide details and a copy of the approval or submission).*		X

IV. Enclosures (tick if applicable)

- ○ Full proposal (if 'yes' to any of the questions 1 until 10)
- ○ Informed consent form (if 'yes' to question 11)
- X Device report (if 'yes' to question 12)
- ○ Approval other HREC-committee (if 'yes' to question 13)
- X Any other information which might be relevant for decision making by HREC: experiment briefing + consent form
- ○ Data management plan approved by a data steward (if yes to question 5B)

V. Signature(s)

Signature(s) of researcher(s)
Date:

M.J.J. Lissen 3/9/2019

Signature (or upload Electronic Consent) research supervisor (if applicable)
Date:

D.M. Pool 3/9/2019

[3] Note: you have to ensure that collected data is safeguarded physically and will not be accessible to anyone outside the study. Furthermore, the data has to be de-identified if possible and has to be destroyed after a scientifically appropriate period of time. Also ask explicitly for consent if anonymised data will be published as open data.

Appendix1: Privacy and data protection

Please fill this in if you have answered ' yes' to question 11 in the checklist

a. Will the participants have access to their own data? If no, please explain.

-

b. Will covert methods be used? *(e.g. participants are filmed without them knowing)*

-

c. Will any human tissue and/or biological samples be collected? *(e.g. urine)*

-

H

Experiment Briefing

To ensure that all the participants were prepared for their participation in the experiment, a briefing was sent several days in advance. This briefing contained the goal of the experiment, information on the task to be executed and the experimental procedures. Before the start of the experiment, the briefing was discussed with each participant to see if they read the instructions properly and if all possible questions were answered. The briefing can be found on the next page.

Experiment Briefing

The effects of motion feedback on time-varying manual control skills

Thank you for your contribution to this scientific endeavour! You will be participating in a tracking experiment in the SIMONA Research Simulator (SRS) at TU Delft, in which the effects of motion feedback on time-varying manual control skills will be investigated using a pitch control tracking task. This briefing will introduce you to the experiment and what is expected of you as a participant.

Experiment Goal

The goal of this experiment is to investigate the effects of motion feedback on time-varying manual control skills. Compared to experiments in fixed-base simulators, motion-base simulators provide participants with additional feedback that might aid or hinder them in performing the tracking task. Furthermore, the adaptive character of human operators in manual control will be researched by varying the control task over time. The results of this experiment can be used to make recommendations on training procedures and aircraft design.

Experiment Task

The task you will carry out is a single-axis pitch tracking task with compensatory display. In this task, it is your goal to actively minimize the aircraft pitch error in a target-following task. The tracking task can be compared to landing an aircraft using an (pitch) attitude indicator.

The aircraft pitch error will be displayed on the primary flight display using a simplified artificial horizon instrument, as shown in Figure 1. The aircraft's attitude is displayed by fixed wings and the pitch error is displayed using a translating "ground" (illustrated in Figure 1 as the brown shape), on a contrasting background in blue. Note that the error symbol *e* as well as the corresponding arrow, as shown in Figure 1, are not illustrated in the display.

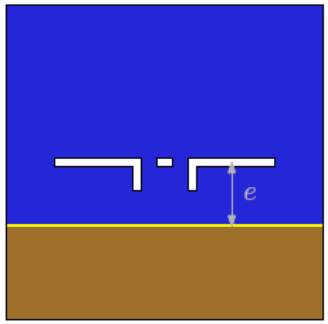

Fig. 1: Experiment display.

During the experiment, you will control the aircraft's pitch attitude by providing smooth control inputs using a side-stick on the right-hand side of the seat. The pitch angle is controlled by fore-aft stick movements. The display is positioned in front of you. Your main objective is to keep the error on the display as close to zero as possible. To correct the error shown in Figure 1, a pitch-down (forward push) input is required. After each run, a score is displayed on the primary flight display to indicate your performance. A lower score indicates a better performance.

The control inputs that are given to the side-stick result in simulator movement. Pushing the side-stick forwards results in tilting forwards, whereas pulling the side-stick backwards results in tilting backwards. The task has been designed so that the pitching motion will remain easily within the simulator's motion capabilities. To get used to the direct control of the simulator's movement, you are advised to start by giving small control inputs during the first motion runs.

In addition, while very unlikely for the current experiment, it is possible that some participants may develop nausea (simulator sickness) during the simulator tests. In case you experience the first symptoms of simulator sickness (feeling very warm, sweating profusely, stomach awareness), you are asked to **inform the experimenter**, as then experiment will, unfortunately, be discontinued.

Experiment Procedures

During the experiment you will perform several different conditions in which the control tasks changes in difficulty in between and/or during runs. The different conditions will be presented to you in a random order. After you have completed a run for each condition once, you will be given a different random set of conditions, which is repeated until a satisfactorily consistent performance has been attained for all conditions. The researcher will keep track of your performance and will announce when the experiment has been completed.

Each run lasts 100 seconds. Short breaks can be taken between runs to alleviate any discomfort that might occur due to controlling the side-stick or after sitting in a fixed position for a prolonged period of time. Longer breaks will be taken after every 16-20 tracking runs, where you will be taken out of the simulator for 15-20 minutes. The experiment will last approximately 3 hours.

For each tracking run, the subsequent procedure will be followed:

1. The researcher applies the settings for the next run.
2. The researcher checks whether the participant is ready to proceed (i.e., simulator sickness symptoms) and initiates the run after a countdown from 3 (3-2-1-go).
3. The participant performs the tracking task.
4. The participant will be notified of their performance in the completed run in terms of error score displayed on the primary flight display after the completed run.

Contact information researcher:	Contact information research supervisor
Menno Linssen	dr. ir. Daan Pool
m.j.j.linssen@student.tudelft.nl	d.m.pool@tudelft.nl
+31 6 15078052	+31 15 2789611

Thank you for participating!

Experiment Consent Form

All the participants for the experiment had to approve of voluntarily being part of the experiment by signing an experiment consent form. This consent form contained several statements on their cooperation, safety regulations and data and results processing. Only after the participant ticked all the boxes the experiment could be conducted. All participants signed the form. The form can be found on the next page.

Experiment Consent Form

The effects of motion feedback on time-varying manual control skills

I hereby confirm, by ticking each box, that:

1. I volunteer to participate in the experiment conducted by the researcher (**Menno Linssen**) under supervision of **dr.ir. Daan Pool** from the Faculty of Aerospace Engineering of TU Delft. I understand that my participation in this experiment is voluntary and that I may withdraw and discontinue participation at any time, for any reason. ☐
2. I have read the experiment briefing and confirm that I understand the experiment instructions and have had all remaining questions answered to my satisfaction. ☐
3. I understand that my participation involves performing a simple manual control task in a motion-base simulator setup. ☐
4. I confirm that the researcher has provided me with detailed safety and operational instructions for the hardware (simulator setup, hydraulic sidestick, fire escape ladder) used in the experiment. ☐
5. I understand that the researcher will not identify me by name in any reports or publications that will result from this experiment, and that my confidentiality as a participant in this study will remain secure. ☐
6. I understand that this research study has been reviewed and approved by the TU Delft Human Research Ethics Committee (HREC). To report any problems regarding my participation in the experiment, I know I can contact the researchers using the contact information below or, if necessary, the TU Delft HREC (hrec@tudelft.nl). ☐
7. I have been given a copy of this consent form. ☐

My Signature	Date
My Printed Name	Signature of researcher

Contact information researcher:	Contact information research supervisor
Menno Linssen	dr. ir. Daan Pool
m.j.j.linssen@student.tudelft.nl	d.m.pool@tudelft.nl
+31 6 15078052	+31 15 2789611

J

Balanced Latin Square Runtables

The scientific article and Chapter 7 discussed that for the experiment a balanced Latin square schedule was used for the order of runs to be executed by each participant. This balanced Latin square matrix involved a scrambled order of the eight testing conditions as well as the four forcing function realizations, yielding a unique order of combinations for each participant. In this way, the order in which the runs are presented to each participant had no effect on the results. An example of the balanced Latin square runtables for the first 4 repetitions for Participant 1 are shown in the 3 pages hereafter.

TV Dynamics with Motion

SIMONA Experiment

Run Tables

Participant: 1

Menno Linssen M.J.J.Linssen@student.tudelft.nl

Daan Pool D.M.Pool@tudelft.nl

September 2019

Training

Date:	
Start time:	
End time:	

Run #	Condition - Motion	Phase	Comments
			TRAINING
			TRAINING
			TRAINING
			TRAINING
			TRAINING
			TRAINING
			TRAINING
			TRAINING

Run table 1 of 12

Date:	
Start time:	
End time:	

Run #	Condition - Motion	Phase	Comments
	5: SI - Motion	4: Phase 4	
	7: SI 2 DI - Motion	2: Phase 2	
	1: SI - No Motion	4: Phase 4	
	4: DI 2 SI - No Motion	3: Phase 3	
	6: DI - Motion	3: Phase 3	
	8: DI 2 SI - Motion	1: Phase 1	
	2: DI - No Motion	2: Phase 2	
	3: SI 2 DI - No Motion	1: Phase 1	

Run table 2 of 12

Date:	
Start time:	
End time:	

Run #	Condition - Motion	Phase	Comments
	7: SI 2 DI - Motion	4: Phase 4	
	4: DI 2 SI - No Motion	1: Phase 1	
	5: SI - Motion	3: Phase 3	
	8: DI 2 SI - Motion	2: Phase 2	
	1: SI - No Motion	2: Phase 2	
	3: SI 2 DI - No Motion	4: Phase 4	
	6: DI - Motion	1: Phase 1	
	2: DI - No Motion	3: Phase 3	

Run table 3 of 12

Date:	
Start time:	
End time:	

Run #	Condition - Motion	Phase	Comments
	4: DI 2 SI - No Motion	4: Phase 4	
	8: DI 2 SI - Motion	4: Phase 4	
	7: SI 2 DI - Motion	3: Phase 3	
	3: SI 2 DI - No Motion	2: Phase 2	
	5: SI - Motion	1: Phase 1	
	2: DI - No Motion	1: Phase 1	
	1: SI - No Motion	3: Phase 3	
	6: DI - Motion	2: Phase 2	

Run table 4 of 12

Date:	
Start time:	
End time:	

Run #	Condition - Motion	Phase	Comments
	8: DI 2 SI - Motion	3: Phase 3	
	3: SI 2 DI - No Motion	3: Phase 3	
	4: DI 2 SI - No Motion	2: Phase 2	
	2: DI - No Motion	4: Phase 4	
	7: SI 2 DI - Motion	1: Phase 1	
	6: DI - Motion	4: Phase 4	
	5: SI - Motion	2: Phase 2	
	1: SI - No Motion	1: Phase 1	

Bibliography

[1] D.M. Pool. *Objective Evaluation of Flight Simulator Motion Cueing Fidelity Through a Cybernetic Approach*. 2012.

[2] L.R. Young. On Adaptive Manual Control. *Ergonomics*, 12:635–674, 1969.

[3] D.T. McRuer and H.R. Jex. A Review of Quasi-Linear Pilot Models. *IEEE Transactions on Human Factors in Electronics*, HFE-8 No 3(3), 1967.

[4] M. Mulder, D.M. Pool, D.A. Abbink, E.R. Boer, P.M.T. Zaal, F.M. Drop, K. Van Der El, and M.M. Van Paassen. Manual Control Cybernetics: State-of-the-Art and Current Trends. *IEEE Transactions on Human-Machine Systems*, 48(5):468–485, 2018.

[5] H.A. van Grootheest, D.M. Pool, M.M. van Paassen, and M. Mulder. Identification of Time-Varying Manual Control Adaptations with Recursive ARX Models. (January), 2018.

[6] W. Plaetinck, D.M. Pool, M.M. van Paassen, and M. Mulder. Online Identification of Pilot Adaptation to Sudden Degradations in Vehicle Stability. *IFAC-PapersOnLine*, 51(34):347–352, 2019.

[7] A. Popovici, P.M.T. Zaal, and D.M. Pool. Dual Extended Kalman Filter for the Identification of Time-Varying Human Manual Control Behavior. (June), 2017.

[8] P.M.T. Zaal. Manual Control Adaptation to Changing Vehicle Dynamics in Roll–Pitch Control Tasks. *Journal of Guidance, Control, and Dynamics*, 39(5):1046–1058, 2016.

[9] P.M.T. Zaal and D.M. Pool. Multimodal Pilot Behavior in Multi-Axis Tracking Tasks with Time-Varying Motion Cueing Gains. (January), 2014.

[10] R.A. Hess. Modeling Human Pilot Adaptation to Flight Control Anomalies and Changing Task Demands. *Journal of Guidance, Control, and Dynamics*, 39(3):655–666, 2016.

[11] R.A. Hess. Modeling Pilot Control Behavior with Sudden Changes in Vehicle Dynamics. *Journal of Aircraft*, 46(5):1584–1592, 2009.

[12] M.M. van Paassen and M. Mulder. Identification of Human Operator Control Behaviour in Multiple-Loop Tracking Tasks. *IFAC Proceedings Volumes*, 31(26):455–460, 1998.

[13] D.T. McRuer, R.E. Magdaleno, and G.P. Moore. A Neuromuscular Actuation System Model. *IEEE Transactions on Man-Machine Systems*, 9(3):61–71, 1968.

[14] R.J.A.W. Hosman and J.C. van der Vaart. Effects of vestibular and visual motion perception on task performance. *Acta Psychologica*, 48(1-3):271–287, 1981.

[15] J.R. Schiess and V.R. Roland. Kalman Filter Estimation of Human Pilot Model Parameters. (November 1975):1–7, 1975.

[16] W.H. Levison, S. Baron, and D.L. Kleinman. A Model for Human Controller Remnant. *IEEE Transactions on Man-Machine Systems*, 10(4):101–108, 1969.

[17] A. M. de Vroome, A. R. Valente Pais, D. M. Pool, M. M. van Paassen, and M. Mulder. Identification of Motion Perception Thresholds in Active Control Tasks. (August):1–20, 2009.

[18] F.M. Nieuwenhuizen, P.M.T. Zaal, M. Mulder, M.M. Van Paassen, and J.A. Mulder. Modeling Human Multichannel Perception and Control Using Linear Time-Invariant Models. *Journal of Guidance, Control, and Dynamics*, 31(4):999–1013, 2008.

[19] D. M. Pool, M. Mulder, M. M. Van Paassen, and J C. Van Der Vaart. Effects of Peripheral Visual and Physical Motion Cues in Roll-Axis Tracking Tasks. *Journal of Guidance, Control, and Dynamics*, 31(6):1608–1622, 2008.

[20] P.M.T. Zaal, D.M. Pool, M. Mulder, M.M. Van Paassen, and J.A. Mulder. Identification of Multimodal Pilot Control Behavior in Real Flight. *Journal of Guidance, Control, and Dynamics*, 33(5):1527–1538, 2010.

[21] P.M.T Zaal, D.M. Pool, Q.P. Chu, M. Mulder, M.M. Van Paassen, and J.A. Mulder. Modeling Human Multimodal Perception and Control Using Genetic Maximum Likelihood Estimation. *Journal of Guidance, Control, and Dynamics*, 32(4):1089–1099, 2009.

[22] P.M.T Zaal, D.M. Pool, M. Mulder, and M.M. Van Paassen. Multimodal Pilot Control Behavior in Combined Target-Following Disturbance-Rejection Tasks. *Journal of Guidance, Control, and Dynamics*, 32(5):1418–1428, 2009.

[23] F.M. Drop, D.M. Pool, M. Mulder, and H.H. Bülthoff. Constraints in Identification of Multi-Loop Feedforward Human Control Models. *IFAC-PapersOnLine*, 49(19):7–12, 2016.

[24] Magdaleno R.E R.L. Stapleford, D.T. McRuer. Pilot Describing Function Measurements in a Multiloop Task. (2), 1967.

[25] R.J.A.W. Hosman. *Pilot's Perception and Control of Aircraft Motions*. 1996.

[26] P.M.T. Zaal, D.M. Pool, J. De Bruin, M. Mulder, and M.M. Van Paassen. Use of Pitch and Heave Motion Cues in a Pitch Control Task. *Journal of Guidance, Control, and Dynamics*, 32(2):366–377, 2009.

[27] E.R. Boer and R.V. Kenyon. Estimation of Time-Varying Delay Time in Nonstationary Linear Systems: An Approach to Monitor Human Operator Adaptation in Manual Tracking Tasks. *IEEE Transactions on Systems, Man, and Cybernetics Part A:Systems and Humans.*, 28(1):89–99, 1998.

[28] L. R. Young, D. M. Green, J. L. Elkind, and J. A. Kelly. the Adaptive Dynamic Response Characteristics of the Human Operator in Simple Manual Control. Techn Note D-2255. *NASA contractor report. NASA CR. United States. National Aeronautics and Space Administration*, (July 1963):1–97, 1963.

[29] P.M.T. Zaal and B. Sweet. Identification of Time-Varying Pilot Control Behavior in Multi-Axis Control Tasks. pages 1–20, 2013.

[30] R.F.M. Duarte, D.M. Pool, M.M. van Paassen, and M. Mulder. Experimental Scheduling Functions for Global LPV Human Controller Modeling. *IFAC-PapersOnLine*, 50(1):15853–15858, 2017.

[31] T.K. Mandal and Y. Gu. Online Pilot Model Parameter Estimation Using Sub-Scale Aircraft Flight Data. *2016 AIAA Guidance, Navigation, and Control Conference*, (January), 2016.

[32] J. Rojer, D.M. Pool, M.M. van Paassen, and M. Mulder. UKF-based Identification of Time-Varying Manual Control Behaviour. *IFAC-PapersOnLine*, 2019.

[33] L. Ljung. *System Identification Theory for the User*, volume 25. 1987.

[34] N. Roggenkämper, D.M. Pool, F.M. Drop, M.M. van Paassen, and M. Mulder. Objective ARX Model Order Selection for Multi-Channel Human Operator Identification. 2016.

[35] K. van der El, J. Morais Almeida, D.M. Pool, M.M. van Paassen, and M. Mulder. The Effects of Motion Feedback in Manual Preview Tracking Tasks. (August), 2017.

[36] A.K. Tangirala. *Principles of System Identification: Theory and Practice*. 2015.